

Synthesis and Characterization of Gold Nanostructures for Healthcare Applications

Navadecho Chankhunthod

Submitted in accordance with the requirements for the degree
of Doctor of Philosophy

School of Chemical and Process Engineering (SCAPE)
The University of Leeds

December 2019

Dedicate to my family

Declaration

The candidate confirms that the work submitted is his own, except where work which has formed part of jointly authored publications has been included. The contribution of the candidate and the other to this work has been explicitly indicated below. The candidate confirms that appropriate credit has been given within the thesis where reference has been made to the work of others.

S. Ye, S. D. Connell, J. R. McLaughlan, L. Roach, Z. Aslam, **N. Chankhunthod**, A. P. Brown, R. Brydson, R. J. Bushby, K. Critchley, P. L. Coletta, A. F. Markham and S. D. Evans. *Advanced Functional Materials*, 2020 (Just accepted)

The work in this paper contributes to Chapter 5 of my thesis. I contributed in EELS experiment section including characterizations and discussions for the first draft of the paper.

N. Chankhunthod, Z. Aslam, K. Critchley, S. D. Evans and R. Brydson, *J. Phys.: Conf. Ser.*, 2017, **902**, 012007

The work in this paper contributes to Chapter 6 of my thesis. I contributed all experimental data including characterization and discussion and wrote the first draft of the paper.

This copy has been supplied on the understanding that it is copyright materials and that no quotation from the thesis may be published without proper acknowledgement.

© 2019 The University of Leeds and Navadecho Chankhunthod

Acknowledgement

I would like to express my sincere gratitude to my supervisor Prof. Rik Brydson, for his kindness, and for continuous support and guidance throughout my PhD study. No words can express my appreciation to him. I am very lucky to have the best professor to be my Ph.D. supervisor. Without his supervision, this thesis would not be possible.

I also would like to special thanks Prof. Stephen Evans and Dr. Kevin Critchley, my co-supervisors, for their support and suggestions in their MNP group meetings. I also wish to thank Dr. Sunjie Ye for her generous recommendations. Special thanks to Lucien Roach and Tahani Albogami for their useful help and guidance for the synthesis of gold nanorods. Additionally, my sincere thanks to Dr. Joshua Cottom for guiding me in COMSOL modelling.

My special thanks go to Leeds Electron Microscopy and Spectroscopy Centre (LEMAS), School of Chemical and Process Engineering (SCAPE), University of Leeds for technical instrument support including: Dr. Nicole Hondow, Mr. Stuart Micklethwaite, Mr. John Harrington, and especially Dr. Zabeada Aslam, who provided continual help with my TEM studies. I would also like to thank Dr. Faith Bamiduro for supporting me with experimental work and particle characterization.

I would like to thank Prof. Andrew Nelson, Dr. Nicola William and Dr. Joshua Owen who provided valuable help on the membrane interaction with nanoparticles.

Specially, I would express my sincere thanks to my Thai friends: Dr. Yothin Chimupala and Dr. Thanisorn Mahatnirunkul for numerous assistances, inspiration and making this journey joyful and fun. I would like to give all acknowledgement to Ministry of Higher Education, Science, Research and Innovation, The Royal Thai Government, Thailand for a financial support throughout my study in UK.

Specially, I deeply thank my parents for their continuous support and for continued inspiration and encouragement to me. This thesis is for you, my dearest father and mother.

Lastly, I would express my special thanks to Miss Onruthai Phondon for her endless love and support over the years. Will you marry me?

Navadecho Chankhunthod

Abstract

Functionalized gold nanostructures with well-defined geometry and controlled optical properties can potentially play an important role in healthcare applications such as biosensing, photocatalysis, drug delivery, photothermal therapy and imaging due to their unique properties. This thesis aims to develop a novel Au nanostructure for healthcare applications, using an effective synthesis protocol in order to produce a suitable Au nanostructure with NIR absorption, high thermal stability and low toxicity. Well-controlled, reproducible Au nanostructures with NIR absorption spectra, including gold nanoparticles (NPs), nanorods (NRs), nanobipyramids (NBPs) and nanotriangles (NTs) have been synthesised using a wet-chemical synthesis approach and characterized using dynamic light scattering and transmission electron microscopy.

The optical and plasmonic properties of the Au nanostructures were investigated using uv-vis spectroscopy, finite element modelling (FEM) and STEM/low-loss EELS analysis was employed. EELS results exhibited good agreement with uv-vis spectra and FEM modeling and revealed the size- and shape-dependent plasmonic properties and showed that NIR absorption can be altered by increasing the curvature of particles.

The thermal stability of Au nanostructures, which is important for photothermal therapy applications, was investigated using in-situ TEM heating. It was found that the thermal stability of Au nanostructures decreased in the order : AuNPs > AuNTs > AuNBPs > AuNRs. The proposed useful temperature ranges whereby heating does not significantly affect the optical properties were up to 100°C, 200°C, 800°C, for CTAB-capped AuNRs, CTAB-capped AuNBPs and CTAC-stabilized AuNTs, respectively. The thermal stability of particles was increased by surface functionalization of the NPs from a CTAB coating, through a PSS coating and finally to a silica coating. Thermal deformation arose from curvature-driven surface diffusion.

Finally, the biocompatibility of Au nanostructures, in terms of the effect of size, morphology, and surface coating, was investigated by their electrochemical interaction with a model membrane based on DOPC on an Hg/Pt electrode. Only smaller Au nanostructures with a diameter of ca. 20 nm exhibited a significant interaction. However, the effect of the surface coating was found to be a more significant effect with the order of interaction with the model membrane ranging from CTAB > PSS > CTAC > citrate coated Au nanostructures.

Thus overall, potential biocompatible candidates for healthcare applications are proposed to be citrate-, PSS- or silica-coated gold nanostructures with NIR absorption and dimensions larger than approximately 20-25 nm.

Table of Contents

<i>Declaration</i>	<i>iii</i>
<i>Acknowledgement</i>	<i>iv</i>
<i>Abstract</i>	<i>v</i>
<i>Table of Contents</i>	<i>vi</i>
<i>List of Tables</i>	<i>xi</i>
<i>List of Figures</i>	<i>xii</i>
<i>List of Abbreviations</i>	<i>xix</i>
Chapter 1 Introduction	1
1.1 Background and rationale	1
1.2 Aims and objectives	3
1.3 Layout of the thesis	4
1.4 List of publications and presentations	5
1.5 References	5
Chapter 2 Literature Review	7
2.1 General Information on plasmonic metallic nanostructures	7
2.1.1 Silver nanoparticles.....	7
2.1.2 Gold nanoparticles (AuNPs)	7
2.1.3 Gold nanorods (AuNRs)	8
2.1.4 Gold nanobipyramids (AuNBPs)	8
2.1.5 Gold nanotriangles (AuNTs).....	8
2.2 Wet-chemical synthesis methods	8
2.2.1 AuNPs	10
2.2.2 AuNRs.....	10
2.2.2.1 Seed mediated growth method	10
2.2.2.2 Silver-assisted seedless method.....	11
2.2.3 Gold nanobipyramids (AuNBPs)	12
2.2.4 Gold nanotriangles (AuNTs).....	12
2.3 Growth mechanism of Au nanostructures	13

2.3.1 Gold nanospheres.....	13
2.3.2 Gold nanorods.....	13
2.3.3 Gold nanobipyramids.....	15
2.3.4 Gold nanotriangles.....	15
2.4 Surface modification of AuNRs.....	15
2.3.1 Surface coating.....	16
2.3.2 Ligand exchange.....	16
2.4 Surface plasmon resonance (SPR) of metallic nanostructures.....	16
2.4.1 Bulk and surface plasmon resonances.....	16
2.4.2 Localized surface plasmon resonance (LSPR).....	17
2.4.2.1 Fundamentals of electromagnetic interaction.....	19
2.5.1 Mie Theory and Gans approximation.....	20
2.6 Previous EELS studies on Au nanostructures.....	22
2.7 Surface plasmon oscillation decay.....	27
2.8 Application of gold nanostructures in healthcare application.....	27
2.8.1 Plasmon-enhanced spectroscopy and sensing applications.....	27
2.8.2 Photothermal therapy and imaging.....	27
2.9 Thermal stability of Au nanostructures.....	28
2.9.1 Melting point of gold nanoparticles.....	28
2.9.2 Observations from photothermal therapy.....	29
2.9.3 Deformation mechanism.....	30
2.10 Toxicology of Au nanostructures.....	31
2.11 Electrochemical behavior of phospholipid membrane for nanoparticle interaction.....	33
2.12 Conclusion.....	33
2.13 References.....	34
<i>Chapter 3 Synthesis and characterisation methods.....</i>	<i>44</i>
3.1 Synthesis methods.....	44
3.1.1 Synthesis of AuNPs.....	44
3.1.1.1 Reagents.....	44
3.1.1.2 Synthesis procedure.....	44
3.1.2 Synthesis of CTAB capped AuNRs.....	46
3.1.2.1 Reagents.....	46

3.1.2.2 Synthesis procedure	46
3.1.3 Synthesis of AuNBPs.....	48
3.1.3.1 Reagents:	48
3.1.3.2 Synthesis procedure.....	48
3.1.4 Synthesis of AuNTs	50
3.1.4.1 Reagents:	50
3.1.4.2 Synthesis procedure.....	50
3.1.5 Surface modification of AuNRs.....	50
3.1.5.1 PSS coating.....	52
3.1.5.2 Citrate stabilized AuNRs	52
3.1.5.3 Silica coating	52
3.2 Characterization methods	52
3.2.1 Ultraviolet and visible (UV/vis) spectroscopy.....	52
3.2.1.1 Basic principles.....	52
3.2.1.2 Practical details.....	53
3.2.2 COMSOL modelling on uv/vis spectra.....	54
3.2.3 Dynamic light scattering (DLS) and Zeta potential measurement.....	54
3.2.3.1 Basic principles of DLS.....	55
3.2.3.2 Basic principles of Zeta potential measurement.....	56
3.2.3.3 Practical details.....	56
3.2.4 Transmission electron microscopy (TEM)	57
3.2.4.1 Basic principle of conventional TEM (CTEM).....	57
3.2.4.2 Practical details.....	60
3.2.5 Scanning transmission electron microscopy (STEM).....	61
3.2.5.1 Basic principles of STEM [33-35, 39].....	61
3.2.5.2 Basic principles of electron energy-loss spectroscopy (EELS).....	63
3.2.5.1 Practical details.....	64
3.3 References	64
<i>Chapter 4 Structural characterization and the optical properties of synthesized gold nanostructures</i>	<i>69</i>
4.1 Characterization of AuNPs.....	69
4.2 Characterization of AuNRs	73
4.3 Characterization of AuNBPs.....	81
4.4 Characterization of AuNTs	85
4.5 Surface modification of AuNRs.....	89

4.6 Summary of results	92
4.7 References	92
<i>Chapter 5 Plasmonic properties of gold nanostructures.....</i>	95
5.1 Finite Element modelling of the optical response of isolated AuNPs and AuNRs in a medium.....	95
5.1.1 Modelling methodology.....	95
5.1.2 Results.....	96
Au nanospheres.....	96
Au nanorods.....	98
5.2 Experimental procedure	101
5.2.1 Gold nanostructures	101
5.2.2 Plasmonic characterization using electron energy loss spectroscopy – experimental details	101
5.3 Results	102
5.3.1 The experimental EELS spectra of Au nanostructures	102
Au nanospheres.....	102
Au nanorods.....	104
Au nanobipyramids.....	106
Au nanotriangles.....	108
5.3.2 Coupling between Au nanostructures	110
5.4 Conclusion.....	111
5.5 References	112
<i>Chapter 6 Thermal stability of gold nanostructures.....</i>	115
6.1 Experimental procedure	116
6.1.1 Preparation of gold nanostructures	116
6.1.2 Materials Characterization and TEM heating experiments.....	116
In-situ TEM heating experiments	116
6.2 Results and discussion.....	118
6.2.1 The effect of size and geometry on the thermal stability of Au nanostructures	118
Citrate-stabilized AuNPs	118
CTAB-capped AuNBPs.....	121
CTAC-stabilized AuNTs	123
Fast-ramp heating	124

6.2.2 The effect of surface modification on the thermal stability of Au nanostructures	126
6.2.3 Thermal deformation mechanism	130
Low temperature in-situ TEM heating experiments	130
6.3 Conclusions	131
6.4 References	132
<i>Chapter 7 Interaction of gold nanostructures with a model phospholipid monolayer membrane.....</i>	<i>135</i>
7.1 Experimental procedure	136
7.1.1 Preparation of gold nanostructures	136
7.1.2 Materials characterization	136
7.1.3 Electrochemical flow system	137
7.2 Results and discussion.....	139
7.3 Conclusion	147
7.4 References	148
<i>Chapter 8 Conclusions and future work.....</i>	<i>150</i>
8.1 Research summary	151
8.2 Main findings from the research.....	152
8.3 Future work	153

List of Tables

Table 2-1: Summary of key literature articles concerned with the synthesis of Au nanostructures with well-defined structures	9
Table 6-1: Summary of the rate of change of Au nanostructure morphology with respect to particle dimensions.	121
Table 7-1: Characteristics of the Au nanostructures tested using RCV	137

List of Figures

Figure 1–1: Schematic diagram of the number of publications which are related to the study of Au nanostructures for biomedical applications -searched from the Scopus database by using the keywords: gold AND nano* AND biomedical AND application in the title, abstract and keywords.	1
Figure 1–2: Schematic diagram of the number of publications which are related to the study of Au nanostructures in the field of surface plasmon and plasmonic searched from the Scopus database by using the keywords: gold AND nano* AND plasmonic AND surface plasmon in the title, abstract and keywords.	2
Figure 1–3: Schematic diagram of the number of publications which are related to the study of Au nanostructures in the field of thermal properties (in blue colour), searched from the Scopus database by using the keywords: gold AND nano* AND thermal properties AND deformation OR reshaping OR surface diffusion in the title, abstract, keywords, and in the field of toxicology (shown in red colour), by using of the keywords: gold AND nano* AND toxicity in the title, abstract.	3
Figure 2–1: schematic diagram illustrating the three primary synthesis methods for AuNRs with different rod structures. [figure taken from [14]]	12
Figure 0–2: schematic diagram representing the structural development of Au nanostructures including AuNRs, AuNBPs, and AuNTs. The arrows with green colour illustrate the growth direction of nanostructures. [figure adapted from [40]].....	14
Figure 2–3: Colour of Au colloids with different aspect ratio AuNRs. [figure taken from[56]].	17
Figure 2–4: (a) Schematic diagram of LSPR excitation in spherical metal nanoparticles, (b) corresponding absorption spectrum in the visible region [figure taken from [57]].....	18
Figure 2–5: LSPR excitation of metal nanorods along two different axes (a) longitudinal and (b) transverse plasmon modes and (c) their corresponding absorption spectrum. [figure taken from [57]].....	19
Figure 2–6: The simulated LSPR excitations of an AuNBP presenting 4 distinct plasmonic resonance modes labelled as B-E. [Image taken from [19]].....	21
Figure 2–7: The simulated LSPR excitation of an AuNT showing a dipolar plasmonic resonance at 776 nm. [figure taken from[61]]	22
Figure 2–8: TEM bright field micrograph of AuNTs with an average edge length of about 60 nm and their plasmonic resonance spectrum. [figure taken from [22]].....	22
Figure 2–9: TEM image, EELS spectra and intensity map of the spatial distribution of the surface plasmon at 2.45 eV for AuNPs with different particle sizes of 25 and 35 nm [64].	23

Figure 2–10: Examples of EELS spectra of AuNRs and maps of the spatial distribution of the plasmon resonance mode, with associated TEM images. [a-d) figures taken from [64] and e-f) figures taken from [63]]	24
Figure 2–11: A comparison between simulations and experimental EELS spectra and intensity maps of the plasmon resonance modes of AuNRs. Image taken from [65].	25
Figure 2–12: Example of EELS spectra of AuNBPs and maps of the spatial distribution of the different plasmon resonance modes, together with a STEM HAADF image. [figure taken from [69]].....	26
Figure 2–13: Example of EELS spectra and spatial distribution maps of surface plasmon resonance modes in AgNTs showing three resonance modes which are localised at positions indicated as A, B, and C position in b). [Image taken from [70]]	26
Figure 2–14: Experimental and theoretical melting point temperature versus diameter for gold nanoparticles. Figure taken from [82].	29
Figure 2–15: Heating profile and simulated deformation of AuNR with AR of 3.3 at 150°C. Figure taken from [87].....	31
Figure 2-16: RCV profile of DOPC and related phase of the phospholipids on the Hg/Pt at a certain potential.....	34
Figure 3–1: Flowchart representing the Au nanoparticles synthesis procedure.	45
Figure 3–2: Au nanorod synthesis procedure.	47
Figure 3–3: Au nanobipyramid synthesis procedure.	49
Figure 3–4: Au nanotriangle synthesis procedure.	51
Figure 3–5: a) schematic of a gold nanorod covered by positively charged CTAB and b) Surface modification of CTAB AuNRs with negatively charged PSS layer using a layer by layer technique, adapted from [12].....	51
Figure 3–6: A schematic diagram of UV-vis spectroscopy.....	53
Figure 3–7: Example of UV-vis spectra of Au NRs with different aspect ratios: a) showing the Au colloid colour [23] and; b) showing results for different aspect ratios from 1.5 to 3.5 [24].....	54
Figure 3–8: a) TEM image of NRs and b) angle-dependent decay rate vs plot. Data taken from [27, 28]......	56
Figure 3–9: Example of a) DLS output figure taken from [32] and b) Zeta potential curve obtained using Malvern Zetasizer ZS1 software.	57
Figure 3–10: schematic diagram showing the main components of a conventional TEM, taken from [33].	58
Figure 3–11: TEM bright field image (a), and HRTEM image (b) of gold nanoparticles with a selected area electron diffraction pattern shown in (c), figures taken from [38]......	60
Figure 3–12: Example of EDX spectra of Au nanoparticle sample.	61

Figure 3–13: schematic diagram showing the main components of dedicated STEM. Image taken from [33]. Note: in this case the electron gun is at the bottom of the column.....	62
Figure 3–14: schematic diagram representing STEM imaging modes using different detectors. Inset shows: 1) BF (bottom) and 2) HAADF imaging (top), taken from [33].....	62
Figure 3–15: Example of an EELS spectrum of metallic nanoparticles corresponding to: a) zero-loss and low-loss region of gold NPs [42]; and b) core-loss EELS region of silver NPs [34].....	63
Figure 4–1: AuNPs with successive seed growth steps: a) UV-vis spectra of AuNPs obtained at each growth step from the seed to step 10; b) TEM bright field images taken from samples extracted at the different growth steps; c) their respective size distributions derived from TEM imaging; d) the uv-vis extinction peak maxima at different particle diameters derived from the TEM images.....	70
Figure 4–2: Intensity-weighted DLS particle size distribution curves of AuNPs for the different growth steps with average hydrodynamic diameters indicated.	72
Figure 4–3: TEM average size versus DLS size distribution of the AuNP samples, using a straight line as a guideline of linear relationship between DLS and TEM size measurement with a slope of 0.87 and an intercept of 6.2.....	73
Figure 4–4: UV-vis absorption spectra of CTAB-capped AuNRs with various ARs. Inset shows the change in colour of as-synthesized AuNRs from purple to soft-pink colour indicating the increase in rod AR.	74
Figure 4–5: a) Longitudinal SPR absorption peak maxima of CTAB-capped AuNRs for different ARs. b) AR of as-synthesized CTAB-capped AuNRs as a function of the amount of silver nitrate added, using a straight line to draw a guideline of each point representing AR increased with an increase of amount of AgNO_3	74
Figure 4–6: a) TEM images of sample 1 which is CTAB capped AuNRs with ARs of 1.6 ± 0.3 (Length $\sim 36.1 \pm 4.2$ nm and Width $\sim 22.5 \pm 3.3$ nm); b) TEM images of sample 2 which is CTAB capped AuNRs with ARs of 2.3 ± 0.4 (Length $\sim 47.4 \pm 5.3$ nm and Width $\sim 20.6 \pm 3.2$ nm); c) TEM images of sample 3 which is CTAB capped AuNRs with ARs of 3.1 ± 0.6 (Length $\sim 52.6 \pm 5.0$ nm and Width $\sim 17.6 \pm 2.6$ nm); d) TEM images of sample 4 which is CTAB capped AuNRs with ARs of 3.5 ± 0.7 (Length $\sim 56.2 \pm 7.1$ nm and Width $\sim 16.2 \pm 2.5$ nm); e) TEM images of sample 5 which is CTAB capped AuNRs with ARs of 4.1 ± 0.3 (Length $\sim 60.6 \pm 6.8$ nm and Width $\sim 14.9 \pm 2.1$ nm); f) Size distributions of CTAB capped AuNRs sample 1 derived from TEM imaging, showing an AR of 1.6 ± 0.3 ; g) Size distributions of CTAB capped AuNRs sample 2 derived from TEM imaging, showing an AR of 2.3 ± 0.4 ; h) Size distributions of CTAB capped AuNRs sample 3 derived from TEM imaging, showing an AR of 3.1 ± 0.6 ; i) Size distributions of CTAB capped AuNRs sample 4 derived from TEM	

imaging, showing an AR of 3.5 ± 0.7 .; j) Size distributions of CTAB capped AuNRs sample 5 derived from TEM imaging, showing an AR of 4.1 ± 0.3 75

Figure 4–7: a) Electron diffraction pattern of a group of AuNRs shown in the image inset; b) HRTEM image of an AuNR, showing (220) lattice fringes along the axis and hence the growth direction of the rod..... 80

Figure 4–8: DLS results showing particle size distribution by intensity of CTAB-capped AuNRs with various ARs indicated by sample 1, 2, 3, 4, and 5..... 81

Figure 4–9: a) UV-vis absorption spectra of the three AuNBP samples exhibiting longitudinal SPRs at 800, 780, 760 nm for samples 1, 2 and 3, respectively; b) TEM micrographs of sample 1 before purification; and c) HRTEM showing a 0.234 nm lattice spacing corresponding to $\langle 110 \rangle$ growth direction in both the tip and middle of an AuNBP; d) Size distributions of CTAB-capped AuNBPs sample 1, showing an AR of 3.5 ± 0.3 82

Figure 4–10: UV-vis Absorption spectra of sample 1 of AuNBPs before and after purification (a) and their TEM images (b). 85

Figure 4–11: UV-vis spectra of AuNTs produced using different synthesis conditions denoted as samples 1 - 5. 86

Figure 4–12: a) HRTEM image of AuNTs in sample 1; TEM BF images of as-synthesized AuNTs from samples 1, 2, 4 and 5 are shown in b), c), d), and e), respectively; f) Size distributions of AuNT samples 1, 2, and 5 with average size of 38.4 ± 8.5 , 46.4 ± 6.0 , and 99.8 ± 24.4 nm, respectively..... 87

Figure 4–13: An example of dynamic light scattering results for AuNT sample 5, showing size distribution by intensity..... 88

Figure 4–14: UV-vis spectra of as-synthesized CTAB-capped AuNRs compared with PSS-AuNRs. 89

Figure 4–15: TEM images of a) CTAB coated-AuNRs (yellow), b) PSS modified-AuNRs (blue), and c) silica coated-AuNRs (black), illustrating the presence of a distinct surface layer surrounding AuNRs using colour lines drawing as a guideline to define surfactant layers. . 90

Figure 4–16: TEM-EDX spectra and maps from a) CTAB-rods and b) surface modified PSS-rods. 91

Figure 5–1: Modelling the extinction spectra of a 100 nm diameter AuNPs in water. Inset shows the electric field distribution excited from 575 nm plane wave. The plane wave incident radiation with a red arrow..... 96

Figure 5–2: Simulated extinction spectra of AuNPs in vacuum with increasing AuNP’s radius from $r=5$ nm to $r=50$ nm. 97

Figure 0–3: Comparison of measured (dash line) and simulated extinction spectra (solid line) of AuNPs..... 99

Figure 5–4: Simulated extinction spectra of an isolated AuNR (non-coating) in vacuum with an AR of 4.2. Inset shows the electric field distribution excited by an 860 nm plane wave (the longitudinal SPR mode) which is concentrated at the tips of the rod.....	98
Figure 0–5: Comparison of measured (red line) and simulated extinction spectra (blue line) of AuNPs with AR of 4.2.....	101
Figure 5–6: The shifts in simulated extinction spectra of a surface coated AuNR of AR= 4.2 resulting from different coating parameters.	100
Figure 5–7: The red-shift in simulated extinction spectra of PSS- and CTAB-coated AuNRs. Inset shows the layer of surface coating and the electric field distribution.....	100
Figure 5–8: simulated extinction spectra of a 3.2 nm thick CTAB-coated AuNR in a water medium $n=1.33$, with increasing AR from 1 to 5.....	101
Figure 5–9: TEM micrographs of AuNP with diameter of 20x25 nm: a) bright field image and b) HAADF image. c) SI map showing the plasmonic mode over the energy range 2.2 - 2.4 eV. d) EELS spectrum (following ZLP subtraction) at the position indicated by a blue box in a) illustrating a resonant peak at 2.36 eV (525 nm).....	103
Figure 0–10: Example of Gaussian fitting with the selected energy range (2.2-2.5eV) of the EELS spectrum for AuNPs with diameter of 20x25 nm. The Gaussian fitting illustrated the maxima peak at 2.360.01 eV.....	106
Figure 5–11: STEM micrographs of a single AuNR with AR of 2.6 (60.1 nm long and 23.8 nm width): a) bright field image and b) HAADF image. c) SI map showing the longitudinal and transverse plasmonic modes of the AuNR with the stated energy ranges. d) EELS spectra of the single AuNR at two different positions shown in a) by the blue and orange coloured boxes, showing resonant peaks at 1.74 eV (712 nm) and 2.38 eV (526 nm), respectively.	105
Figure 5–12: STEM micrographs of a longer AuNR with AR of 4.75 (75.4 nm long and 15.9 nm width): a) bright field image and b) HAADF image. c) SI map showing the SPR modes of the AuNR with the stated energy ranges. d) EELS spectra of the single AuNR at different positions shown in a) by the blue and orange coloured boxes, showing resonant peaks at 1.22 eV (1000 nm) and 1.80 eV (680 nm) along with a potential peak at 2.33 eV (535 nm), respectively.	106
Figure 5–13: a) STEM bright field image of AuNBP with AR of 3.1 (length/width of 68.8/22.4) with three different EELS data acquisition positions denoted as tip (A), side (B), and middle (C), respectively: b) STEM HAADF image: c) SI map showing the spatial distribution of SPR modes at the different positions with the stated selected energy ranges: d) EELS spectra of the AuNBP extracted from the positions indicated in the HAADF image in (a).....	107
Figure 5–14: a) STEM bright field image of an AuNBP with AR of 2.4 (length/width of 47.5/19.8) with different EELS data acquisition positions denoted as tip (A) and middle (C):	

b) STEM HAADF image c) SI map showing the spatial distribution of SPR modes at the different positions with the stated selected energy ranges: d) EELS spectra of the AuNBP extracted from the positions indicated in the HAADF image in (a).....	108
Figure 5–15: a) and b) Bright field STEM and HAADF images of an AuNT with an edge length of 74.48 nm. c) SI map illustrating three plasmonic modes with the selected energy ranges indicated. d) EELS spectra of the AuNT at the different locations indicated in (b): tip (A), centre (B), and edge (C).	109
Figure 5–16: a) and b) Bright field STEM and HAADF images of an AuNT with an edge length of 190 nm. c) SI map illustrating three plasmonic modes with the selected energy ranges indicated. d) EELS spectra of the AuNT at the different locations indicated in (b): tip (A), centre (B), and edge (C). (Sample courtesy of Dr Sunjie Ye)	109
Figure 5–17: STEM micrographs and their relative energy filtered SI maps over the stated energy ranges: a) two closely spaced spheres; b) a cluster of triangles; c) two triangles separated by a gap of a few nm; and d) a cluster of Au nanostructures.	110
Figure 5–18: STEM BF images of Au nanostructures, including: a) an unsymmetrical AuNP: b) an AuNR with hemispherical caps of different radii of curvature: and c) a large AuNT with very sharp tips, together with associated SI maps over the given energy ranges indicated.	111
Figure 6–1: In-situ TEM heating experimental set up: a) schematic of Si ₃ N ₄ heating chip; b) The TEM heating set up steps: 1) drop 2 µl of Au nanostructures on the back of heating chips; 2) mount TEM heating chip in TEM heating holder; 3) load TEM heating holder into the TEM; and 4) connect all wires with controller unit and set up heating experiment.....	117
Figure 6–2: TEM micrographs of TEM heating chip with selected AuNRs at the centre.	117
Figure 6–3: a) TEM micrographs of a 45 nm diameter citrate-stabilized AuNP at different temperatures: RT, 200°C, 600°C, 800°C and 1100°C; b) The change in particle diameter with temperature and the associated linear fit. Change the AR to particles diameter	118
Figure 6–4: a) TEM micrographs of a CTAB-coated AuNR with an AR of 3.82 (rod 4) at different temperatures: RT, 50°C, 150°C, 300°C, 600°C and 800°C.	119
Figure 6–5: a) TEM micrographs of CTAB-capped AuNBPs at different heating temperatures: RT, 200°C, 400°C, 600°C and 800°C; b) The change in AR with heating temperature for two different AuNBPs with an AR of about 2.5 (length 67.5 nm and width 26.6 nm).....	123
Figure 6–6: a) TEM micrographs of CTAC-stabilized AuNTs at different heating temperatures: RT, 600°C, 900°C, 1050°C and 1100°C; b) The change in edge length with heating temperature for AuNTs with initial edge lengths of 104.6 nm (black), 83.0 nm (red), and 69.2 nm (blue).....	125

Figure 6–7: Example of TEM images of fast ramp, in-situ TEM heating experiments on AuNRs and AuNPs. The TEM micrograph before heating is shown on the left and after heating is presented on the right hand side.	126
Figure 6–8: a) TEM micrographs of PSS-coated AuNRs with an AR of 3.83 (rod 2) at different temperatures: RT, 300°C, 600°C, 800°C and 1100°C; b) The change in AR with temperature and associated linear fits for different AR rods. Note: The change in dark blue graph is taken from AuNPs heat treatment.	127
Figure 6–9: a) Examples of TEM micrographs from in-situ TEM heating experiment on silica-coated AuNRs at different temperatures: RT, 300°C, 600°C, 800°C and 1100°C.	129
Figure 6–10: TEM images of AuNRs from in-situ TEM heating experiments at low temperature: a) 100 °C and b) 150 °C for 15 mins, illustrating surface melting starting from tip and redeposition in the middle of the rods. (c) TEM micrograph of an AuNBP during heat treatment at 250 °C for 15 mins, showing similar behaviour to the results from the AuNRs.	130
Figure 7–1: Schematic diagram of the electrochemical flow system (figure taken from Ref. [1])	138
Figure 7–2: Images of the experimental set up: a) flow cell and b) sample and electrolyte loading platform.....	139
Figure 7–3: DLS particle size distributions of dispersions of CTAB-AuNRs and PSS AuNRs.	140
Figure 7–4: RCV of DOPC coated on an Hg electrode in 0.1 mol.dm ⁻³ PBS before (black line) and after (red line) exposure to: a) 2.5 mmol.dm ⁻³ citrate-AuNP1 with particle size d~20.9 nm; b) 2.8 mmol.dm ⁻³ citrate-AuNP2 with d~36.6 nm; c) 3.2 mmol.dm ⁻³ citrate-AuNP3 with d~58.3 nm.	141
Figure 7–5: RCV of DOPC coated on an Hg electrode in 0.1 mol.dm ⁻³ PBS before (blue line) and after (red line) exposure to: a) 5nm-comercial citrate-AuNP; b) 50-nm-comercial-citrate-AuNP; c) 50-nm-inhouse-citrate-AuNP; and d) pure citrate. [Figure taken from Ref. [11]]	142
Figure 7–6: RCV of DOPC coated on an Hg electrode in 0.1 mol.dm ⁻³ PBS before (blue line) and after (red line) exposure to: a) pure 0.2 M CTAB; b) 17.2 mmol.dm ⁻³ CTAB-AuNR1 with an AR of 1.6; c) 18.4 mmol.dm ⁻³ CTAB-AuNR2 with AR of 3.1; d) 10.6 mmol.dm ⁻³ CTAB-AuNR3 with AR of 3.5.	144
Figure 7–7: RCV of DOPC coated on an Hg electrode in 0.1 mol.dm ⁻³ PBS before (blue line) and after (red line) exposure to: a) pure 0.2mg/10mL DI water PSS; b) 14.7 mmol.dm ⁻³ PSS-AuNR1 with an AR of 1.6; c) 14.2 mmol.dm ⁻³ PSS-AuNR2 with AR of 3.1; and d) 15.8 mmol.dm ⁻³ PSS-AuNR3 with AR of 3.5.	145

Figure 7–8: RCV of DOPC coated on an Hg electrode in 0.1 mol.dm⁻³ PBS before (blue line) and after (red line) exposure to 33.5 mmol.dm⁻³ CTAC-AuNTs with an edge length of 99.8 nm 146

Figure 7–9: Schematic view of NPs interaction with the phospholipid membrane, including a) deposited DOPC monolayer on the Hg surface; b) small NPs adsorbed on the monolayer with large interfacial contact area illustrated in blue area; and c) large NPs adsorbed on the monolayer showing smaller interfacial contact area. (Figure taken from Ref.[7]). 147

List of Abbreviations

AA	Ascorbic acid
AgNPs	Silver nanoparticles
AR	Aspect ratio
AuNBPs	Gold nanobipyramids
AuNPs	Gold nanoparticles
AuNRs	Gold nanorods
AuNTs	Gold nanotriangles
BDAC	Benzyltrimethylammonium chloride
BF	Bright field
CTAB	Cetyltrimethylammonium bromide
CTAC	Cetyltrimethylammonium chloride
CTEM	Conventional transmission electron spectroscopy
DDA	Discrete Dipole Approximation
DF	Dark field
DLS	Dynamic light scattering
DOPC	Dioleoyl-phosphatidylcholine
EDX	Energy dispersive X-ray spectroscopy
EELS	Electron energy loss spectroscopy
ELNES	Electron energy loss near field structure
EXELFS	Extended electron energy loss fine structures
FEM	Finite element modelling
FWHM	Full width half maximum
HAADF	High angle annular dark field
HRTEM	High resolution transmission electron microscope
LSPR	Localised surface plasmon resonance
MNPs	Metal nanoparticles
MUA	11-mercaptoundecaonic acid
NIR	Near infrared
PBS	Phosphate buffered saline
PEG	Polyethyleneglycol
PPA	Polyphthalamide
PSS	Poly(sodium-4-styrenesulfonate)
RCV	Rapid cyclic voltammetry
SAED	Selected area electron diffraction
SI	Spectroscopic Image

SPR	Surface plasmon resonance
STEM	Scanning electron microscope
TEM	Transmission electron microscope
UDP	Under deposition potential
ZLP	Zero loss peak

Chapter 1 Introduction

1.1 Background and rationale

The research area of Nanotechnology was originally proposed by Richard Feynman in 1959 [1] and is usually defined as the science and engineering of systems which have dimension < 100 nm to give size dependent property and function for specific applications. Progress in engineered nanomaterials has exponentially increased and one of the most widely used nanomaterials in biomedical applications are gold nanostructures [2, 3], as shown by the increase in the number of publications represented in figure 1-1. In part, this is due to the inertness of gold and potentially its low toxicity. Amongst the various morphologies, gold nanoparticles (AuNPs) and gold nanorods (AuNRs) have gained the most attention owing to their unique optical and electronic properties as well as their size-, shape and environment-dependent surface plasmon resonance (SPR) behaviour [4-6]. This is seen in figure 1-2. For biomedical application, ideally the SPR can be tuned into the NIR region, where tissue exhibits a low absorption of the light [4-6]. These issues highlight the importance of the study of synthesis methods and surface functionalization of Au nanostructures.

Number of publications

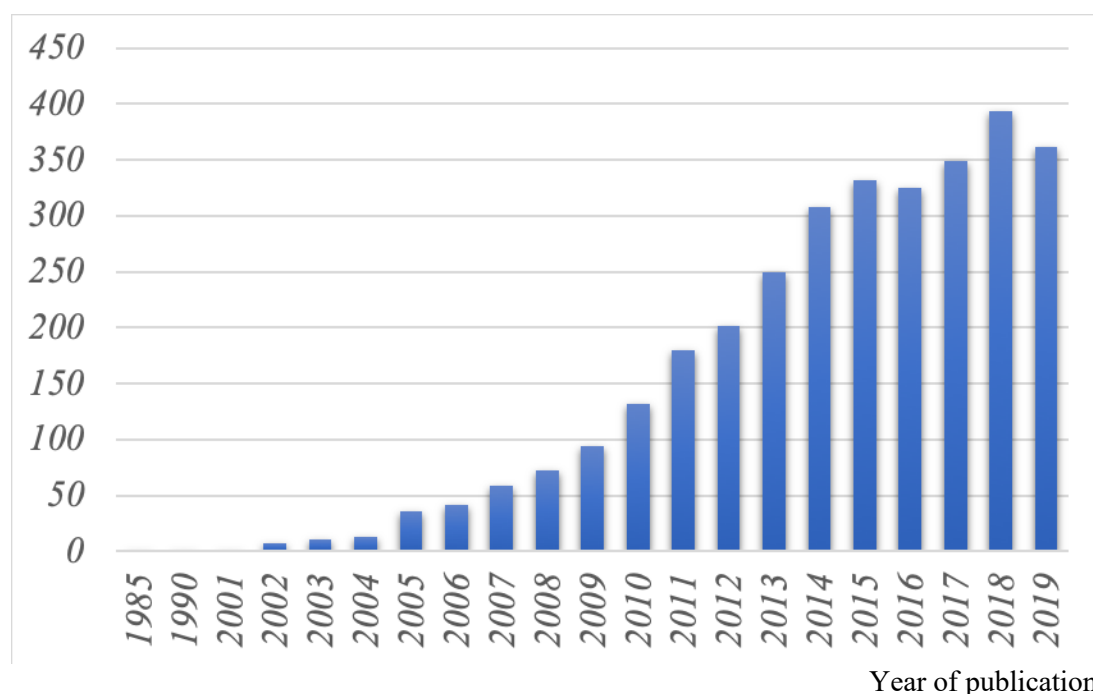


Figure 1-1: Schematic diagram of the number of publications which are related to the study of Au nanostructures for biomedical applications -searched from the Scopus database by using the keywords: gold AND nano* AND biomedical AND application in the title, abstract and keywords.

Number of publications

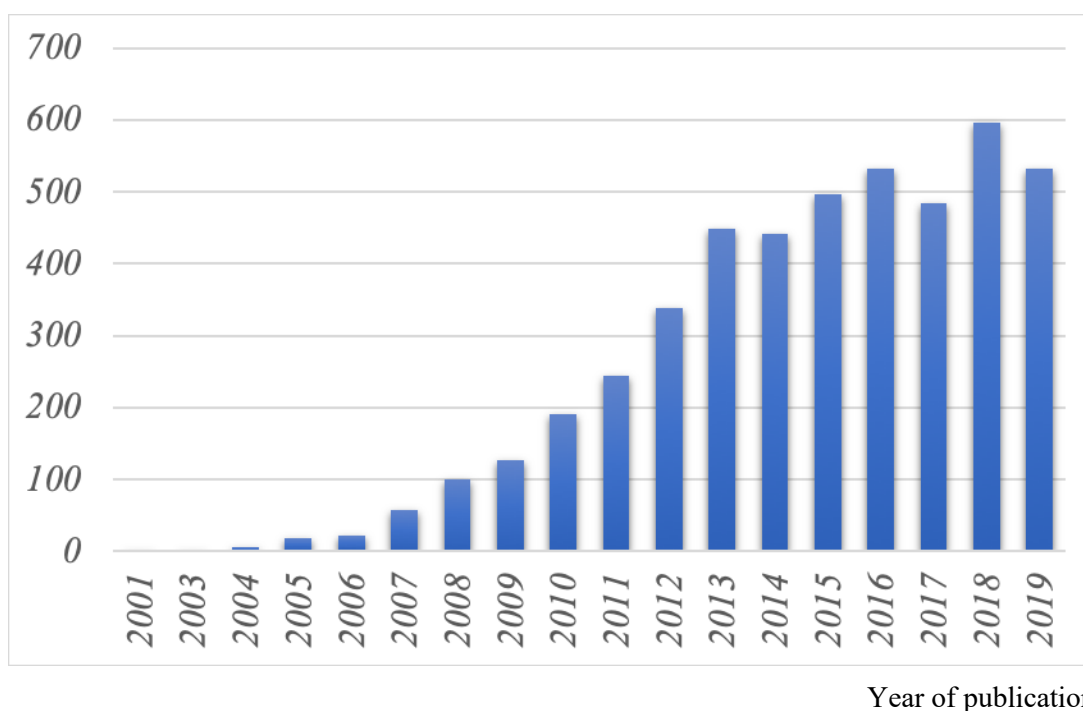


Figure 1–2: Schematic diagram of the number of publications which are related to the study of Au nanostructures in the field of surface plasmon and plasmonic searched from the Scopus database by using the keywords: gold AND nano* AND plasmonic AND surface plasmon in the title, abstract and keywords.

Au nanostructures such as AuNPs [7, 8] and AuNRs [8-10] have been exploited in photothermal therapy. This takes advantage of the light-heat conversion properties [11] of Au nanostructures. When Au nanostructures are excited using a laser energy tuned to the specific SPR of the particles, this can cause a temperature rise in the local environment [11, 12] which can be used to destroy surrounding cells. If Au nanostructures can be targeted to specific regions, such as cancerous tumours, this can be used as therapeutic tool.

However, these complex gold nanostructures have also been reported to change their morphology during heat treatment and issues may then arise about the effectiveness of heat-conversion as the SPR is very sensitive to particle size and shape. Thus, study of the thermal stability of Au nanostructures is a key topic that needs to be investigated in order to gain a better understanding of the properties, as illustrated in figure 1-3 (blue histogram).

Although gold nanostructures have been intensively studied in potential healthcare applications, there remains concern about their safety. Many researchers have studied the toxicology of Au nanostructures, as shown in figure 1-3, shown in the red histogram.

Number of publications

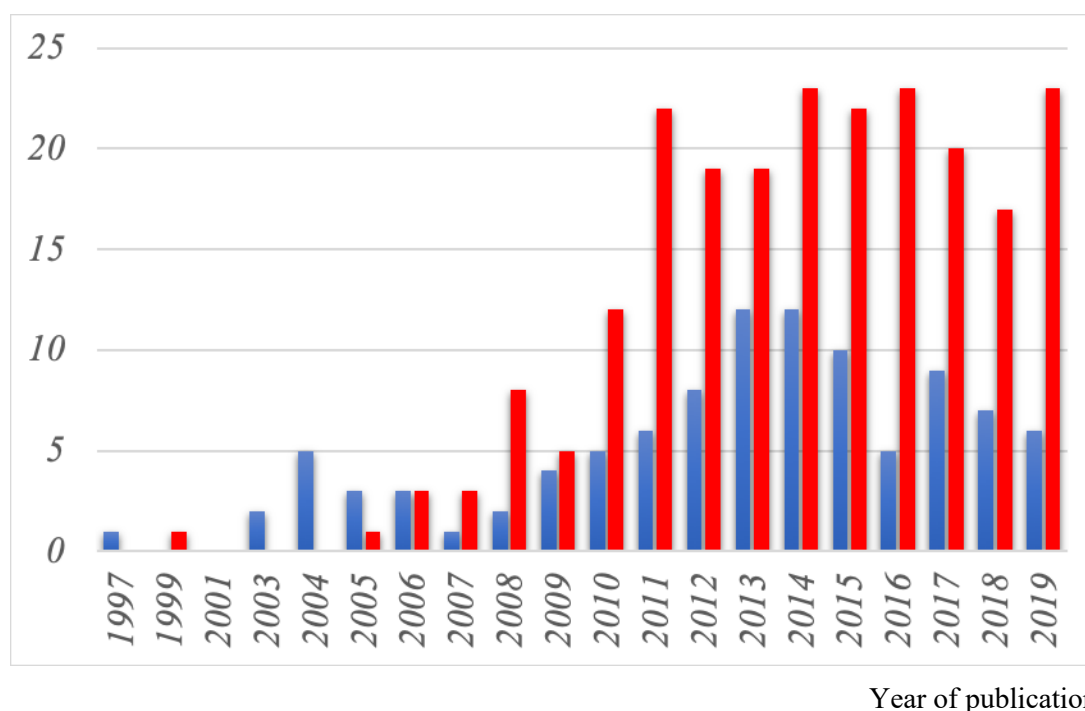


Figure 1–3: Schematic diagram of the number of publications which are related to the study of Au nanostructures in the field of thermal properties (in blue colour), searched from the Scopus database by using the keywords: gold AND nano* AND thermal properties AND deformation OR reshaping OR surface diffusion in the title, abstract, keywords, and in the field of toxicology (shown in red colour), by using of the keywords: gold AND nano* AND toxicity in the title, abstract.

1.2 Aims and objectives

In this research, I have chosen specific wet-chemical synthesis methods to produce homogenous Au nanostructures with well-defined morphologies, including gold nanoparticles (AuNPs), gold nanorods (AuNRs), gold nanobipyramids (AuNBPs) and gold nanotriangles (AuNTs).

The overall aim of this research was to develop a novel Au nanostructure for healthcare applications, using an effective synthesis protocol in order to produce a suitable Au nanostructure with NIR absorption, high thermal stability and low toxicity. This required some development of existing synthesis methods and an understanding of the growth mechanisms of Au nanostructures. It also required study of the optical, plasmonic, and thermal properties as well as the deformation mechanism of Au nanostructures.

Specific objectives of the research were as follows;

- 1) To conduct a literature review of previous work as background to this thesis;

- 2) To synthesise, via wet chemical synthesis methods, homogeneous Au nanostructures with well-defined shapes, including AuNPs, AuNRs, AuNBPs, and AuNTs with absorption spectra that can be tuned over NIR region;
- 3) To investigate the growth mechanism of Au nanostructures;
- 4) To investigate the effect of size, shape, and surface coating on the optical properties using uv-vis spectroscopy;
- 5) To investigate the plasmonic properties of individual Au nanoparticles and coupling effect of Au nanostructures using electron energy loss spectroscopy;
- 6) To investigate the effect of size, shape, and surface coating on the thermal stability of Au nanostructures during in-situ TEM heating;
- 7) To reveal the deformation mechanisms of Au nanostructures using low temperature in-situ TEM heating;
- 8) To investigate the effect of size and surface coating of Au nanostructures on their interaction with model phospholipid membranes;

1.3 Layout of the thesis

The thesis consists of eight chapters which may be summarised as follows:

Chapter 1 includes the background rationale of the research, the overall aims and objectives of the study and an outline of the thesis structure.

Chapter 2 introduces the background of Au nanostructures including AuNPs, AuNRs, AuNBPs, and AuNTs especially their synthesis methods, growth mechanisms and surface modification. Previous work on their plasmonic behaviour, thermal stability and toxicological behaviour is also reviewed in this chapter.

Chapter 3 reviews the synthesis methods used in the thesis as well and describes the principles and practical details of the characterization methods employed.

Chapter 4 presents the characterization of synthesized Au nanostructures using dynamic light scattering (DLS) and transmission electron microscopy (TEM). UV-vis spectroscopy is used to examine the optical properties of Au nanostructures.

Chapter 5 describes and discusses the characteristic plasmonic properties of the Au nanostructures by comparing results obtained from uv-vis spectroscopy, simulated spectra and EELS measurements.

Chapter 6 describes the thermal properties of Au nanostructures using in-situ TEM heating experiments. Thermal deformation mechanisms are discussed.

Chapter 7 presents a toxicological study of Au nanostructures via study of the electrochemical interaction with a model phospholipid monolayer membrane.

Chapter 8 summarizes the research and discussed the potential for future study.

1.4 List of publications and presentations

Part of this work has been published in the paper as following;

S. Ye, S. D. Connell, J. R. McLaughlan, L. Roach, Z. Aslam, N. **Chankhunthod**, A. P. Brown, R. Brydson, R. J. Bushby, K. Critchley, P. L. Coletta, A. F. Markham and S. D. Evans. *Advanced Functional Materials*, 2020 (Just accepted)

For this paper, I contributed in EELS experiment section including characterizations and discussions for the first draft of the paper.

N. **Chankhunthod**, Z. Aslam, K. Critchley, S. D. Evans and R. Brydson, *J. Phys.: Conf. Ser.*, 2017, **902**, 012007

It was presented at the Electron Microscopy and Analysis Group Conference 2017 (EMAG2017) at MMC2017 in Manchester, UK in a poster presentation session.

1.5 References

- [1] Feynman, R.P. *There's Plenty of Room at the Bottom: An Invitation to Enter a New Field of Physics*. Presented at the Annual Meeting of the American Physical Society, December 29, 1959, California Institute of Technology, Pasadena, CA. <http://www.zyvex.com/nanotech/feynman.html>.
- [2] Elahi, N., Kamali, M., Baghersad, M.H., *Recent biomedical application of gold nanoparticles: A review*. Talanta, 2018. **184**: p. 537-556
- [3] Zhao, P., Li, N., Astruc., D., *State of the art in gold nanoparticle synthesis*. Coord. Chem. Rev., 2013. **257**: pp. 638-665
- [4] Cao, J. Sun, T., and Grattan, H.T.V. *Gold nanorods-based localized surface plasmon resonance biosensors: A review*. Sensor and Actuators B: Chemical, 2014. **195**: p.332-351.
- [5] Murphy, C. J. et al. *Anisotropic metal nanoparticles: Synthesis, assembly, and optical applications*. J Phys Chem B, 2005. **109**: 13857–13870.
- [6] Dreaden, E. C. et al., *The golden age: gold nanoparticles for biomedicine*. Chem. Soc. Rev, 2012. **41**: 2740–2779.
- [7] Gharatape, A. et al., Engineered gold nanoparticles for photothermal cancer therapy and bacteria killing. RCS Adv., 2016. **6**: 111482-111516.

- [8] Riley, R. S, and Day, E. S., *Gold nanoparticle-mediated photothermal therapy: applications and opportunities for multimodal cancer treatment*. Nanomedicine and nanobiotechnology, 2017. **9**(4): 10.1002.
- [9] Kang, X., et al. *Photothermal therapeutic application of gold nanorods-porphyrin-trastuzumab complexes in HER2-positive breast cancer*. Sci Rep, 2017. **7**: 42069.
- [10] Ali, K., et al. *AuNRs for inhibiting cancer cell migration Moustafa R*. Proceedings of the National Academy of Sciences, 2017. **114**(28): E5655-E5663.
- [11] Jiang, K., Smith, D.A., Pinchuk, A., *Size-Dependent Photothermal Conversion Efficiencies of Plasmonically Heated Gold Nanoparticles*. The Journal of Physical Chemistry C. 2013.**117** (51), 27073-27080.
- [12] Roper, D. K., Ahn, W., Hoepfner, M., *Microscale Heat Transfer Transduced by Surface Plasmon Resonant Gold Nanoparticles*. Journal of Physical Chemistry C, 2007. **111** (9): 3636-3641.

Chapter 2 Literature Review

This chapter provides background information on plasmonic metallic nanostructures, and specifically gold nanostructures, including gold nanoparticles (AuNPs), gold nanorods (AuNRs), gold nanobipyramids (AuNBPs), and gold nanotriangles (AuNTs) and their plasmonic properties. I review the simple wet chemical synthesis approaches used to fabricate Au nanostructures which absorb in the NIR region. A literature review of previous work on electron energy loss spectroscopy (EELS) and the thermal stability studies of Au nanostructures is also provided. Lastly, the toxicology of Au nanostructures is discussed.

2.1 General Information on plasmonic metallic nanostructures

2.1.1 Silver nanoparticles

Nobel metal nanoparticles (MNPs) have received much attention in wide range of research which has arisen from their size- and shape- dependent properties. Amongst these, silver nanoparticles (AgNPs) are a candidate for a wide range applications due to their high electrical and thermal conductivity, chemical stability and catalytic ability, surface-enhanced Raman scattering capability for medical imaging and sensing, and useful spectral range (400 - 530 nm) for bacterial and fungal protective activity [1, 2]. AgNPs can be synthesised by various techniques with diameters ranging from 1 – 100 nm. Wet chemical synthesis is one of the most popular routes for synthesis of AgNPs via chemical reduction. The use of weak reduction agents such as citrate results in large particles with a wide size distribution. On the other hand, use of a strong reductant such as borohydride generates smaller particles [3]. By increasing particle size, a tuneable optical absorption peak of AgNPs can be obtained between 400 nm and 530 nm [4, 5]. A major issue for silver nanostructures is their dissolution and the associated toxicity of silver ions that limits their use outside anti-microbial applications [1, 6].

2.1.2 Gold nanoparticles (AuNPs)

Since the introduction of the citrate stabilized synthesis method for AuNPs by Turkevich et al. [7] in 1951, AuNPs have become one of the most interesting materials due to their relatively easy synthesis process and their unique properties dependent on their size and shape. Due to these size-dependent properties, the development of fabrication methods for controlling size and shape has been intensively studied. In brief, the synthesis method for AuNPs involves the reduction of an Au precursor (usually HAuCl_4) by citrate as a reducing

and stabilizing agent under boiling conditions. The size of AuNPs can be controlled by varying the synthesis parameters and the ratio of Au and citrate [7, 8].

For AuNPs in aqueous solution, the optical absorption peak lies between 500 nm to 550 nm depending on particle size in the range from 1 to 100 nm [9, 10]. The absorption peak shifts to longer wavelength (red-shift) as the particle size increases. AuNPs have been widely used in biomedical applications such as biosensing [11], optical imaging [12] and photothermolysis of cancerous tissue [13].

2.1.3 Gold nanorods (AuNRs)

Gold nanorods (AuNRs) exhibit two distinct surface plasmon modes consisting of a longitudinal and a transverse resonance. The longitudinal surface plasmon resonance is the most interesting as the absorption resonance can be tunable into the near infrared (NIR) region that is the biologically preferred range for tissue penetration. NIR light can more deeply penetrate biological tissues with less absorption and scattering than for visible light [14-17].

2.1.4 Gold nanobipyramids (AuNBPs)

AuNBPs are another elongated Au nanostructure whose longitudinal surface plasmon mode can be tuned over the NIR region. AuNBPs consist of two pentagonal pyramids connected with the same base and lying along the same longitudinal axis. AuNBPs possess four distinct plasmonic resonances which are longitudinal and transverse modes similar to those of AuNRs, as well as the quadrupole and octupole resonance modes. Due to the unique reported properties of AuNBPs, such as their increased chemical stability and higher local electric field enhancement at the tip relative to AuNRs [18, 19], this makes them very promising plasmonic nanomaterials.

2.1.5 Gold nanotriangles (AuNTs)

Au nanotriangles have received much attention due to their excellent localized surface plasmon resonances (LSPR) and their unique shape which exhibits distinct dipolar and quadrupolar modes. Literature documents the production of uniform AuNTs with edge lengths ranging from 50 to 150 nm which results in a LSPR of between 600 to 800 nm [20-22]. The challenge of refining AuNTs via a facile synthesis method to achieve NIR region absorption is of interest in terms of healthcare applications.

2.2 Wet-chemical synthesis methods

Au nanostructures have been fabricated by various methods with several shapes and dimensions described in the literature. All synthesis methods are designed to optimize a well-

defined shape with a high yield. I briefly review some of the more useful methods below and a summary is provided in Table 2.1.

Table 2-1: Summary of key literature articles concerned with the synthesis of Au nanostructures with well-defined structures

Ref/Year	Sample	Synthesis method	Precursors
Turkevich et al./ 1951 [7]	AuNP, Diameter (D)~10-20 nm	Citrate reduction at 100°C	HAuCl ₄ , Sodium citrate
Natan et al./ 2000 [23]	AuNP, D~ up to 100 nm	Seeding mediated via citrate reduction	HAuCl ₄ , Sodium citrate
Murphy et al./ 2001 [24]	AuNP, D~ up to 180 nm	Reduction by AA and CTAB	HAuCl ₄ , AA, CTAB
Puntes et al./ 2011 [26]	AuNP, D~ up to 200 nm	Kinetically controlled seeded growth strategy via citrate reduction	HAuCl ₄ , Sodium citrate
Jenna et al./ 2001 [28]	AuNR, penta-twinned crystals (5% yield)	Seed mediated method with citrate capped seed	Seed: HAuCl ₄ , Sodium citrate, NaBH ₄ Growth: CTAB, HAuCl ₄ , AgNO ₃ , AA, Seeds
Nikoobakht and El-Sayed/ 2003 [29]	AuNR, single crystal (99% yield) with AR 1.5-4.7	Seed mediated method with CTAB capped seed	Seed: HAuCl ₄ , CTAB, NaBH ₄ Growth: CTAB, HAuCl ₄ , AgNO ₃ , AA, Seeds
Jenna et al./ 2005 [30]	AuNR, single crystal with smaller size (AR 2-5)	Silver-assisted seedless method	HAuCl ₄ , NaBH ₄ , CTAB, HAuCl ₄ , AgNO ₃ , AA, HCl
Lui et al./ 2005 [34] and Lee et al./ 2015 [35]	AuNBP, single twined crystals (<60% yield)	Seed-growth method with citrate capped seed	Seed: HAuCl ₄ , CTAB, NaBH ₄ Growth: CTAB, HAuCl ₄ , AgNO ₃ , HCl, AA, Seeds

Table 2-1: Summary of key literature articles concerned with the synthesis of Au nanostructures with well-defined structures (continued)

Ref/Year	Sample	Synthesis method	Precursors
Mirkin et al./ 2005 [36]	AuNT, 100-200 nm Edge length	Seed-growth method	Seed: Citrate, NaBH ₄ , HAuCl ₄ , Growth: CTAC, HAuCl ₄ , NaI, AA
Chen et al./ 2014 [22]	AuNT, 40-120 nm edge length	Seedless growth method	CTAC, HAuCl ₄ , KI, NaOH, AA

2.2.1 Gold nanoparticles (AuNPs)

The seeded growth of AuNPs using sodium citrate as a reducing agent with seed-mediated synthesis strategies to obtain nanoparticles up to and over 100 nm in diameter were introduced by Natan et al. [23]. Cetyltrimethylammonium bromide (CTAB) and ascorbic acid (C₆H₈O₆, AA) have also been used as reducing agents to produce monodispersed AuNPs up to 180 nm [24]. However, citrate-stabilized AuNPs appear better candidates for applications such as therapy and sensing because the sodium citrate can be easily exchanged with thiolated molecules on gold surface [25]. Thus, a method employing citrate reduction was used in this thesis following a modified seed growth method proposed by Puntès and co-workers [26] which can achieve AuNPs up to ~200 nm in diameter.

2.2.2 Gold nanorods (AuNRs)

The seed-mediated growth approach is commonly used for the synthesis of colloidal AuNRs because this method can provide high yields and a well-controlled aspect ratio of the rods [14, 27] using uncomplicated experimental steps. Furthermore, this route is easy to modify and flexible for producing more complicated shapes of Au nanostructure.

2.2.2.1 Seed mediated growth method

Jena and colleagues [28] demonstrated an easy way to grow AuNRs in 2001. There are two growth steps including the preparation of a seed solution and a growth solution. The seed solution is introduced by mixing ice-cold sodium borohydride (NaBH₄) to reduce gold chloride (HAuCl₄) in the present of sodium citrate. This produces citrate-capped Au seeds. Then a certain amount of seed solution is injected into the growth solution to allow the growth of NRs. The growth solution consists of a gold salt (HAuCl₄), a surfactant acting as a template for rod growth (CTAB), silver nitrate (AgNO₃) for controlling and improving the yield, and

AA as a reducing agent. The disadvantage of this route is low rod yield, ~5% compared to spherical particles, which requires further purification to obtain solely nanorods.

Nikoobakht and El-Sayed [29] made significant improvements in 2003 by using the strong stabilizer CTAB instead of citrate when forming the seed solution. In their work, the amount of Ag ions was modified to control the aspect ratio of the synthesized AuNRs. The seed solution was prepared via the reduction of HAuCl_4 by the rapid injection of ice-cold NaBH_4 in the presence of CTAB. The growth solution was prepared by mixing HAuCl_4 with CTAB followed by the injection of AgNO_3 into the solution. Then, the ascorbic acid was added. This method resulted in very high yields of AuNRs (~ 99%) with a uniform aspect ratio ranging from 1.5 to 4.7. In order to achieve higher aspect ratios up to 10, a slight modification was made by employing a new co-surfactant called BDAC in the growth solution. Because of the high quality of the rods with a controlled aspect ratio, this method has been widely employed for the growth of AuNRs over the last two decades.

2.2.2.2 Silver-assisted seedless method

In 2005, a further method was introduced by Jena [30] called the silver-assisted seedless method. This involved directly injecting NaBH_4 into the growth solution rather than the use of an AuNR seed solution. It provided smaller single crystalline AuNRs with an aspect ratio of 2 to 5 via a one-step synthesis route. AuNRs have also been used as seeds for the fabrication more complex structures of Au nanostructures such as nanocube, dog-bones, and dumbbell NRs [27, 31-33].

Due to the different output structures including penta-twinned and single crystal AuNRs via the various methods summarised in figure 2-1, it is of interest to study the synthesis of homogeneous and finely controlled AuNRs from both seed mediated methods with citrate-capped and CTAB-capped AuNRs, as well as the seedless methods. Also, complex anisotropic Au nanostructures including sharp-tip AuNRs (bipyramids), as well as Au nanoplates can be synthesized using these methods.


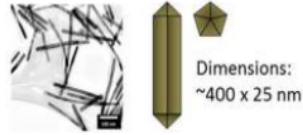

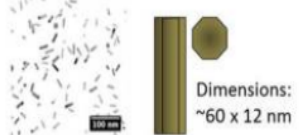
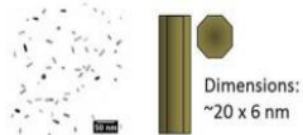
<u>Year</u>	<u>Seed</u>	<u>Growth Solution</u>	<u>AuNR Properties/Structure</u>	<u>Notes</u>	
2001	 3.5 nm Citrate AuNP	HAuCl ₄ , CTAB, Ascorbic Acid	 Dimensions: ~400 x 25 nm	<ul style="list-style-type: none"> • 5% rod yield (by shape) • AR 6-20 • Penta-twinned crystals 	
2003	 1.5 nm CTAB AuNP		HAuCl ₄ , CTAB, AgNO ₃ , Ascorbic Acid	 Dimensions: ~60 x 12 nm	<ul style="list-style-type: none"> • 95% rod yield (by shape) • 15% rod yield (total gold) • AR 1.5-5.0 • Single crystals
2005	-- No Seed BH ₄ ⁻ addition		HAuCl ₄ , CTAB, AgNO ₃ , Ascorbic Acid	 Dimensions: ~20 x 6 nm	<ul style="list-style-type: none"> • Undetermined yield • AR 1.5-5.0 • Single crystals

Figure 2–1: schematic diagram illustrating the three primary synthesis methods for AuNRs with different rod structures. [figure taken from [14]]

Among these wet-chemical synthesis methods, the seed mediated method proposed by Nikoobakht and El-Sayed [29] can provide high yields of rods as well as a better control of AR and is used in this thesis with kinetic control achieved using HCl in order to slow down the growth rate and achieve a higher rod AR.

2.2.3 Gold nanobipyramids (AuNBPs)

AuNBPs can be synthesized using a seed mediated growth method using citrate-stabilized seeds, as described by Lui et al [34]. This approach involves both a seed and growth step. This method offers an easy way to modify the AR of the bipyramids by varying the amount of seed. However, the yield of AuNBP was lower than 60% with a by-product of spherical particles. Thus purification of AuNBPs is required and surfactant depletion flocculation with BDAC has been examined by Lee et al [35]. BDAC with a higher micelle concentration than CTAB can induce flocculation of the high surface area bipyramids, while lower contact area spherical particles will remain in the supernatant.

2.2.4 Gold nanotriangles (AuNTs)

A seedless synthesis has been proposed for well-defined size and shape controlled Au nanotriangles through the reduction of a gold precursor (HAuCl₄) using cetyltrimethylammonium chloride (CTAC) as the shape directing agent. The original seed-mediated growth was proposed by Mirkin et al. [36] and can be used to prepare 100-200 nm edge length AuNTs. However, Chen et al. [22] proposed a very high yield (>90%) method for AuNTs with an edge length of 40-120 nm using a seedless synthesis approach. This method used CTAC mixed with KI, followed by the addition of the gold salt mixed with

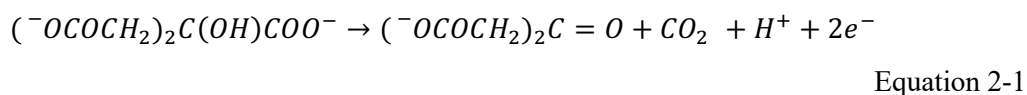
NaOH solution. AA was then introduced to reduce Au ions. Finally, pH control was employed by injecting a certain amount of NaOH. This provided monodispersed AuNTs via a one-step synthesis method which would be of benefit in providing tailored AuNTs with specific NIR absorption.

2.3 Growth mechanism of Au nanostructures

In typical wet chemical synthesis, precursors act as building blocks to create nuclei and crystalline structures. In this section, nucleation, growth and crystallization will be considered. The details of the growth mechanisms of Au nanostructures with different shapes including spheres, rods, bi-pyramids and triangular plates are described below.

2.3.1 Gold nanospheres

AuNPs can be synthesized by a citrate reduction method with a modified seed growth procedure. According to Turkevich et al. [7], sodium citrate acts as both a starting nucleation agent and a growth agent. This nucleating agent causes gold ions to chemically bind to form complexes which grow and rearrange to produce AuNPs. The sodium citrate oxidation reaction at 100°C reduces Au^{III} chloride to Au^I chloride and ultimately forms AuNPs. The chemical reaction equations are described in equations 2-1 to 2-3 [37]:



AuNPs of increasing size can be achieved by injecting more gold precursor at each growth step. The hypothesis of this mechanism is that initially formed AuNPs act as a seed and then Ostwald ripening occurs as large NPs grow as a result of atom transfer through solution from smaller and less stable NPs [26, 38, 39].

2.3.2 Gold nanorods

AuNTs can be synthesised with a modified seed-mediated method consisting of a seed step and subsequent growth steps. In the seed process, a single crystal gold nanoparticle seed is produced which is then used as a starting template for crystalline growth of rod shaped particles which growth along {110} planar facet, as schematically illustrate in figure 2-2.

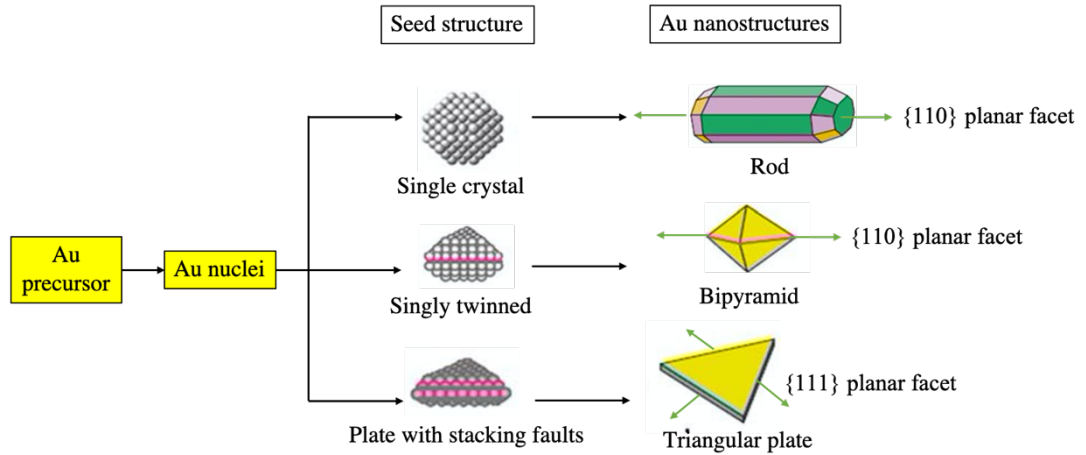


Figure 2–2: schematic diagram representing the structural development of Au nanostructures including AuNRs, AuNBPs, and AuNTs. The arrows with green colour illustrate the growth direction of nanostructures. [figure adapted from [40]]

CTAB is a cationic surfactant that plays an important role in controlling directional growth of the rod structure. It consists of a hydrophobic head and hydrophilic tail [41] that can form CTAB micelles binding gold chloride ions at the head and creating seed particles. Au ions are encapsulated in the presence of CTAB and guided to the tips as a result of electrical double layer integration between the micelles and the AuNRs. A difference in collision rate of the micelle at the tip and the side is the key to induce rod formation; a faster rate occurs at the tips rather than in the middle part of the rod [42]. Equation 2-4 presents the chemical reaction equation [42, 43] of AuNRs in the presence of CTAB. Au^{III} is reduced to Au^I by the addition of AA. AA acts as a weak reducing agent for the gold ions. The growth rate of AuNRs becomes faster when the AA concentration is increased.



Gold particles then result from electron transfer at the surface of the gold seed in the presence of CTAB, represented by equations 2-5 and 2-6



Adding varying amounts of silver nitrate allows better control in rod shape formation, although the effect of silver ions is not clearly understood. Nikoobakht and El-Sayed proposed that Ag^+ adsorbs at the gold surface and then forms AgBr, reducing the bromide ion charge density. Silver ions can cause repulsion between the headgroup of CTAB and the gold surface, resulting in templated elongation of AuNRs [29]. A second mechanism has been proposed by Murphy and co-workers, who suggested that AgBr adsorbs at surface facets slowing down rod formation and causing the formation of single crystalline AuNRs [44]. A higher of silver concentration result in an increase of ARs. By adding silver nitrate an ionic strength is decrease lead to an increase in the yield of the rods. HCl is introduced to lower the pH of the

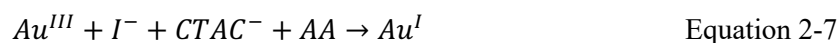
growth solution which reduces the amount of ascorbate anions which are a stronger reducing agent than AA. This leads to a decrease in the reducing power causing slower growth and providing higher aspect ratio NRs.

2.3.3 Gold nanopyramids

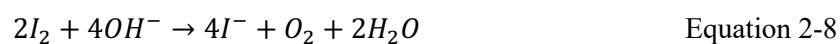
In the mechanism proposed for AuNRs, Ag ions are absorbed only at the surface of Au facets leading to growth of rods in one direction along the <110> growth axis [26]. Due to the use of citrate-capped seeds as a growth template, individually singly twinned seeds [45, 46] are formed which act as nuclei for bi-pyramid shape formation, see figure 2-2. Nanostructures then grow along the twinning axis leading to a step growth along this direction. Ag ions can stabilize an open step site and lead to the formation of a bipyramidal structure [46].

2.3.4 Gold nanotriangles

AuNTs can be fabricated via a one step seedless growth protocol with CTAC as surfactant and iodide ions as a structure-directing agent. From this synthesis method, a planar twinned structure is created as a gold seed to nucleate the growth of gold in {111} planar facet, illustrating in figure 2-2. pH control is achieved by adding sodium hydroxide during the synthesis. Au^{III} is rapidly reduced to Au^I by AA injection as illustrated in equation 2-7:



Finally, sodium hydroxide is again injected to induce reduction and the formation of AuNTs [22]:



2.4 Surface modification of Au nanorods (AuNRs)

AuNRs from the seed mediated method are covered by a positively charged CTAB bilayer. CTAB promotes the formation of the rod structure and also acts as a surfactant. CTAB can prevent agglomeration of AuNRs keeping them stable over several weeks.

Free CTAB molecules are very cytotoxic to human cells, however there are some arguments between toxicity of gold NPs. CTAB coating surrounding Au NRs is reported to be non-toxic [47, 48]. Attempts to remove excess CTAB from the synthesized AuNRs suspension have been intensively investigated [51]. Although excess CTAB molecules could be removed by centrifugation to purify AuNRs following synthesis, residual CTAB molecule may still be left on the surface of the nanoparticles. However if CTAB were completely removed, this may cause irreversible agglomeration of AuNRs. A low concentration of CTAB may result

in the low stability of AuNR suspensions and limit their use, e.g. CTAB-capped AuNRs in a high concentration of salt or buffer for sensing applications. Various surface modification techniques have been introduced to overcome this CTAB problem. There are two basic approaches consisting of either surface coating or ligand exchange.

2.3.1 Surface coating

Surface coating consists of layer by layer electrostatic deposition with negatively charged molecules to cover the positively charged surface of CTAB-capped AuNRs. Negatively charged molecules including poly(sodium-4-styrenesulfonate) (PSS) and polyphthalamide (PPA) are commonly used [47]. Moreover, silver [52] and silica [53] coating can also be employed in surface functionalization. The easy and fast procedure of surface modification is an advantage but the weak electrostatic absorption may cause stability problems in long-term application.

2.3.2 Ligand exchange

To improve stability and biocompatibility, ligand exchange to replace CTAB bilayers by a thiol-terminated ligand and form Au-S covalent bonds [47], such as thiol-terminated polyethylglycol (PEG) [54] or 11-mercaptoundecaonic acid (MUA) [55, 56]. However, PEG-coated AuNRs may result in incomplete removal of CTAB due to the large size of the PEG molecule. Thus, MUA which has a smaller size has been proposed for completely replacing CTAB.

2.4 Surface plasmon resonance (SPR) of metallic nanostructures

2.4.1 Bulk and surface plasmon resonances

As is well known in nanoscale science, the physical and chemical properties of a material significantly change and often exhibit unique size-dependent properties as compared to the bulk material. This results in a change in colour of Au colloids, AuNPs present a red colour, while AuNRs with various aspect ratios exhibit a range of different colours, as shown in figure 2-3.

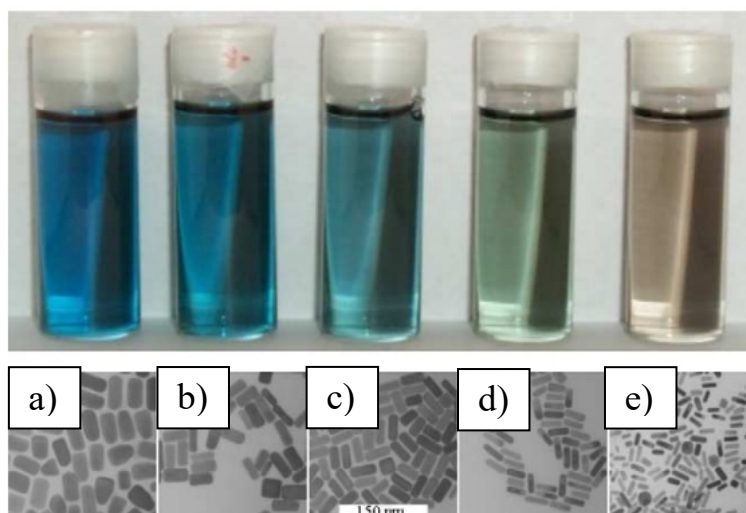


Figure 2–3: Colour of Au colloids with different aspect ratio AuNRs. [figure taken from[56]].

Bulk or volume plasmons are collective oscillations of the whole volume of free electron gas in a metal occurring when a metal interacts strongly with radiation such as light. It is a function of the free electron density, N , and in the simple free electron approximation, the volume plasmon energy varies as the square root of N . A surface plasmon resonance (SPR) arise from plasmons confined at the surface of metal particles. SPR is the phenomenon of collective electron oscillation of the metal particles with a specific resonance frequency, occurring when the specific frequency of incident light matches with the natural resonant frequency of the confined surface electrons [48, 58]. For an infinite, planar surface, the surface plasmon resonance energy is the volume plasmon energy divided by the square root of 2. For more complex shapes, the SPR energy will change and be shape and size dependent.

2.4.2 Localized surface plasmon resonance (LSPR)

A localized surface plasmon resonance (LSPR) is the spatially localized collective electron oscillation resulting from direct light irradiation. LSPRs are highly localized to individual particles and depend sensitively on the composition, size and shape of the material. Via the design and synthesis of nanostructures, manipulating the components, their shape and size, the LSPR absorption region of a particular nanostructure can be tuned through the visible, to the near infrared and infrared region of the electromagnetic spectrum providing applications in (photo)catalysis, biomedicine and sensing using a specifically designed wavelength.

Figure 2-4 illustrates the excitation of LSPRs in spherical nanoparticles. A LSPR occurs when the electric field of incident light interacts with free electrons in metal nanoparticles creating Coulombic repulsive forces to separate the free electron gas and the metallic ion cores. Then, (opposite) restoring forces are set up to return the free electrons to their original positions [59]. This LSPR oscillation of the free electrons leads to strong absorption of light in metal

nanoparticles, such as gold, silver and copper. There is only one strong absorption band for spherical nanoparticles. For AuNRs, they are two distinct absorption bands: longitudinal and transverse plasmon modes of electron oscillation corresponding to the long and short axes of the rods, respectively. The transverse plasmon band is sensitive to the width of the AuNRs, while the longitudinal plasmon band depends on the aspect ratio of the AuNRs. There is a red-shift in the absorption spectrum with increasing AR of the AuNRs, while the transverse mode stays roughly constant. However, both modes are very sensitive to the refractive index of the surrounding materials. The diagram illustrating the excitation of LSPR and absorption bands of nanorods is presented in figure 2-5.

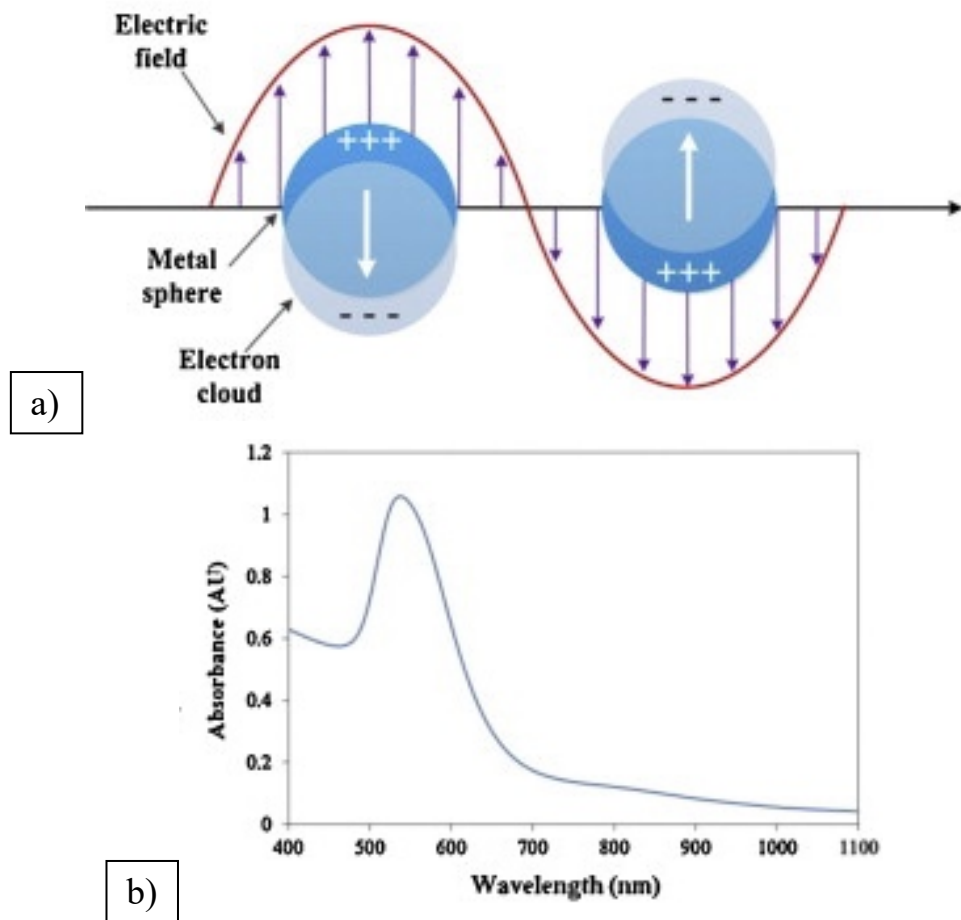


Figure 2-4: (a) Schematic diagram of LSPR excitation in spherical metal nanoparticles, (b) corresponding absorption spectrum in the visible region [figure taken from [58]]

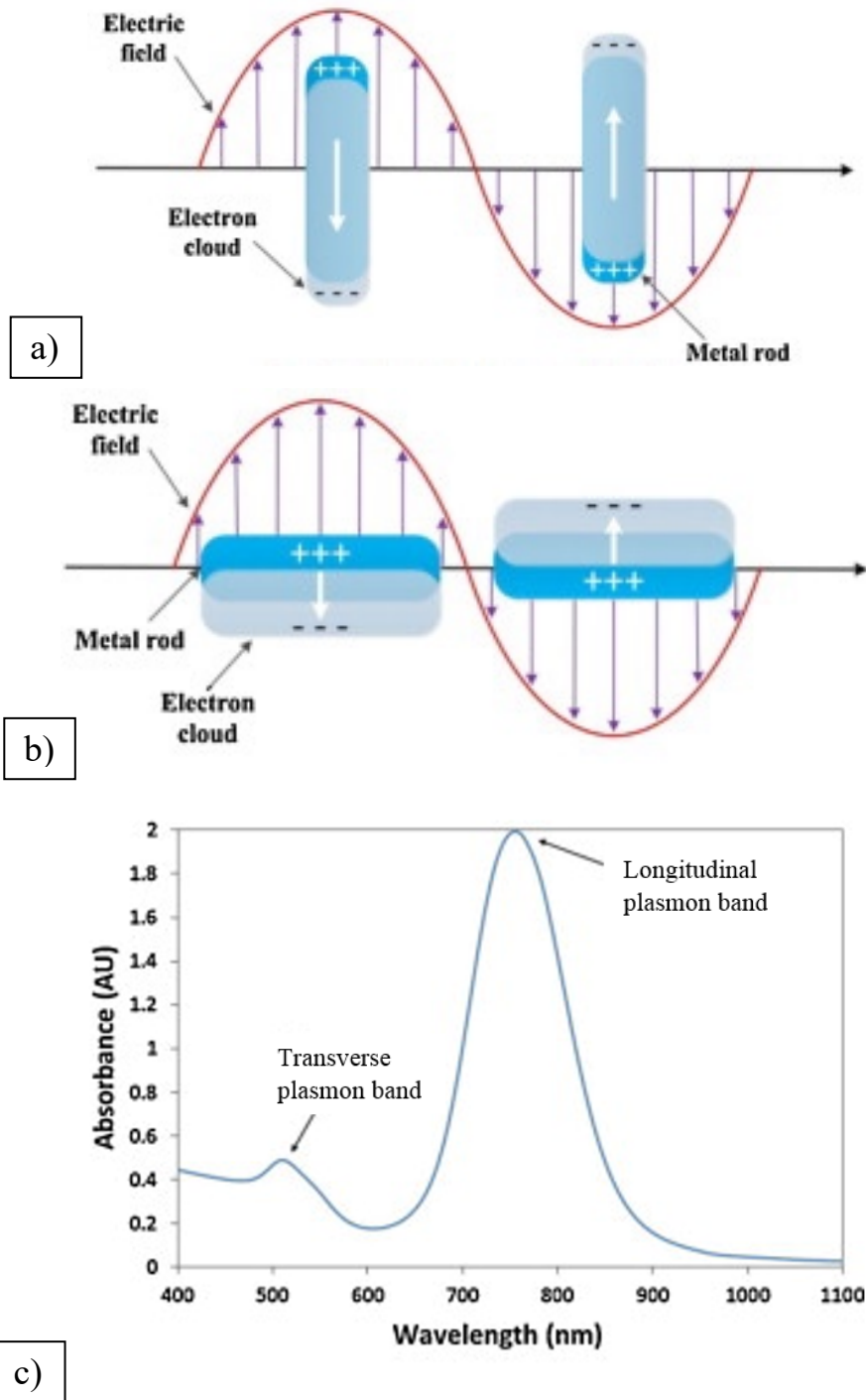


Figure 2-5: LSPR excitation of metal nanorods along two different axes (a) longitudinal and (b) transverse plasmon modes and (c) their corresponding absorption spectrum. [figure taken from [58]]

2.4.2.1 Fundamentals of electromagnetic interaction

Absorption, scattering and transmission all occur when light passes through a medium. When light interacts with a medium, it can cause absorption which may result in heat or can scatter

or reflect light through different angles. Alternatively light can pass directly through a medium without changing its original direction, called transmission.

All phenomena can be expressed by the Beer Lambert law where the interaction is proportional to the intensity of incoming light divided by the transmitted light. The absorbance (A) of the sample and the intensity of incidence (I_o) and transmission (I) are given by:

$$A = \log_{10} \frac{I_o}{I} \quad \text{Equation 2-11}$$

The absorbance is sometimes referred to as the extinction of light. The probability of extinction of the light is given by the extinction cross section (σ_{ext}) which is the result of both scattering and absorption as shown in equation

$$\sigma_{ext} = \sigma_{scat} + \sigma_{abs} \quad \text{Equation 2-12}$$

2.5.1 Mie Theory and Gans approximation

The excitation of LSPRs is strongly dependent on size, shape, and composition of the materials which leads to a strong absorption of light. According to Mie theory [48, 57-59], the solution of Maxwell's equation can express this light absorption in spherical particles through the extinction cross section (σ_{ext}), as shown in equation 2-13. This approximation assumes Rayleigh scattering involving plane wave monochromatic light incident on a spherical particle, which is smaller in size than the wavelength of the light, in a non-absorbing medium.

$$\sigma_{ext} \approx \sigma_{abs} = 4\pi k R^3 \text{Im} \left(\frac{\epsilon_p - \epsilon_m}{\epsilon_p + 2\epsilon_m} \right) \quad \text{Equation 2-13}$$

$$\sigma_{scat} = 8\pi k^4 R^6 \left| \frac{\epsilon_p - \epsilon_m}{\epsilon_p + 2\epsilon_m} \right|^2 \quad \text{Equation 2-14}$$

where R is radius of spherical particles, k is the wave number, ϵ_m and ϵ_p are the dielectric constants of the surrounding medium and the particles respectively. For Au and Ag nanospheres, the plasmonic absorption lies in the visible region which makes them useful for many applications.

In case of nanorods shape, the rods are categorized as ellipsoidal nanoparticles according the Gans approximation [60, 61]. Thus, to explain the optical properties of the rods, the LSPR is divided into two distinct plasmon modes. Gans theory can be expressed as in equation 2-15 [51], as a form of σ_{ext} . The aspect ratio (AR) is defined as length (L) divided by the width (2R) of the rods. A small change in these components may lead to a significant change in the optical properties.

$$\sigma_{ext} = \frac{2\pi N V \epsilon_m^{\frac{3}{2}}}{3\lambda} \sum_j \frac{\frac{1}{P_j^2} \epsilon_i}{(\epsilon_r + (\frac{1-P_j}{P_j}) \epsilon_m)^2 + \epsilon_i^2} \quad \text{Equation 2-15}$$

Where N refers to the electron density or number of electron per unit volume, ε_i and ε_r the imaginary and real parts of the dielectric constant of the particle while V is the rod volume and P_j is the polarization factor which refers to each axis.

$$P_{jlength} = \frac{1-e^2}{e^2} \left(\frac{1}{2e} \ln \left(\frac{1+e}{1-e} \right) - 1 \right) \quad \text{Equation 2-16}$$

$$P_{jwidth} = \frac{1-P_{jlength}}{2} \quad \text{Equation 2-17}$$

$$e = \sqrt{1 - \left(\frac{2R}{L} \right)^{-2}} \quad \text{Equation 2-18}$$

The LSPR of AuNBPs have been simulated using finite difference time domain (FDTD) simulation by Li et al. [19]. The computational model of AuNBPs consisted of two circular cones connected at the base and having spherical tips. The extinction spectra were calculated using equation 2-19 and the result is represented in figure 2-5 for AuNBPs with a length of 116.4 nm and width 38.0 nm. The coordinates in this equation are in the spherical system where φ is the azimuthal angle which integrates over all the spherical surface and θ is the polar angle between the plane wave excitation and the direction perpendicular to the length axis.

$$C_{ext} = \left\langle \frac{1}{2} [C_{ext}^{\parallel}(\theta) + C_{ext}^{\perp}(\theta)] \right\rangle_{\theta, \varphi} \quad \text{Equation 2-19}$$

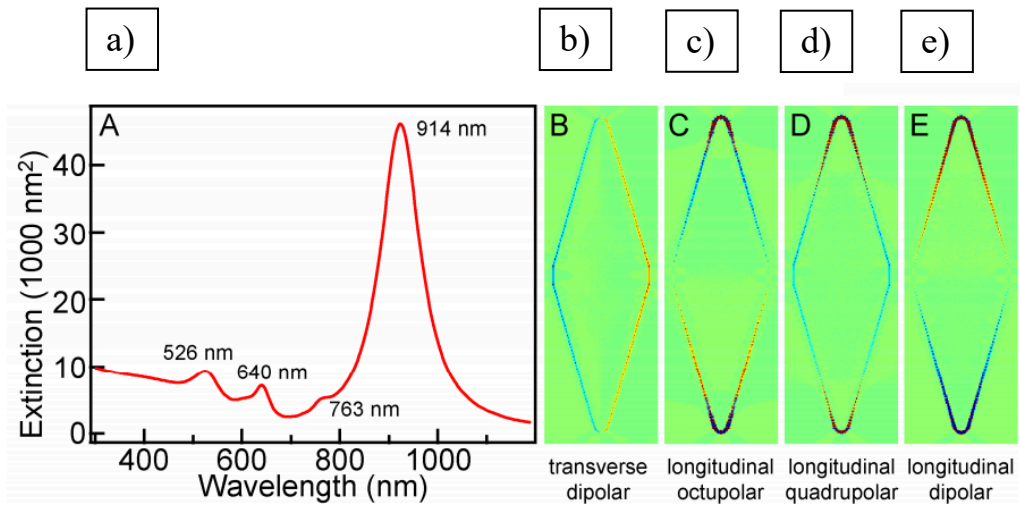


Figure 2-6: The simulated LSPR excitations of an AuNBP presenting 4 distinct plasmonic resonance modes labelled as B-E. [Image taken from [19]]

Figure 2-7 illustrates the calculated dipolar resonance of an AuNT with an edge length of 160 nm and a thickness of 30 nm showing the LSPR at 776 nm [62]. However, the experimental UV-vis spectra of synthesised AuNTs are slightly different from the simulations in that they exhibit a broad peak in the spectrum (figure 2-8). This result consists of three identified plasmonic modes, reviewed in the following EELS section.

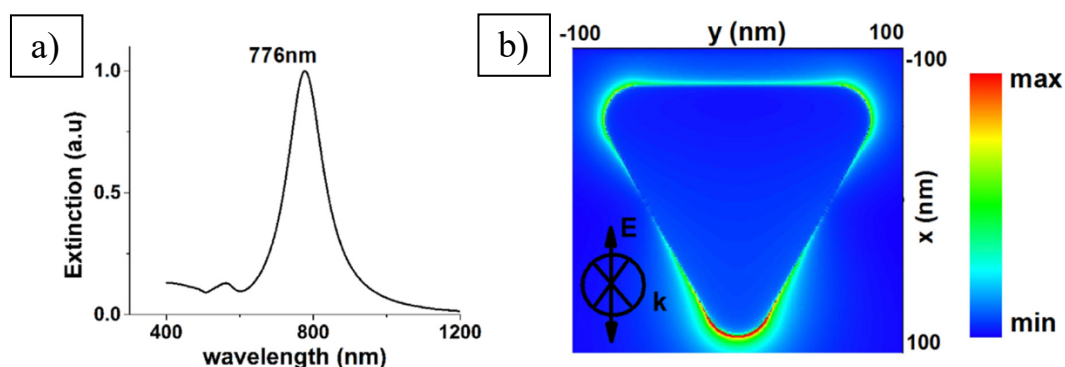


Figure 2–7: The simulated LSPR excitation of an AuNT showing a dipolar plasmonic resonance at 776 nm. [figure taken from[62]]

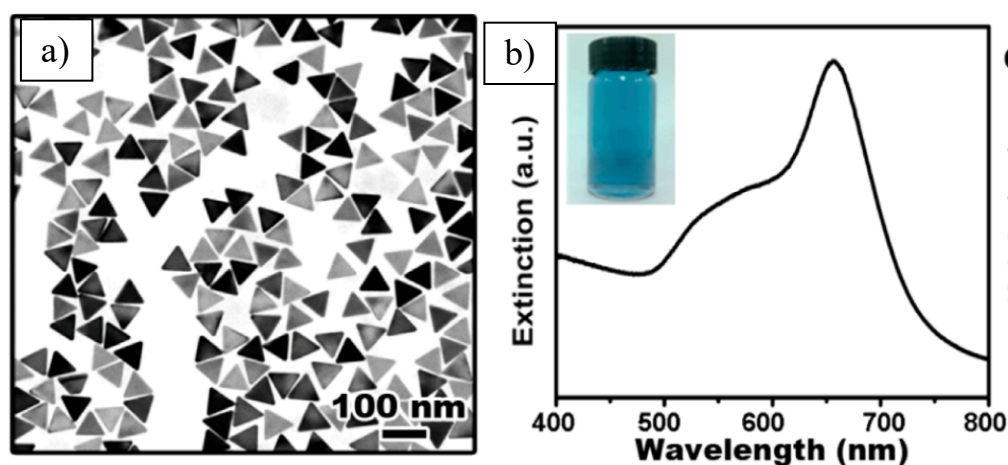


Figure 2–8: TEM bright field micrograph of AuNTs with an average edge length of about 60 nm and their plasmonic resonance spectrum. [figure taken from [22]]

2.6 Previous EELS studies on Au nanostructures.

Surface plasmons of metal nanoparticles including Ag and Au have received much attention over the past decade due to their potential use in surface-enhanced Raman spectroscopy and biomedicine applications [63, 64]. Metal nanoparticles are usually investigated by optical spectroscopy such as UV-vis spectroscopy. Such optical measurements generate a result that is an averaged measurement over all nanoparticles in the sample. Direct measurement of the optical properties of individual particles or single complexed nanostructures is required in order to be able to correlate a distinct particle with a particular surface plasmon energy and a plasmon mode. This can provide a more fundamental understanding of plasmonic metal nanoparticles.

Recent advances in TEM, particularly monochromated electron sources, can overcome this situation. Although the surface plasmon resonances in gold nanostructures are at very low energies and substantially overlap with the tail of the zero loss peak, high energy resolution

electron energy loss (EELS) techniques in STEM mode can be employed to investigate and provide localized spectra and surface plasmon modes of nanoparticles. This technique involves passing a focused electron beam close to the surface of metal nanoparticles (the moving electron beam creates a varying electric field) and acquiring the energy loss spectrum of the transmitted electrons [64, 65].

A number of researchers have studied EELS of Au nanostructures. Individual AuNRs and AuNPs were studied by Bosman and co-workers [65]. Similar results were published by N’Gom et al [64]. It was shown that for spherical Au particles, the surface plasmon energy was 2.45 ± 0.25 eV and it was shown that there was an unchanged position for two different particle sizes of 25 and 35 nm. EELS spectra of AuNPs are presented in figure 2-9. AuNRs exhibited two distinct plasmon resonances as seen in UV-vis absorption spectra. One plasmon resonance corresponds to the transverse electron oscillation with an energy about 2.5 eV. Significantly this resonance energy matches with the plasmon mode of AuNPs. The other plasmon mode is related to longitudinal oscillation of electrons along the long axis. It has been found that the longitudinal plasmon mode depends sensitively on the AR of the rod causing a red-shift in energy with increasing AR. An example of EELS spectra and plasmon resonance energy maps (as a function of spatial position) of AuNRs is presented in figure 2-10. Two plasmon resonance modes are seen corresponding to about 1.70 eV and 2.40 eV for the longitudinal and transverse modes, respectively.

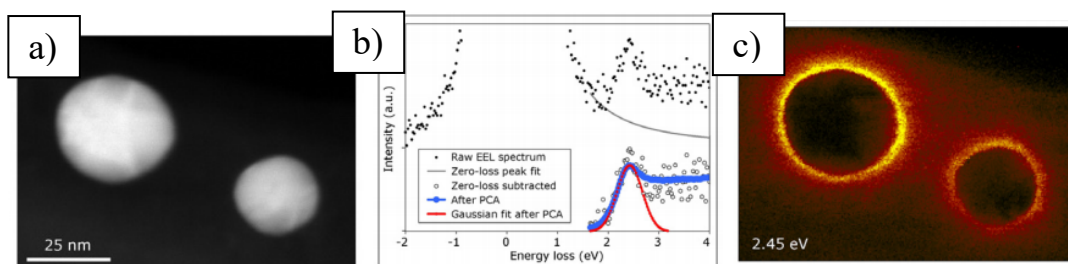


Figure 2–9: TEM image, EELS spectra and intensity map of the spatial distribution of the surface plasmon at 2.45 eV for AuNPs with different particle sizes of 25 and 35 nm [65].

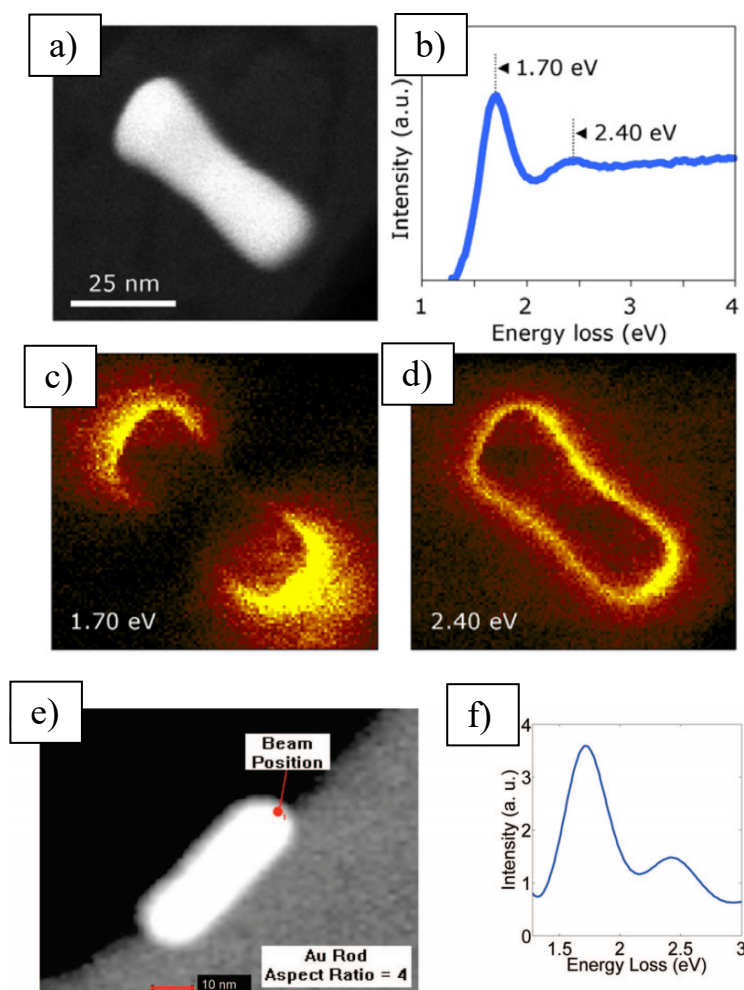


Figure 2–10: Examples of EELS spectra of AuNRs and maps of the spatial distribution of the plasmon resonance mode, with associated TEM images. [a-d] figures taken from [65] and e-f) figures taken from [64]]

Complex systems of Au-based NRs have also been theoretically studied in order to compare with EELS measurements. Calculated EELS spectra were reported by Chu et al. [66]. Figure 2-11 displays the calculated EELS spectra (top) compared with experimental result (bottom) that exhibit two plasmon resonance energies 1.76 eV and 2.34 eV for AuNRs, 85 nm in length and 27 nm in width.

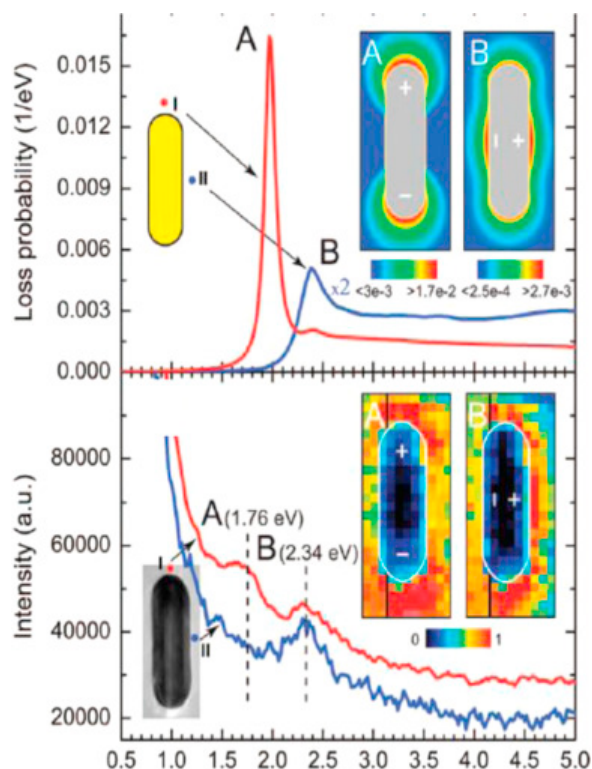


Figure 2–11: A comparison between simulations and experimental EELS spectra and intensity maps of the plasmon resonance modes of AuNRs. Image taken from [66].

Strong coupling between the plasmonic resonances of AuNRs have been studied by EELS. For two nanorods separated by a 10 nm gap, it was found that there was a red-shift in the LSPR, as compared to individual nanorods [64]. Moreover, the spatial distribution of plasmon modes of more complex Au nanostructures have been studied, for example dumbbell-shaped AuNRs [67], Au nanoprisms [68] as well as complex Ag-Au NRs [69].

Figure 2-12 shows that there are four distinct LSPR modes for AuNBPs [70]. The plasmon resonance modes are mainly located at the tip of the long axis, the tip of the short axis, and the sides of AuNBPs. It was found that the mode at the tips of the long and short axes relates to longitudinal and transverse LSPRs, respectively. Thus the position of the longitudinal mode depends on the AR of the bipyramid. Another mode is referred to as the quadrupolar LSPR located at the side that depends on the size and shape of the bipyramids.

For Ag nanotriangles, the work conducted by Nelayah et al. [71] presents EELS spectra of the nanoparticles and their plasmonic mode, as shown in figure 2-13. There are three plasmonic resonance modes occurring at the tip, the edge, and in the middle of the edge of an AgNT. According to the literature, the major peaks are located at 1.9, 2.9, and 3.4 eV for an AgNT with an edge length of 78 nm. The LSPR modes are size dependent in that there is an energy decrease (a red-shift in wavelength) as the edge length increases. Similar results were presented for AuNTs in the EELS work of Losquin et al. [72]. However, a slight change in

length, width, and composition of the nanostructure strongly affected the spatial distribution of the plasmon mode.

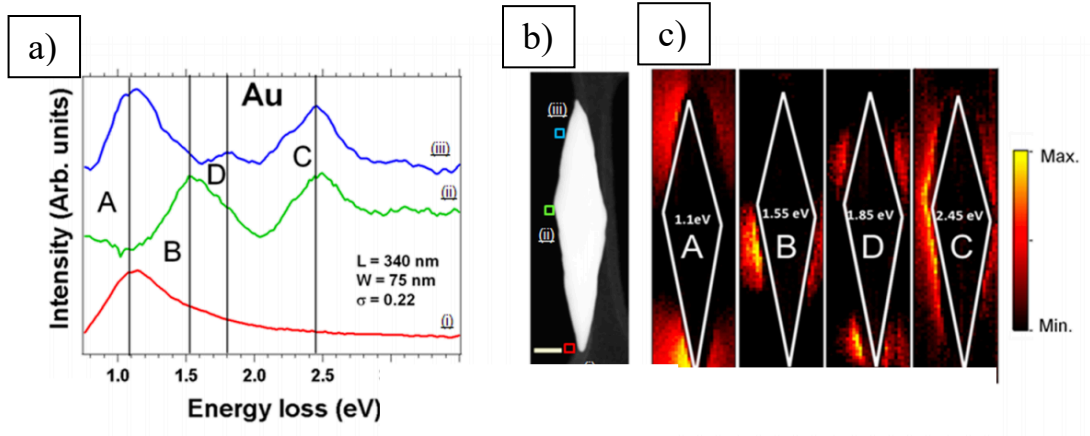


Figure 2-12: Example of EELS spectra of AuNBPs and maps of the spatial distribution of the different plasmon resonance modes, together with a STEM HAADF image. [figure taken from [70]]

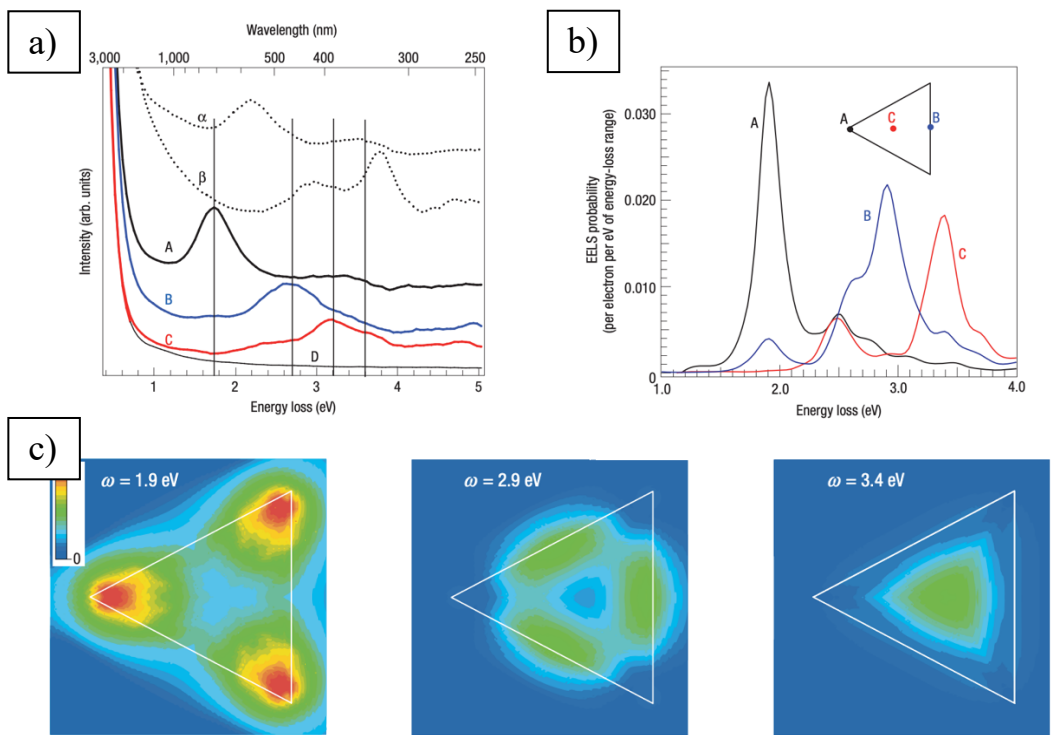


Figure 2-13: Example of EELS spectra and spatial distribution maps of surface plasmon resonance modes in AgNTs showing three resonance modes which are localised at positions indicated as A, B, and C position in b). [Image taken from [71]]

2.7 Surface plasmon oscillation decay

There are two types of relaxation of SPRs including radiative and non-radiative decay [73]. Firstly, radiative decay refers to strong light scattering from Au nanostructures and is very useful for biological imaging. For example, in case of AuNRs, NIR light is used for NIR imaging. The light scattering strongly depends on the AR of the rods [74]. Additionally, different types of scattering, both elastic and inelastic, are used in the techniques of fluorescence imaging or two-photon excitation.

Electron-phonon interactions resulting from electron-hole recombination are an example of non-radiative decay. Excited electrons transfer energy to the nanoparticle lattice during a timescale of ~ 1 ps, causing hot particle lattices. Then, the nanoparticle lattice exchanges energy with the surrounding medium within ~ 100 ps [75, 76]. This interaction is a phonon-phonon interaction. By inducing laser power of about 100 nJ, the excited electron can be heated up to several thousand Kelvin, however only a few tens of degrees increase in the temperature of the nanoparticle lattice and surrounding medium occurs [76]. This type of decay makes Au nanostructures with NIR resonance useful for photothermal therapy.

2.8 Application of Au nanostructures in healthcare application

Size, shape, structure and composition, as well as the refractive index of the surrounding medium are the keys for the unique optical properties of Au nanostructures. This promises a broad range of application such as catalysis, surface-enhanced Raman spectroscopy, sensing, especially in healthcare applications.

2.8.1 Plasmon-enhanced spectroscopy and sensing applications

One example of the application of LSPR is in sensors. The detection of the refractive index change surrounding a sensing surface is the basic principle of sensing [48]. Changes in refractive index alters the energy transferred to the free electron resulting in a shift in the LSPR, there may even be a small change arising from interaction with a biomolecule. Also, a strong local field enhancement induced at the gold surface during SPR can be used to improve the detection sensitivity for detecting a change in refractive index and to enhance the scattering from chemical species absorbed at the Au surface known as surface-enhanced Raman spectroscopy.

2.8.2 Photothermal therapy and imaging

Au nanostructures such as NPs [77], nanoshells [78], nanocages [79] and nanorods [76, 80] can be tuned so that the optical peak absorption lies in the NIR region. This is of interest since the NIR region contains a “water window” where light is highly transmitted through

biological tissue with little absorption. The nanostructures can absorb irradiated light and then generate heat. This heat generated during the relaxation of plasmon excitations can cause a localized photothermal effect resulting in heating and potential damage to nearby cells and tissues. The temperature that are required to kill tumour cells is defined above 40°C and the gold nanostructure can increase the temperature in the order of 40°C to 70°C [81, 82]. According to Haung et al. [81], breast cancer cells were damaged using AuNRs 820nm NIR laser at 35 W/cm². There was the local temperature increased to 47°C within 4-6 minutes. They also illustrated that the risen local temperature depended on nanoparticles' concentration. In 2018 Zhang et al. [82] illustrated the tumor cells' killing percentages were increased as the local temperature of the tumors increased from 43°C to 49°C. Zhou and co-workers [83] irradiated a 980 nm laser power at 1.0 W/cm² and it was found that the local temperature has risen over 50°C and caused damage to the tumor cells. Engineered Au nanostructures can be functionalised with biomolecules that enable specific targeting to the surface of tumour cells, which can then be photothermally destroyed producing no damage to surrounding healthy tissues. Moreover, imaging applications can be enabled by integrating the scattering and absorption properties of Au nanostructures for contrast enhancement in cancer detection.

2.9 Thermal stability of Au nanostructures

AuNRs appear a good candidate for photothermal therapy for cancer treatment. AuNRs can be tuned over the NIR region via a refined synthesis approach for AuNRs. In case of AuNRs, it has been shown that the longitudinal surface plasmon resonance is very sensitive to the AR of the rods. However, this means that even a small change of the AR can cause large differences in absorption spectra.

2.9.1 Melting point of Au nanoparticles

In 1975, Ph. Buffat and J-P Borel [84] demonstrated using in-situ TEM heating experiments that gold nanoparticles exhibited a size effect in relation to their melting temperature. Figure 2-14 shows the melting temperature decrease as a function of the decrease in nanoparticle diameter – this was undertaken with spherical nanoparticles. This, in principle, this enables the prediction of the melting temperature for relevant Au nanostructures.

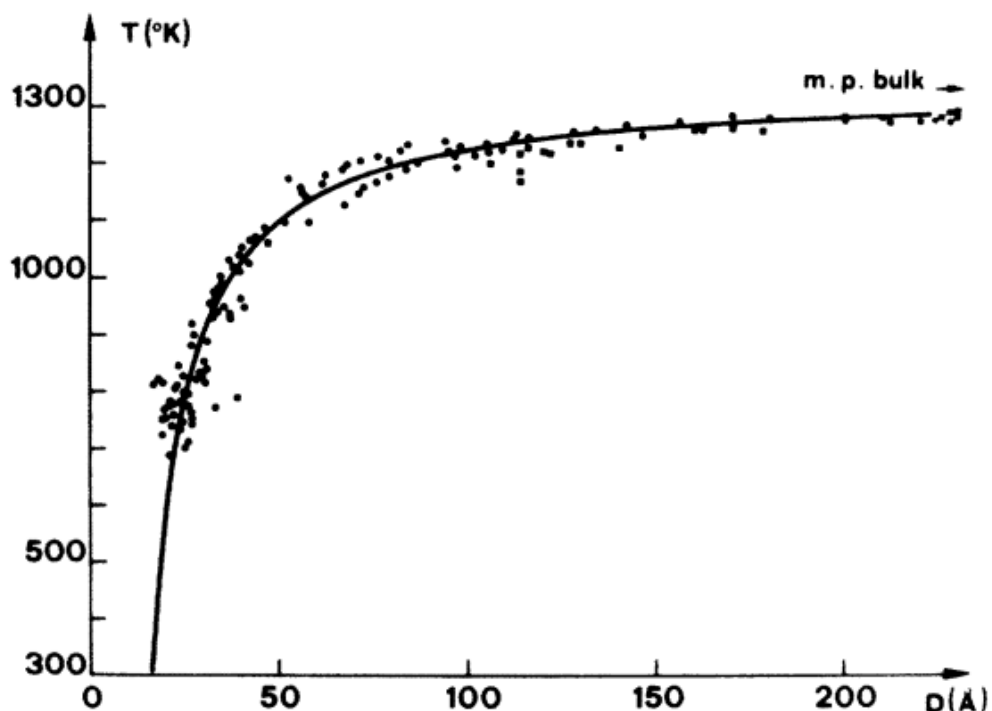


Figure 2–14: Experimental and theoretical melting point temperature versus diameter for gold nanoparticles. Figure taken from [84].

2.9.2 Observations from photothermal therapy

Much research has been reported about the decrease of the AR of AuNRs during conventional heating and pulsed laser induced heating which is used in photothermal therapy. The thermal stability of AuNRs has been studied by using pulsed laser irradiation and thermal annealing of AuNRs. In 2005, the thermal stability was investigated by Petrova et al [85]. AuNRs were deposited on a glass slide and thermally annealed at different temperatures. UV-vis and SEM results revealed that at temperatures higher than 25°C AuNRs changed rapidly to AuNPs within 15 min. Also, higher temperatures than 70°C arising from femtosecond pulsed laser irradiation can cause structural changes of AuNRs [86]. A similar result was reported by Murphy et al [87]. After heating AuNRs solution to a boiling state (ca. 100°C), the rods were observed to shorten and become spheres. The temperature changes during pulsed laser irradiation have been reported in Ref [88]. A near infrared laser was used to measure the temperature increase in an Au dispersion. After 2 min of irradiation with an 808 nm laser, the AuNR dispersion exhibited an average temperature change of approximately 30-5°C (the highest temperatures were 70-100°C).

2.9.3 Deformation mechanism

The deformation of Au nanostructures occurs well below the melting point of bulk gold (1064°C). However, it has been shown that the thermal deformation of Au nanostructures is initiated at very low temperatures and increases as the temperature increases. Significantly it depends on the size and shape of the nanostructure. In case of AuNRs, the thermal stability has been shown to reduce with increasing rod AR [75]. Surface diffusion to minimize surface energy at the tip of the rods was first used to explain this reshaping. However, due to the observation of deformation at such low temperatures, curvature driven surface diffusion proposed by Taylor et al.[89] was used to explain the observed phenomena. In brief, the literature proposes that a longer AR rod with a high radius of curvature at the tip is easier to reshape than a shorter one. Equation 2-20 presents the rate of change of a surface point to the curvature driven surface diffusion.

$$\frac{dn}{dt} = v = B\nabla^2 K \quad \text{Equation 2-20}$$

where $K = 1/R_x + 1/R_y$ is the surface mean curvature, the parameter $B = \frac{\Omega^{\frac{4}{3}}\gamma_s D_s}{kT}$, γ_s is the free energy, Ω is the atomic volume, k is Boltzmann's constant, T is temperature and D_s is the diffusivity tensor related to the diffusion coefficient. The equation was solved using finite difference methods and the change in shape plotted as shown in Figure 2-14. According to the literature [89, 90], the activation energy (E_a) is predicted to be a function of the mean surface curvature expressed in the following equation.

$$E_a \propto \frac{1}{K} \quad \text{Equation 2-21}$$

By applying a constant of proportional C and deriving the curvature (K) at the tip of the rods from a model of ellipsoidal nanorods, the curvature is given by

$$K = \frac{c(2a^2+(c^2-a^2)\cos^2\beta)}{2a(a^2+(c^2-a^2)\cos^2\beta)^{\frac{3}{2}}} \quad \text{Equation 2-22}$$

where $\beta = 0$, $a = \text{length}/2$, $c = a/AR$. Then the predicted activation energy is given by equation 2-23.

$$E_a = \frac{C}{K} = \frac{2aC}{(AR^2+1)} \quad \text{Equation 2-23}$$

From the activation energy, it was shown that short AR rods possess a high activation energy for surface diffusion leading to a barrier to reshaping, but the longer AR rods allow easy deformation below the melting point.

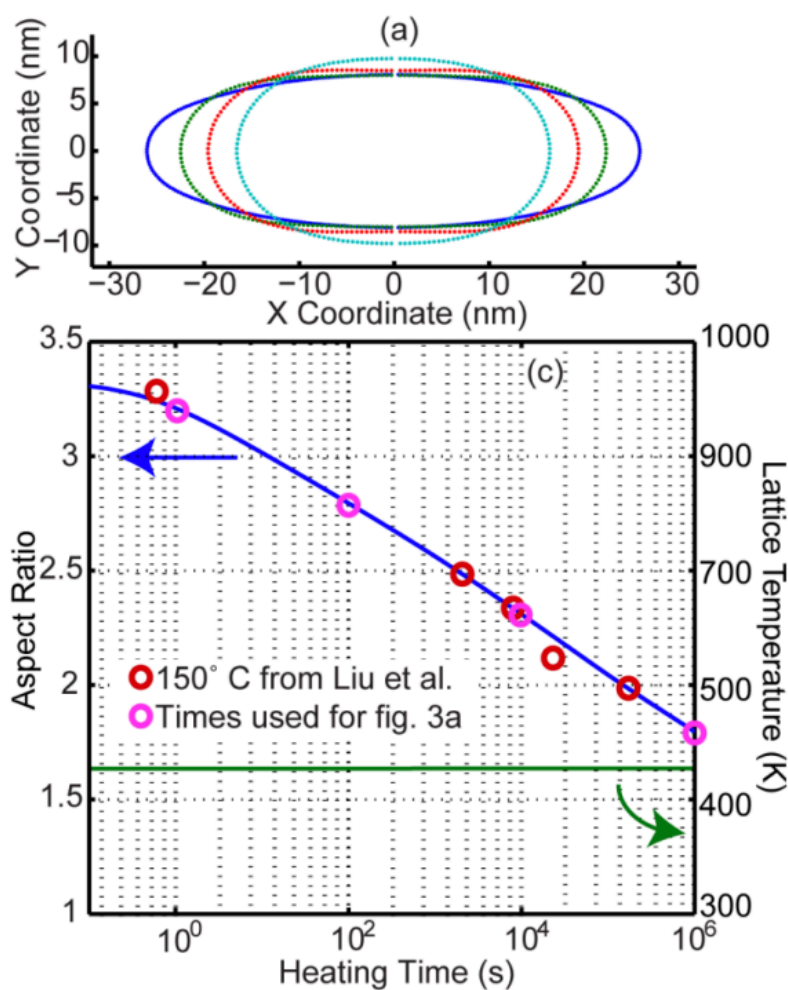


Figure 2–15: Heating profile and simulated deformation of AuNR with AR of 3.3 at 150°C. Figure taken from [88].

2.10 Toxicology of Au nanostructures

AuNPs have attracted attention in the field of biomedical applications including bio-imaging, drug delivery, biosensing and photothermal therapy [91-95]. One of the important issues arising from these potential applications is the concern about their safety and toxicity in both in-vitro and in-vivo environments. In general, the toxicity of AuNPs depends on size, shape, aggregation, concentration, and surface chemistry [95, 96]. According to Goodman et al. [98] and Conner et al. [50], citrate-stabilized AuNPs proved to be non-toxic up to a gold concentration of 250 mM on exposure to human leukaemia cells (K562) while surface coated AuNPs present cytotoxicity only at 25mM. Also, 18 nm diameter AuNPs have been reported to penetrate cells without toxicity and cell injury [50]. It was reported that 5-15 nm AuNPs are more active in an organ distribution study (involving the liver and spleen) than 50-100 nm particles [96]. Similar results were reported for ultrasmall AuNPs (1.4 nm in diameter) which can cause toxicity as they can easily bind to DNA and affect genes [99]. 20-100 nm diameter

AuNPs exhibit no effect on retina microvascular endothelial cells [100]. There is also a report that AuNPs with a 25nm diameter exhibit low toxicity but cause disruption in human hepatocellular carcinoma HepG2 cells [101]. The size distribution effect could arise from the large surface to volume ratio of smaller nanoparticles which provides more interfacial contact surface area leading to an increase surface particle activity [102, 103].

The effect of Au nanoparticle shape on toxicity have also been investigated. Elongated Au nanostructures such as rods cubes, and triangles have been found to be more toxic to human prostate cancer cells (PC3) [104] and human skin keratinocyte cells (HaCaT) [105] than for the case of AuNPs. Similar reports have shown that AuNR demonstrated high toxicity to HaCaT cells [106] as a result of the CTAB coating layers. Schaeuelin and co-worker [107] proposed the influence of surface charge on Au nanostructure toxicity. It was found that whilst both positively and negatively charged AuNPs were toxic, positively charged particles exhibited increased toxicity [97, 107]. For example, CTAB-capped Au structures which have a positively surface charge presented high toxicity [104, 105]. CTAC-coated AuNPs also present a positively charged particle surface similar to CTAB which may result in higher toxicity. However, PSS-coated AuNRs (positively charged) demonstrated less toxicity in human leukaemia (HL60) cells while PEG-coated AuNRs from ligand exchange can eliminate toxicity [83] due to their neutral surface charge (the zeta potential is zero) [108]. Lui et al. [109] reported that silica-coated AuNPs with diameters between 50-300 nm showed lower toxicity than CTAB-capped AuNPs in human breast cancer cells (MCF-7). Although much research has reported that AuNPs do show a toxicity effect on cell cultures, some studies have argued that AuNPs do not exhibit toxicity. This depends on size, shape, surface coating, and the particular cell culture studies. Surface modification of Au nanostructures could have a significant influence on toxicity and intensive research to provide sufficient data on specific cell cultures could extend the use of Au nanostructures in healthcare applications.

2.11 Electrochemical behavior of phospholipid membrane for nanoparticle interaction

Dioleoyl-phosphatidylcholine (DOPC) consists of negatively charged phosphate group and positively charged amine group. DOPC is the most abundant phospholipid in eukaryotic cells which make them become popular for nanoparticle sensor applications. According to the previous work conducted by Nelson et al. [110-114], DOPC in PBS buffer on Hg/Pt electrodes has been used in electrochemical studies for screening of nanoparticle interactions. In the DOPC voltammogram, there consist of three main RCV profiles named as area A, B, and C as illustrated in figure 2-16.

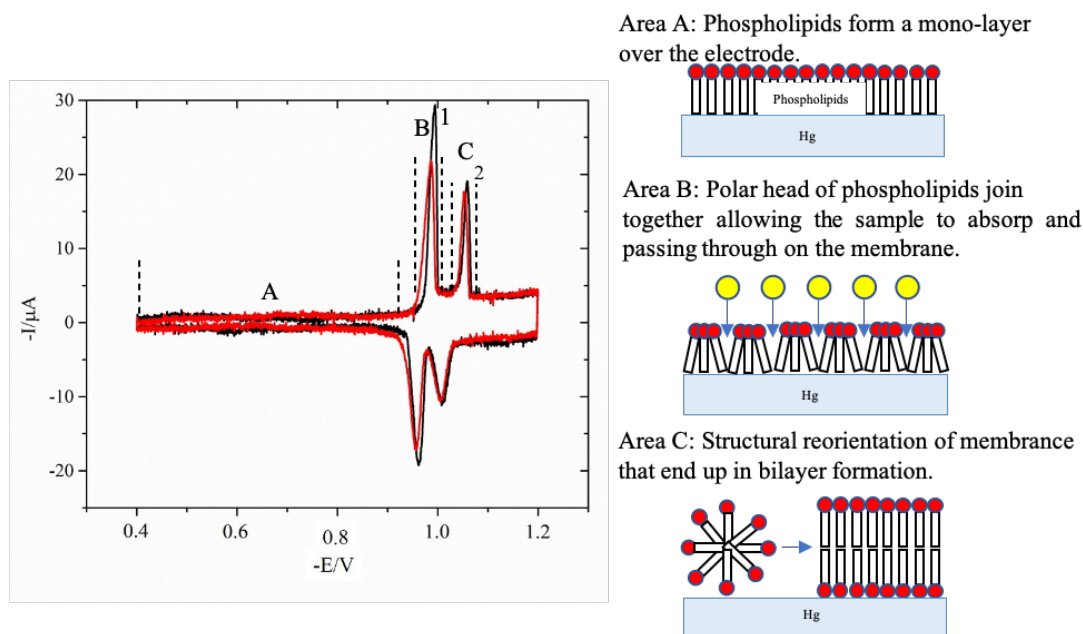


Figure 2-16: RCV profile of DOPC and related phase of the phospholipids on the Hg/Pt at a certain potential

In area A, phospholipids are formed a monolayer over the electrode correspond to the potential between -0.40 and -0.90 V. Once the potential increase to -0.93 V in area B, polar head of phospholipid join together allowing the sample to absorb and passing through on the membrane. If the nanoparticles interact with the membrane, there will be a depression of the RCV profile in this region. The peak occurs at over -1.0 V correspond to area C. This illustrates structural reorientation of membrane that end up in bilayer formation. In the reversal if the potential scan, the reversal of the structural reorientation was occurred and eventually turned in a monolayer membrane. The interaction of nanoparticles corresponds to an increase in the base line of RCV profile illustrated the penetration of nanoparticles into the DOPC layers.

2.12 Conclusion

Widespread use of Au nanostructures in many research applications is a result of their unique shape-dependant properties. In this chapter, background on the optical properties and LSPR of AuNPs, AuNRs, AuNBPs, and AuNTs have all been detailed. Previous work on the plasmonic properties measured both optically and by EELS, the thermal stability and the toxicology of gold nanostructures have been reviewed.

From this review it is clear that a better understanding of the fundamental properties of gold NPs such as the plasmonic and thermal properties and their interaction with cells are required. Based on the literature review in this chapter, a common concept underpinning the synthesis

of Au nanostructures involves the use of a surfactant to generate different types of morphology and also homogeneity during wet-chemical synthesis. By varying synthesis parameters, the fabricated Au nanostructures can be tuned to absorb over the NIR region. It is important to have better understanding of synthesis methods and growth mechanisms so as to provide homogeneity in samples and it is also clear that a better understanding of the influence of the surfactant coating on the properties is desirable. This would help in the design and synthesis of Au nanostructures for specific healthcare applications.

This thesis presents a body of research on different Au nanostructures including AuNPs, AuNRs, AuNBPs, and AuNTs. It includes the development of synthesis methods, optical characterisation and the measurement of plasmonic properties, assessment of the thermal stabilities and toxicology in terms of their interaction with a model phospholipid membrane.

2.13 References

- [1] Tran, Q.H., V.Q. Nguyen, and A.-T. Le, *Silver nanoparticles: synthesis, properties, toxicology, applications and perspectives*. Advances in Natural Sciences: Nanoscience and Nanotechnology, 2013. **4**(3): p. 033001.
- [2] Li, W.-R., et al., *Antibacterial activity and mechanism of silver nanoparticles on Escherichia coli*. Applied Microbiology and Biotechnology, 2010. **85**(4): p. 1115-1122.
- [3] Martínez-Abad, A., *13 - Silver-based antimicrobial polymers for food packaging*, in *Multifunctional and Nanoreinforced Polymers for Food Packaging*, J.-M. Lagarón, Editor. 2011, Woodhead Publishing. p. 347-367.
- [4] Abou El-Nour, K.M.M., et al., *Synthesis and applications of silver nanoparticles*. Arabian Journal of Chemistry, 2010. **3**(3): p. 135-140.
- [5] Quang Huy, T., N. Van Quy, and L. Anh-Tuan, *Silver nanoparticles: synthesis, properties, toxicology, applications and perspectives*. Advances in Natural Sciences: Nanoscience and Nanotechnology, 2013. **4**(3): p. 033001.
- [6] Greulich, C., et al., *The toxic effect of silver ions and silver nanoparticles towards bacteria and human cells occurs in the same concentration range*. RSC Advances, 2012. **2**(17): p. 6981-6987.
- [7] Turkevich, J., P.C. Stevenson, and J. Hillier, *A study of the nucleation and growth processes in the synthesis of colloidal gold*. Discussions of the Faraday Society, 1951. **11**(0): p. 55-75.

- [8] Das, M., et al., *Review on gold nanoparticles and their applications*. Toxicology and Environmental Health Sciences, 2011. **3**(4): p. 193-205.
- [9] Eustis, S. and M.A. El-Sayed, *Why gold nanoparticles are more precious than pretty gold: Noble metal surface plasmon resonance and its enhancement of the radiative and nonradiative properties of nanocrystals of different shapes*. Chemical Society Reviews, 2006. **35**(3): p. 209-217.
- [10] Yeh, Y.-C., B. Creran, and V.M. Rotello, *Gold nanoparticles: preparation, properties, and applications in bionanotechnology*. Nanoscale, 2012. **4**(6): p. 1871-1880.
- [11] Li, J., et al., *Simultaneous enzymatic and SERS properties of bifunctional chitosan-modified popcorn-like Au-Ag nanoparticles for high sensitive detection of melamine in milk powder*. Talanta, 2015. **140**: p. 204-211.
- [12] Tucker-Schwartz, J.M., et al., *In vivo imaging of nanoparticle delivery and tumor microvasculature with multimodal optical coherence tomography*. Biomedical Optics Express, 2014. **5**(6): p. 1731-1743.
- [13] Ju, H., R.A. Roy, and T.W. Murray, *Gold nanoparticle targeted photoacoustic cavitation for potential deep tissue imaging and therapy*. Biomedical Optics Express, 2013. **4**(1): p. 66-76.
- [14] Lohse, S.E. and C.J. Murphy, *The Quest for Shape Control: A History of Gold Nanorod Synthesis*. Chemistry of Materials, 2013. **25**(8): p. 1250-1261.
- [15] Steven, L.J., *Corrigendum: Optical properties of biological tissues: a review*. Physics in Medicine and Biology, 2013. **58**(14): p. 5007.
- [16] Pastrana, E., *Near-infrared probes*. Nat Meth, 2013. **10**(1): p. 36-36.
- [17] Smith, A.M., M.C. Mancini, and S. Nie, *Bioimaging: Second window for in vivo imaging*. Nat Nano, 2009. **4**(11): p. 710-711.
- [18] Kou, X., et al., *Growth of Gold Bipyramids with Improved Yield and Their Curvature-Directed Oxidation*. Small, 2007. **3**(12): p. 2103-2113.
- [19] Li, Q., et al., *Production of Monodisperse Gold Nanobipyramids with Number Percentages Approaching 100% and Evaluation of Their Plasmonic Properties*. Advanced Optical Materials, 2015. **3**(6): p. 801-812.

- [20] Scarabelli, L., et al., *Monodisperse Gold Nanotriangles: Size Control, Large-Scale Self-Assembly, and Performance in Surface-Enhanced Raman Scattering*. ACS Nano, 2014. **8**(6): p. 5833-5842.
- [21] Kuttner, C., et al., *Seeded Growth Synthesis of Gold Nanotriangles: Size Control, SAXS Analysis, and SERS Performance*. ACS Applied Materials & Interfaces, 2018. **10**(13): p. 11152-11163.
- [22] Chen, L., et al., *High-Yield Seedless Synthesis of Triangular Gold Nanoplates through Oxidative Etching*. Nano Letters, 2014. **14**(12): p. 7201-7206.
- [23] Brown, K.R., D.G. Walter, and M.J. Natan, *Seeding of Colloidal Au Nanoparticle Solutions. 2. Improved Control of Particle Size and Shape*. Chemistry of Materials, 2000. **12**(2): p. 306-313.
- [24] Jana, N.R., L. Gearheart, and C.J. Murphy, *Seeding Growth for Size Control of 5–40 nm Diameter Gold Nanoparticles*. Langmuir, 2001. **17**(22): p. 6782-6786.
- [25] Sellers, H., et al., *Structure and binding of alkanethiolates on gold and silver surfaces: implications for self-assembled monolayers*. Journal of the American Chemical Society, 1993. **115**(21): p. 9389-9401.
- [26] Bastús, N.G., J. Comenge, and V. Puntes, *Kinetically Controlled Seeded Growth Synthesis of Citrate-Stabilized Gold Nanoparticles of up to 200 nm: Size Focusing versus Ostwald Ripening*. Langmuir, 2011. **27**(17): p. 11098-11105.
- [27] Scarabelli, L., et al., *A “Tips and Tricks” Practical Guide to the Synthesis of Gold Nanorods*. The Journal of Physical Chemistry Letters, 2015. **6**(21): p. 4270-4279.
- [28] Jana, N.R., L. Gearheart, and C.J. Murphy, *Wet Chemical Synthesis of High Aspect Ratio Cylindrical Gold Nanorods*. The Journal of Physical Chemistry B, 2001. **105**(19): p. 4065-4067.
- [29] Nikoobakht, B. and M.A. El-Sayed, *Preparation and Growth Mechanism of Gold Nanorods (NRs) Using Seed-Mediated Growth Method*. Chemistry of Materials, 2003. **15**(10): p. 1957-1962.
- [30] Jana, N.R., *Gram-Scale Synthesis of Soluble, Near-Monodisperse Gold Nanorods and Other Anisotropic Nanoparticles*. Small, 2005. **1**(8-9): p. 875-882.
- [31] Ratto, F., et al., *Size and shape control in the overgrowth of gold nanorods*. Journal of Nanoparticle Research, 2010. **12**(6): p. 2029-2036.

- [32] Khlebtsov, B.N., et al., *Overgrowth of Gold Nanorods by Using a Binary Surfactant Mixture*. Langmuir, 2014. **30**(6): p. 1696-1703.
- [33] Zhang, Q., et al., *Facet Control of Gold Nanorods*. ACS Nano, 2016. **10**(2): p. 2960-2974.
- [34] Liu, M. and P. Guyot-Sionnest, *Mechanism of Silver(I)-Assisted Growth of Gold Nanorods and Bipyramids*. The Journal of Physical Chemistry B, 2005. **109**(47): p. 22192-22200.
- [35] Lee, J.-H., et al., *Bipyramid-templated synthesis of monodisperse anisotropic gold nanocrystals*. Nature Communications, 2015. **6**(1): p. 7571.
- [36] Millstone, J.E., et al., *Observation of a Quadrupole Plasmon Mode for a Colloidal Solution of Gold Nanoprisms*. Journal of the American Chemical Society, 2005. **127**(15): p. 5312-5313.
- [37] Tyagi, H., et al., *A Facile pH Controlled Citrate-Based Reduction Method for Gold Nanoparticle Synthesis at Room Temperature*. Nanoscale Research Letters, 2016. **11**(1): p. 362.
- [38] Gentry, S.T., S.F. Kendra, and M.W. Bezpalko, *Ostwald Ripening in Metallic Nanoparticles: Stochastic Kinetics*. The Journal of Physical Chemistry C, 2011. **115**(26): p. 12736-12741.
- [39] Lifshitz, I.M. and V.V. Slyozov, *The kinetics of precipitation from supersaturated solid solutions*. Journal of Physics and Chemistry of Solids, 1961. **19**(1): p. 35-50.
- [40] Panikkanvalappil, S. R. et al. *Anisotropic nanomaterials: structure, growth, assembly, and functions*. Nano reviews. 2011, **2**(10): p. 3402
- [41] Ahmad, I., *Evaporation induced self-assembly and characterization of gold nanorods*, in *Physics of Interfaces and Nanomaterials* Faculty of Science and Technology. 2015, University of Twente.
- [42] Pérez-Juste, J., et al., *Gold nanorods: Synthesis, characterization and applications*. Coordination Chemistry Reviews, 2005. **249**(17): p. 1870-1901.
- [43] Pérez-Juste, J., et al., *Electric-field-directed growth of gold nanorods in aqueous surfactant solutions*. Advanced Functional Materials, 2004. **14**(6): p. 571-579.
- [44] Sau, T.K. and C.J. Murphy, *Seeded high yield synthesis of short Au nanorods in aqueous solution*. Langmuir, 2004. **20**(15): p. 6414-6420.

- [45] Chhatre, A., R. Thakkar, and A. Mehra, *Formation of Gold Nanorods by Seeded Growth: Mechanisms and Modeling*. *Crystal Growth & Design*, 2018. **18**(6): p. 3269-3282.
- [46] Guo, Z., et al., *High-purity gold nanobipyramids can be obtained by an electrolyte-assisted and functionalization-free separation route*. *Colloids and Surfaces A: Physicochemical and Engineering Aspects*, 2012. **414**: p. 492-497.
- [47] Rayavarapu, R.G., et al., *In vitro toxicity studies of polymer-coated gold nanorods*. *Nanotechnology*, 2010. **21**(14): p. 145101.
- [48] Cao, J., *Creation of novel gold-nanorod-based localized surface plasmon resonance biosensors*, in *School of Engineering and Mathematical Sciences*. 2013, City University London.
- [49] Lin, J., et al., *Penetration of Lipid Membranes by Gold Nanoparticles: Insights into Cellular Uptake, Cytotoxicity, and Their Relationship*. *ACS Nano*, 2010. **4**(9): p. 5421-5429.
- [50] Connor, E.E., et al., *Gold Nanoparticles Are Taken Up by Human Cells but Do Not Cause Acute Cytotoxicity*. *Small*, 2005. **1**(3): p. 325-327.
- [51] Mehtala, J.G., et al., *Citrate-Stabilized Gold Nanorods*. *Langmuir*, 2014. **30**(46): p. 13727-13730.
- [52] Zhang, J., M. Wang, and T.J. Webster, *Silver-coated gold nanorods as a promising antimicrobial agent in the treatment of cancer-related infections*. *International journal of nanomedicine*, 2018. **13**: p. 6575-6583.
- [53] Ashrafi, S., et al., *Thermal Distribution of Silica Coated Gold Nano Rods in Tissue-like Phantom as in Vitro Model for Plasmonic Photo Thermal Therapy*. *Biomedical and Pharmacology Journal*, 2016. **9**: p. 1189-1201.
- [54] Schulz, F., et al., *Effective PEGylation of gold nanorods*. *Nanoscale*, 2016. **8**(13): p. 7296-7308.
- [55] Su, L., et al., *A Fast and Efficient Replacement of CTAB with MUA on the Surface of Gold Nanorods Assisted by a Water-Immiscible Ionic Liquid*. *Small*, 2017. **13**(11): p. 1602809.
- [56] He, J., et al., *The facile removal of CTAB from the surface of gold nanorods*. *Colloids and Surfaces B: Biointerfaces*, 2018. **163**: p. 140-145.

- [57] Pérez-Juste, J., et al., *Gold nanorods: Synthesis, characterization and applications*. Coordination Chemistry Reviews, 2005. **249**(17–18): p. 1870-1901.
- [58] Cao, J., T. Sun, and K.T.V. Grattan, *Gold nanorod-based localized surface plasmon resonance biosensors: A review*. Sensors and Actuators B: Chemical, 2014. **195**: p. 332-351.
- [59] Petryayeva, E. and U.J. Krull, *Localized surface plasmon resonance: Nanostructures, bioassays and biosensing—A review*. Analytica Chimica Acta, 2011. **706**(1): p. 8-24.
- [60] Sprünken, D.P., et al., *Influence of the Local Environment on Determining Aspect-Ratio Distributions of Gold Nanorods in Solution Using Gans Theory*. The Journal of Physical Chemistry C, 2007. **111**(39): p. 14299-14306.
- [61] Link, S., M.B. Mohamed, and M.A. El-Sayed, *Simulation of the Optical Absorption Spectra of Gold Nanorods as a Function of Their Aspect Ratio and the Effect of the Medium Dielectric Constant*. The Journal of Physical Chemistry B, 1999. **103**(16): p. 3073-3077.
- [62] Vasista, A.B. and G.V.P. Kumar, *Quantum emitter coupled to plasmonic nanotriangle: Spatially dependent emission and thermal mapping*. Optics Communications, 2016. **381**: p. 227-233.
- [63] Colliex, C., M. Kociak, and O. Stéphan, *Electron Energy Loss Spectroscopy imaging of surface plasmons at the nanometer scale*. Ultramicroscopy, 2016. **162**: p. A1-A24.
- [64] N’Gom, M., et al., *Single Particle Plasmon Spectroscopy of Silver Nanowires and Gold Nanorods*. Nano Letters, 2008. **8**(10): p. 3200-3204.
- [65] Michel, B., et al., *Mapping surface plasmons at the nanometre scale with an electron beam*. Nanotechnology, 2007. **18**(16): p. 165505.
- [66] Chu, M.-W., et al., *Probing Bright and Dark Surface-Plasmon Modes in Individual and Coupled Noble Metal Nanoparticles Using an Electron Beam*. Nano Letters, 2009. **9**(1): p. 399-404.
- [67] Rodríguez-González, B., et al., *Surface Plasmon Mapping of Dumbbell-Shaped Gold Nanorods: The Effect of Silver Coating*. Langmuir, 2012. **28**(24): p. 9063-9070.
- [68] Losquin, A., et al., *Unveiling Nanometer Scale Extinction and Scattering Phenomena through Combined Electron Energy Loss Spectroscopy and Cathodoluminescence Measurements*. Nano Letters, 2015. **15**(2): p. 1229-1237.

- [69] Mayer, M., et al., *Controlled Living Nanowire Growth: Precise Control over the Morphology and Optical Properties of AgAuAg Bimetallic Nanowires*. Nano Letters, 2015. **15**(8): p. 5427-5437.
- [70] Arenal, R., et al., *Local Plasmonic Studies on Individual Core–Shell Gold–Silver and Pure Gold Nano-Bipyramids*. The Journal of Physical Chemistry C, 2014. **118**(44): p. 25643-25650.
- [71] Nelayah, J., et al., *Mapping surface plasmons on a single metallic nanoparticle*. Nature Physics, 2007. **3**(5): p. 348-353.
- [72] Losquin, A., et al., *Unveiling Nanometer Scale Extinction and Scattering Phenomena through Combined Electron Energy Loss Spectroscopy and Cathodoluminescence Measurements*. Nano letters, 2015. **15**.
- [73] Sönnichsen, C., et al., *Drastic Reduction of Plasmon Damping in Gold Nanorods*. Physical Review Letters, 2002. **88**(7): p. 077402.
- [74] Zhu, J., et al., *Shape dependent resonance light scattering properties of gold nanorods*. Materials Science and Engineering: B, 2005. **121**(3): p. 199-203.
- [75] Link, S. and M.A. El-Sayed, *Shape and size dependence of radiative, non-radiative and photothermal properties of gold nanocrystals*. International Reviews in Physical Chemistry, 2000. **19**.
- [76] Huang, X., I.H. El-Sayed, and M.A. El-Sayed, *Applications of Gold Nanorods for Cancer Imaging and Photothermal Therapy*, in *Cancer Nanotechnology: Methods and Protocols*, S.R. Grobmyer and B.M. Moudgil, Editors. 2010, Humana Press: Totowa, NJ. p. 343-357.
- [77] Huang, X. and M.A. El-Sayed, *Gold nanoparticles: Optical properties and implementations in cancer diagnosis and photothermal therapy*. Journal of Advanced Research, 2010. **1**(1): p. 13-28.
- [78] Morton, J.G., et al., *Nanoshells for Photothermal Cancer Therapy*, in *Cancer Nanotechnology: Methods and Protocols*, S.R. Grobmyer and B.M. Moudgil, Editors. 2010, Humana Press: Totowa, NJ. p. 101-117.
- [79] Au, L., et al., *Gold Nanocages for Cancer Imaging and Therapy*, in *Cancer Nanotechnology: Methods and Protocols*, S.R. Grobmyer and B.M. Moudgil, Editors. 2010, Humana Press: Totowa, NJ. p. 83-99.
- [80] Wei, A., A.P. Leonov, and Q. Wei, *Gold Nanorods: Multifunctional Agents for Cancer Imaging and Therapy*, in *Cancer Nanotechnology: Methods and Protocols*,

- S.R. Grobmyer and B.M. Moudgil, Editors. 2010, Humana Press: Totowa, NJ. p. 119-130.
- [81] Huang, X., et al., *Determination of the Minimum Temperature Required for Selective Photothermal Destruction of Cancer Cells with the Use of Immunotargeted Gold Nanoparticles*. Photochemistry and Photobiology, 2006. **82**(2): p. 412-417.
- [82] Zhang, Y., et al., *Temperature-dependent cell death patterns induced by functionalized gold nanoparticle photothermal therapy in melanoma cells*. Scientific Reports, 2018. **8**(1): p. 8720.
- [83] Doughty C V et al. *Nanomaterial Applications in Photothermal Therapy for Cancer*. Materials (Basel, Switzerland). 2019. 12(5): p. 779.
- [84] Buffat, P. and J.P. Borel, *Size effect on the melting temperature of gold particles*. Physical Review A, 1976. **13**(6): p. 2287-2298.
- [85] Petrova, H., et al., *On the temperature stability of gold nanorods: comparison between thermal and ultrafast laser-induced heating*. Physical Chemistry Chemical Physics, 2006. **8**(7): p. 814-821.
- [86] Zou, R., et al., *Thermal stability of gold nanorods in an aqueous solution*. Colloids and Surfaces A: Physicochemical and Engineering Aspects, 2010. **372**(1-3): p. 177-181.
- [87] Jana, N.R., et al., *Anisotropic Chemical Reactivity of Gold Spheroids and Nanorods*. Langmuir, 2002. **18**(3): p. 922-927.
- [88] Mackey, M.A., et al., *The Most Effective Gold Nanorod Size for Plasmonic Photothermal Therapy: Theory and In Vitro Experiments*. The Journal of Physical Chemistry B, 2014. **118**(5): p. 1319-1326.
- [89] Taylor, A.B., A.M. Siddiquee, and J.W.M. Chon, *Below Melting Point Photothermal Reshaping of Single Gold Nanorods Driven by Surface Diffusion*. ACS Nano, 2014. **8**(12): p. 12071-12079.
- [90] Combe, N., P. Jensen, and A. Pimpinelli, *Changing Shapes in the Nanoworld*. Physical Review Letters, 2000. **85**(1): p. 110-113.
- [91] Zhang, Y., et al., *Effect of Size, Shape, and Surface Modification on Cytotoxicity of Gold Nanoparticles to Human HEP-2 and Canine MDCK Cells*. Journal of Nanomaterials, 2012. **2012**: p. 7.
- [92] Yu, C. and J. Irudayaraj, *Multiplex Biosensor Using Gold Nanorods*. Analytical Chemistry, 2007. **79**(2): p. 572-579.

- [93] Imura, K., T. Nagahara, and H. Okamoto, *Near-field optical imaging of plasmon modes in gold nanorods*. The Journal of Chemical Physics, 2005. **122**(15): p. 154701.
- [94] Jain, P.K., I.H. El-Sayed, and M.A. El-Sayed, *Au nanoparticles target cancer*. Nano Today, 2007. **2**(1): p. 18-29.
- [95] Huang, X., et al., *Cancer Cell Imaging and Photothermal Therapy in the Near-Infrared Region by Using Gold Nanorods*. Journal of the American Chemical Society, 2006. **128**(6): p. 2115-2120.
- [96] Zhang, X.-D., et al., *Toxicologic effects of gold nanoparticles in vivo by different administration routes*. International journal of nanomedicine, 2010. **5**: p. 771-781.
- [97] Yah, C.S., *The toxicity of Gold Nanoparticles in relation to their physiochemical properties*. Biomedical Research, 2013. **24**: p. 400-413.
- [98] Goodman, C.M., et al., *Toxicity of Gold Nanoparticles Functionalized with Cationic and Anionic Side Chains*. Bioconjugate Chemistry, 2004. **15**(4): p. 897-900.
- [99] Chen, Y.-S., et al., *Assessment of the In Vivo Toxicity of Gold Nanoparticles*. Nanoscale research letters, 2009. **4**(8): p. 858-864.
- [100] Kim, G.-Y., et al., *Optimized coverage of gold nanoparticles at tyrosinase electrode for measurement of a pesticide in various water samples*. Journal of Hazardous Materials, 2008. **156**(1): p. 141-147.
- [101] Wei, X.-L., et al., *Disruption of HepG2 cell adhesion by gold nanoparticle and Paclitaxel disclosed by in situ QCM measurement*. Colloids and Surfaces B: Biointerfaces, 2007. **59**(1): p. 100-104.
- [102] Vakurov, A., R. Brydson, and A. Nelson, *Electrochemical Modeling of the Silica Nanoparticle–Biomembrane Interaction*. Langmuir, 2012. **28**(2): p. 1246-1255.
- [103] Van Doren, E.A.F., et al., *Determination of the volume-specific surface area by using transmission electron tomography for characterization and definition of nanomaterials*. Journal of Nanobiotechnology, 2011. **9**(1): p. 17.
- [104] Carnovale, C., et al., *Identifying Trends in Gold Nanoparticle Toxicity and Uptake: Size, Shape, Capping Ligand, and Biological Corona*. ACS Omega, 2019. **4**(1): p. 242-256.
- [105] Wang, C., et al., *Gold nanoparticle-based colorimetric sensor for studying the interactions of β -amyloid peptide with metallic ions*. Talanta, 2010. **80**(5): p. 1626-1631.

- [106] Chithrani, B.D., A.A. Ghazani, and W.C.W. Chan, *Determining the Size and Shape Dependence of Gold Nanoparticle Uptake into Mammalian Cells*. Nano Letters, 2006. **6**(4): p. 662-668.
- [107] Schaeublin, N.M., et al., *Surface charge of gold nanoparticles mediates mechanism of toxicity*. Nanoscale, 2011. **3**(2): p. 410-420.
- [108] Xie, X., et al., *The Effect of shape on Cellular Uptake of Gold Nanoparticles in the forms of Stars, Rods, and Triangles*. Scientific Reports, 2017. **7**(1): p. 3827.
- [109] Liu, G., et al., *Cytotoxicity of various types of gold-mesoporous silica nanoparticles in human breast cancer cells*. International journal of nanomedicine, 2015. **10**: p. 6075-6087.
- [110] Vakurov, A., R. Brydson, and A. Nelson, *Electrochemical Modeling of the Silica Nanoparticle–Biomembrane Interaction*. Langmuir, 2012. **28**(2): p. 1246-1255.
- [111] Vakurov, A., et al., *ZnO nanoparticle interactions with phospholipid monolayers*. Journal of Colloid and Interface Science, 2013. **404**: p. 161-168.
- [112] Nelson, A. and N. Auffret, *Phospholipid monolayers of di-oleoyl lecithin at the mercury/water interface*. Journal of Electroanalytical Chemistry, 1988. **244**(1-2): p. 99-113.
- [113] Ormategui, N., et al., *Interaction of poly(N-isopropylacrylamide) (pNIPAM) based nanoparticles and their linear polymer precursor with phospholipid membrane models*. Bioelectrochemistry, 2012. **87**: p. 211-219.
- [114] Vakurov, A., et al., *Significance of particle size and charge capacity in TiO₂ nanoparticle-lipid interactions*. Journal of Colloid and Interface Science, 2016. **473**: p. 75-83.

Chapter 3 Synthesis and characterisation methods

This chapter is divided into two sections: 1) nanoparticle fabrication methods and 2) sample characterization. The first section presents the synthesis techniques for Au nanostructures including gold nanoparticles (AuNPs), gold nanorods (AuNRs), gold nanobipyramids (AuNBPs), and gold nanotriangles (AuNTs). The second part describes the material characterisation techniques employed: ultraviolet and visible (UV/vis) spectroscopy, dynamic light scattering (DLS) and zeta potential measurement, transmission electron microscopy (TEM), and scanning transmission electron microscopy (STEM). The basic fundamental theory of each technique, the sample preparation and data analysis are also detailed in this chapter.

3.1 Synthesis methods

There are 4 main types of Au nanostructures synthesized in this project: nanoparticles, nanorods, nanobipyramids, and nanotriangles. In each case, the starting chemicals and fabrication procedures were different in order to achieve controllable size and homogeneity in the samples.

3.1.1 Synthesis of Au nanoparticles (AuNPs)

3.1.1.1 Reagents:

- Gold (III) chloride trihydrate (HAuCl_4): $\geq 99.9\%$ purity from Sigma-Aldrich
- Trisodium citrate ($\text{Na}_3\text{C}_6\text{H}_5\text{O}_7$): $\geq 99.0\%$ purity from Sigma-Aldrich.
- Deionized (DI) water

3.1.1.2 Synthesis procedure

AuNPs of a variety of controllable sizes were fabricated via citrate reduction of HAuCl_4 with a modified seed growth method. The method was slightly adapted from the literature [1, 2] in order to obtain a range of uniform increasing sizes of AuNPs. There were 2 steps in the synthesis method:

- 1) *Seed solution*: a solution of 2.2 mM of trisodium citrate in 150 mL Milli-Q water was placed into a round bottom flask with a closable lid to prevent evaporation.

This was then heated up with vigorous magnetic stirring until it started boiling. The gold precursor (1 mL of 2.5 mM H_{AuCl}₄) was injected into the flask. Au seeds were formed resulting in a soft-pink solution within 15 min.

- 2) *Growth solution*: the reaction temperature of the seed solution was reduced down to 90 to provide temperature control. 1 mL of 6 mM trisodium citrate was then injected into the vessel and then left for 2 min to allow reaction. After that, 1 mL of 2.5 mM of H_{AuCl}₄ was added into the flask. After 30 min reaction time, 5 mL of the solution were taken out for characterization via UV-vis spectroscopy and TEM. This step of synthesis was repeated up to 10 times to obtain progressively larger AuNPs with sizes up to about 80 nm. The synthesis procedure is illustrated schematically in figure 3-1.

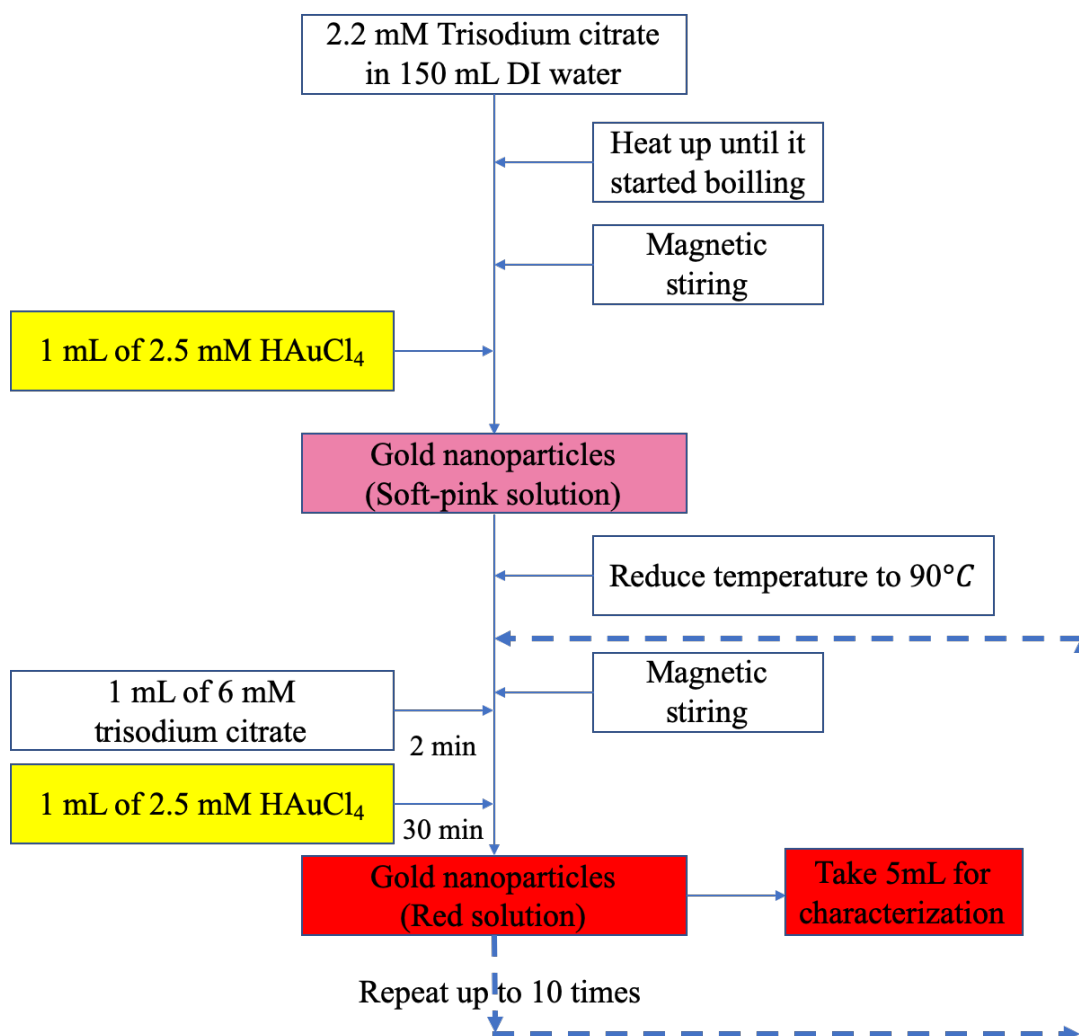


Figure 3–1: Flowchart representing the Au nanoparticles synthesis procedure.

3.1.2 Synthesis of CTAB capped Au nanorods (AuNRs)

3.1.2.1 Reagents:

- Gold (III) chloride trihydrate (HAuCl_4): $\geq 99.9\%$ purity from Sigma-Aldrich
- Hexadecyltrimethylammonium bromide (CTAB): $\geq 99.0\%$ purity from Sigma-Aldrich.
- Silver nitrate (AgNO_3): $\geq 99.9\%$ purity from Alfa Aesar.
- L-(+)-ascorbic acid (AA): $\geq 99.0\%$ purity from Alfa Aesar.
- Sodium borohydride (NaBH_4): $\geq 98.0\%$ purity from Fisher Scientific
- Deionized (DI) water

3.1.2.2 Synthesis procedure

The CTAB-capped AuNRs were synthesized following a seed-mediated method adapted from Nikoobakht and El-Sayed [3] to obtain single AuNRs with various aspect ratios (ARs). In this work, kinetic control with pH adjustment was introduced to slow down the growth rate and achieve a homogenous distribution of AuNRs. There were two steps to the synthesis including preparation of seed and growth solutions as detailed below:

- 1) *Seed solution:* 5 mL of 0.2 M CTAB was gently mixed with 5 mL of 0.5 mM of HAuCl_4 . Then, 0.6 mL of 2 hr aged ice-cold 0.01 M NaBH_4 was rapidly injected and mixed by hand-shaking. The solution was left for 2 hr before use.
- 2) *Growth solution:* 10 mL of growth solution containing 5 mL of 0.2 M CTAB and 5 mL of 1 mM HAuCl_4 was initially prepared in 5 different vessels. Then, 4 mM of AgNO_3 was added in differing amounts (150, 200, 250, 300, and 350 μL) in each of the vessels for obtaining different AR rods, denoted as samples 1-5, respectively. Kinetic control via pH adjustment was achieved via addition of 12 μL of 12 M HCl and gentle mixing. Next, 70 μL of 0.0788 M of ascorbic acid (AA) was mixed into the growth solution resulting in a colourless appearance. The final step was to rapidly inject 12 μL seed solution into the growth solution without any mixing. This was incubated at 30 for 5 hr. Note that the colour of the solution gradually changed within 20-30 min depending on the aspect ratio of the rods; the colour change of longer NRs was slower than for shorter rods.

The as-prepared AuNRs were centrifuged at 10000 rpm for 10 min. The supernatant was removed and the precipitate was redispersed with the same amount of DI water, this being performed twice. This repeated centrifugation and redispersion (C/R) step needs to be completed to remove excess CTAB which causes toxicity associated with membrane reduction [4-7]. Figure 3-2 presents the synthesis flowchart of Au nanorods. The centrifuged

AuNR samples prepared with 350 μL of AgNO_3 were used as the main sample for further experiment and characterization.

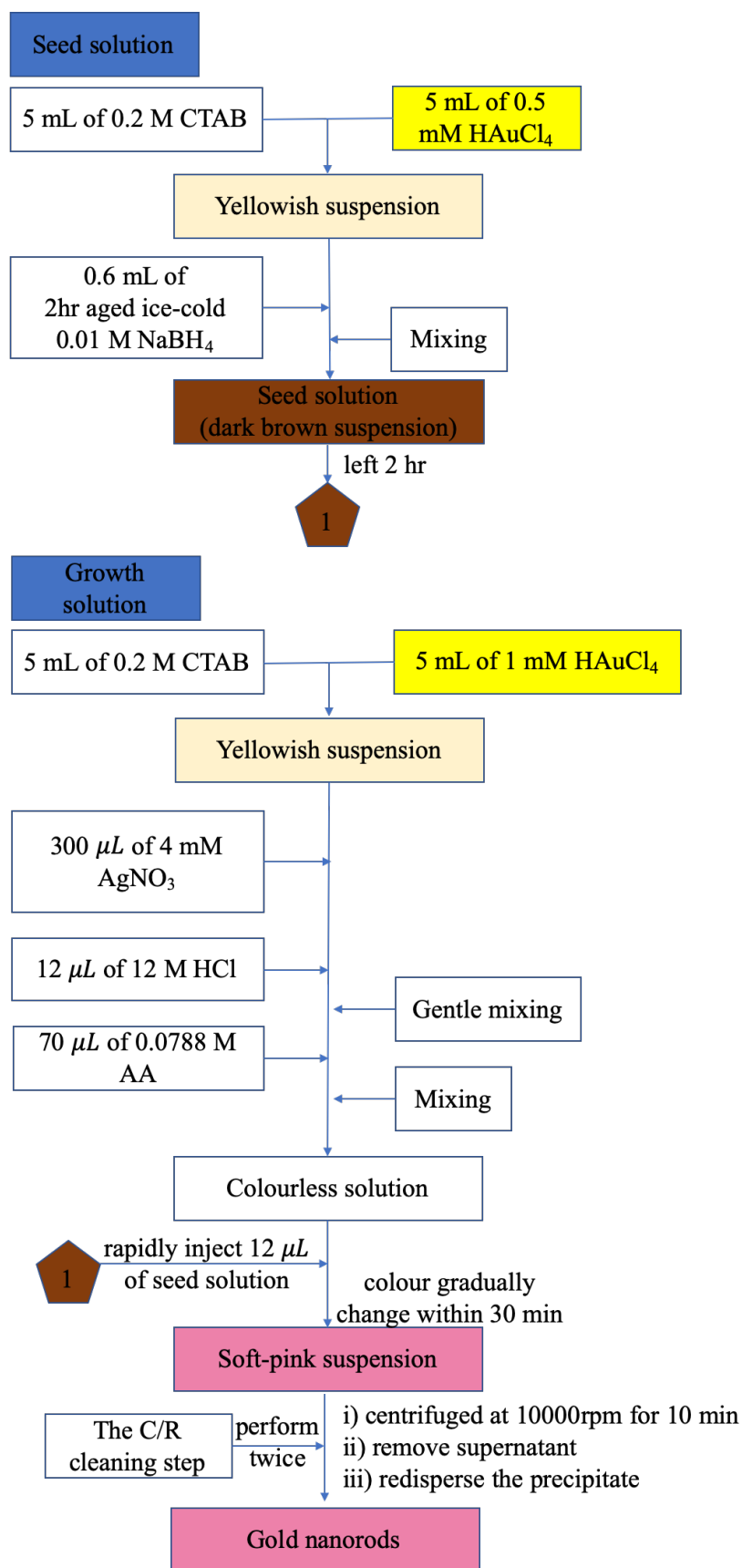


Figure 3–2: Au nanorod synthesis procedure.

3.1.3 Synthesis of Au nanobipyramids (AuNBPs)

3.1.3.1 Reagents:

- Gold (III) chloride trihydrate (HAuCl_4): $\geq 99.9\%$ purity from Sigma-Aldrich
- Trisodium citrate ($\text{Na}_3\text{C}_6\text{H}_5\text{O}_7$): $\geq 99.0\%$ purity from Sigma-Aldrich.
- Hexadecyltrimethylammonium bromide (CTAB): $\geq 99.0\%$ purity from Sigma-Aldrich.
- Silver nitrate (AgNO_3): $\geq 99.9\%$ purity from Alfa Aesar.
- L-(+)-ascorbic acid (AA): $\geq 99.0\%$ purity from Alfa Aesar.
- Sodium borohydride (NaBH_4): $\geq 98.0\%$ purity from Fisher Scientific
- Deionized (DI) water

3.1.3.2 Synthesis procedure

In order to prepare controlled size homogeneous AuNBPs, a seed mediated method involving a citrate-stabilized seed and a growth solution was employed as described in literature with some slight modifications [8-10]. Brief details of the fabrication method are presented below:

- 1) *Seed solution*: 0.25 mL of 10 mM HAuCl_4 was mixed with 18.95 mL of DI water. Then, 0.5 mL of freshly prepared 10 mM sodium citrate was added into the vessel. Finally, 0.3 mL of ice-cold 10 mM NaBH_4 was rapidly injected and mixed by hand-shaking. The solution was magnetically stirred at 500 rpm for 2 hr and left to cool down to room temperature before use.
- 2) *Growth solution*: a growth solution containing 5 mL of 1.2 M CTAB and 0.25 mL of 10 mM HAuCl_4 was initially mixed with 60 μL of 10 mM of AgNO_3 . Then, 12 μL of 12 M HCl was added and gently mixed for kinetic growth control. Next, 40 μL of 0.1 M of AA was mixed into the growth solution resulting in a colourless appearance. The final step was to rapidly inject 80 μL seed solution into the growth solution without any mixing. In this work, different AR of AuNBPs could be obtained by varying the seed amount (80, 100, 150 μL). The final solution was stirred at 400 rpm for 2hr and aged overnight before use.

The as-grown AuNBPs were cleaned using the C/R step twice (10000 rpm) in order to stop the reaction and remove the remaining precursors. The final product was redispersed in DI water for further use. The synthesis procedure is shown schematically in figure 3-3.

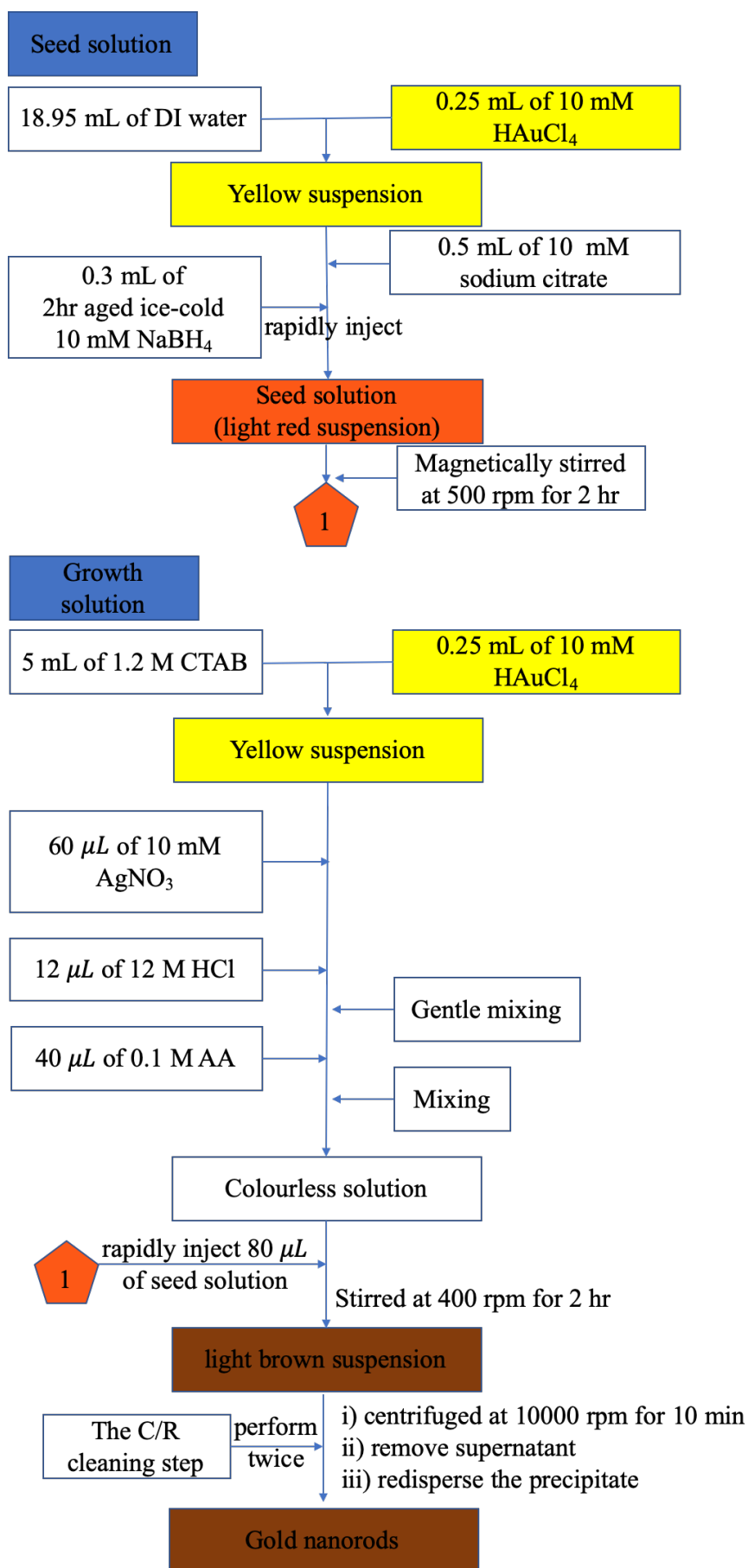


Figure 3-3: Au nanobipyramid synthesis procedure.

3.1.4 Synthesis of Au nanotriangles (AuNTs)

3.1.4.1 Reagents:

- Gold (III) chloride trihydrate (HAuCl_4): $\geq 99.9\%$ purity from Sigma-Aldrich
- Hexadecyltrimethylammonium chloride (CTAC): $\geq 98.0\%$ purity from Sigma-Aldrich.
- Potassium iodide (KI): $\geq 99.0\%$ purity from Sigma-Aldrich.
- L-(+)-ascorbic acid (AA): $\geq 99.0\%$ purity from Alfa Aesar.
- Sodium borohydride (NaBH_4): $\geq 98.0\%$ purity from Fisher Scientific
- Deionized (DI) water

3.1.4.2 Synthesis procedure

Monodispersed AuNTs were synthesized by a pH adjustment seedless synthesis described by Chen and co-workers [11]. In this growth process, CTAC were used as a surfactant and iodide ions were used as a structure-directing agent. NaOH was employed to adjust the pH of the growth solution. The details of the fabrication are described as follows (see figure 3-4). A growth solution containing 8 ml DI water, 1.6 ml of 0.1 M CTAC, and 75 μL of 0.01M KI were mixed together. Then, a mixture of 1016 μL of 10 mM HAuCl_4 and 101.5 μL of 0.1 M NaOH was created. Next, the sodium tetrachloroaurate solution was added into the growth solution, followed by the addition of 80 μL of 64 mM AA. The solution changed colour from yellowish to clear. Finally, 10 μL of 0.1 M NaOH were rapidly injected into the solution and quickly shaken for 1-2 seconds. The colour of the final solution gradually changed to red, then purple, and became blue within 10-15 minutes.

3.1.5 Surface modification of Au nanorods (AuNRs)

CTAB-capped AuNRs synthesized following the modified seed mediated synthesis method, as described in the previous section, were surface modified. Free CTAB is known to disrupt membranes as described before in section 3.1.2. The general idea of surface modification is to cover CTAB by coating the positively surface of CTAB rods with negatively charged PSS (as illustrated in figure 3-5). Then, a layer by layer coating of AuNRs can be achieved with citrate stabilized layers on top of the PSS layer which will be used in future applications. Surface modification procedures were followed from the literature, as described below [13-16].

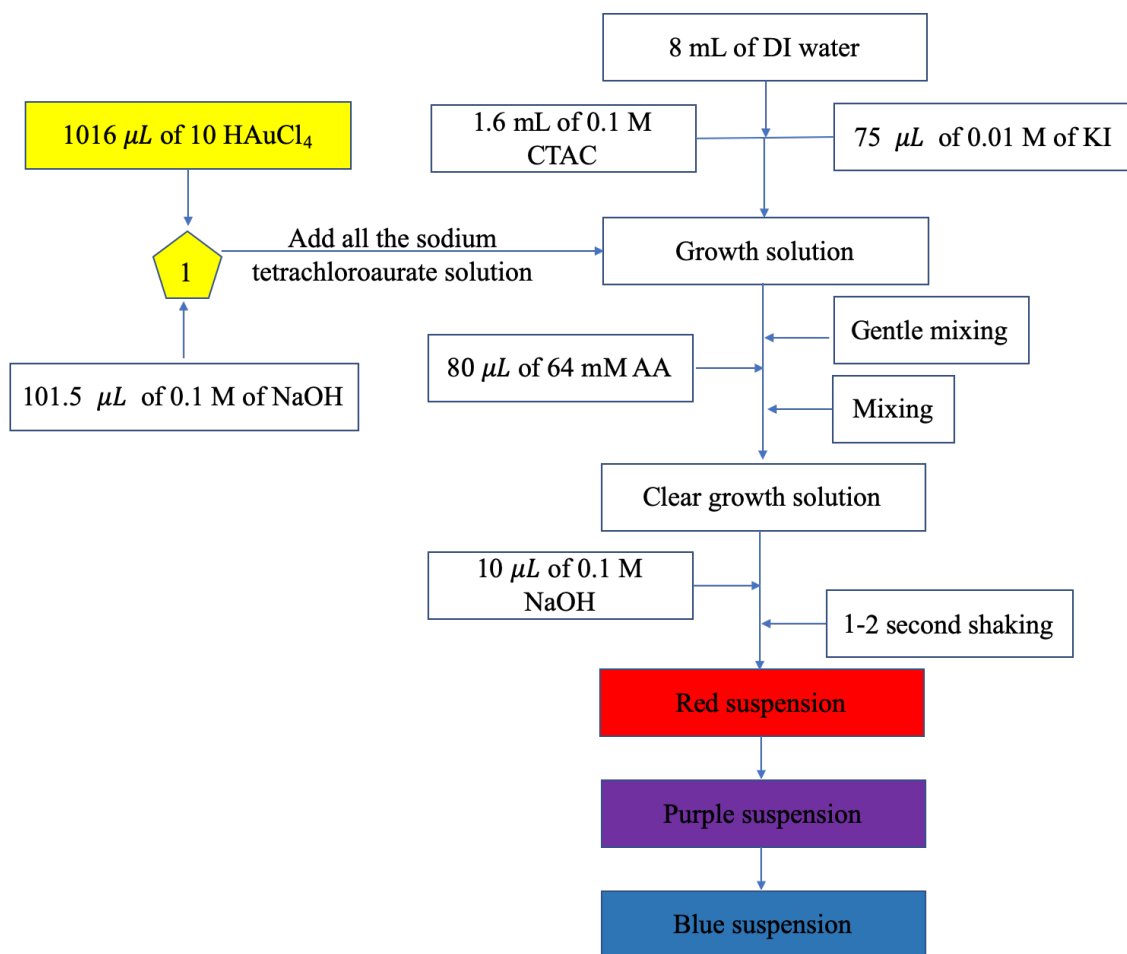


Figure 3–4: Au nanotriangle synthesis procedure.

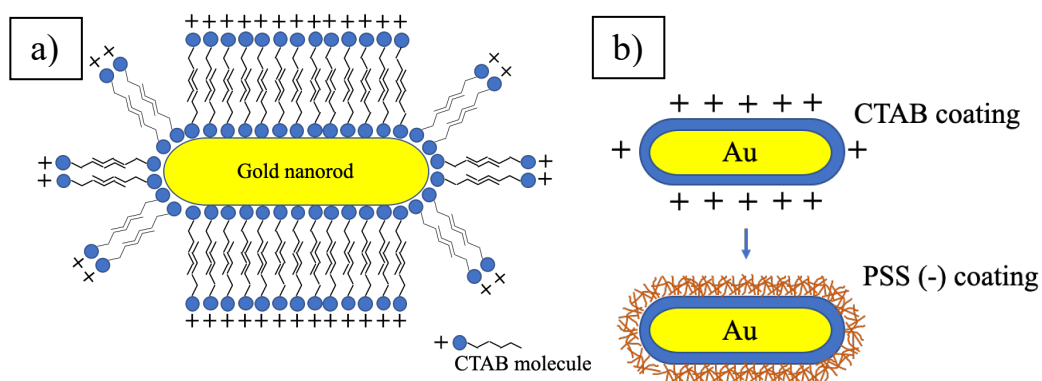


Figure 3–5: a) schematic of a gold nanorod covered by positively charged CTAB and b) Surface modification of CTAB AuNRs with negatively charged PSS layer using a layer by layer technique, adapted from [12]

3.1.5.1 PSS coating

Briefly, as-synthesised AuNRs were centrifuged at 14000 rpm for 30 min. The supernatant was removed and the precipitate was decanted with same amount of DI water in order to remove free excess CTAB. The diluted CTAB AuNRs were added drop-wise into a 5 mL of mixture consisting of 10mg/mL of PSS and 5 mM NaCl in the same volume ratio. This mixture was kept at 30 for 4 hr and 500 rpm magnetic stirring to ensure coating completion. Then, the C/R cleaning step was performed twice with 1 mg/mL of PSS. A 30-min time delay was applied in each step of the C/R process to allow completion of the PSS coating.

3.1.5.2 Citrate stabilized AuNRs

For citrate stabilized AuNRs, the PSS-AuNRs were twice cleaned using the C/R process with 5 mM of sodium citrate. There was a 30 min time interval between each C/R process for the surface modification reaction.

3.1.5.3 Silica coating

Silica coating of AuNRs was carried out using a sol gel protocol described in literature [17]. Briefly, after the 2nd C/R process, the synthesised CTAB-capped AuNRs were diluted with 20mL water, then 200 μ L of 0.1 M NaOH was mixed with the solution. The coating step involved injection of 60 μ L of 20% TEOS in methanol with magnetic stirring. The same amount of TEOS was again added after both 30 min and 60 min, and then the solution was left overnight to allow silica coating.

3.2 Characterization methods

3.2.1 Ultraviolet and visible (UV/vis) spectroscopy

3.2.1.1 Basic principles

UV-vis spectroscopy is a useful technique to examine the optical properties of metal NPs such as Au and Ag. It measures the intensity of light passing through a specimen and hence investigates the absorption and scattering of radiation by a material via an extinction spectrum. The sample (dispersion) is loaded between a light source and a detector, then light is irradiated either passing through or reflected from the sample. The wavelength of radiation can be varied over a region of interest. The intensity of the incident and transmitted radiation is calculated and processed together with the background radiation. The result is plotted as a function of extinction and wavelength [18, 19]. The absorbance (A) of the sample and the

intensity of incident (I_o) and transmitted (I) radiation follow the Beer-Lambert Law [20], given by equation 3-1.

$$A = \log_{10} \frac{I_o}{I} \quad \text{Equation 3-1}$$

The absorbance of a solution relies on the assumption that it is proportional to both the concentration (c) of the solution and the light path length (l) which is equal to the width of the cuvette.

$$A \propto c \quad \text{Equation 3-2}$$

$$A \propto l \quad \text{Equation 3-3}$$

The Beer-Lambert formula can be rewritten by applying a proportionality constant (ϵ), known as the extinction coefficient and the absorbance can be expressed as equation 3-4.

$$A = \log_{10} \frac{I_o}{I} = \epsilon cl \quad \text{Equation 3-4}$$

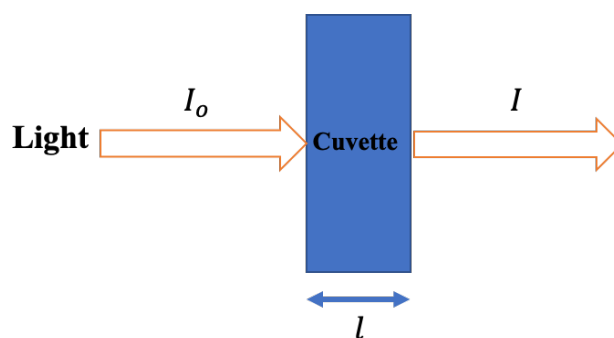


Figure 3–6: A schematic diagram of UV-vis spectroscopy.

The extinction spectrum of metal NPs is sensitive to their local structure including size, shape, composition, and aggregation state of the sample. For example, the absorption spectrum of spherical AuNPs with a diameter about 20 nm has a maximum which lies at about 520 nm [21]. Meanwhile AuNRs exhibit two LSPR excitations which are the longitudinal and transverse modes [21, 22]. The transverse mode lies at about 520-525 nm matching that of spherical AuNPs. For the longitudinal mode, it is an order of magnitude more intense than the transverse mode and lies above 600 nm depending on the AR of the AuNRs, as presented in figure 3-7.

3.2.1.2 Practical details

After using the C/R process twice so as to remove free excess CTAB, all as-synthesised Au nanostructures were then examined in terms of their optical absorption spectrum by UV-vis spectroscopy using a Perkin-Elmer lambda35 model spectrophotometer. In brief, a UV-vis cuvette containing 1 mL of the Au nanostructure dispersion was put in the spectrophotometer and an extinction spectrum from 400 to 900 nm was collected.

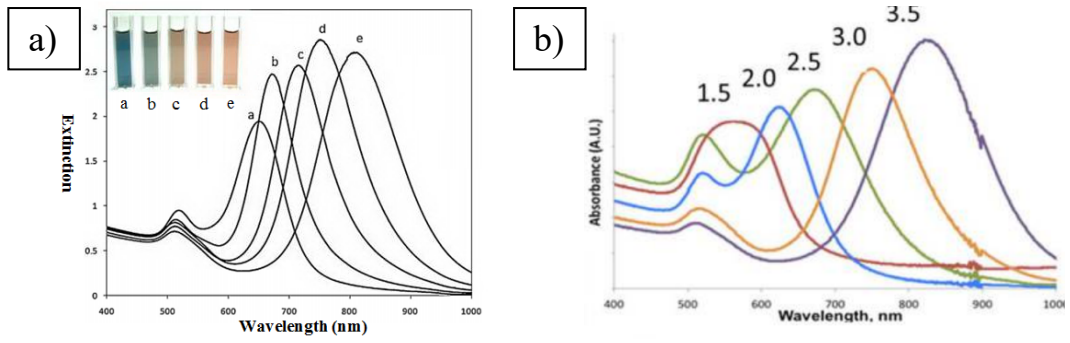


Figure 3–7: Example of UV-vis spectra of Au NRs with different aspect ratios: a) showing the Au colloid colour [23] and; b) showing results for different aspect ratios from 1.5 to 3.5 [24].

3.2.2 COMSOL modelling on uv/vis spectra

COMSOL modelling of absorption spectra was performed following the description in the PhD thesis of Cottom [25]. Briefly, finite element modelling (FEM) was used and simulated using COMSOL Multiphysics 5.2a software together with RF module which allowed modelling of the electromagnetic waves in the frequency domain. The basic idea is that the nanoparticles were placed in the middle of a homogenous medium and an incident plane wave was defined, as in equation 3-5, in the z-direction. The COMSOL function, *Electromagnetic Wave, Frequency Domain* was used calculate the scattered field under the boundary conditions.

$$E_0 * \exp(-i*(emw.k0 * n_a) * -z) \quad \text{Equation 3-5}$$

where, n_a is the refractive index of the surrounding medium (note vacuum = 1), $emw.k0$ is the wave number in free space which is a built-in function, and E_0 refers to electric field strength and is set to 1 for all simulations.

The NP was created using a built-in geometry tool via CAD software and was situated in the centre of the medium. Then, the material properties for gold and vacuum were defined with COMSOL predefined properties for all model parts. After pre-assignment, the model was set to solve the extinction cross section using volume and surface integrals shown in equations 3-7 and 3-8.

$$\text{Extinction cross section} = \text{Absorption} + \text{Scattering} \quad \text{Equation 3-6}$$

$$\text{Absorption} = \text{vol_int}(emw.Qh)/I \quad \text{Equation 3-7}$$

$$\text{Scattering} = \text{surf_int}(nrealPoav)/I \quad \text{Equation 3-8}$$

Where, $emw.Qh$ is the power loss density function, $nrealPoav$ is the scattered Poynting vector associated with energy flux of the electromagnetic field in all x, y, and z directions ($nrealPoav = n_x * emw.relPoavx + n_y * emw.relPoavy + n_z * emw.relPoavz$),

$Zconst$ is a Comsol constant for the impedance of free space, and I refers to the incident intensity ($E_0^2 x n_a / 2x Zconst$).

The results were shown as input frequency and relative spectra with an electric field distribution map surrounding the NPs.

3.2.3 Dynamic light scattering (DLS) and Zeta potential measurement

3.2.3.1 Basic principles of dynamic light scattering (DLS)

Dynamic light scattering (DLS) is a universal method to characterize the size of NPs and their size distribution in a liquid dispersion. During the DLS measurement, the intensity of incident and scattered light in different directions are measured. Both the intensity and the direction of the scattered light change over time due to the random Brownian motion of NPs in the liquid. For spherical NPs, the diffusion coefficient (D_f) determines the NP motion as described by the Stokes-Einstein equation [26, 27].

$$D_f = \frac{k_B T}{6\pi\eta R_H} \quad \text{Equation 3-9}$$

where, k_B , R_H , T and η denote the Boltzmann constant, hydrodynamic radius, sample temperature and viscosity of surrounding medium, respectively. This allows extraction of the hydrodynamic radius of the NPs.

For non-spherical NPs such as rods, both rotational diffusion (D_R) and translation diffusion (D_T) determine the motion, and the decay rate of the rod NPs is given by equation 3-10.

$$\Gamma = q^2 D_T + 6D_R \quad \text{Equation 3-10}$$

where, q is the scattering wave vector.

An example of this evaluation is the angle-dependent DLS measurements of $\beta - FeOOH$ NRs [28]. A Γ vs q^2 plot provided the value of D_R by extrapolation of q to zero whilst D_T was given by the slope of curve represented in figure 3-8. The plot exhibited no effect of D_R due to the linear line passing through the origin of the graph. Therefore, the value of D_T extracted from the slope of graph was $7 \times 10^{-12} \text{ m}^2/\text{s}$ [28]. This value of D_T was used to calculate the average R_H by substitution of equation 3-10 into 3-11.

$$R_H = \frac{k_B T}{6\pi\eta\Gamma} q^2 \quad \text{Equation 3-11}$$

Moreover, the stick hydrodynamic theory [29] and Broearsma's relationship [30] can also be used to calculate diffusion coefficients using the true diameter (length and width) derived from TEM imaging. Here the value of D_T from the observed length and width are 7.09×10^{-12} and $6.84 \times 10^{-12} \text{ m}^2/\text{s}$, respectively. These values were then compared with the DLS results. Thus, the hydrodynamic radius of non-spherical NPs can be determined from these approximations.

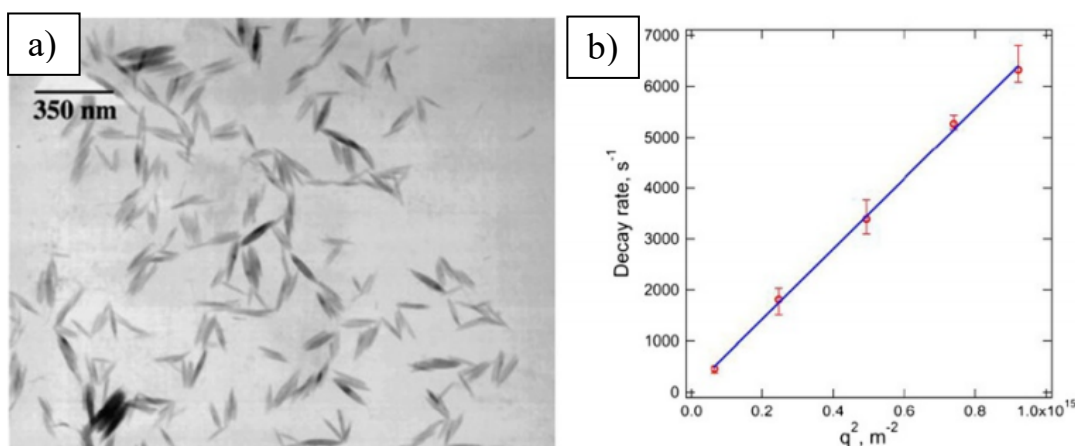


Figure 3–8: a) TEM image of NRs and b) angle-dependent decay rate vs q^2 plot. Data taken from [27, 28].

3.2.3.2 Basic principles of Zeta potential measurement

The Zeta potential is a surface charge measurement of NPs contained in a liquid suspension derived from measuring the particle diffusion coefficients under applied potentials. The zeta potential value reveals the electrostatic repulsion among the particles, contributing to system stability. Higher zeta potentials result in a more stable system. Smoluchiwski theory can be applied to measure Zeta potentials assuming the Debye length is smaller than particle radius, and where surface conductivity is negligible [31]. Another approach is called the Debye-Huckel approximation used when the Debye length is larger than the particle radius.

3.2.3.3 Practical details

1 mL of all individual as-synthesised Au nanostructures was put in a UV-vis cuvette (for DLS analysis) and surface zeta potential cell and examined in a Malvern Zetasizer ZS1 for particle size and zeta potential measurement. The parameters of water were used for the DLS measurement and the result is an average of 10 measurements. An example of the DLS and Zeta potential output is illustrated in figure 3-9. The characteristic size distribution of DLS measurement can be converted from intensity, into either volume or number plots. The latter often highlights smaller particle size fractions in the dispersion, as the scattered intensity varies as the sixth power of particle size.

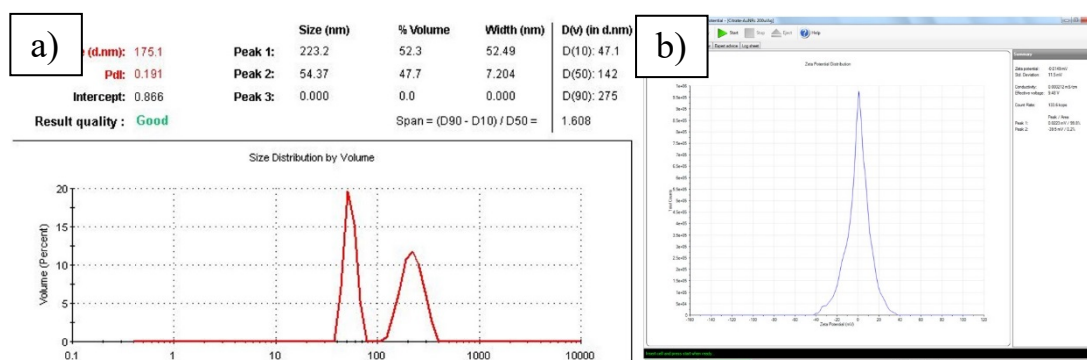


Figure 3–9: Example of a) DLS output figure taken from [32] and b) Zeta potential curve obtained using Malvern Zetasizer ZSI software.

3.2.4 Transmission electron microscopy (TEM)

Transmission electron microscopy (TEM) is a very useful characterization technique for directly imaging Au nanostructures and to measure the electron energy-loss (EEL) spectrum of the sample. The basics of TEM is described in this section.

3.2.4.1 Basic principle of conventional TEM (CTEM)

1) Electron gun

TEM is a universal technique used to examine nanoscale materials and operates under a high vacuum environment. In CTEM, electrons are generated from an electron source and then accelerated down through the microscope column passing through the specimen. The electrons are scattered and potentially diffracted by the material and electromagnetic lenses can be used to form TEM images which can be displayed on a screen or camera and used to investigate atomic structure [33-37]. The basic layout and components of a CTEM are presented in figure 3-10.

An electron gun is located at the top of the microscope column and is used to generate electrons. A thermionic gun contains a heated filament or cathode, an anode, and a Wehnelt cylinder, see figure 3-10. For thermionic electron emission, a high current is passed through the tungsten filament causing a high temperature and electrons are emitted from the surface of the filament. These electrons are then accelerated to high energy towards a positive anode. The Wehnelt cylinder is used to confine and focus the electron beam before injecting them into the TEM column [33-36]. This research employed a TEM which uses thermally assisted field emission (Schottky emission) gun which allows generation of a very fine electron beam size down to 1 nm [37]. Here, although the filament is heated, an applied electric field is also employed to reduce the work function for electron emission. Then, electrons from the heated filament can tunnel out through the potential barrier before being accelerated.

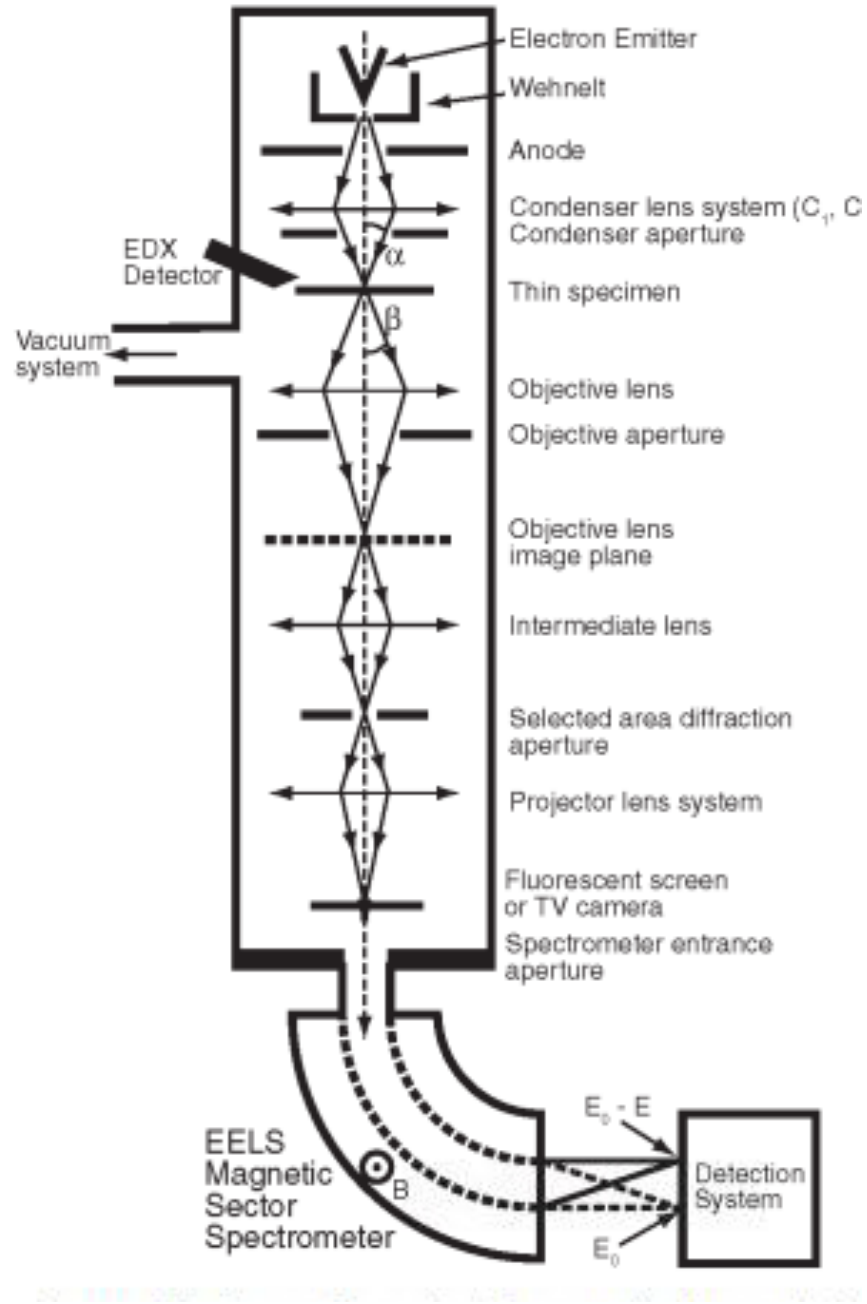


Figure 3–10: schematic diagram showing the main components of a conventional TEM, taken from [33].

2) Electromagnetic lenses and apertures

Electromagnetic lenses are used to control the electron beam focus, the microscope magnification, and the illumination of the specimen. A magnetic lens exhibits the same optical behaviour as a thin glass lens which can be described by the optical thin lens equations 3-12 and 3-13. The image magnification is defined as the ratio of image size (V) to real object size (U) and the relation between focal length (f) of the lens, object distance (u), and image distance (v) is described below.

$$m = \frac{V}{U} = \frac{\text{Image Size (V)}}{\text{Object Size (U)}} \quad \text{Equation 3-12}$$

$$\frac{1}{f} = \frac{1}{u} + \frac{1}{v} \quad \text{Equation 3-13}$$

Electromagnetic lenses are used to confine and focus the electron beam along the optic axis in the TEM column resulting in the final TEM image. They create an induction force which acts on electrons as described in equation 3-14. The focal length of electromagnetic lenses is modified by a change of current in the lens resulting in a change in magnetic field.

$$\vec{F} = -e(\vec{E} + \vec{v} \times \vec{B}) \quad \text{Equation 3-14}$$

where, \vec{E} , \vec{B} , \vec{v} , and e refer to an electric field, magnetic field, electron velocity and electron charge, respectively.

In CTEM, transmitted and scattered electrons are collected by an objective lens, which forms the initial magnified image. Then, this objective image is focused and magnified by an intermediate lens and subsequently a projector lens system before passing to a fluorescent screen or optical camera (based on a scintillator and charge coupled diode array).

3) *Electron imaging mechanisms*

Mass-thickness contrast, diffraction contrast and high resolution TEM (HRTEM) phase contrast are typical imaging mechanisms in CTEM. Firstly, mass-thickness contrast is generated from the different scattering effects when electron interacts with the specimen. In a high mass or a thicker area, electrons will scatter more than in a thin area, sometimes this results in high angle scattering or even back-scattering [33-36]. This process results in fewer electrons and hence darker contrast in the electron image which reaches the detector. On the other hand, brighter contrast results from a low mass or thinner area.

Diffraction contrast is evident in bright field (BF) and dark field (DF) images. For BF imaging, only undiffracted electrons transmitted passing through the specimen are collected and used to construct the image achieved by inserting an objective aperture in the back of focal plane of the objective lens. DF images are constructed as a reversal of BF images, when the objective aperture is used to allow only diffracted electrons to contribute to the image. Diffraction contrast is sensitive to crystallinity and alterations in crystallinity, such as defects. HRTEM images are employed to characterize lattice spacings, and hence the crystalline phase and growth direction. HRTEM is achieved at very high image magnifications and is formed by collecting both transmitted and scattered electrons which have different phases following diffraction of the electron wave. These electron waves interact forming an interference pattern associated with the lattice.

Imaging of the back focal plane of the objective lens allows observation of the electron diffraction pattern. Using an aperture in the image plane at one of the projector's lens further

down the column allows formation of selected area electron diffraction (SAED) from a particular region in the specimen image. Examples of electron imaging are shown in figure 3-11.

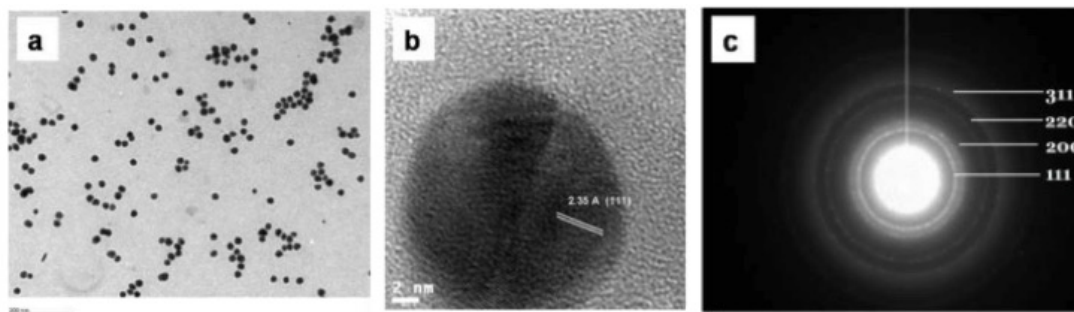


Figure 3–11: TEM bright field image (a), and HRTEM image (b) of gold nanoparticles with a selected area electron diffraction pattern shown in (c), figures taken from [38].

4) Energy dispersive X-ray (EDX) spectroscopy

Elemental analysis using Energy dispersive X-ray (EDX) spectroscopy identifies the specific energies of the characteristic X-rays emitted from the specific elements contained in the specimen [33, 35, 36]. When the electron beam passes through the specimen, energy can be transferred causing electron excitation and ionisation. This causes excitation and ejection of an inner shell electron causing a hole in the inner shell. Relaxation of an outer shell electron from a higher energy level allows the atom to get back into the ground state. However this de-excitation process causes emission of a characteristic X-ray, the energy of which relates to elements in the specimen. This X-ray intensity is plotted as a function of energy, resulting in specific X-ray peaks associated with each element. Figure 3-12 represents an EDX spectrum of AuNPs, exhibiting an Au peak at 2.14 keV.

3.2.4.2 Practical details

After C/R cleaning process, all TEM samples were prepared by dropping 2 μ L of the Au nanoparticle suspension onto a 400 mesh holey carbon film supported on a Cu grid (Agar Scientific) and leaving to dry naturally at room temperature. Using the LEMAS facility in the School of Chemical and Process Engineering at the University of Leeds, all CTEM images were characterized in BF, SAED and HRTEM imaging modes using a FEI Tecnai G2 TEM/STEM operated at an accelerating voltage of 200 kV and fitted with a Gatan Orius 600C camera. EDX spectroscopy was performed using an EDX detector (Oxford Instruments AZTEC). All images and data processing was undertaken using digital micrograph software (Gatan).

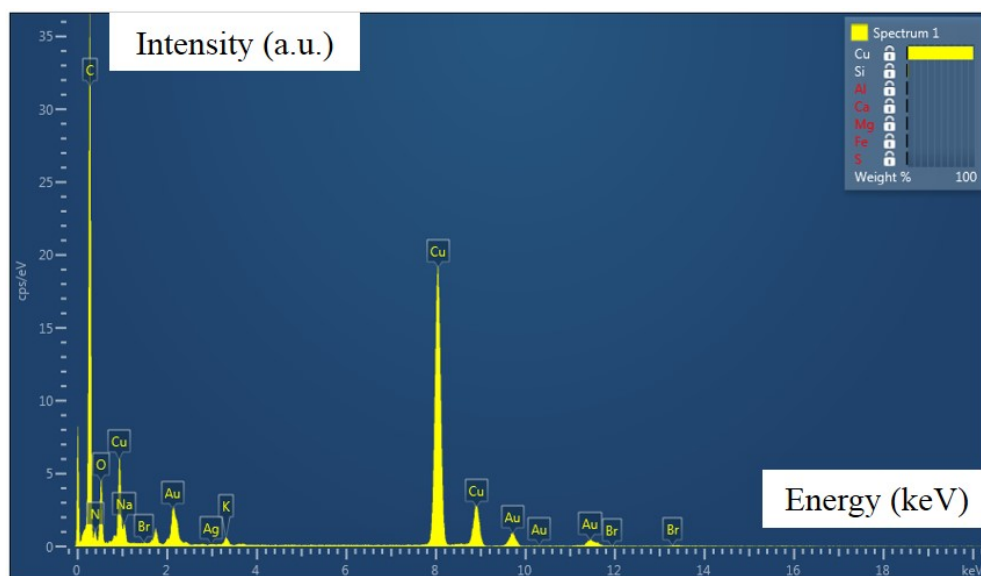


Figure 3–12: Example of EDX spectra of Au nanoparticle sample.

3.2.5 Scanning transmission electron microscopy (STEM)

3.2.5.1 Basic principles of STEM

Scanning transmission electron microscopy (STEM) is a TEM technique where the electron beam passing through the sample is focused by probe-forming lenses to a fine spot and scanned across the sample. The interaction at each point is collected and recorded in transmission as a function of probe position [33-35]. In STEM mode, the electron beam is not focused after passing through the sample but its intensity is detected. Scan coils direct the beam as a raster scan over the area of interest and the intensity at each point is recorded to form the final image [39]. The advantage of STEM mode is the improvement in analytical spatial resolution. The basic components of STEM are presented in figure 3-13.

However, imaging modes in STEM are different from CTEM. Bright field (BF) and high angle annular dark field (HAADF) images are the most common in STEM as represented in figure 3-14. In BF, the detector is placed on the optic axis (beam axis). The images from this BF mode essentially are equivalent but smaller (in term of scattering angle) to those of the conventional TEM. In HAADF imaging, an annular detector is used and only high angle elastic scattered electrons are detected. HAADF intensity arises from Rutherford scattering from the atomic nuclei and hence intensity increases with atomic number and sample thickness.

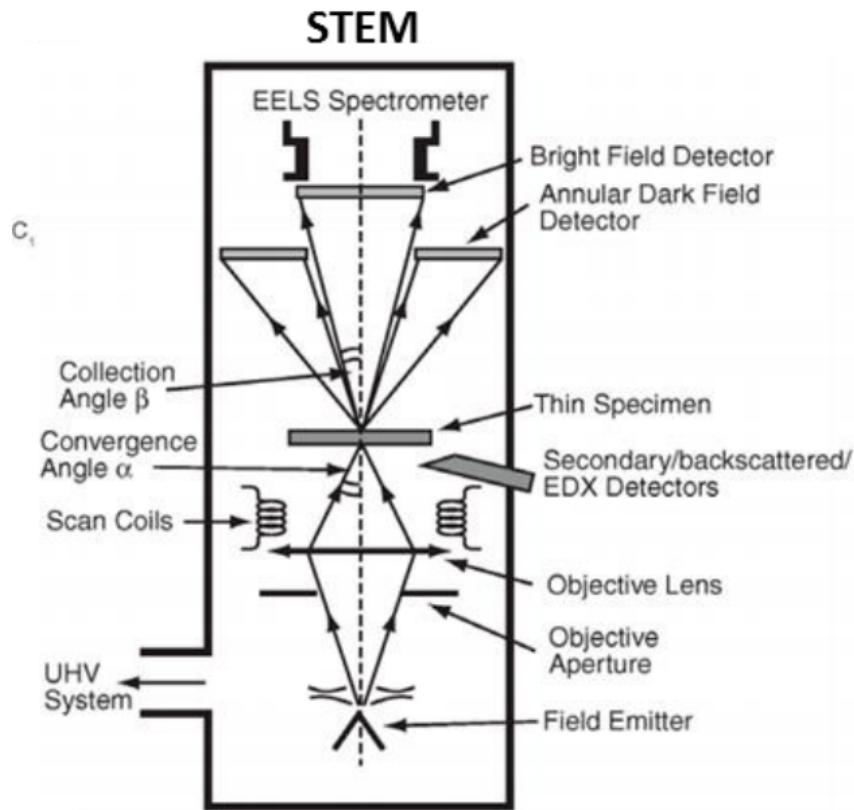


Figure 3–13: schematic diagram showing the main components of dedicated STEM. Image taken from [33]. Note: in this case the electron gun is at the bottom of the column.

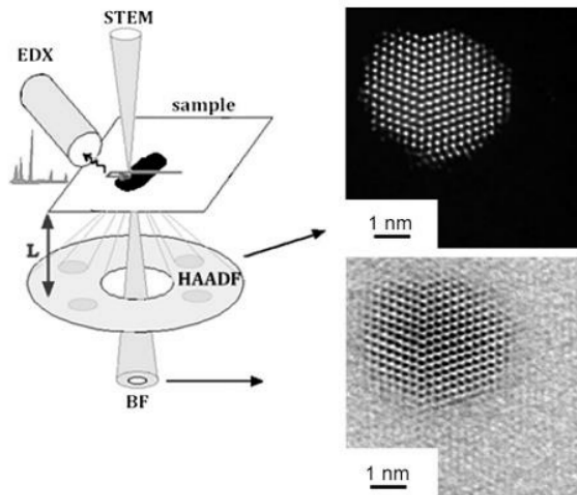


Figure 3–14: schematic diagram representing STEM imaging modes using different detectors. Inset shows: 1) BF (bottom) and 2) HAADF imaging (top), taken from [33]

3.2.5.2 Basic principles of electron energy-loss spectroscopy (EELS)

Electron energy-loss spectroscopy is an analytical technique which measures the kinetic energy variation of the transmitted electrons with high spatial and energy resolution resulting from the inelastic scattering of fast electrons within the specimen. This technique measures the transmitted electron intensity passing through the specimen and categorizes it according to the difference in energy and hence energy loss [33, 34]. EELS can be used to identify chemical properties such as the type of atom and its bonding in the sample as well as electronic properties such as plasmon resonances at a specific location. By combining EELS with the STEM technique (STEM-EELS), it is potentially possible to investigate this information at atomic resolution.

An EELS spectrum normally presents the energy loss (eV) from the incident beam energy on the x-axis and relative intensity on the y-axis. The EELS spectrum can be divided into 3 regions: the zero loss, low-loss and core-loss regions according to their different form of excitations and is represented in figure 3-15. The zero loss region exhibits elastic scattering and quasi-elastic phonon scattering of electrons which pass through the sample. For a thin sample, this zero loss peak (ZLP) is the most dominant peak in the EELS spectrum. This peak is located at 0 eV with the highest intensity for the case of a thin specimen [40, 41]. The full width at half maximum (FWHM) of this peak reflects the energy spread of the electron source and resolution of the EEL magnetic prism spectrometer.

The low-loss region contains information about excitation of outer shell and valence electrons. Only a small amount of energy is required to excite these electrons [41]. The plasmon oscillation of metal NPs corresponds to the UV-vis spectrum and can be determined using low-loss EELS.

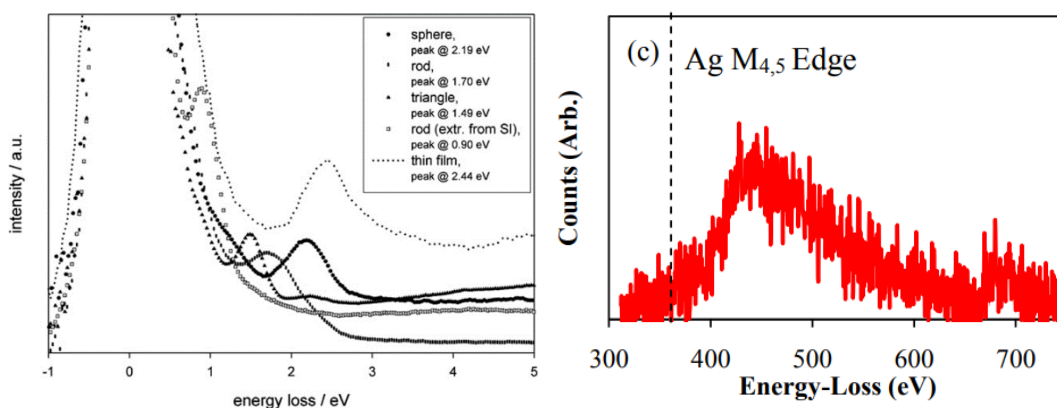


Figure 3–15: Example of an EELS spectrum of metallic nanoparticles corresponding to: a) zero-loss and low-loss region of gold NPs [42]; and b) core-loss EELS region of silver NPs [34].

Energy losses above 50 eV are categorized as the core-loss region, where inner shell electrons can be excited to any of the unoccupied electronic states. This excitation provides localized elemental composition via the observation of unique steps in the EELS spectrum called ionisation edges. These edges can be used to identify bonding and local structure via the electron energy loss near edge structure (ELNES). Also, in principle bond lengths and coordination numbers can be investigated via the extended electron energy loss fine structure (EXELFS).

3.2.5.1 Practical details

1 μL of the as-synthesised Au nanoparticle suspensions was dropped onto a 400 mesh lacey carbon film supported on a Cu grid and left to dry naturally at room temperature (as an initial attempt). Subsequently, non-porous, pure silicon 5 nm thick TEM window support films (purchased from EM Resolutions) were also used to improve the data quality. All STEM-EELS spectra were collected over the low-loss region from 0 -3 eV using a monochromated electron source in a FEI Titan Themis Cubed 300 TEM operating at 300 kV. The energy dispersion was 0.01 eV and the energy resolution was ca. 0.25-0.3 V. All image and data processing was conducted using Gatan digital micrograph software.

3.3 Conclusion

These synthesis methods of Au nanostructures allow better control of their size and shape by modifying synthesis parameters, leading to the potential novel synthesis methods that can be altered their SPR into the NIR regions. Furthermore, the characterised methodologies would allow the investigation of Au nanostructures and their optical properties for both suspension and individual particles as in focus of this thesis. To study optical and plasmonic properties, STEM/TEM measurement can reveal the spatial resolution of individual Au nanostructures that may help to provide better understanding of localised SPR field enhancement and design gold nanostructures with SPR near NIR region. TEM imaging of TEM heating experiment may be used to demonstrate the thermal stability study and deformation mechanism. By using these methodologies, the potential candidates for healthcare applications can be proposed.

3.4 References

- [1] Bastús, N.G., J. Comenge, and V. Puntes, *Kinetically Controlled Seeded Growth Synthesis of Citrate-Stabilized Gold Nanoparticles of up to 200 nm: Size Focusing versus Ostwald Ripening*. Langmuir, 2011. **27**(17): p. 11098-11105.

- [2] Bastús, N.G., et al., *Synthesis of Highly Monodisperse Citrate-Stabilized Silver Nanoparticles of up to 200 nm: Kinetic Control and Catalytic Properties*. Chemistry of Materials, 2014. **26**(9): p. 2836-2846.
- [3] Nikoobakht, B. and M.A. El-Sayed, *Preparation and Growth Mechanism of Gold Nanorods (NRs) Using Seed-Mediated Growth Method*. Chemistry of Materials, 2003. **15**(10): p. 1957-1962.
- [4] Rayavarapu, R.G., et al., *In vitro toxicity studies of polymer-coated gold nanorods*. Nanotechnology, 2010. **21**(14): p. 145101.
- [5] Cao, J., *Creation of novel gold-nanorod-based localized surface plasmon resonance biosensors*, in *School of Mathematics, Computer Science & Engineering*. 2013, City University London.
- [6] Connor, E.E., et al., *Gold Nanoparticles Are Taken Up by Human Cells but Do Not Cause Acute Cytotoxicity*. Small, 2005. **1**(3): p. 325-327.
- [7] Lin, J., et al., *Penetration of Lipid Membranes by Gold Nanoparticles: Insights into Cellular Uptake, Cytotoxicity, and Their Relationship*. ACS Nano, 2010. **4**(9): p. 5421-5429.
- [8] Lee, J.-H., et al., *Bipyramid-templated synthesis of monodisperse anisotropic gold nanocrystals*. Nature Communications, 2015. **6**: p. 7571.
- [9] Li, Q., et al., *Production of Monodisperse Gold Nanobipyramids with Number Percentages Approaching 100% and Evaluation of Their Plasmonic Properties*. 2015. **3**(6): p. 801-812.
- [10] Qi, Y., et al., *Highly improved synthesis of gold nanobipyramids by tuning the concentration of hydrochloric acid*. 2016. **18**(7): p. 190.
- [11] Chen, L., et al., *High-Yield Seedless Synthesis of Triangular Gold Nanoplates through Oxidative Etching*. Nano Letters, 2014. **14**(12): p. 7201-7206.
- [12] Cao, J., T. Sun, and K.T.V. Grattan, *Gold nanorod-based localized surface plasmon resonance biosensors: A review*. Sensors and Actuators B: Chemical, 2014. **195**: p. 332-351.
- [13] Jayabal, S., et al., *A gold nanorod-based localized surface plasmon resonance platform for the detection of environmentally toxic metal ions*. Analyst, 2015. **140**(8): p. 2540-2555.

- [14] Mehtala, J.G., et al., *Citrate-Stabilized Gold Nanorods*. Langmuir, 2014. **30**(46): p. 13727-13730.
- [15] Ye, S., et al., *Engineering Gold Nanotubes with Controlled Length and Near-Infrared Absorption for Theranostic Applications*. 2015. **25**(14): p. 2117-2127.
- [16] Chen, L.-l., et al., *Multilayered polyelectrolyte-coated gold nanorods as multifunctional optical contrast agents for cancer cell imaging*. Journal of Zhejiang University. Science. B, 2010. **11**(6): p. 417-422.
- [17] Ashrafi, S., et al., *Thermal Distribution of Silica Coated Gold Nano Rods in Tissue-like Phantom as in Vitro Model for Plasmonic Photo Thermal Therapy*. Biomedical and Pharmacology Journal, 2016. **9**: p. 1189-1201.
- [18] Tissue, B.M., *Ultraviolet and Visible Absorption Spectroscopy, in Characterization of Materials*. 2002.
- [19] Faust, B., *Ultraviolet/Visible Spectroscopy, in Modern Chemical Techniques: An Essential Reference for Student and Teachers*. 1997, The Royal Society of Chemistry. p. 92-115.
- [20] Swinehart, D.F., *The Beer-Lambert Law*. Journal of Chemical Education, 1962. **39**(7): p. 333.
- [21] Amendola, V., et al., *Surface plasmon resonance in gold nanoparticles: a review*. J Phys Condens Matter, 2017. **29**(20): p. 203002.
- [22] Chen, H., et al., *Gold nanorods and their plasmonic properties*. Chemical Society Reviews, 2013. **42**(7): p. 2679-2724.
- [23] Hormozi-Nezhad, M.R., H. Robotjazi, and M. Jalali-Heravi, *Thorough tuning of the aspect ratio of gold nanorods using response surface methodology*. Anal Chim Acta, 2013. **779**: p. 14-21.
- [24] Lohse, S.E. and C.J. Murphy, *The Quest for Shape Control: A History of Gold Nanorod Synthesis*. Chemistry of Materials, 2013. **25**(8): p. 1250-1261.
- [25] Cottom, J.W., *Fabrication and Characterization of an Adaptable Plasmonic Nanorods Array, in School of Chemical and Process Engineering*. 2017, The University of Leeds.
- [26] Edward, J.T., *Molecular volumes and the Stokes-Einstein equation*. Journal of Chemical Education, 1970. **47**(4): p. 261.

- [27] Farrell, D., et al., *Optical and electron microscopy studies of Schiller layer formation and structure*. J Colloid Interface Sci, 2009. **331**(2): p. 394-400.
- [28] Lim, J., et al., *Characterization of magnetic nanoparticle by dynamic light scattering*. Nanoscale Research Letters, 2013. **8**(1): p. 381.
- [29] Vasanthi, R., S. Bhattacharyya, and B. Bagchi, *Anisotropic diffusion of spheroids in liquids: Slow orientational relaxation of the oblates*. 2002. **116**(3): p. 1092-1096.
- [30] Broersma, S., *Rotational Diffusion Constant of a Cylindrical Particle*. 1960. **32**(6): p. 1626-1631.
- [31] Lionberger, R.A. and W.B. Russel, *A Smoluchowski theory with simple approximations for hydrodynamic interactions in concentrated dispersions*. Journal of Rheology, 1997. **41**(2): p. 399-425.
- [32] Nobbmann, U. *D90, D50, D10, AND SPAN – FOR DLS?* 2016 [cited 2019 December]; Available from: <https://www.materials-talks.com/blog/2016/08/25/d90-d50-d10-and-span-for-dls/>.
- [33] Brydson, R., et al., *Analytical Transmission Electron Microscopy*. Reviews in Mineralogy and Geochemistry, 2014. **78**(1): p. 219-269.
- [34] Eccles, J.W.L., *An Electron Energy Loss Spectroscopy Study of Metallic Nanoparticles of Gold and Silver*. 2010, The University of Manchester.
- [35] Chimupala, Y., *Synthesis and Characterization of the TiO₂(B) phase*. 2015, The University of Leeds.
- [36] Goodhew, P.J.e.a., *Electron microscopy and analysis*. 2001, London: Taylor & Francis.
- [37] McGinn, J.B., et al., *100 kV Schottky electron gun*. 1991. **9**(6): p. 2925-2928.
- [38] Syed, A., et al., *Extracellular Biosynthesis of Monodispersed Gold Nanoparticles, Their Characterization, Cytotoxicity Assay, Biodistribution and Conjugation with Doxorubicin*. Journal of Nanomedicine & Nanotechnology, 2013. **4**: p. 156.
- [39] Nellist, S.J.P.a.P.D., *Scanning Transmission Electron Microscopy: Imaging and Analysis*. 2011, New York, NY, United States: Springer-Verlag New York Inc.
- [40] Egerton, R.F., *Electron energy-loss spectroscopy in the TEM*. Reports on Progress in Physics, 2008. **72**(1): p. 016502.

- [41] Brydson, R., *Electron energy loss spectroscopy*. Vol. 48. 2001, Oxford: Bios in association with Royal Microscopical Society.
- [42] Schaffer, B., et al., *Monochromated, spatially resolved electron energy-loss spectroscopic measurements of gold nanoparticles in the plasmon range*. *Micron*, 2009. **40**(2): p. 269-273.

Chapter 4 Structural characterization and the optical properties of synthesized gold nanostructures

In order to obtain controllable and homogeneous Au nanostructures, it is necessary to develop an understanding of the synthesis of Au nanostructures. This chapter focuses on the characterization of synthesized Au nanostructures including gold nanoparticles (AuNPs), gold nanorods (AuNRs), gold nanobipyramids (AuNBPs), and gold nanotriangles (AuNTs). The optical properties of the nanostructures were investigated by UV-vis spectroscopy and the size, morphology and structure explored using TEM imaging and dynamic light scattering. Their crystallographic structures and growth mechanisms are also discussed in this chapter.

4.1 Characterization of Au nanoparticles (AuNPs)

AuNPs were fabricated by a citrate reduction method with a seeded growth step by step procedure modified from the literature [1, 2], as detailed in chapter 3. Briefly, 1 mL of 2.5 mM gold precursors (HAuCl_4) were injected into 2.2 mM boiling sodium citrate to originate seed growth of AuNPs resulting in a soft-pink colour within 15 min. Reaction control was achieved by a reduction of the reaction temperature to 90. Then 5 mL of solution was then pipetted out for characterization. A specific amount of sodium citrate (1 mL, 6 mM) and gold precursor (1 mL, 2.5 mM) was injected before taking a 5 mL of the suspension out for investigation by TEM imaging and UV-vis spectroscopy. The step of synthesis was repeated up to ten times to obtain progressively larger AuNPs with sizes up to about 80 nm.

It was found that a set of controllable, near spherical AuNPs with sizes ranging from approximately 20 to 60 nm were synthesized. UV-vis spectra showed that the extinction peak maximum shifted from 522 nm to 538 nm corresponding to the original seed through to step 10 of the growth, see Figure 4-1a. This red-shift of the extinction spectrum for each growth step resulted from the increasing size of the AuNPs, in agreement with literature [1-3] and similar to the simulated extinction spectra of AuNPs presented in chapter 5, section 5.1.2.

TEM micrographs shown in Figure 4-1b were used to confirm the growth of the AuNPs. The average size of AuNPs increased from the original seed of 20.9 ± 2.7 nm to 36.6 ± 5.0 nm, 45.1 ± 5.5 nm, and 58.3 ± 6.5 nm after growth steps 3, 6, and 10, respectively. Size distribution profiles of the as-synthesized AuNPs are presented in figure 4-1c. AuNP seeds showed good homogeneity in terms of size, similar to the AuNPs from the growth step 10 sample. However

AuNP growth step 3 and 6 samples contained bimodal size distributions with the presence of both small and large spherical particles. Plotting the uv-vis extinction peak maxima from figure 4-1a versus the average particle size derived from TEM, shown in figure 4-1d, reveals a near-linear relationship between the two quantities.

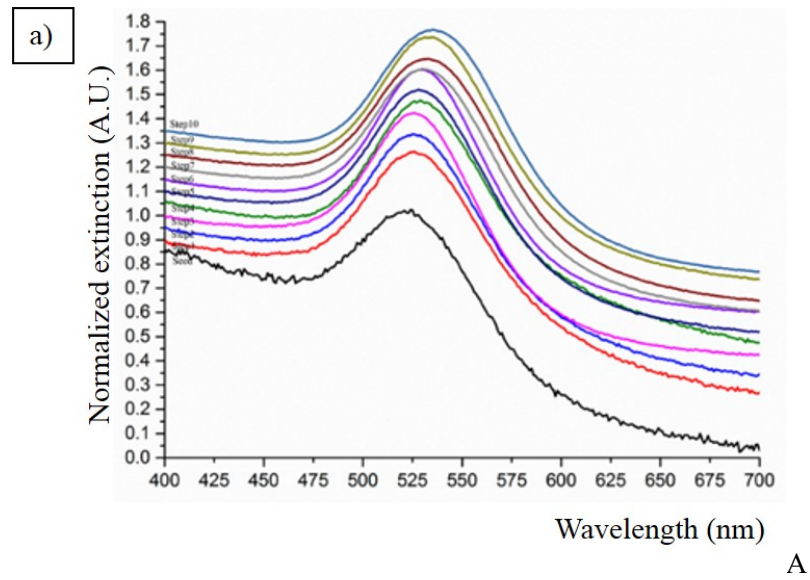


Figure 4-1: AuNPs with successive seed growth steps: a) UV-vis spectra of AuNPs obtained at each growth step from the seed to step 10.

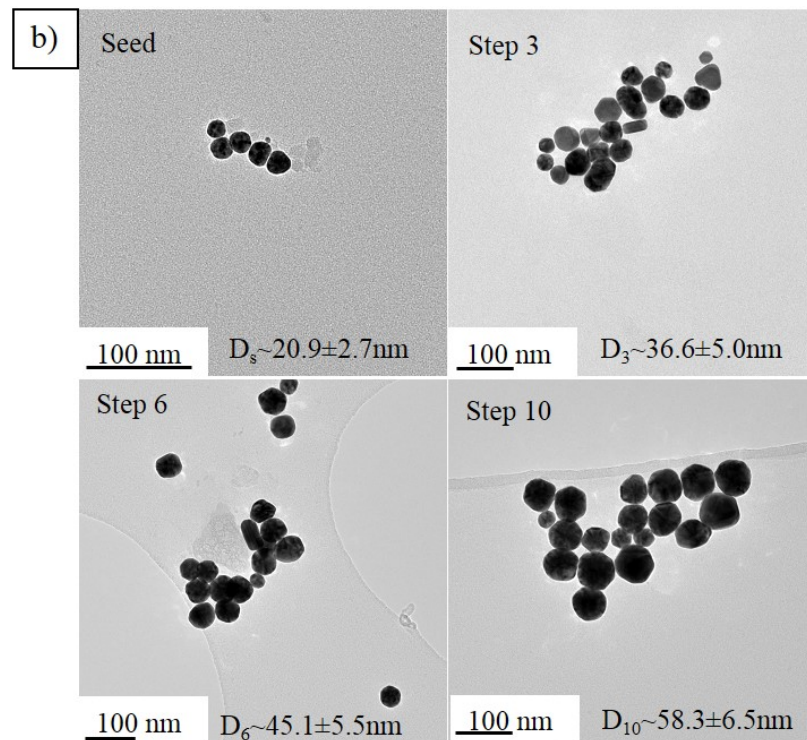


Figure 4-1: b) TEM bright field images taken from samples extracted at the different growth steps.

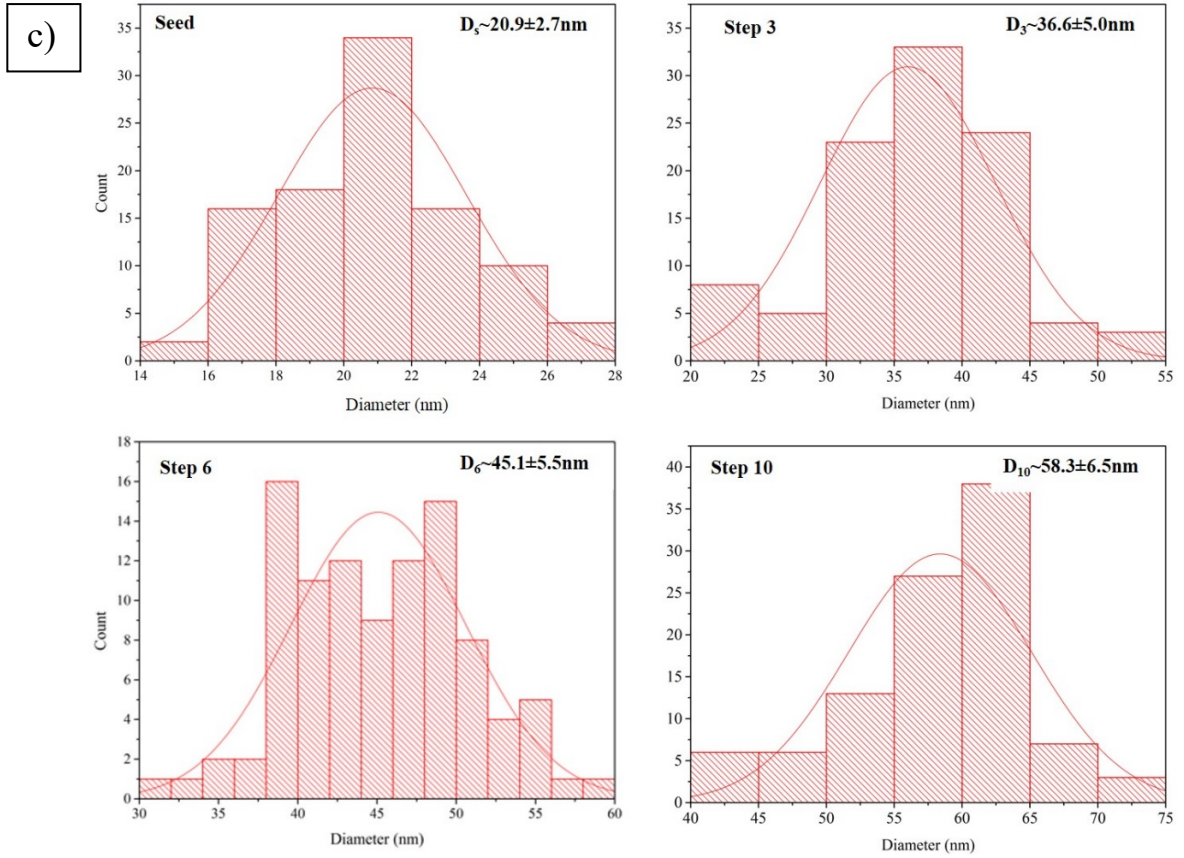


Figure 4-1: c) their respective size distributions derived from TEM imaging.

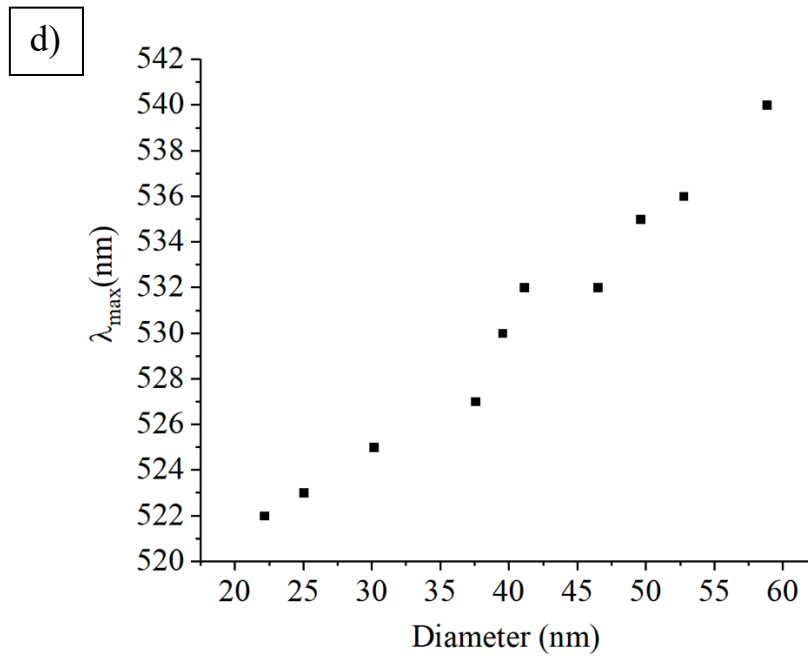


Figure 4-1: d) the uv-vis extinction peak maxima at different particle diameters derived from the TEM images.

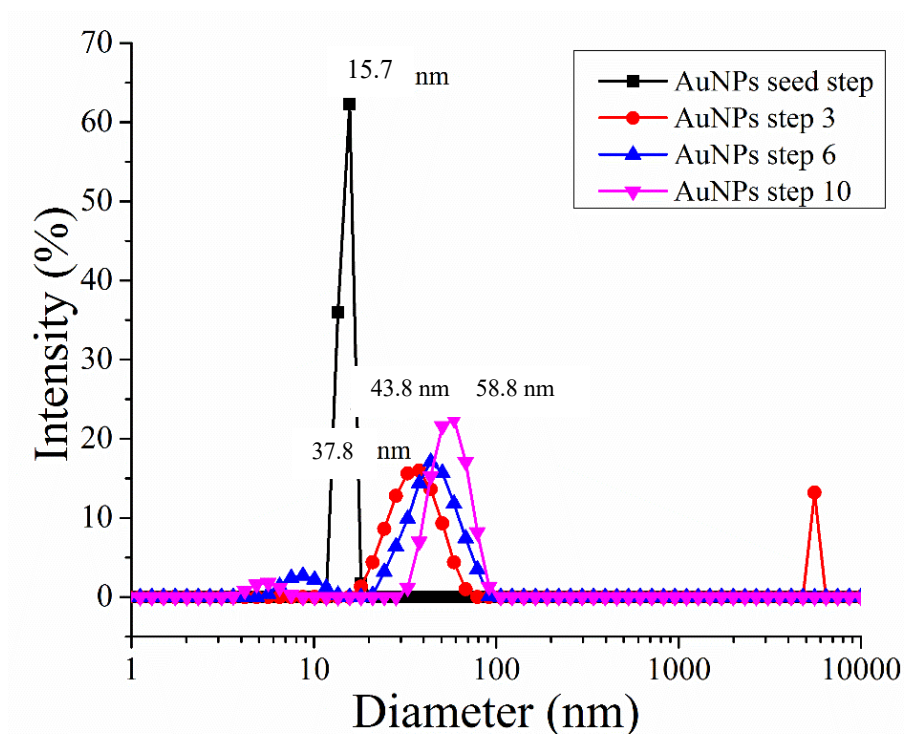


Figure 4–2: Intensity-weighted DLS particle size distribution curves of AuNPs for the different growth steps with average hydrodynamic diameters indicated.

Additionally, DLS analysis of the different AuNP growth steps was conducted to confirm the increase in particle size, illustrated in figure 4-2. DLS revealed that the average hydrodynamic diameter increased from 15.7 to 59.8 nm as synthesis growth steps increased up to step 10.

The average hydrodynamic size from DLS shows good a good correlation with the average size obtained from TEM micrographs, shown in figure 4-3 which exhibits a slope of approximately unity. DLS results suggest that there are two peaks in the size distribution of AuNPs after growth steps 3, 6 and 10, with a peak appearing below 10 nm. The presence of this small peak matched with TEM imaging which indicated the presence of small AuNPs in each of these samples. These small NPs are likely to be residual seeds resulting from the injection of Au precursor to initiate the growth step, whereas the broad main peaks in AuNPs step 3, 6, and 10 samples are a result of the growth. It is clear that DLS would be an initial characterization method that works well for spherical particles and is able to detect the presence of any aggregation in samples [4, 5], see for example the AuNPs step 3 sample DLS plot in Figure 4-2.

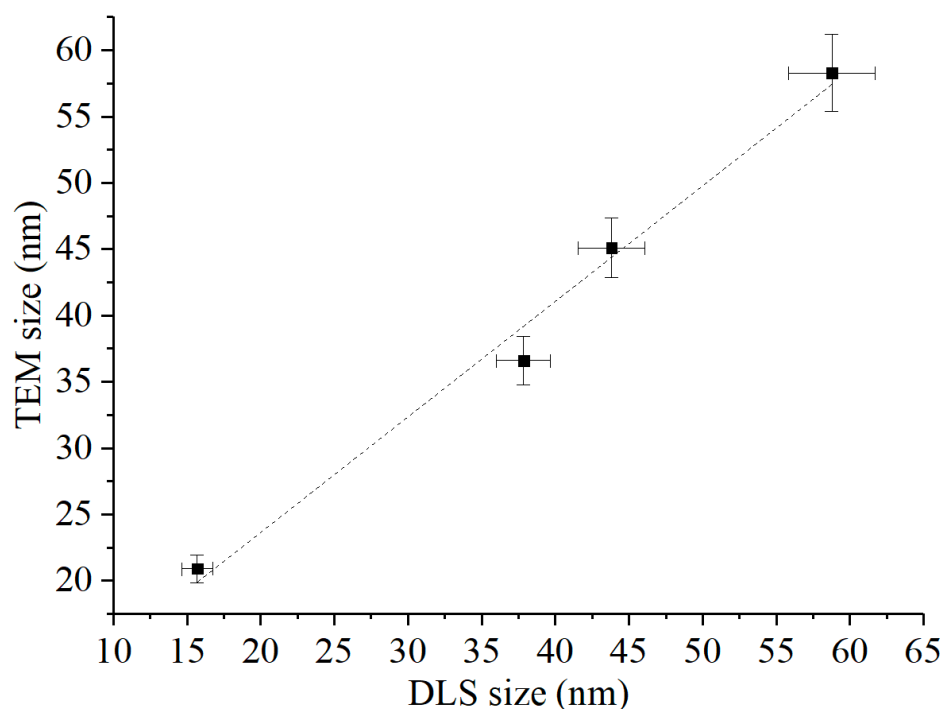


Figure 4-3: TEM average size versus DLS size distribution of the AuNP samples, using a straight line as a guideline of linear relationship between DLS and TEM size measurement with a slope of 0.87 and an intercept of 6.2.

4.2 Characterization of Au nanorods (AuNRs)

CTAB-capped AuNRs with various ARs were synthesized by the kinetically controlled modified synthesis method described in chapter 3. By adding HCl to lower the pH, the growth kinetics were slowed down resulting in higher AR nanorods [6]. Different amounts of AgNO_3 were added to provide different ARs, denoted as samples 1-5, respectively. Well-controlled and reproducible AuNRs with various ARs were produced. The results showed that colour of the dispersion gradually changed from colourless to brown. Eventually over 20-30 min, it turned to a purple/soft-pink depending on the final AR (inset figure 4-4). As-synthesized CTAB-capped AuNRs (samples 1-5) were characterized by UV-vis, TEM and DLS to investigate their particle size distributions shown in figures 4-4 to 4-8 respectively.

The longitudinal SPR peak maxima (λ_{max}) of AuNR samples 1, 2, 3, 4, and 5 were at 574, 648, 712, 740, and 796 nm, respectively (figures 4-4 and 4-5a). Statistical measurements of particle size were conducted by measuring 100 particles per sample from TEM images using ImageJ software. The AR of AuNRs were measured to be 1.6 ± 0.3 , 2.3 ± 0.4 , 3.1 ± 0.6 , 3.5 ± 0.7 , 4.1 ± 0.3 for samples 1-5, respectively as seen in figures 4-6a-e and figures 4-6f-j which show the individual size distributions. Figure 4-5a shows an approximately linear relationship between λ_{max} and nanorod AR as measured by TEM. It was found that the AR of AuNRs increased as the amount of AgNO_3 increased as illustrated in figure 4-5b. In comparison, the calculated

LSPR peak of AuNRs using the discrete dipole approximation (DDA) is given by [7]. For an AuNR with AR of 3.1 (sample 3), the calculated LSPR is at 715.6 nm which is in excellent agreement with the experimental uv-vis spectrum (712 nm). Also, this showed good agreement with simulated extinction spectra of CTAB-capped AuNR by COMSOL modelling in chapter 5, section 5.1.2.

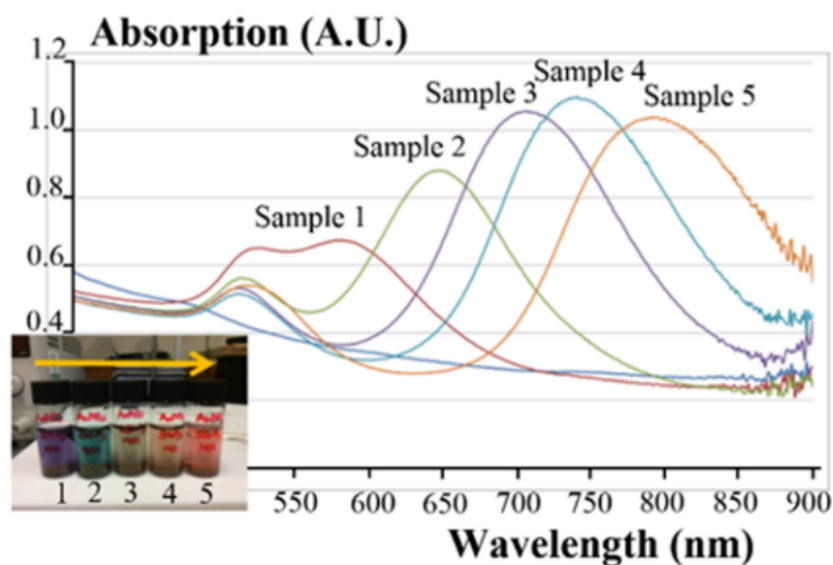


Figure 4-4: UV-vis absorption spectra of CTAB-capped AuNRs with various ARs. Inset shows the change in colour of as-synthesized AuNRs from purple to soft-pink colour indicating the increase in rod AR.

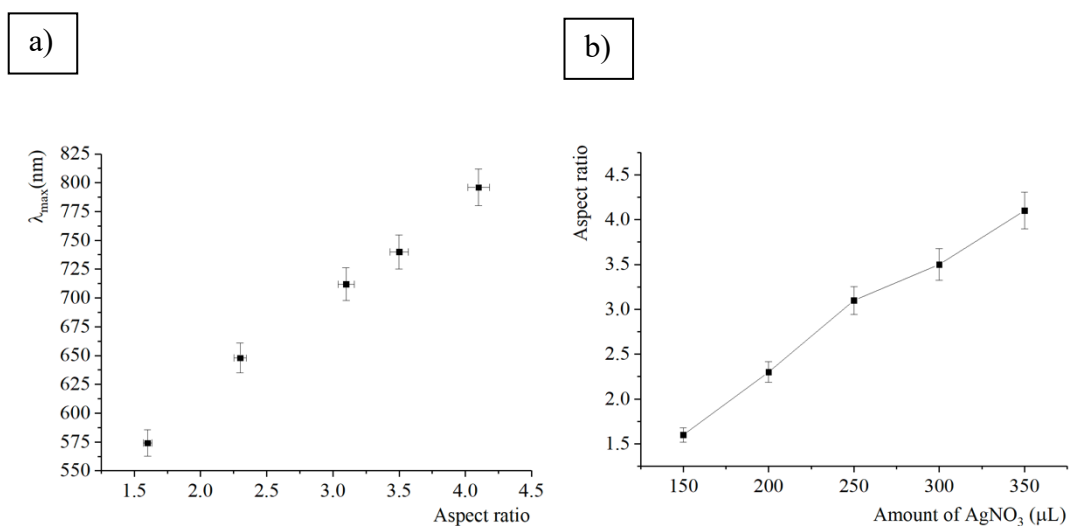


Figure 4-5: a) Longitudinal SPR absorption peak maxima of CTAB-capped AuNRs for different ARs. b) AR of as-synthesized CTAB-capped AuNRs as a function of the amount of silver nitrate added, using a straight line to draw a guideline of each point representing AR increased with an increase of amount of AgNO₃.

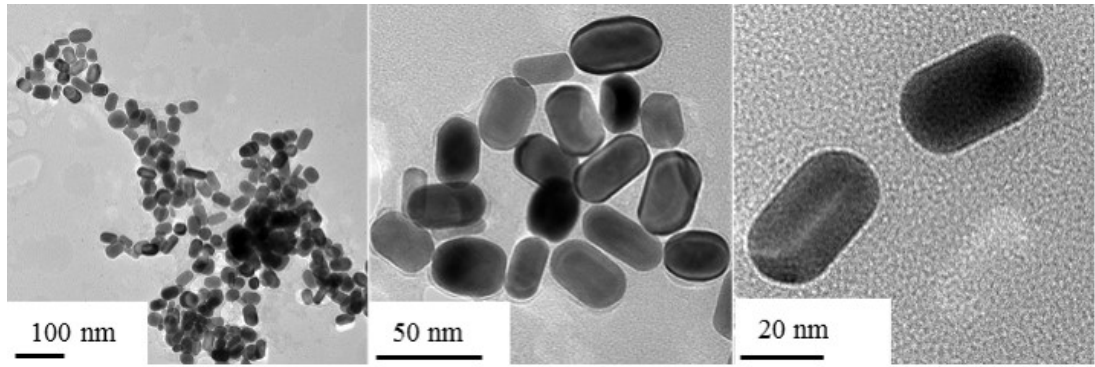


Figure 4-6: a) TEM images of sample 1 which is CTAB capped AuNRs with ARs of 1.6 ± 0.3 (Length $\sim 36.1 \pm 4.2$ nm and Width $\sim 22.5 \pm 3.3$ nm)

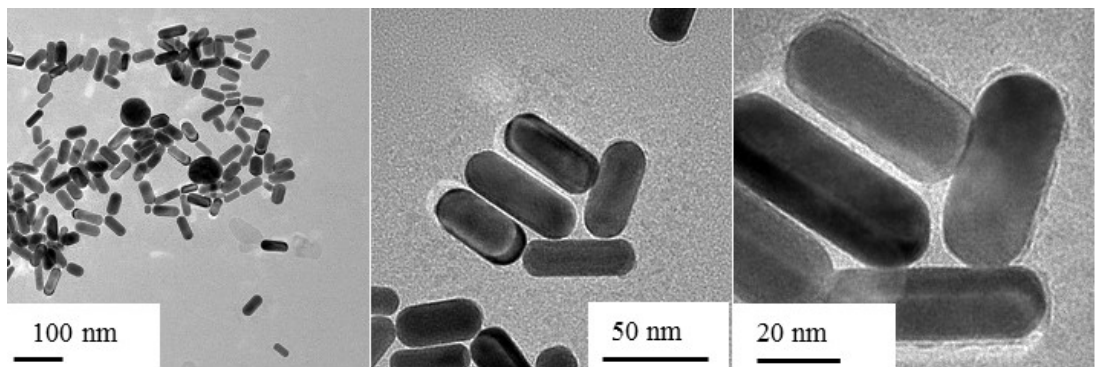


Figure 4-6: b) TEM images of sample 2 which is CTAB capped AuNRs with ARs of 2.3 ± 0.4 (Length $\sim 47.4 \pm 5.3$ nm and Width $\sim 20.6 \pm 3.2$ nm)

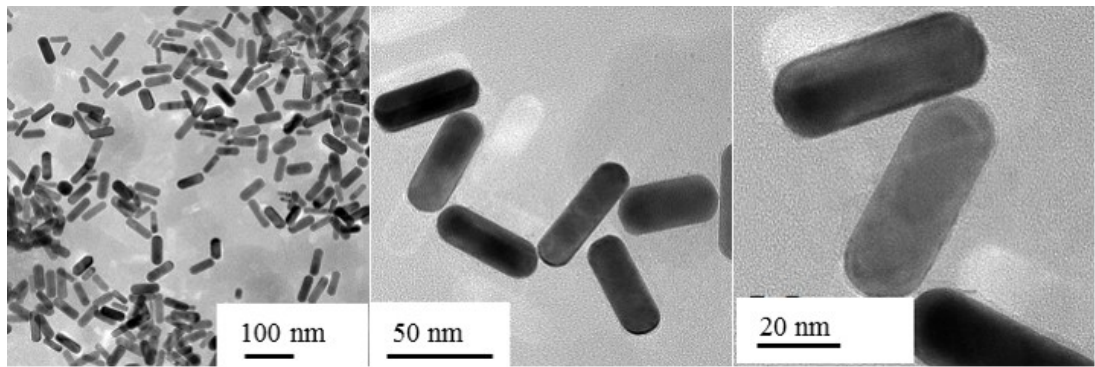


Figure 4-6: c) TEM images of sample 3 which is CTAB capped AuNRs with ARs of 3.1 ± 0.6 (Length $\sim 52.6 \pm 5.0$ nm and Width $\sim 17.6 \pm 2.6$ nm)

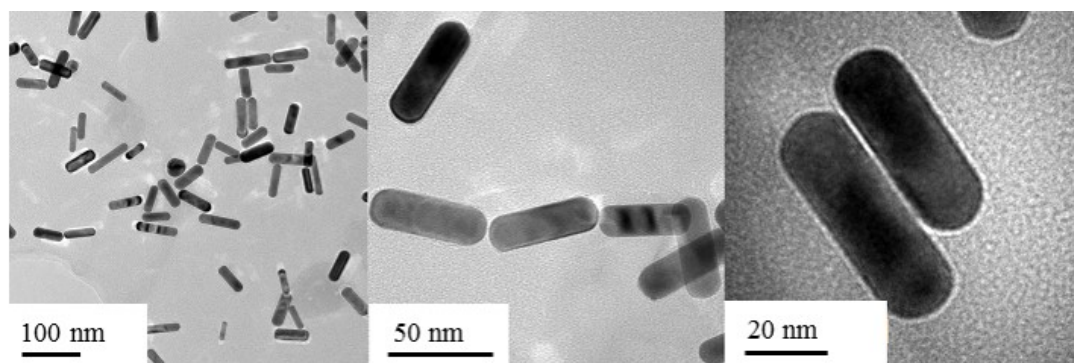


Figure 4-6: d) TEM images of sample 4 which is CTAB capped AuNRs with ARs of 3.5 ± 0.7 (Length $\sim 56.2 \pm 7.1$ nm and Width $\sim 16.2 \pm 2.5$ nm)

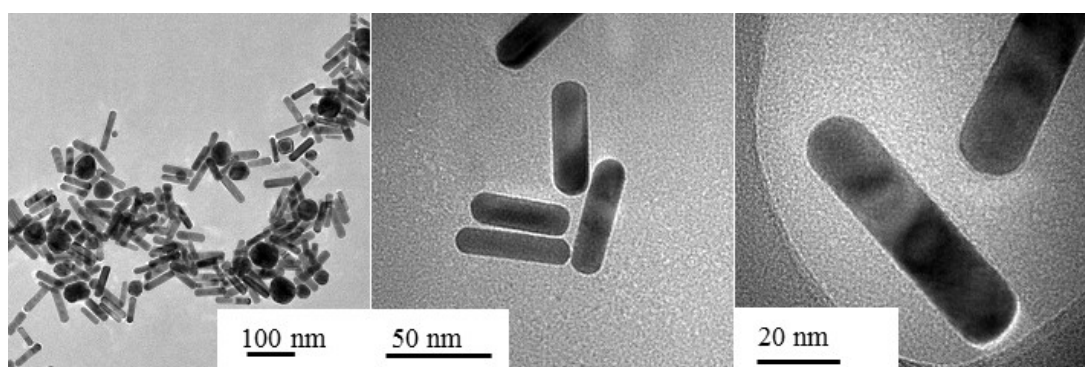


Figure 4-6: e) TEM images of sample 5 which is CTAB capped AuNRs with ARs of 4.1 ± 0.3 (Length $\sim 60.6 \pm 6.8$ nm and Width $\sim 14.9 \pm 2.1$ nm)

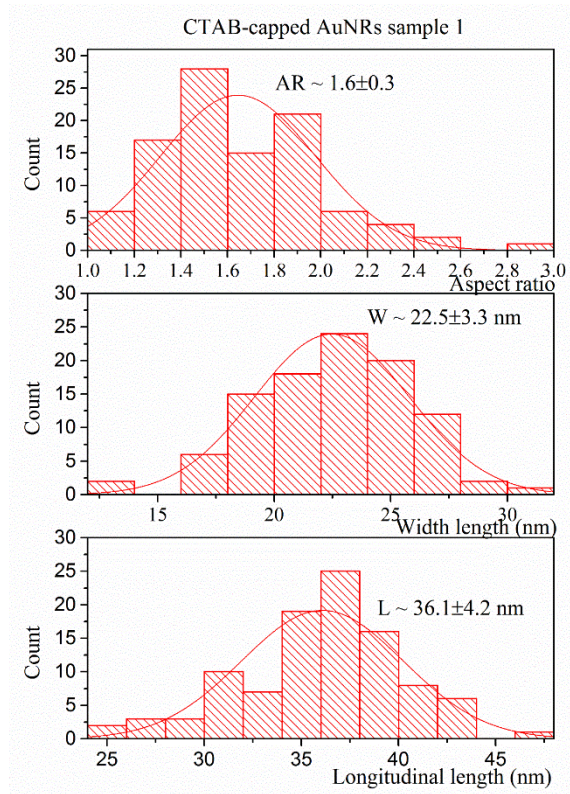


Figure 4-6: f) Size distributions of CTAB capped AuNRs sample 1 derived from TEM imaging, showing an AR of 1.6 ± 0.3

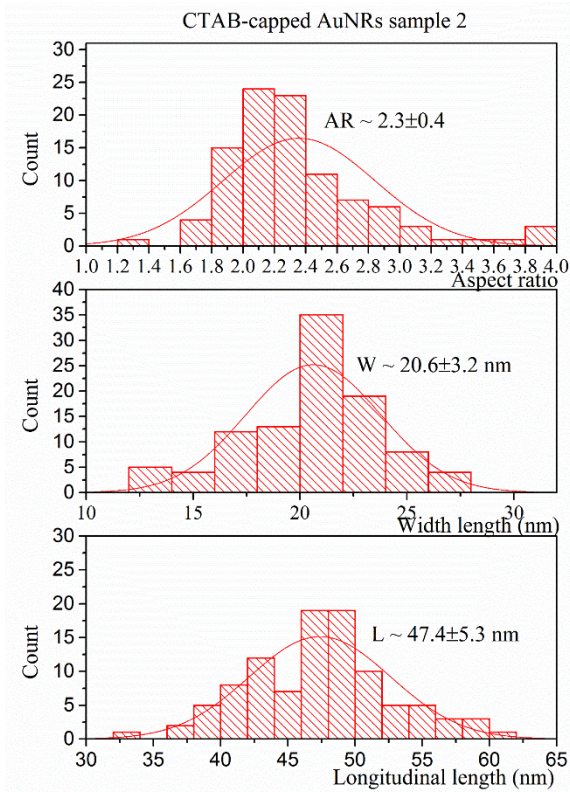


Figure 4-6: g) Size distributions of CTAB capped AuNRs sample 2 derived from TEM imaging, showing an AR of 2.3 ± 0.4 .

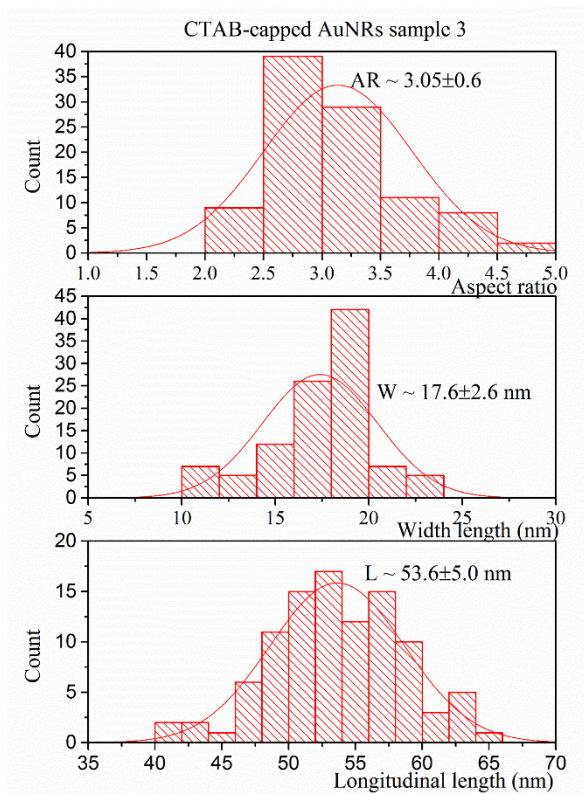


Figure 4-6: h) Size distributions of CTAB capped AuNRs sample 3 derived from TEM imaging, showing an AR of 3.1 ± 0.6 .

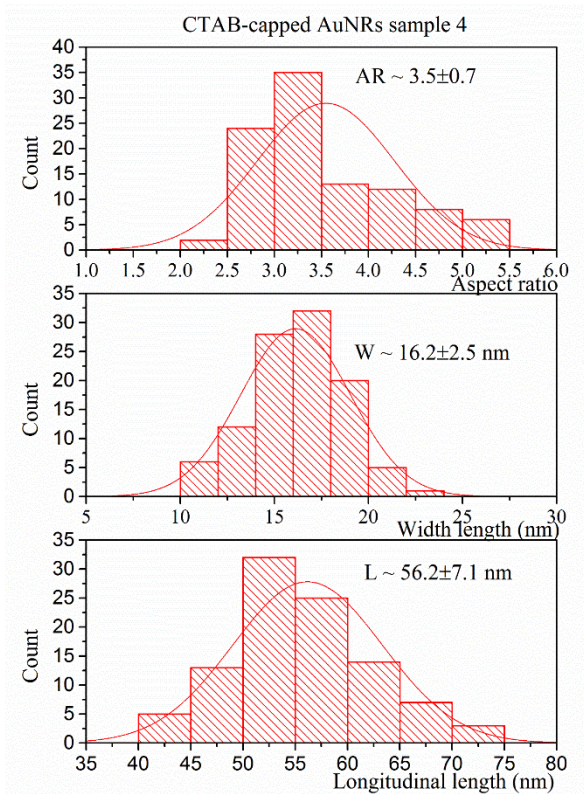


Figure 4-6: i) Size distributions of CTAB capped AuNRs sample 4 derived from TEM imaging, showing an AR of 3.5 ± 0.7 .

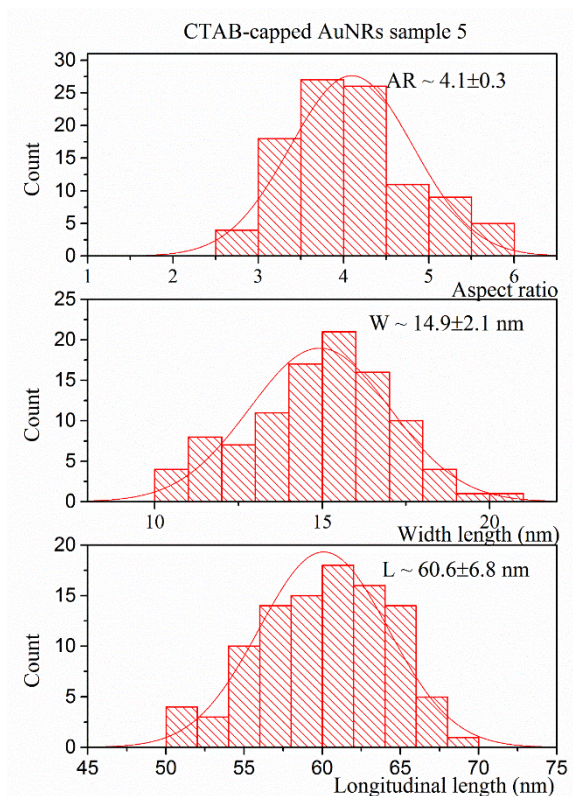


Figure 4-6: j) Size distributions of CTAB capped AuNRs sample 5 derived from TEM imaging, showing an AR of 4.1 ± 0.3 .

The samples demonstrated a red-shift of the absorption spectra as a function of increasing AR. This is in agreement with the literature [8-10] and the modelling results in chapter 5. The longitudinal surface plasmon resonance (SPR) results from electron oscillation along the long axis of the rods. The longitudinal SPR of as-synthesized AuNRs increases from 575 nm to 800 nm with increasing AR, ranging from the visible region to NIR. Only a small change in AR results in a significant change in the absorption spectra showing that the longitudinal SPR is very sensitive to the AR. The UV-vis absorption spectra also exhibit a transverse SPR representing the oscillation of electron over the short axis of the rods. The SPR position is at approximately 520 nm and did not vary significantly between the different samples, in agreement with literature [11, 12]. The transverse SPR of AuNRs matched with that of 20 nm diameter spherical AuNPs which had a resonance peak located around 520 nm (see figure 4-1a). However, there was a very broad transverse SPR in sample 5 (orange line) arising as a result of the additional presence of various sizes of spherical nanoparticles.

HRTEM and selected area electron diffraction (SAED) were performed to confirm the presence of as-synthesized AuNRs and to confirm that they were single crystal in nature. An SAED pattern of a group of AuNRs (inset in figure 4-7a) illustrates fcc Au lattice reflections of (111), (200), (220), and (311) [13]. An HRTEM image of a single crystal nanorod in figure 4-7b exhibits a crystallographic lattice spacing of 0.148 nm along the rod axis which can be

assigned to the (220) spacing of fcc Au. This demonstrated that the growth direction of AuNRs is along the $\langle 220 \rangle$ direction along the rod axis with the long facets of the rod being (002) planes.

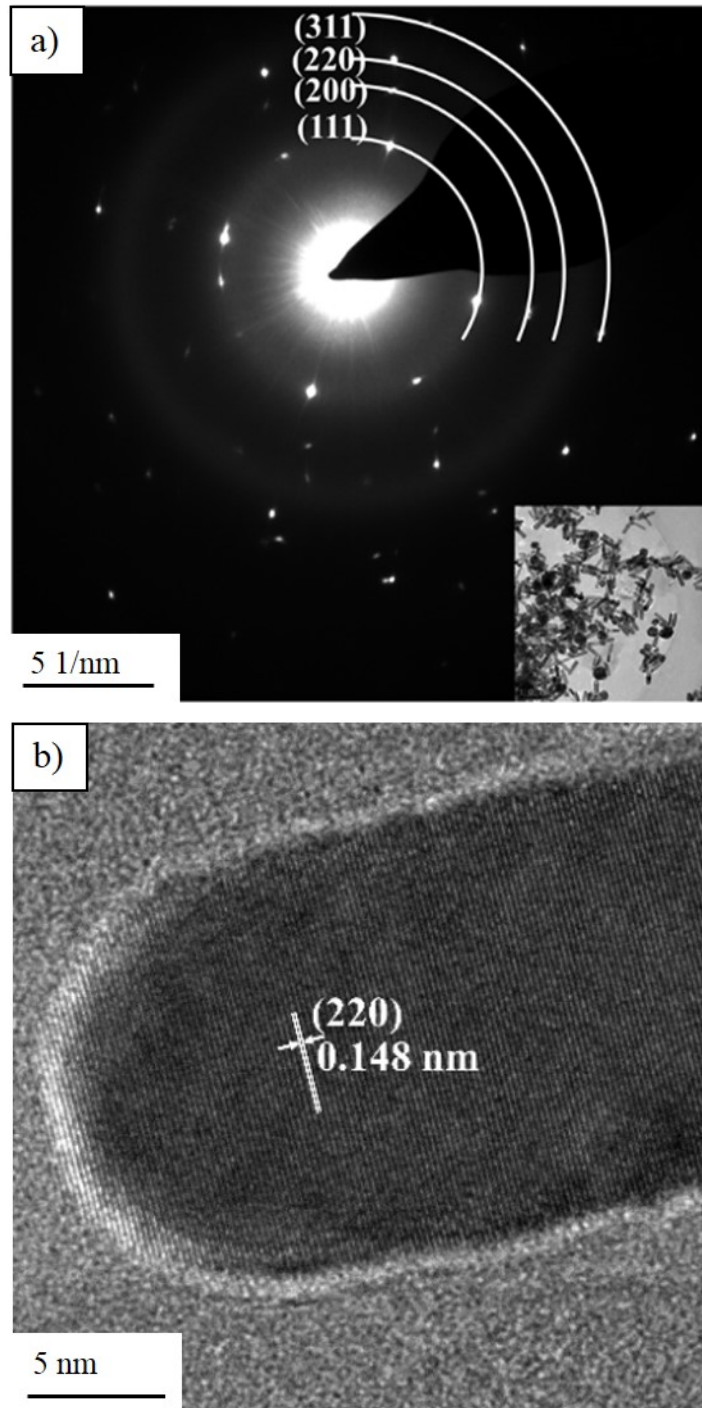


Figure 4-7: a) Electron diffraction pattern of a group of AuNRs shown in the image inset; b) HRTEM image of an AuNR, showing (220) lattice fringes along the axis and hence the growth direction of the rod.

The simple steps of the kinetically controlled synthesis method demonstrated reproducibility, indicating a promising method that can be modified to provide a tunable AR of CTAB-capped AuNRs for promising applications in the NIR region. The AuNRs synthesized by this method were used for further study of surface modification.

We noticed differences in the DLS results for the AuNRs, shown in figure 4-8, from those of the AuNPs. The size distribution curves of the AuNRs derived from DLS exhibited two peaks: a small particle diameter and a large particle diameter peak due to their rod shaped geometry. The relative intensity of the small diameter peak increased with an increase in rod AR. Moreover, the peak maximum of the large diameter peak increases with AR, derived from TEM. However, sample 5 showed some anomalies compared to samples 3 and 4, seen in figure 4-8. These two DLS peaks refer to the rotational diffusion (the small diameter peak) and translational diffusion (the larger diameter peak) coefficients. This means that it is not straightforward to extract the average hydrodynamic diameter of AuNRs using DLS. The relative intensity of the small peak reflects rotational diffusion parallel to the rod-axis which strongly depends on the AR of the AuNRs [6], as seen in figure 4-8

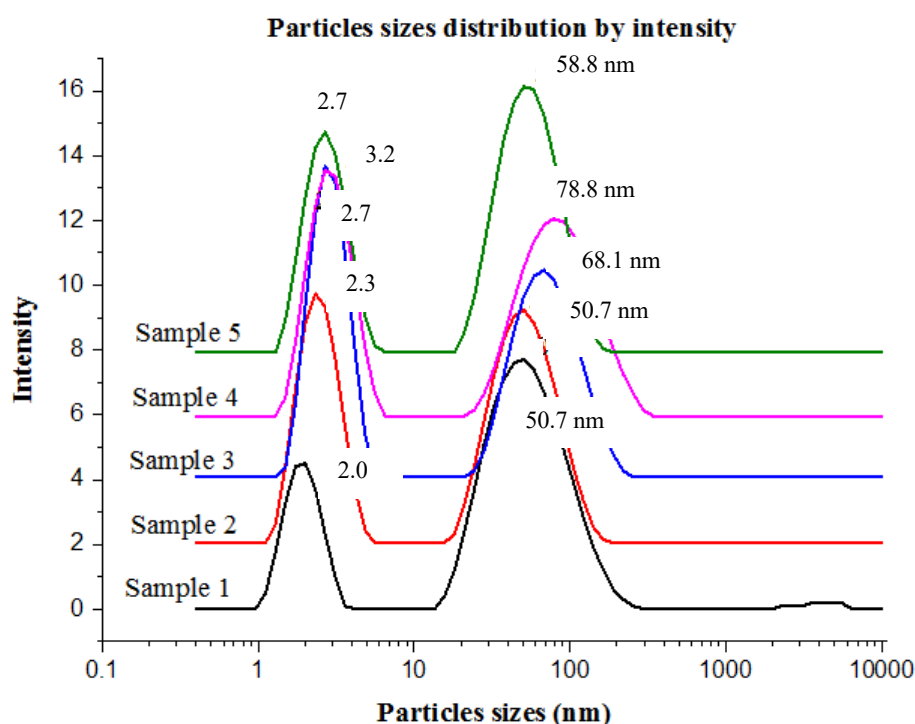


Figure 4-8: DLS results showing particle size distribution by intensity of CTAB-capped AuNRs with various ARs indicated by sample 1, 2, 3, 4, and 5.

4.3 Characterization of gold nanobipyramids (AuNBPs)

AuNBPs were fabricated by a modified citrate-seed mediated method as detailed in chapter 3. The citrate-seed solution was employed in order to produce the bi-pyramidal structure

while the growth solution was slightly modified from the literature [7, 14, 15]. The amount of seed solution, i.e. 80, 100, and 150 μL was varied to manipulate the AR of the AuNBPs corresponding to samples 1-3, respectively. The samples were characterized by both UV-vis spectroscopy and TEM imaging. DLS results for AuNBPs exhibited characteristics of elongated particles, i.e. both rotational and translational diffusion features similar to the case of AuNRs. Again this implies that DLS is not straightforward technique to analyse AuNBPs and hence was not undertaken in any detail.

UV-vis spectra shown in figure 4-9a illustrated that AuNBPs exhibited SPR peaks similar to AuNRs showing both longitudinal and transverse SPRs. For AuNBPs, the FWHM of the longitudinal SPRs were significantly narrower when compared with those of the AuNRs. By applying a seed injection of 80 μL (sample 1), AuNBPs with an SPR in the NIR region were achieved. The longitudinal SPRs of samples 1, 2 and 3 were 800, 780, and 760 nm, respectively. By using the DDA approximation equation for LSPR peak [7], the SPR of AuNBP sample 1 with an AR of 3.5 should be located at 754 nm however, the experimental UV-vis is slightly higher than expected at about 800 nm.

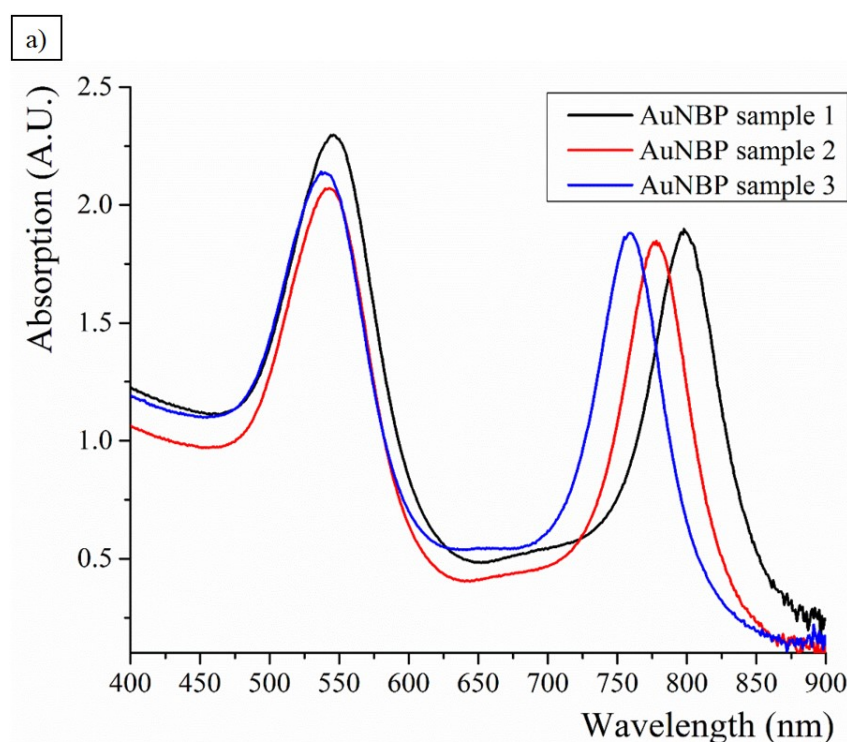


Figure 4-9: a) UV-vis absorption spectra of the three AuNBP samples exhibiting longitudinal SPRs at 800, 780, 760 nm for samples 1, 2 and 3, respectively.

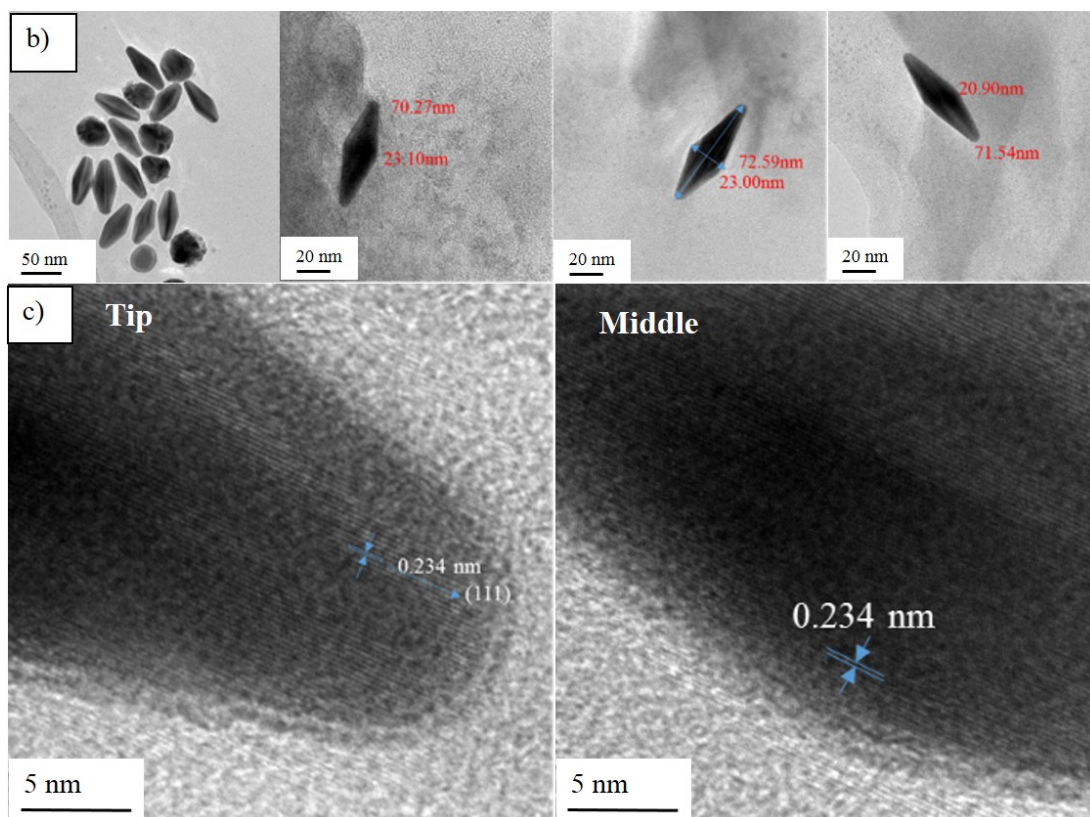


Figure 4-9: b) TEM micrographs of sample 1 before purification; and c) HRTEM showing a 0.234 nm lattice spacing corresponding to $\langle 110 \rangle$ growth direction in both the tip and middle of an AuNBP.

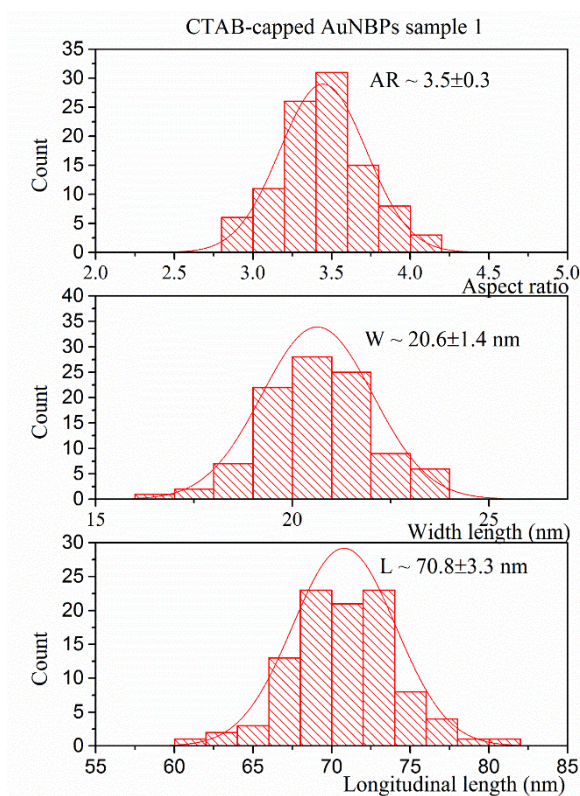


Figure 4-9: d) Size distributions of CTAB-capped AuNBPs sample 1, showing an AR of 3.5 ± 0.3 .

However, all as-synthesized AuNBP samples contained a lot of spherical NPs as by-products which was evidenced by the high intensity of transverse SPR compared to the longitudinal SPR. In general, the percentage of AuNBPs to AuNPs was approximately 60:40 as seen in figure 4.9b. As discussed in the previous section, only AuNBPs with uv-vis extinction spectra in the NIR region are of interest in terms of healthcare applications. Therefore, only sample 1 of the AuNBPs were fully characterized and chosen for further processing. The AuNBPs from sample 1 were analysed to be 70.8 ± 3.3 nm in length and 20.6 ± 1.4 nm in width with an AR of 3.5 ± 0.3 derived from measurement of 100 particles (size distribution presented in figure 4-9d). In addition, the crystalline structure at both the tip and the middle of the AuNBPs was examined by HRTEM (figure 4-9c). Clear lattice fringes are near parallel to the growth axis and the lattice spacing was measured as 0.234 nm corresponding to facets of the AuNBPs, which are perpendicular to the $\langle 110 \rangle$ growth direction along the long axis of the rods [14, 15]. AuNBPs grow from twinned seeds in the citrate-capped seed solution in the presence of Ag ions. The proposed mechanism of the unique bipyramidal step is described as follows. The growth of $\{110\}$ facets along the twining axis is perpendicular to the growth of $\{111\}$ facets. The growth rate of $\{110\}$ is faster than the perpendicular direction resulting in the particle elongation (similar to the rod). Unique steps appear in this surface and lead to one dimensional growth along the $\langle 110 \rangle$ direction. Due to the high radius of curvature at the tip, the surfactant (CTAB) is likely to be less concentrated than on the bipyramid facet. This allows Ag ions to deposit in these gaps. This results in a stepped faceted growth along the long axis. The steps of the AuNBP have a more open channel than the AuNR due to the twinned citrate-capped seed. Additionally, these steps are not thermodynamically stable so allowing Ag ions to deposit (underpotential deposition (UDP)) and resulting in increasing thermodynamic stability [14-16]. [16]

Surfactant depletion to induce agglomeration of the spherical nanoparticles as described in [14] was employed to purify AuNBPs by adding a specific amount of 0.2M CTAB surfactant to induce spherical and bipyramidal separation. After leaving overnight, a pink supernatant was carefully removed and the precipitate was redispersed with DI water. TEM images and UV-vis spectra of the post purification product showed fewer AuNPs and a lower AR of AuNBPs as shown in figure 4-10. Additionally, the intensity of longitudinal SPR from UV-vis spectra decreased indicating unsuccessful purification of AuNBPs and leaving the AuNBPs with a shorter AR. The TEM size distribution of the post purification AuNBPs was found to be smaller in AR down to 2.5 ± 0.2 (length of 65.3 ± 3.8 nm and width of 26.3 ± 1.7 nm).

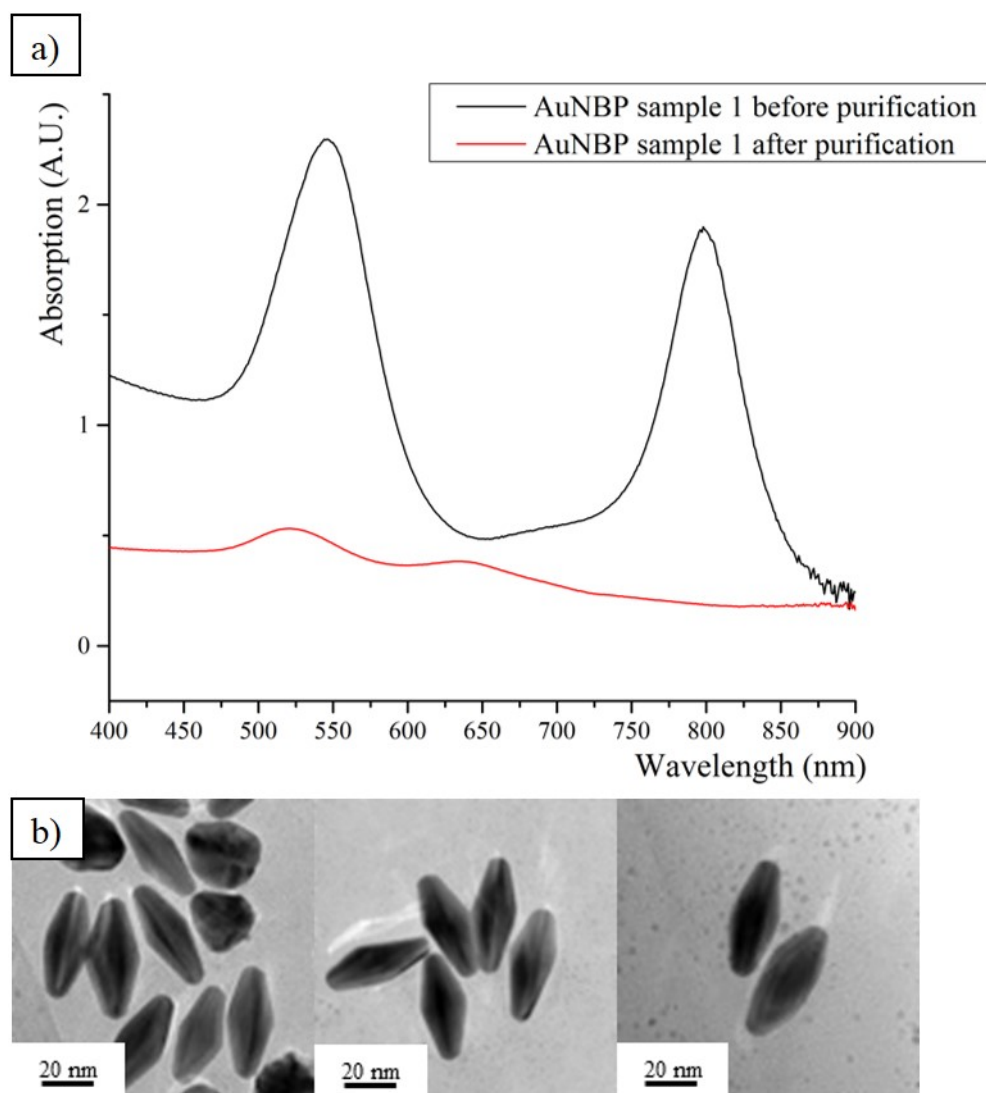


Figure 4–10: *Uv-vis Absorption spectra of sample 1 of AuNBPs before and after purification (a) and their TEM images (b).*

4.4 Characterization of Au nanotriangles (AuNTs)

AuNTs were synthesized according to a pH adjustment seedless synthesis method [17] as described in chapter 3. The as-synthesized samples exhibited a blue colour of the suspension indicating the formation of AuNTs. UV-vis absorption spectra are shown in figure 4-11. In sample 1 (black line), a sharp peak was clearly observed at 625 nm and this SPR peak can be assigned to an in-plane SPR mode of the AuNTs. Furthermore, a shoulder SPR peak located at about 550 nm indicated an out of plane SPR mode and/or the presence of irregular NPs. The average edge length of AuNTs can be tuned by varying both the concentration of iodide which acts as structural formation agent and also sodium hydroxide. As shown in the UV-vis spectra, there was a slight shift of SPR peaks from samples 2 to 5 which is related to the size of the triangles. An increased red-shift in SPR represents a larger edge length of the AuNTs

in a good agreement with literature [17-19] and confirmed by TEM imaging (Figure 4-12a-e). Samples 1, 2, 4 and 5 were subsequently considered due to their differing uv-vis profiles.

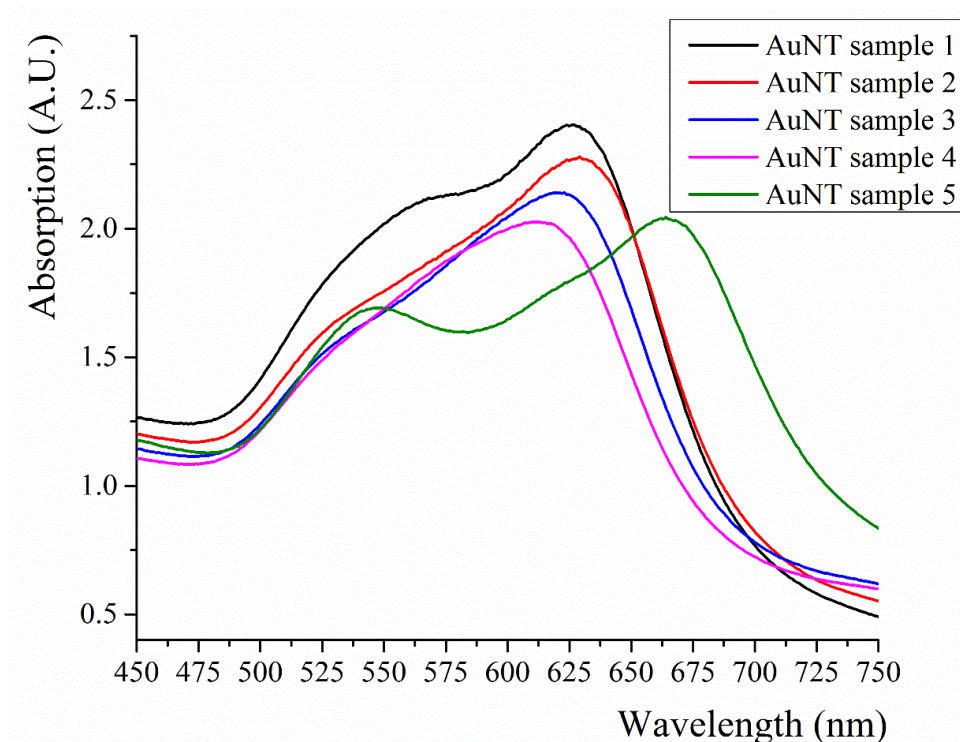


Figure 4–11: UV-vis spectra of AuNTs produced using different synthesis conditions denoted as samples 1 - 5.

Generally, TEM showed a relatively broad size distribution with the presence of some irregular shaped NTs. The results showed that the AuNTs had two different sizes (large and small NTs). The average edge lengths of AuNTs in samples 1, 2 and 5 were 38.4 ± 8.5 , 46.4 ± 6.0 , and 99.8 ± 24.4 nm, respectively, as presented in figure 4-12. Sharp-tip AuNTs were apparent in samples 2 and 5 indicating optimized synthesis conditions for a particular iodide concentration (60-80 μ L of 0.01M KI). HRTEM imaging showed a lattice spacing of 0.231 nm, which is in a good agreement with the literature [17]. The triangular structure arises from gold nuclei growing along the most favorable facet with stacking faults to form plate-like structures which produces $\{111\}$ planar facets. Selective adsorption of the surfactant (CTAC) occurs on the $\{111\}$ planar facet of AuNTs [17-19].

Experimentally, a broad SPR peak (pink line) appeared in the UV-vis spectrum of sample 4 resulting from an increase in the iodide concentration from sample 2 to sample 4, indicating the production of irregularly shaped AuNPs which was confirmed by TEM imaging (figure 4-12d).

In sample 5, the idea of pH adjustment (inducing a lower pH) was employed. The amount of sodium hydroxide was reduced in order to achieve larger triangles. However, in the uv-vis

spectrum there was also a characteristic peak evident at 530 nm, illustrating the presence of both AuNPs and AuNTs in the sample. TEM imaging of this sample also revealed the presence of both small and large AuNTs (figure 4.12f) which relates to a weak shoulder at 625 nm and a strong SPR peak at 660 nm in the uv-vis spectrum in figure 4.11.

An example of the DLS size distribution is shown in figure 4-13. These results show that the average hydrodynamic diameter of AuNTs from DLS are in agreement with the TEM imaging results. This is attributed to the fact that DLS cannot distinguish between the spherical particles and planar particles showing smaller average sizes of AuNTs.

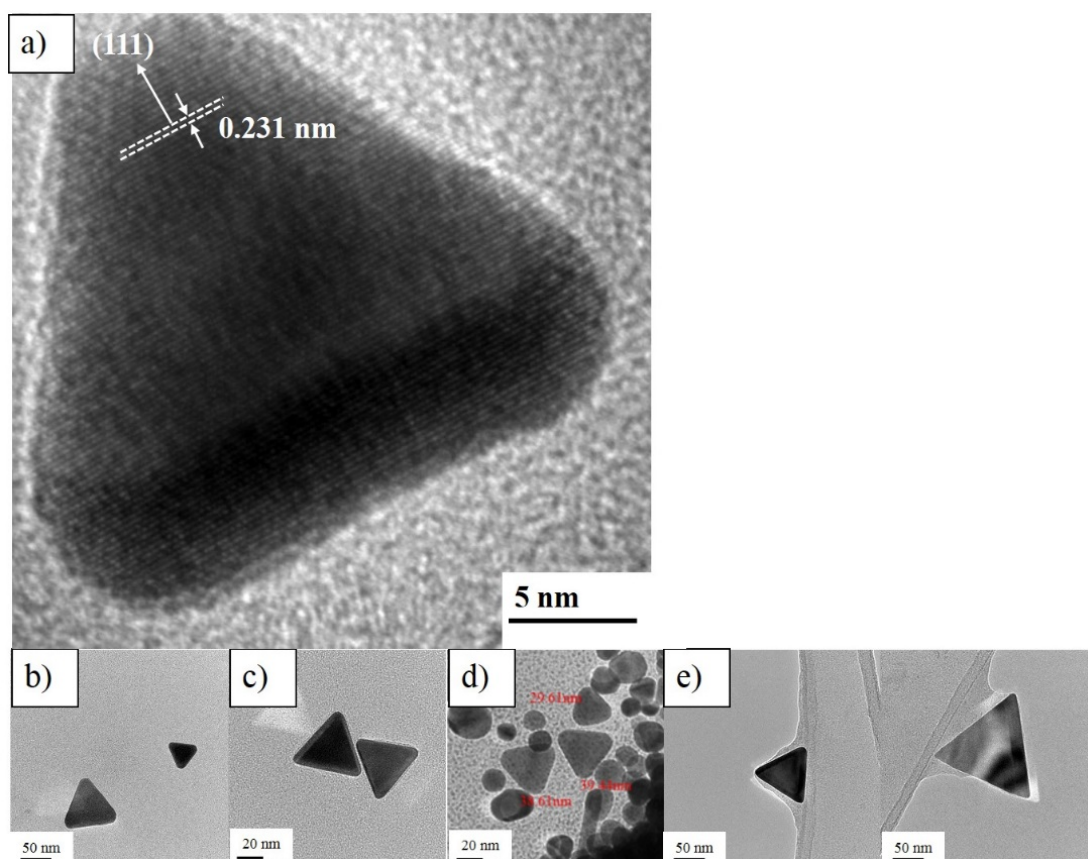


Figure 4–12: a) HRTEM image of AuNTs in sample 1; TEM BF images of as-synthesized AuNTs from samples 1, 2, 4 and 5 are shown in b), c), d), and e), respectively.

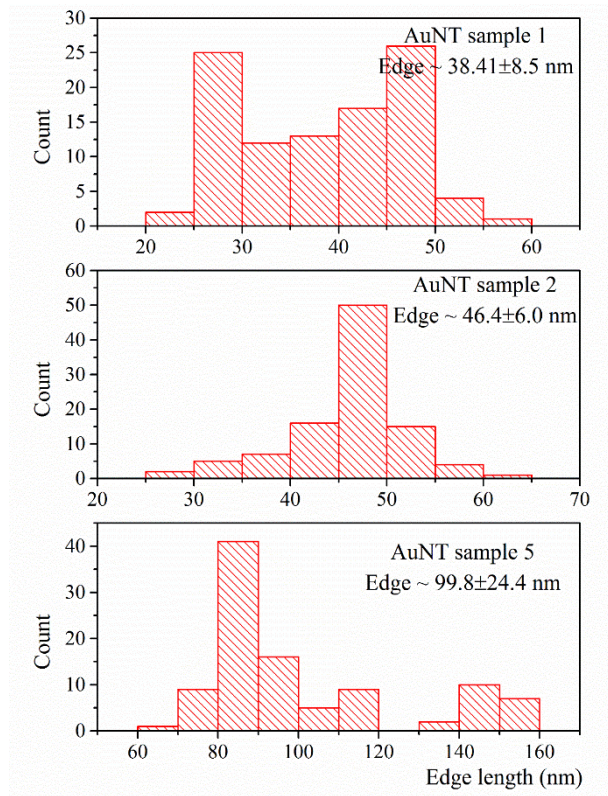


Figure 4-12: *f)* Size distributions of AuNT samples 1, 2, and 5 with average size of 38.4 ± 8.5 , 46.4 ± 6.0 , and 99.8 ± 24.4 nm, respectively.

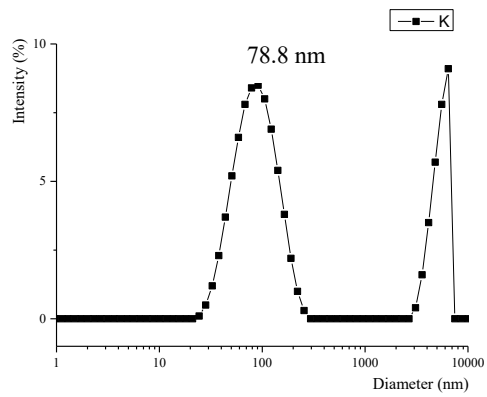


Figure 4-13: An example of dynamic light scattering results for AuNT sample 5, showing size distribution by intensity.

4.5 Surface modification of Au nanorods (AuNRs)

CTAB-capped AuNRs would be of limited use in biological and sensing applications due to their cytotoxicity. CTAB will interact with some biomolecules and cause toxicity to living cells [12, 20]. To deal with this issue, surface modification of AuNRs was undertaken via layer by layer PSS coating and the samples were characterized by UV-vis spectroscopy, TEM imaging and Zeta potential measurements.

CTAB-capped AuNRs with ARs of about 1.6, 2.9 and 3.4 (as determined from TEM imaging) denoted as CTAB AuNR samples 1, 2 and 3, respectively, were initially investigated. Figure 4-14 illustrates UV-vis absorption spectra of as-synthesized CTAB-capped AuNRs as well as the modified PSS-stabilized AuNRs. The results showed that there was a small (5-10 nm) red-shift to higher wavelength in the PSS surface modified rods (samples 1 and 2). A more significant (about 20 nm) red-shift was found in CTAB AuNR sample 3 which exhibited a broad longitudinal SPR peak. These values for the red-shift were in a good agreement with literature [21, 22]. A surface coating was confirmed by TEM micrographs (see figure 4-15). However there is no clear distinction in the images between CTAB and PSS, as can be seen in figure 4-15. The thickness of the combined CTAB and PSS layers was found to be approximately 3-5 nm. Additionally, a surface modification experiment in collaboration with Tahani Albogami, a PhD student in the School of Physics at the University of Leeds, was undertaken using the silica coating protocol described in chapter 3, section 3.1.4. The results show a distinct silica layer covering the particles, as illustrated in figure 4-15c.

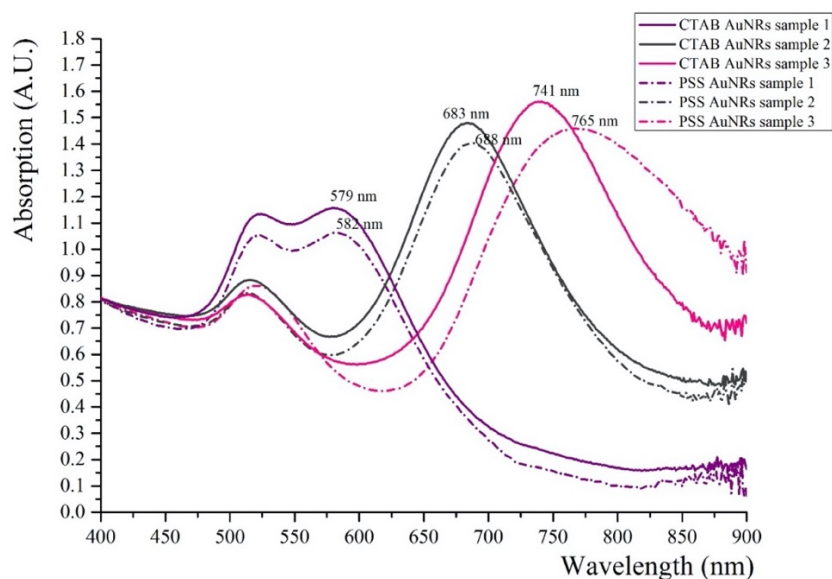


Figure 4-14: UV-vis spectra of as-synthesized CTAB-capped AuNRs compared with PSS-AuNRs.

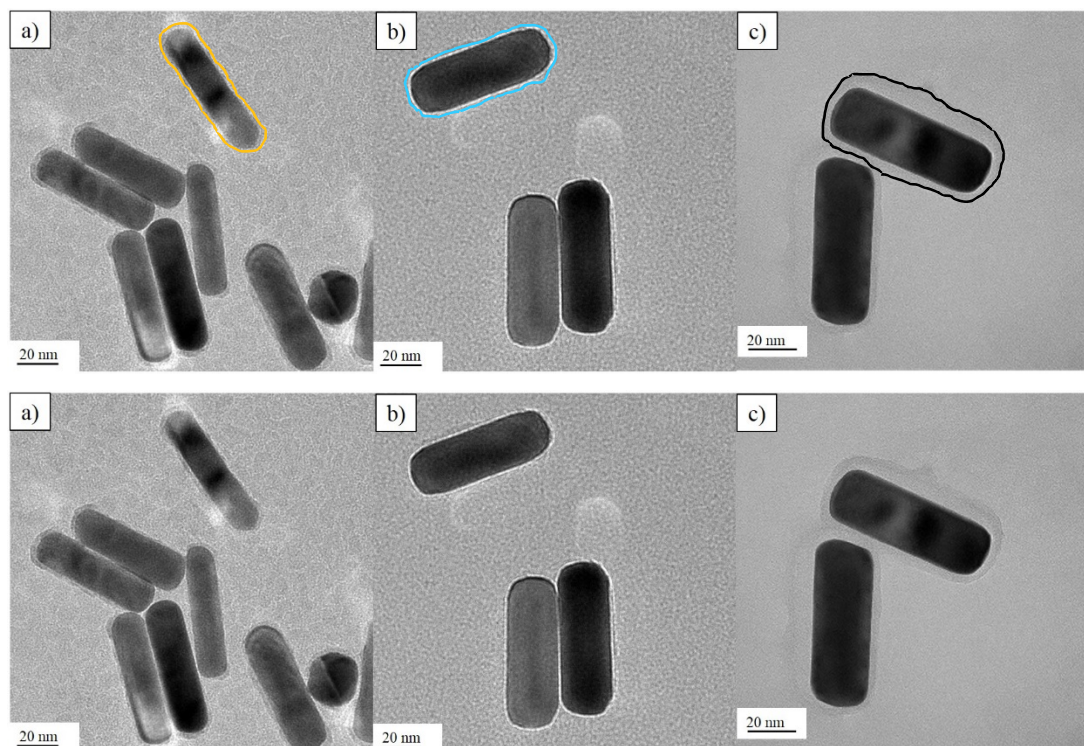


Figure 4-15: TEM images of a) CTAB coated-AuNRs (yellow), b) PSS modified-AuNRs (blue), and c) silica coated-AuNRs (black), illustrating the presence of a distinct surface layer surrounding AuNRs using colour lines drawing as a guideline to define surfactant layers. The unmodified TEM images were presented below.

The surface modification was also confirmed by STEM-EDX in terms of the elemental composition of the sample surface, as shown in figure 4-16. The presence of the CTAB coating was revealed in the EDX spectra (presence of Br) and Br maps. While the presence of PSS surface modification was confirmed by EDX spectra (presence of S) and S maps. The relative amount of Br (in atom% relative to Au) was observed to decrease significantly following surface modification with PSS. The zeta potential of the particles was measured following surface modification. The zeta potential changed from positive (+40.40 mV) in CTAB-capped AuNRs to negative values (-39.8 mV) for surface modified PSS-AuNRs.

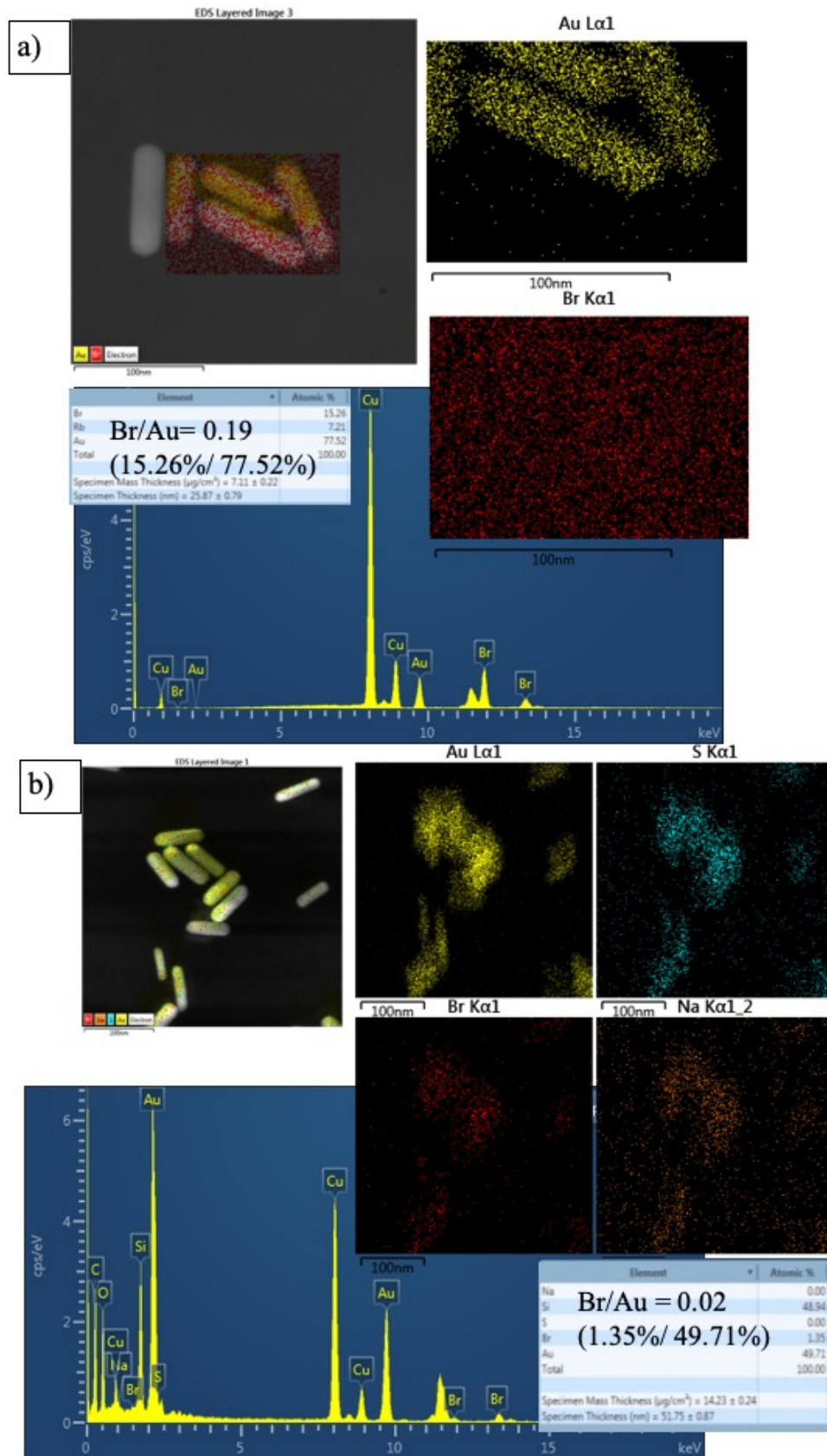


Figure 4-16: TEM-EDX spectra and maps from a) CTAB-rods and b) surface modified PSS-rods.

4.6 Conclusion

In summary, well-controlled and reproducible Au nanostructures including AuNPs, AuNRs, AuNBPs and AuNTs have been synthesized. Firstly, AuNPs were synthesized with a progressive increase in size following each modified growth step. Secondly, well-defined and homogeneous CTAB-capped AuNRs with various ARs were produced. The AR of the rods can be tailored to absorb from the visible to the NIR by varying the amount of AgNO₃ in the growth solution. In addition, surface modification of CTAB-capped AuNRs was achieved via PSS and silica coating. AuNBPs were also synthesized producing different AR structures. This absorption spectra of this nanostructure can be tuned over the NIR region by using different amounts of seed solution. Finally, high yield AuNTs were produced via a one pot seedless synthesis method. To obtain an increase in the average edge length of the triangles, the amount of KI and NaOH were found to be the dominant parameters.

With different seed structures and synthesis conditions, shape-controlled Au nanostructures were achieved. UV-vis spectroscopy revealed that the SPR mode can be tailored to the NIR region, implying that these Au nanostructures would be good candidates for healthcare applications such as photothermal therapy and imaging. Further analysis of these interesting optical and other properties will be presented in subsequent chapters to provide a more in-depth understanding.

4.7 References

- [1] Bastús, N.G., J. Comenge, and V. Puntes, *Kinetically Controlled Seeded Growth Synthesis of Citrate-Stabilized Gold Nanoparticles of up to 200 nm: Size Focusing versus Ostwald Ripening*. Langmuir, 2011. **27**(17): p. 11098-11105.
- [2] Piella, J., N.G. Bastús, and V. Puntes, *Size-Controlled Synthesis of Sub-10-nanometer Citrate-Stabilized Gold Nanoparticles and Related Optical Properties*. Chemistry of Materials, 2016. **28**(4): p. 1066-1075.
- [3] Rodríguez-Fernández, J., et al., *Seeded Growth of Submicron Au Colloids with Quadrupole Plasmon Resonance Modes*. Langmuir, 2006. **22**(16): p. 7007-7010.
- [4] Zheng, T., S. Bott, and Q. Huo, *Techniques for Accurate Sizing of Gold Nanoparticles Using Dynamic Light Scattering with Particular Application to Chemical and Biological Sensing Based on Aggregate Formation*. ACS Applied Materials & Interfaces, 2016. **8**(33): p. 21585-21594.
- [5] Eaton, P., et al., *A direct comparison of experimental methods to measure dimensions of synthetic nanoparticles*. Ultramicroscopy, 2017. **182**: p. 179-190.

- [6] Ahmed, W., A.S. Bhatti, and J.M. van Ruitenbeek, *Efficient seed-mediated method for the large-scale synthesis of Au nanorods*. Journal of Nanoparticle Research, 2017. **19**(3): p. 115.
- [7] Guo, Z., et al., *High-purity gold nanobipyramids can be obtained by an electrolyte-assisted and functionalization-free separation route*. Colloids and Surfaces A: Physicochemical and Engineering Aspects, 2012. **414**: p. 492-497.
- [8] Feng, L., et al., *Preparation of gold nanorods with different aspect ratio and the optical response to solution refractive index*. Journal of Experimental Nanoscience, 2015. **10**(4): p. 258-267.
- [9] Nikoobakht, B. and M.A. El-Sayed, *Preparation and Growth Mechanism of Gold Nanorods (NRs) Using Seed-Mediated Growth Method*. Chemistry of Materials, 2003. **15**(10): p. 1957-1962.
- [10] Gole, A. and C.J. Murphy, *Seed-Mediated Synthesis of Gold Nanorods: Role of the Size and Nature of the Seed*. Chemistry of Materials, 2004. **16**(19): p. 3633-3640.
- [11] Smitha, S.L., et al., *Size-dependent optical properties of Au nanorods*. Progress in Natural Science: Materials International, 2013. **23**(1): p. 36-43.
- [12] Jayabal, S., et al., *A gold nanorod-based localized surface plasmon resonance platform for the detection of environmentally toxic metal ions*. Analyst, 2015. **140**(8): p. 2540-2555.
- [13] Johnson, C.J., et al., *Growth and form of gold nanorods prepared by seed-mediated, surfactant-directed synthesis*. Journal of Materials Chemistry, 2002. **12**(6): p. 1765-1770.
- [14] Lee, J.-H., et al., *Bipyramid-templated synthesis of monodisperse anisotropic gold nanocrystals*. Nature Communications, 2015. **6**: p. 7571.
- [15] Liu, M. and P. Guyot-Sionnest, *Mechanism of Silver(I)-Assisted Growth of Gold Nanorods and Bipyramids*. The Journal of Physical Chemistry B, 2005. **109**(47): p. 22192-22200.
- [16] Fang, C., et al., *Facile Growth of High-Yield Gold Nanobipyramids Induced by Chloroplatinic Acid for High Refractive Index Sensing Properties*. Scientific Reports, 2016. **6**(1): p. 36706.
- [17] Chen, L., et al., *High-Yield Seedless Synthesis of Triangular Gold Nanoplates through Oxidative Etching*. Nano Letters, 2014. **14**(12): p. 7201-7206.

- [18] Scarabelli, L., et al., *Monodisperse Gold Nanotriangles: Size Control, Large-Scale Self-Assembly, and Performance in Surface-Enhanced Raman Scattering*. ACS Nano, 2014. **8**(6): p. 5833-5842.
- [19] Kuttner, C., et al., *Seeded Growth Synthesis of Gold Nanotriangles: Size Control, SAXS Analysis, and SERS Performance*. ACS Applied Materials & Interfaces, 2018. **10**(13): p. 11152-11163.
- [20] Kinnear, C., et al., *Gold Nanorods: Controlling Their Surface Chemistry and Complete Detoxification by a Two-Step Place Exchange*. 2013. **52**(7): p. 1934-1938.
- [21] Mehtala, J.G., et al., *Citrate-Stabilized Gold Nanorods*. Langmuir, 2014. **30**(46): p. 13727-13730.
- [22] Chen, L.-l., et al., *Multilayered polyelectrolyte-coated gold nanorods as multifunctional optical contrast agents for cancer cell imaging*. Journal of Zhejiang University. Science. B, 2010. **11**(6): p. 417-422.

Chapter 5 Plasmonic properties of gold nanostructures

The previous chapters have investigated both the structural characterisation and the optical properties of synthesized Au nanostructures. However in order to provide a full characterization, electron energy loss spectroscopy (EELS) in the TEM can be used to achieve a spatial characterization of the plasmonic modes of nanostructures. This information allows for the prediction of potential plasmonic properties and optimization of their use in healthcare applications. Surface plasmon oscillations can be induced by a fast electron passing nearby a particle [1, 2] and the low loss EEL signal results from the interaction of this electron beam with the particle. This can directly probe plasmonic properties of individual Au nanostructures.

In order to gain a better understanding of the surface plasmons generated within a particular nanostructure, computational simulation of Au nanospheres and Au nanorods were also investigated using COMSOL Multiphysics finite element modeling (FEM) software using plane wave excitation, following the description in [3]. EELS in scanning transmission electron microscopy (STEM) mode was used to achieve spatial characterization of the surface plasmon modes of the Au nanostructures and results were compared with both UV-vis spectra and COMSOL simulations.

5.1 Finite Element modelling of the optical response of isolated AuNPs and AuNRs in a medium

5.1.1 Modelling methodology

The modelling of plasmonic resonances was undertaken to support the experimental data for the case of isolated AuNPs and AuNRs employing the FEM methods described in reference [3] and presented in chapter 3, section 3.2.2. In brief, FEM splits a particular shape into a finite number of elements to provide an accurate representation of the geometry. A set of partial differential equations is solved within each element under boundary conditions and then the results are combined. The FEM software in COMSOL allows simulation of the electromagnetic waves within a specific frequency domain. A plane wave is used to generate the electric field and excite different modes of the nanoparticles. By varying the frequency of the incident plane wave, a range of solutions in terms of wavelength are obtained. The particle is located in the middle of the domain, i.e. a medium with a particular refractive index.

5.1.2 Results

Au nanospheres

A 100 nm diameter Au sphere in water (refractive index of water, $n=1.33$) is used as a modelling example. The extinction spectrum of the AuNP is presented in figure 5-1. The inset shows the electric field distribution for the transverse mode at the resonance wavelength of 575 nm. Then, the model was modified and the effect of varying the diameter of the AuNP was simulated in vacuum ($n=1.00$), in order to compare the results, and this is illustrated in figure 5-2. The results were compared to the experimental optical UV-vis spectra, shown in figure 4-1a. From the simulation, changing refractive index from water to vacuum causes a relative blue-shift in the simulated spectra. It was also found that the simulated extinction spectra are in a agreement with the measured extinction spectra. Also, there was a relative red-shift in the observed experimental data. The simulation results showed a blue-shift with decreasing sphere diameter which is in agreement with the results in chapter 4, section 4.1 and also those in the literature [3-6], see figure 5-3.

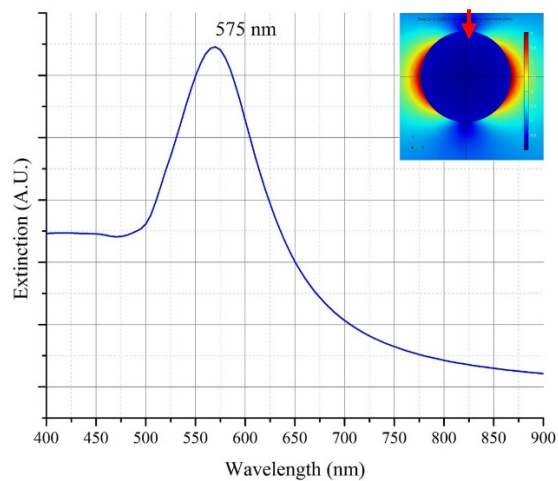


Figure 5-1: *Modelling the extinction spectra of a 100 nm diameter AuNPs in water. Inset shows the electric field distribution excited from 575 nm plane wave. The plane wave incident radiation with a red arrow.*

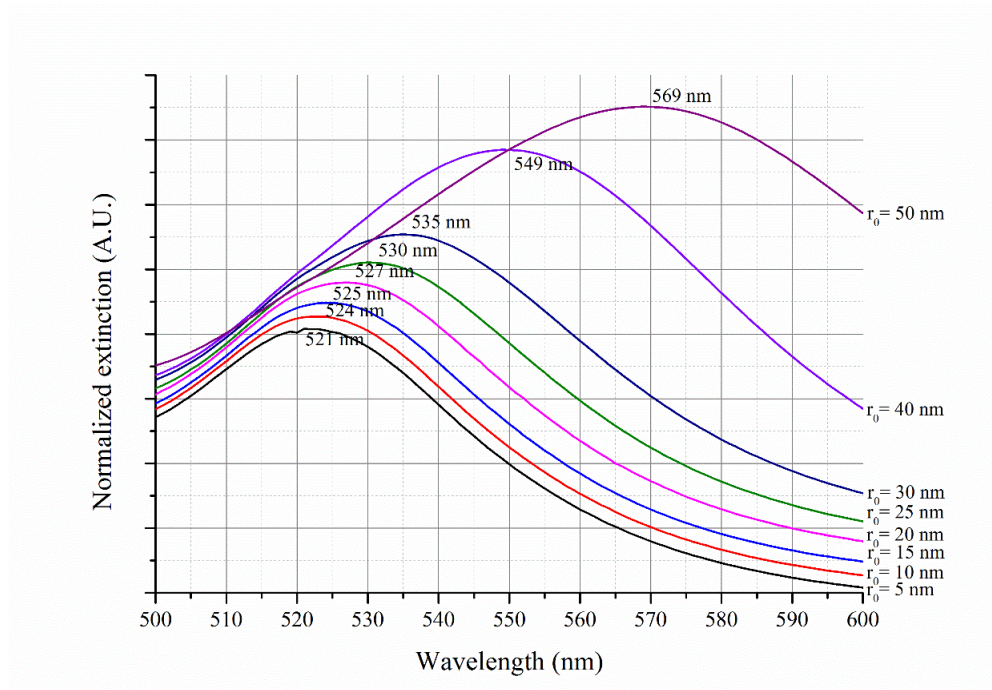


Figure 5–2: Simulated extinction spectra of AuNPs in vacuum with increasing AuNP's radius from $r=5$ nm to $r=50$ nm.

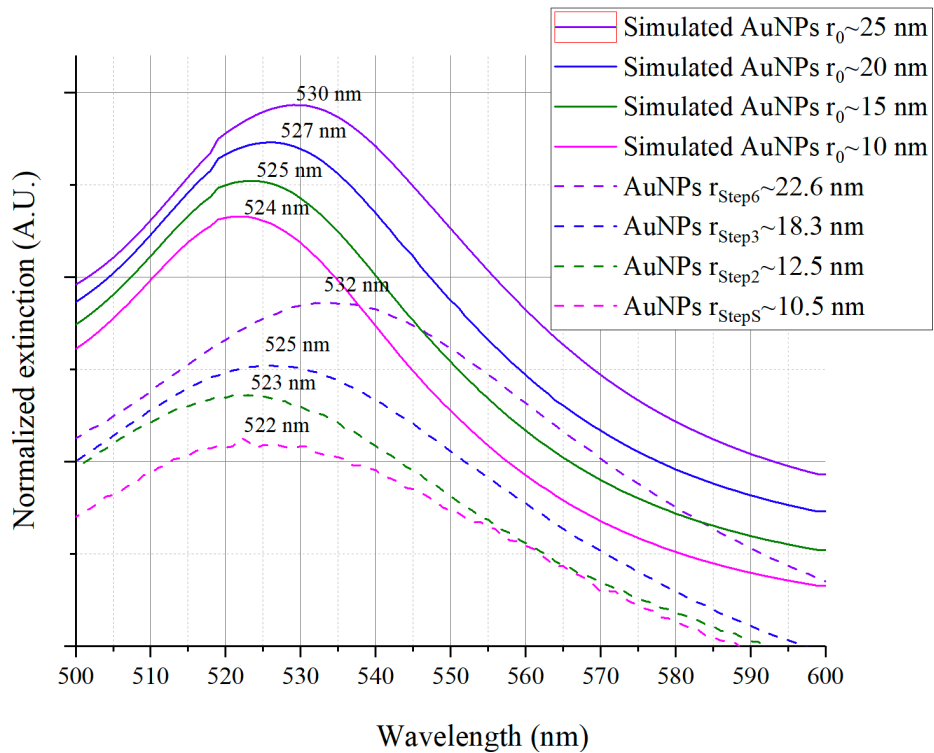


Figure 5–3: Comparison of measured (dash line) and simulated extinction spectra (solid line) of AuNPs.

Au nanorods

An isolated AuNR with an AR of 4.2 (length=84 nm and width=20 nm) was modelled in vacuum without a surface coating. The AuNRs were placed at 45 degrees to the incident plane wave direction so as to excite both the longitudinal and transverse SPR modes. Figure 5-4 shows the simulated extinction spectrum over the wavelength range 400 nm to 900 nm. Characteristic peaks were excited at 860 nm and 520 nm corresponding to the longitudinal and transverse SPR modes, respectively. At 860 nm, the simulated electric field distribution was concentrated at the tips of the AuNR. The simulated spectrum showed a significant red-shift compared to the optical UV-vis spectra of the AuNR sample 5 shown in chapter 4, section 4.2 (which exhibited a longitudinal SPR at about 800 nm). The results from simulated and measured extinction spectra of AuNRs with AR about 4.2 were compared and illustrated in figure 5-5. The experimentally observed relative red-shifts in both AuNPs and AuNRs may arise from variations in the end-cap geometry, the presence of a surface coating (with a different refractive index) and inhomogeneities in the size distributions of the samples, as well as the refractive index of the surrounding medium.

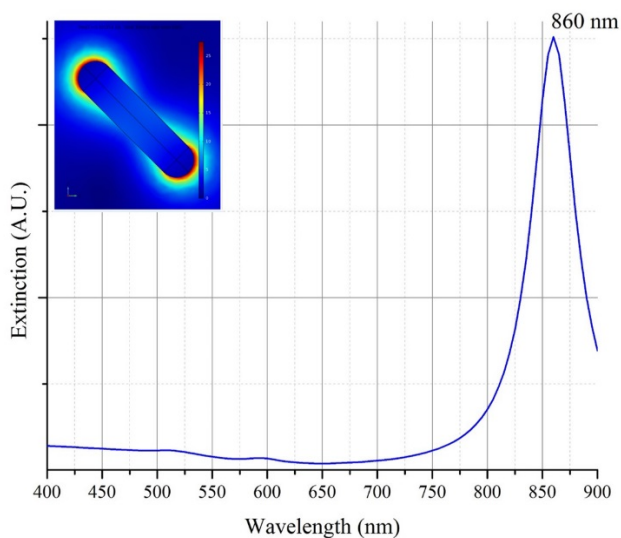


Figure 5–4: Simulated extinction spectra of an isolated AuNR (non-coating) in vacuum with an AR of 4.2. Inset shows the electric field distribution excited by an 860 nm plane wave (the longitudinal SPR mode) which is concentrated at the tips of the rod.

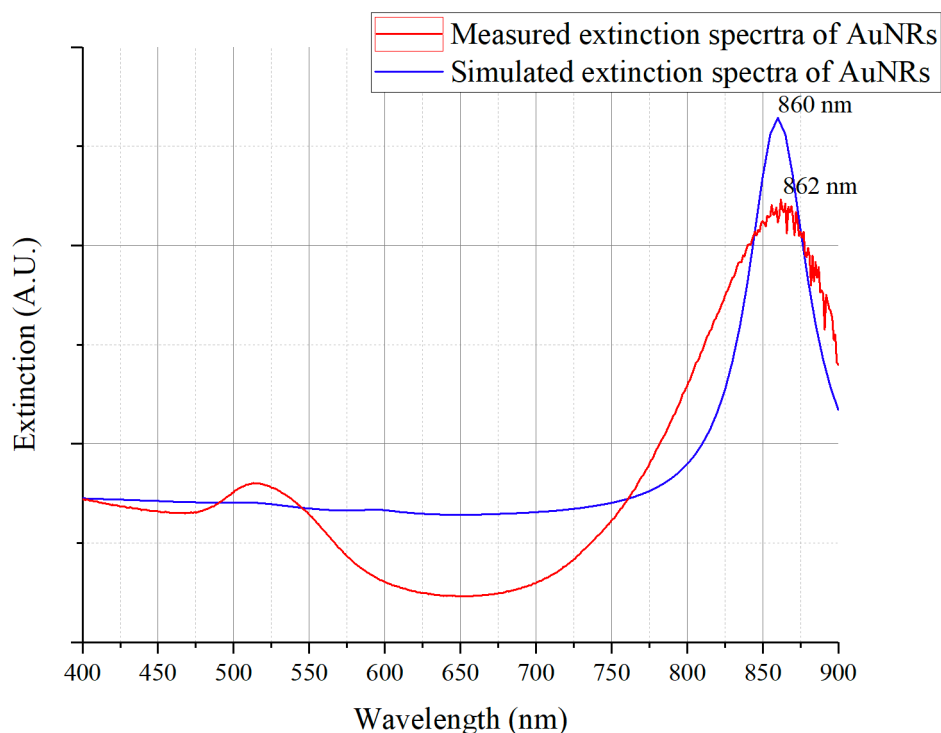


Figure 5-5: Comparison of measured (red line) and simulated extinction spectra (blue line) of AuNRs with AR of 4.2.

These parameters were also investigated for the case of different surface coating layers and the results are presented in figure 5-6. For an AuNR of AR=4.2, better agreement between the modelling and experimental data was achieved when choosing a CTAB layer of thickness 3.2 nm (as reported in Ref. [3] and observed approximately in TEM images in chapter 4) and the refractive index of water which is 1.33575 (green graph). This resulted in a blue shift of the longitudinal mode of 15 nm from the simulated model with a CTAB thickness of 3.2 nm and CTAB refractive index of 1.4785 (blue graph). The effect of surface coating with a 3.2 nm thick CTAB-coated AuNR and a similar PSS coating layer with a refractive index of 1.3875 was also modeled and is presented in figure 5-7. Figure 5-8 shows the effect of increasing AR, there is a red-shift of the longitudinal SPR mode with increasing AR which is in good agreement with the experimental optical UV-vis spectra in chapter 4, section 4.2 and also the literature [3, 7-10].

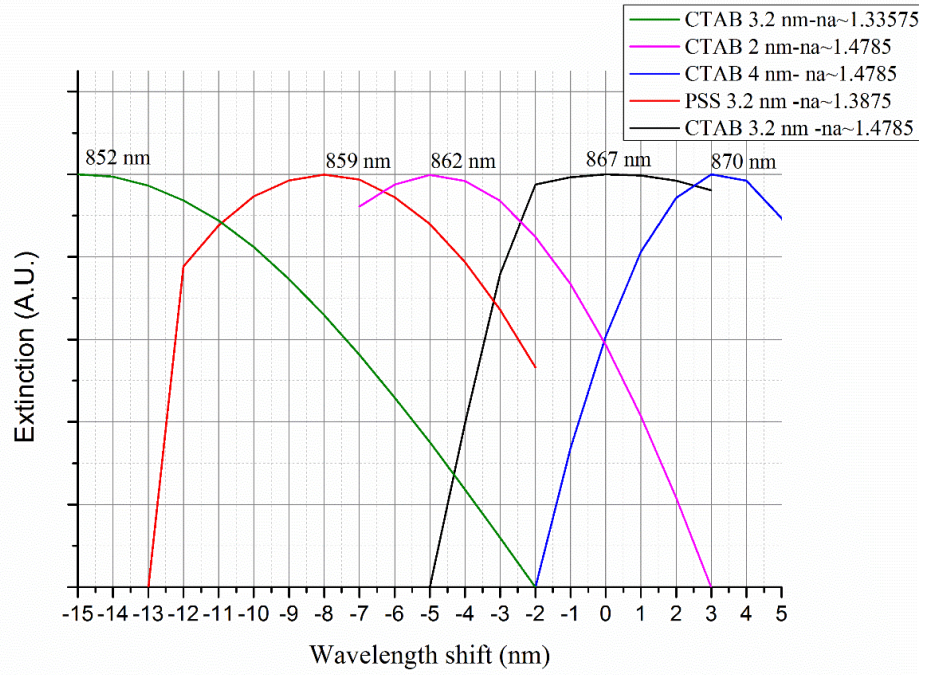


Figure 5-6: The shifts in simulated extinction spectra of a surface coated AuNR of AR= 4.2 resulting from different coating parameters.

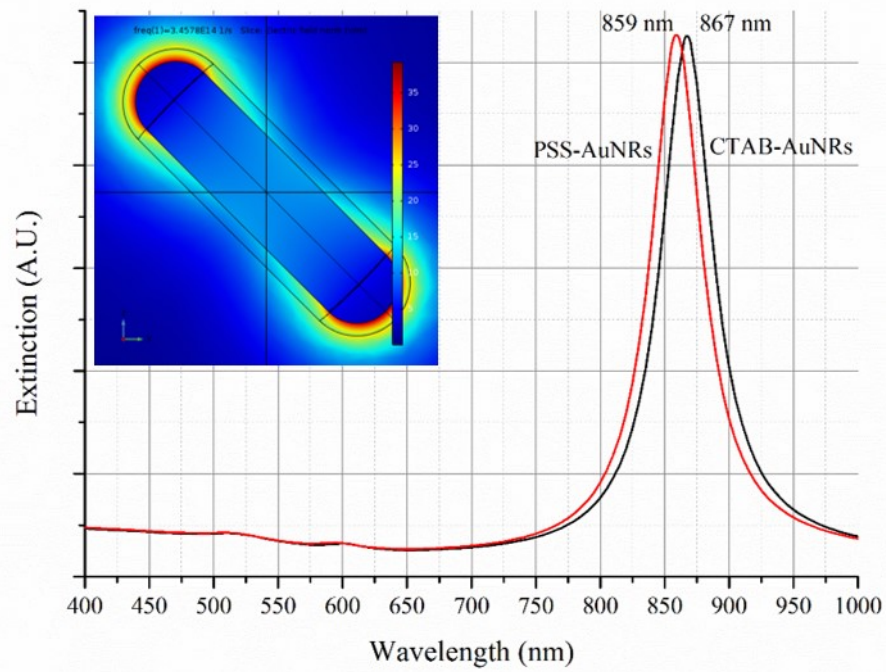


Figure 5-7: The red-shift in simulated extinction spectra of PSS- and CTAB-coated AuNRs. Inset shows the layer of surface coating and the electric field distribution.

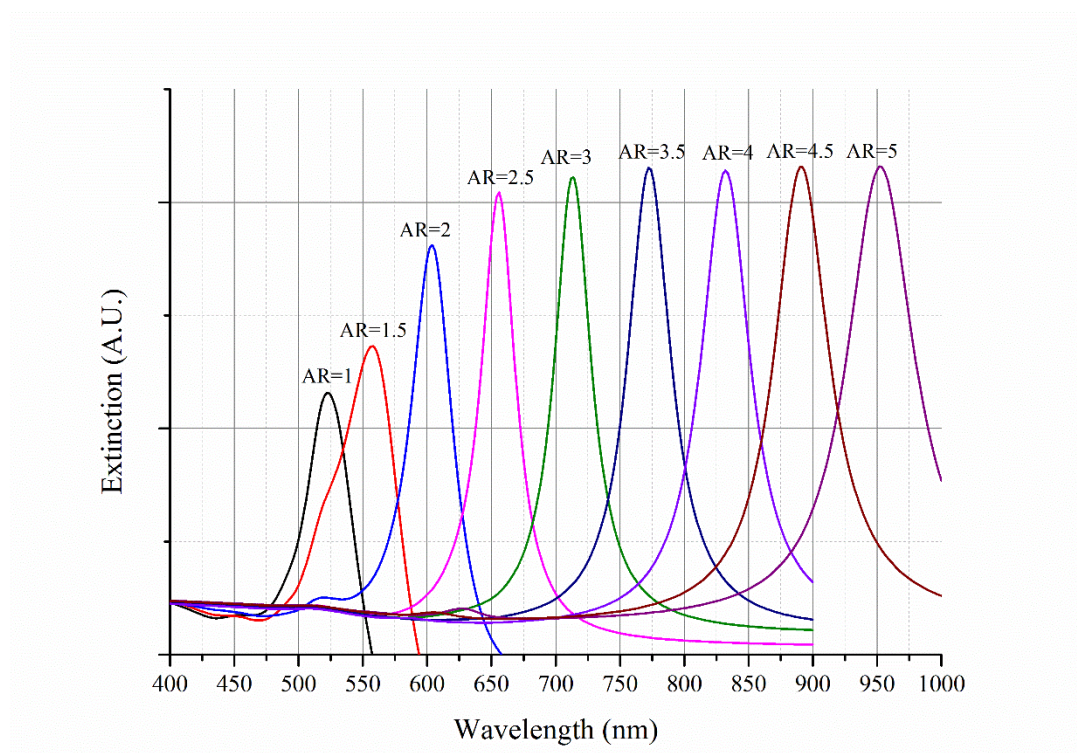


Figure 5–8: simulated extinction spectra of a 3.2 nm thick CTAB-coated AuNR in a water medium $n=1.33$, with increasing AR from 1 to 5.

5.2 Experimental procedure

5.2.1 Gold nanostructures

All samples including AuNPs, AuNRs, AuNBPs, and AuNTs used in this section were freshly synthesized using the procedures described in chapter 3 and characterised using the methods described in chapter 4.

5.2.2 Plasmonic characterization using electron energy loss spectroscopy – experimental details

The electron beam acts as a current carrying wire that generates a radial electric field [11]. This electric field can excite surface electron oscillations also known as localized surface plasmon resonances (LSPR) of the gold particle. When the electron beam passes close to a nanoparticle and causes excitation, the oscillating electrons corresponding to the LSPR can induce an electric field in the particle. This induced electric field interacts with the incident electric field from the electron beam and results in a loss in energy of the electron beam which can be detected in the EEL spectrum. The inelastically scattered electrons pass through an entrance aperture and into the EEL spectrometer which disperses the electrons in terms of their energy loss and then focuses them onto a scintillator coupled to a CCD camera. In STEM

mode, EEL spectra are collected at each probe position creating a spectrum image (SI) and allowing the spatial characterization of the plasmonic properties at a single particle level.

Electron energy loss measurements were performed using a FEI Titan Themis cubed TEM operated at 300kV and fitted with a monochromated electron source. The monochromator was used to achieve an energy resolution of 0.3 eV measured at a dispersion of 0.01 eV/channel. All dispersions of nanostructures were directly drop casted onto non-porous, pure silicon, 5 nm thick TEM support films consisting of 9 small windows (purchased from EMresolutions) and left to dry naturally. Single particles of the Au nanostructures were selected for the acquisition of EEL spectra with sufficient space between particles so as to avoid plasmonic coupling effects.

Only the low-loss energy region from 0-3 eV was considered in this thesis, where the surface plasmon interaction of Au nanostructures is dominant. All data processing was undertaken using Gatan Digital Micrograph software. The EELS data are presented in three dimensional SI maps where the x-y pixel represents the probe position and the z-pixel value the intensity of EELS spectrum integrated over a particular energy range. In this thesis, spectra were acquired with an exposure time of 0.002 seconds/pixel over a selected area to provide a sufficient signal to noise ratio whilst minimizing the effects of sample drift, hydrocarbon contamination and sample damage. The tails of zero-loss peak (ZLP) which forms the background in this energy region was carefully removed using a power law subtraction method [3, 12, 13]. A region of interest (ROI) was carefully selected in x-y pixels and EELS spectra integrated over all selected pixels. EELS spectra were normalized in terms of number of pixels in the ROI. In order to compare the different SI maps and visualize the plasmonic mode of Au nanostructures, the SI maps were normalized to the total electron counts over all selected pixels using the *simple math* option in Digital Micrograph.

5.3 Results

5.3.1 The experimental EELS spectra of Au nanostructures

Au nanospheres

EELS spectra and SPR resonance modes of (an approximately spherical) single gold nanosphere with a diameter of approximately 25 nm is shown in figure 5-9. The blue box indicates the position of the electron beam when acquiring the EELS spectra. The EELS signal after ZLP subtraction and reconstruction with Gaussian fit function to extract the peak position shows a distinct peak at 2.36 eV (corresponding to optical UV-vis absorption wavelength of 525 nm) as displayed in figure 5-9d. Example of Gaussian fitting on EELS

spectra were illustrated in figure 5-10. In this AuNPs' case, the energy range were selected to be 2.2-2.5 eV for the Gaussian fitting. The spatial distribution of the plasmon resonance of the AuNP over the energy range 2.2 - 2.4 eV is shown in figure 5-9c. It shows a uniform distribution of intensity surrounding the particle which corresponds to the dipolar LSPR mode of Au nanoparticles and the result is in good agreement with results for gold nanoparticles of comparable sizes [14]. Comparing with the COMSOL simulations for a 25 nm diameter AuNP in vacuum, see figure 5-2, this showed a maximum extinction of light at a value of 527 nm; the corresponding value for a 20 nm diameter AuNP being 525 nm. This together with comparison with the UV-vis spectra of the 20-nm AuNP suspension (shown in figure 4-1), indicates good agreement between spatially resolved EELS measurements with both the calculations and the experimental UV-vis results.

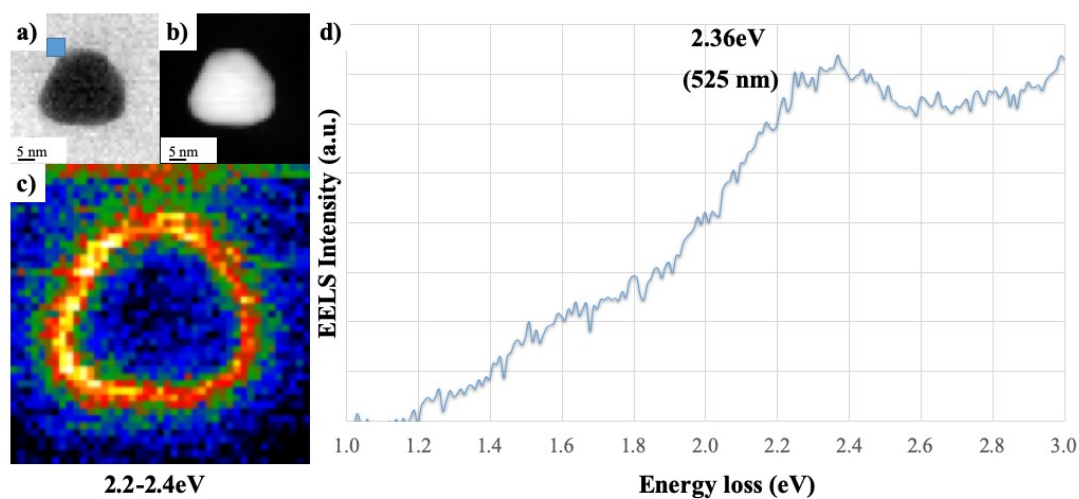


Figure 5–9: TEM micrographs of AuNP with diameter of 20x25 nm: a) bright field image and b) HAADF image. c) SI map showing the plasmonic mode over the energy range 2.2 - 2.4 eV. d) EELS spectrum (following ZLP subtraction) at the position indicated by a blue box in a) illustrating a resonant peak at 2.36 eV (525 nm).

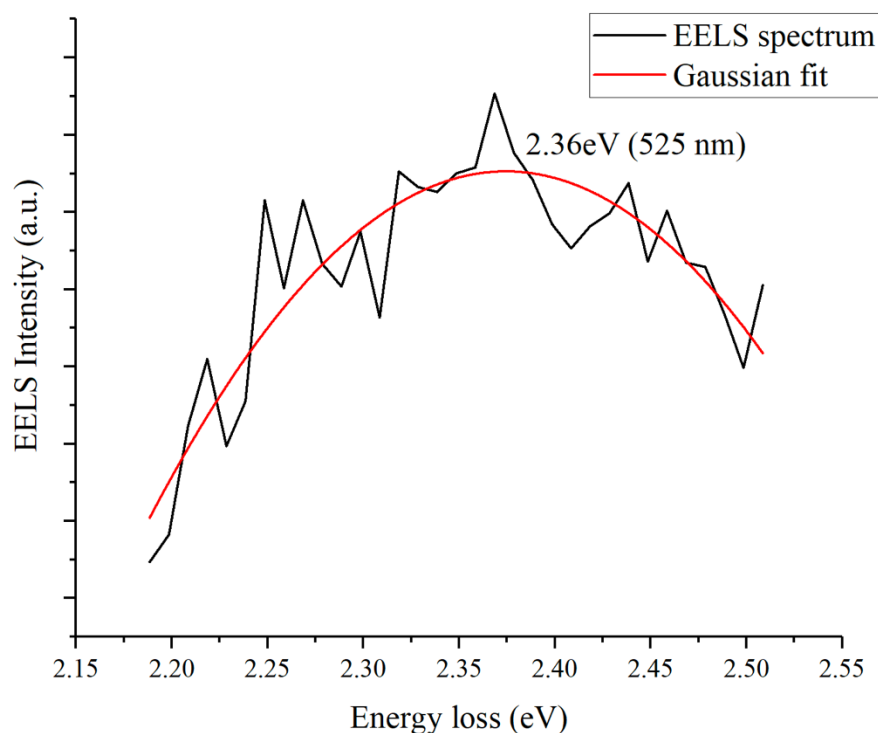


Figure 5–10: Example of Gaussian fitting with the selected energy range (2.2-2.5eV) of the EELS spectrum for AuNPs with diameter of 20x25 nm. The Gaussian fitting illustrated the maxima peak at 2.360.01 eV.

Au nanorods

The experimental EELS spectra of a single AuNR with an AR of 2.6 (60.1nm length and 23.8nm width) together with bright field and HAADF STEM images are presented in figure 5-11. The EELS spectra were collected at the tip (blue box) and the middle (orange box) positions of the AuNR to simulate the two different SPR modes shown in the two distinct EELS spectra in figure 5-11d. The resonance energy at the tip was 1.74 eV (712 nm), whilst in the middle of the rod it was located at 2.38 eV (521 nm), corresponding to the longitudinal and transverse SPR modes, respectively. Energy filtered SI maps were constructed for the energy ranges 1.6 - 1.7 eV for the tip position, and 2.2 - 2.4 eV for the middle of the rod and are shown in figure 5-11c. This revealed the two distinct longitudinal and transverse plasmonic modes of AuNRs. The longitudinal SPR mode is associated with a high intensity at the tip of AuNR and reflects the longitudinal oscillation of electrons that induces a dipole along the rod axis when electron beam is positioned near the tip of the rod. Moreover, the bright field and HAADF images in figure 5-11a and b revealed an asymmetric structure with more curvature at the upper tip compared to bottom part of the rod. This resulted in a higher intensity in the energy filtered SI map in figure 5-11c. On the other hand, the transverse SPR

mode shows a modulated intensity distribution surrounding the particles where the electron motion is perpendicular to the rod axis.

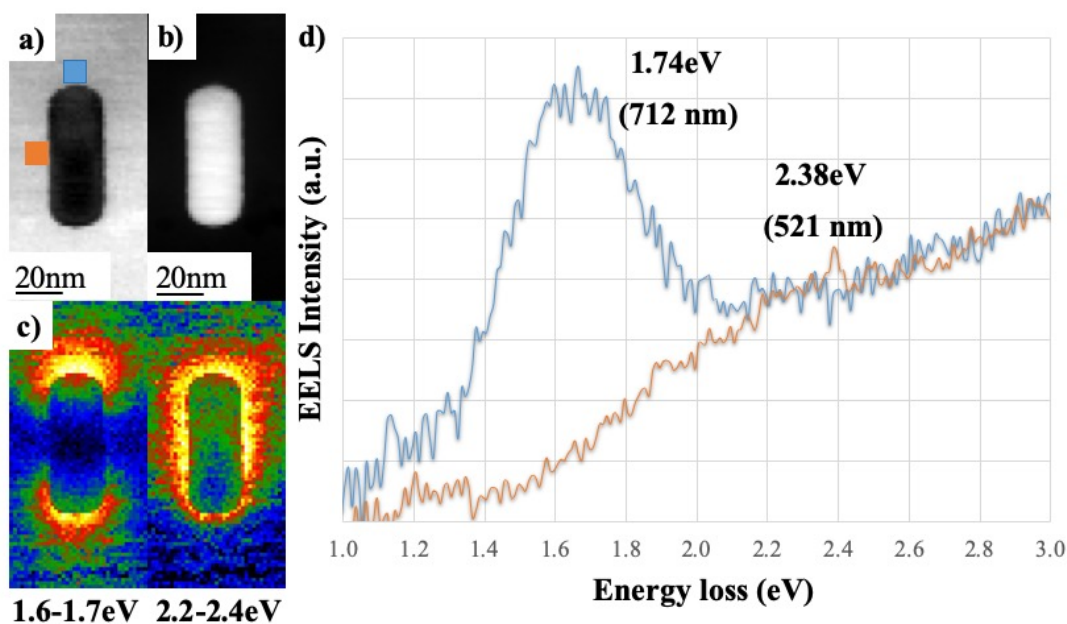


Figure 5–11: STEM micrographs of a single AuNR with AR of 2.6 (60.1 nm long and 23.8 nm width): a) bright field image and b) HAADF image. c) SI map showing the longitudinal and transverse plasmonic modes of the AuNR with the stated energy ranges. d) EELS spectra of the single AuNR at two different positions shown in a) by the blue and orange coloured boxes, showing resonant peaks at 1.74 eV (712 nm) and 2.38 eV (526 nm), respectively.

AuNRs with different ARs were also investigated and an example for a larger AR rod is presented in figure 5-12. For rods with a larger AR, it was found that there was an energy loss shift to lower energies, close to 1.0 eV, which represents the red-shift in the longitudinal SPR mode of AuNRs as the rod AR increases. For example, the optical UV-vis extinction of an AuNR sample with an AR of 2.6 (figure 4-2) showed longitudinal and transverse absorption at 712 nm and 525 nm, respectively.

Generally the optical spectra showed good agreement with the EELS results. Similar to the case of AuNPs, computational simulation was employed to confirm the precision of experimental EELS data collection. It was shown that an AuNR with AR of 2.6 theoretically exhibits the longitudinal extinction at 1.83 eV (675 nm) in vacuum. The slightly red-shifted value observed from the EELS spectra in figure 5-11 can be attributed to the remaining surface coating and/or the effect of the substrate as reported in the literature [2, 3, 14].

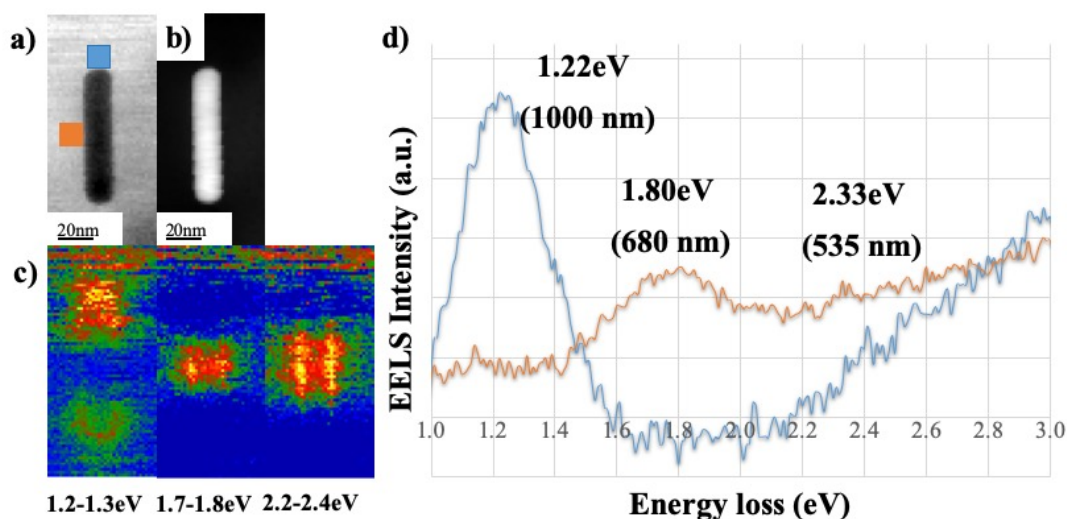


Figure 5–12: STEM micrographs of a longer AuNR with AR of 4.75 (75.4 nm long and 15.9 nm width): a) bright field image and b) HAADF image. c) SI map showing the SPR modes of the AuNR with the stated energy ranges. d) EELS spectra of the single AuNR at different positions shown in a) by the blue and orange coloured boxes, showing resonant peaks at 1.22 eV (1000 nm) and 1.80 eV (680 nm) along with a potential peak at 2.33 eV (535 nm), respectively.

Au nanobipyramids

Au nanobipyramids were also investigated using STEM-EELS measurements in the low-loss region. These nanoparticles have bipyramidal structures with a pentagonal base growing up to form an arrowhead- shaped tip as described in section 4.3. Amongst these AuNBPs, we focused on a particle with AR of 3.1 [Length = 68.8 nm and width = 22.4 nm] which showed an optical absorption maxima in the NIR region, comparable with EELS spectra from an AuNR of a similar AR. Figures 5-13a and b presents STEM bright field and HAADF images of the AuNBP. EELS spectra were extracted from different acquisition positions denoted as the tip (A), side (B), and middle (C), respectively, as presented in HAADF image. After post-analysis of EELS spectra, the dominant SPR modes of the synthesized AuNBP were observed and are presented in figures 5-13c and d. This illustrates the A and C modes which are the typical SPR modes of bipyramidal structures reported in the literature [15]. The A mode is localized at the sharp tip of the particle, whilst the C mode occurred at the short axis (middle part) of the particle. However, there is a report that there are three SPR modes of a bipyramid [15, 16]. A further B mode may possibly be observed at the side facet of the bipyramid in figure 5-13c. The plasmonic peaks were observed to be located at 1.62 eV (765 nm), 2.1 eV (590 nm), and 2.33 eV (530 nm) corresponding to the A, B, and C SPR modes, respectively.

Comparing these results to the optical UV-vis extinction spectra of the AuNBPs, the A-SPR mode matched well with the longitudinal mode of the AuNBPs of AR=3.0 with an absorption maximum of 1.63eV (760 nm) (figure 4-9). The C-SPR mode corresponds to the transverse mode associated with the 2.36 eV (525 nm) absorption maximum of the bipyramidal particles. In the figure 4-9, the UV-vis profile showed a small peak occurring at around 1.9 - 2.1 eV (600 - 650 nm). This could be the B-SPR mode, which is the quadrupole mode. In terms of the EELS SI maps of the plasmonic distribution of the A, B, and C-SPR modes, it is clear that the A mode is a dipolar active mode concentrated at the tip of the bipyramids. The position of this mode is strongly dependent on the sharpness and AR of the bipyramid and exhibited a red-shift to lower energy as the AR increased (compare figures 5-13 and 5-14), which is similar to the situation for AuNRs. The quadrupolar B-mode is not clearly identified, however it could vary as a function of the size and AR. The position of the C-SPR mode is not significantly shifted, similar to the transverse SPR mode of AuNPs and would correspond to resonance along the short axis of the bipyramid. These findings are in a good agreement with previous work [15].

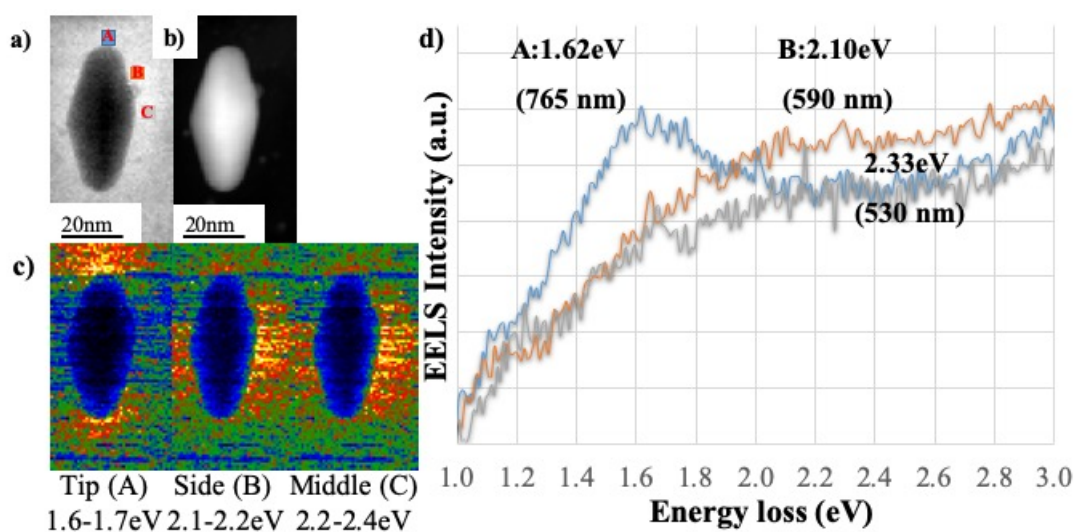


Figure 5–13: a) STEM bright field image of AuNBP with AR of 3.1 (length/width of 68.8/22.4) with three different EELS data acquisition positions denoted as tip (A), side (B), and middle (C), respectively: b) STEM HAADF image: c) SI map showing the spatial distribution of SPR modes at the different positions with the stated selected energy ranges: d) EELS spectra of the AuNBP extracted from the positions indicated in the HAADF image in (a).

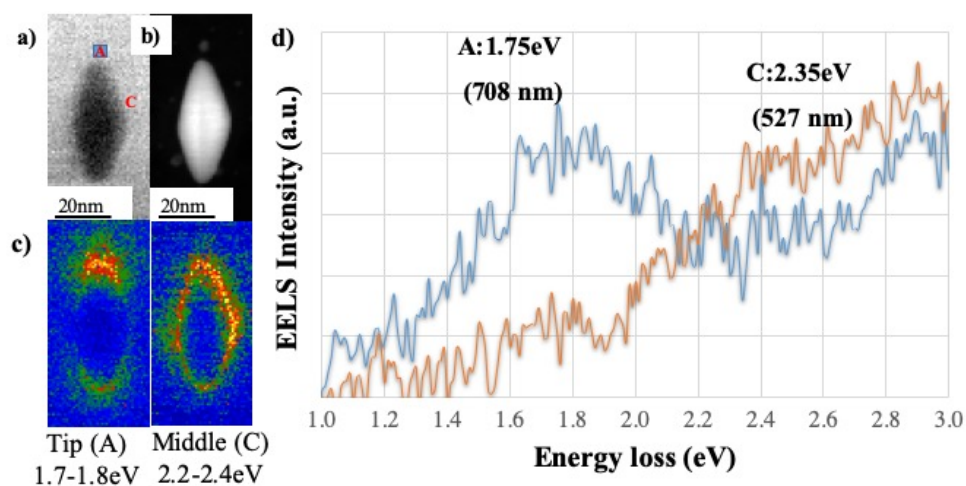


Figure 5–14: a) STEM bright field image of an AuNBP with AR of 2.4 (length/width of 47.5/19.8) with different EELS data acquisition positions denoted as tip (A) and middle (C): b) STEM HAADF image c) SI map showing the spatial distribution of SPR modes at the different positions with the stated selected energy ranges: d) EELS spectra of the AuNBP extracted from the positions indicated in the HAADF image in (a).

Au nanotriangles

EELS measurements were also carried out on the AuNT samples in order to provide more understanding of the plasmonic properties. In figure 5-15a and b both bright field and HAADF STEM images show a regular gold triangle with an edge length of 74.48 nm. Spectra were integrated at the tip (A), the edge (B), and the centre (C) of the triangle and revealed distinct features, illustrated in figure 5-15d. EELS peaks were observed at 1.72 eV (720 nm), 2.12 eV (585 nm), and 3.16 eV (392 nm) with respect to the A, B, and C positions, respectively. The SPR distributions are illustrated in the normalized SI maps shown in figure 5-15c constructed following post data analysis using the energy ranges indicated.

By comparing the spatial characteristics of the SPR modes, three common SPR modes were evident. At 1.72 eV, a well-localized strong resonance was found to be located at the tips of the triangle which is a dipolar plasmonic resonance. The plasmonic distribution at 2.12 eV was localized at the edges of triangles and is related to the in-plane SPR mode. While the plasmonic distribution in the centre, at the energy of 3.16 eV, is relatively weak compared to the others and difficult to see above the noise, this is the bulk volume plasmon resonance of gold. These observed plasmonic SPR modes of the AuNT are in a good agreement with the published experimental and theoretical studies of individual gold nanotriangle particles [17, 18]. Furthermore, the optical UV-vis absorption AuNTs (presented in figure 4-11) showed that a large AuNT sample with average edge length of 99.8 ± 24.4 nm exhibited two distinct peak positions at 1.83 eV (675 nm) and 2.34 eV (530 nm) corresponding to the dipole and in-

plane SPR modes. However a significant red-shift was seen in the EELS spectra relative to UV-vis data, similar to the results for the AuNBPs. The SPR mode of the AuNT depends on both the edge length and sharpness of the tips of the AuNT. Increasing the size of the AuNTs resulted in a red-shift of the EELS spectra, as clearly observed in the EELS measurement of a larger AuNT with edge length of 190nm (illustrated in figure 5-16). Similar results were observed in the optical UV-vis absorption, as well as being predicted by theoretical studies in the literature [19, 20].

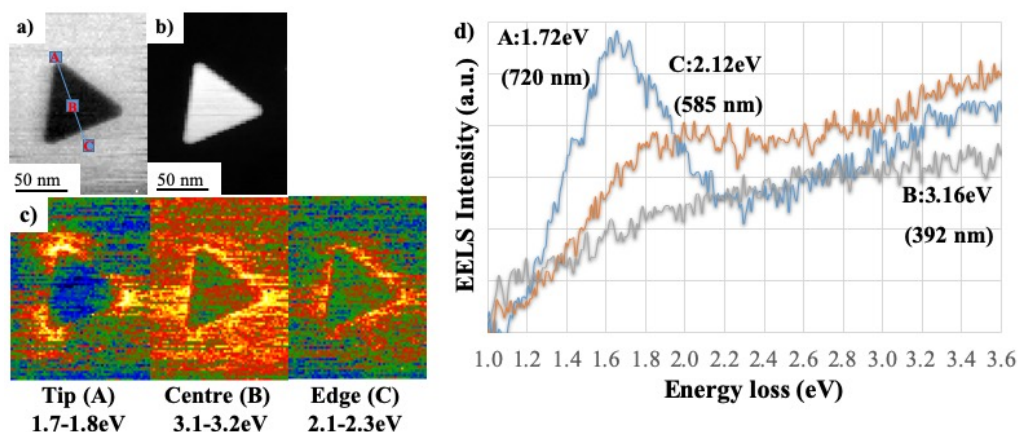


Figure 5–15: a) and b) Bright field STEM and HAADF images of an AuNT with an edge length of 74.48 nm. c) SI map illustrating three plasmonic modes with the selected energy ranges indicated. d) EELS spectra of the AuNT at the different locations indicated in (b): tip (A), centre (B), and edge (C).

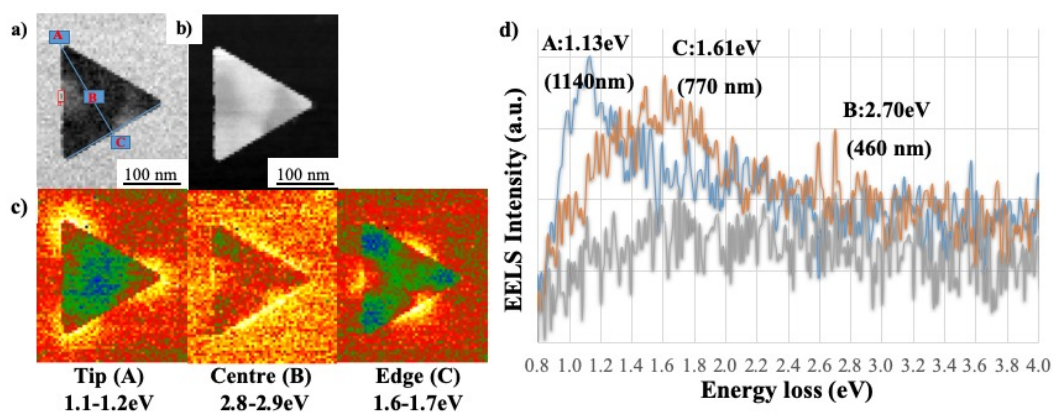


Figure 5–16: a) and b) Bright field STEM and HAADF images of an AuNT with an edge length of 190 nm. c) SI map illustrating three plasmonic modes with the selected energy ranges indicated. d) EELS spectra of the AuNT at the different locations indicated in (b): tip (A), centre (B), and edge (C). (Sample courtesy of Dr Sunjie Ye)

5.3.2 Coupling between Au nanostructures

EELS measurements can also demonstrate the coupling between SPR modes of closely spaced Au nanostructures. Figure 5-17a shows the plasmon mode of a dumbbell-like particle consisting of two touching nanospheres. The plasmonic mode of the combined particle at an energy of 2.4 eV illustrates the strongly enhanced field at the neck between the particles area, indicated in red. A similar effect is seen in the cluster of AuNTs in figure 5-17b, which shows a strong increase in intensity at the regions where the tips are close to a neighbouring NT particle. In figure 5-17c, the spatial distribution of the SPR modes of two triangles located at a distance of a few nm apart is shown. Two SPR modes at 1.7 eV and 2.1 eV are evident. The field distribution at the tips of the NTs are enhanced at an energy of 1.7 eV, whilst over the energy range 2.0 - 2.2 eV, a localized SPR mode was enhanced in the gap between the triangles.

A more complex cluster of Au nanostructures is shown in figure 5-17d, where two SPR modes were evident. At the top-left area of the cluster there was an SPR mode with an energy of 1.7 eV whilst another plasmonic mode was found at 2.4 eV with significant intensity located at the sharp corners of the overall cluster. The cluster is irregular and non-symmetrical and the intensity is considerably higher on the right hand side of the cluster, which exhibits more sharp areas of close contact than the left hand side.

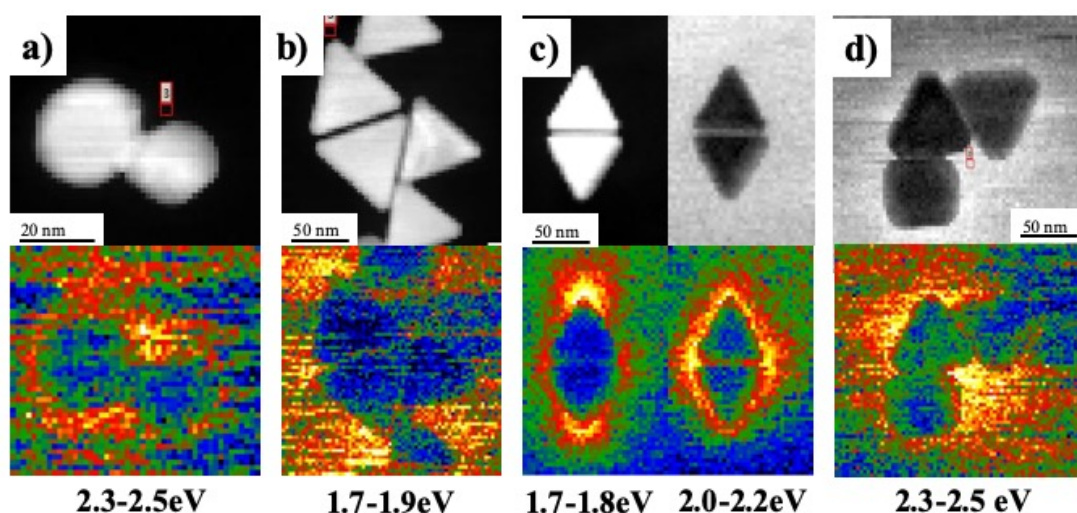


Figure 5–17: STEM micrographs and their relative energy filtered SI maps over the stated energy ranges: a) two closely spaced spheres; b) a cluster of triangles; c) two triangles separated by a gap of a few nm; and d) a cluster of Au nanostructures.

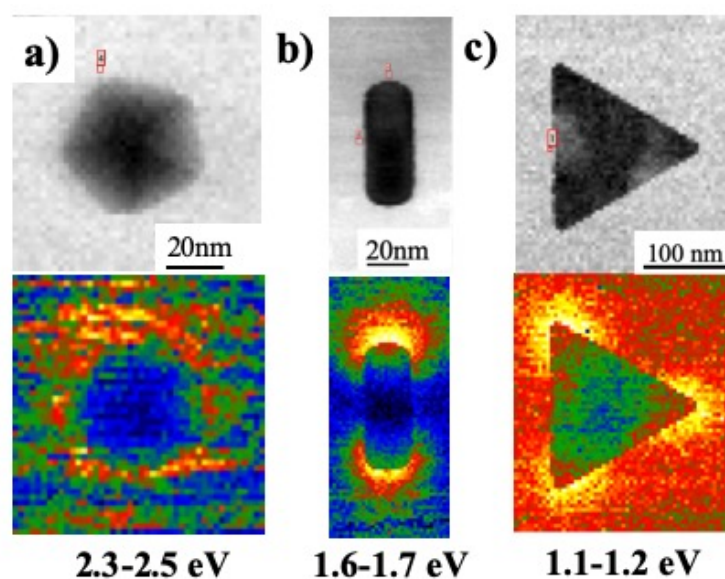


Figure 5–18: STEM BF images of Au nanostructures, including: a) an unsymmetrical AuNP: b) an AuNR with hemispherical caps of different radii of curvature: and c) a large AuNT with very sharp tips, together with associated SI maps over the given energy ranges indicated.

In order to confirm this hypothesis, further investigations of individual unsymmetrical Au particles were undertaken. Figure 5-18a shows the strong intensity of the SPR mode in the elongated area of a distorted AuNP. The SPR distribution at the top and bottom of an AuNR presented in figure 5-18b is asymmetric and is more intense where the hemispherical endcap exhibits a higher degree of curvature. Similarly, in figure 5-18c, the sharpest tips of AuNTs exhibit the most intense SPR mode. These results are in excellent agreement with previous reports [2, 14].

In chapter 4, optical characterization was performed on whole suspensions of Au nanostructures. EELS measurements allow the spatial plasmonic modes of an individual Au nanostructure to be revealed and this can contribute to the design of such particles for photothermal therapy applications in healthcare. The potential of different Au nanostructures is revealed by such plasmonic studies using EELS SI mapping and their thermal stability can be ascertained using in-situ heating which is described and detailed in the next chapter.

5.4 Conclusion

In conclusion, the spatial characterization of the plasmonic properties of Au nanostructures using STEM/low-loss EELS analysis was examined in this chapter. Firstly, FEM simulations of the excitation spectra on isolated particles using plane wave illumination allowed comparisons with the experimental optical spectra and also EELS data. The surface plasmon modes, electric field enhancement, and the coupling effect between nanostructures were then spatially investigated. It was found that EELS results showed good agreement results with

FEM computational simulations and the experimental uv-vis spectra. This confirmed that the optical and plasmonic properties of individual Au nanostructures depend on size and shape.

Furthermore, EELS analysis leads to the suggestion that Au nanostructures including AuNRs and AuNBPs with the energy loss energy of 1.0 - 1.7 eV corresponding to an optical extinction of about 700 - 1000 nm would be a good candidate for photothermal therapy due to their narrow range of optical excitation. While AuNTs and AuNPs exhibited presented a broad range of optical excitation, the strongest SPR mode was clearly observed at a low energy of 1.1 eV (1140 nm) from a very large AuNT with an edge length of approximately 190 nm. Hence, the 1140-nm absorbing AuNT is one of the best candidates for healthcare applications due to well-defined NIR plasmonic properties. The localized SPR maps show a field enhancement localized at the sharp tips of the particles. This field enhancement can be employed to convert light-to-heat and generate sufficient heat for use in thermal therapy. With increased curvature, Au nanostructures could provide high field enhancement at the tips further shifting the SPR mode into the NIR region. Additionally, the effect of coupling needs to be considered as the cluster can exhibit two distinct SPR modes which might directly affect the shift in SPR response and its frequency. These studies highlight parameters in term of selecting and using certain wavelengths for irradiation to activate photothermal therapy.

5.5 References

- [1] Kneipp, K., H. Kneipp, and J. Kneipp, *Probing plasmonic nanostructures by photons and electrons*. Chemical Science, 2015. **6**(5): p. 2721-2726.
- [2] N'Gom, M., et al., *Electron-beam mapping of plasmon resonances in electromagnetically interacting gold nanorods*. Physical Review B, 2009. **80**(11): p. 113411.
- [3] Cottom, J.W., *Fabrication and characterization of an adaptable plasmonic nanorod array for solar energy conversion*, in *School of Chemical and Process Engineering*. 2017, University of Leeds.
- [4] Bastús, N.G., J. Comenge, and V. Puntes, *Kinetically Controlled Seeded Growth Synthesis of Citrate-Stabilized Gold Nanoparticles of up to 200 nm: Size Focusing versus Ostwald Ripening*. Langmuir, 2011. **27**(17): p. 11098-11105.
- [5] Piella, J., N.G. Bastús, and V. Puntes, *Size-Controlled Synthesis of Sub-10-nanometer Citrate-Stabilized Gold Nanoparticles and Related Optical Properties*. Chemistry of Materials, 2016. **28**(4): p. 1066-1075.

- [6] Rodríguez-Fernández, J., et al., *Seeded Growth of Submicron Au Colloids with Quadrupole Plasmon Resonance Modes*. Langmuir, 2006. **22**(16): p. 7007-7010.
- [7] Feng, L., et al., *Preparation of gold nanorods with different aspect ratio and the optical response to solution refractive index*. Journal of Experimental Nanoscience, 2015. **10**(4): p. 258-267.
- [8] Nikoobakht, B. and M.A. El-Sayed, *Preparation and Growth Mechanism of Gold Nanorods (NRs) Using Seed-Mediated Growth Method*. Chemistry of Materials, 2003. **15**(10): p. 1957-1962.
- [9] Gole, A. and C.J. Murphy, *Seed-Mediated Synthesis of Gold Nanorods: Role of the Size and Nature of the Seed*. Chemistry of Materials, 2004. **16**(19): p. 3633-3640.
- [10] Smitha, S.L., et al., *Size-dependent optical properties of Au nanorods*. Progress in Natural Science: Materials International, 2013. **23**(1): p. 36-43.
- [11] Hohenester, U., H. Ditlbacher, and J.R. Krenn, *Electron-Energy-Loss Spectra of Plasmonic Nanoparticles*. Physical Review Letters, 2009. **103**(10): p. 106801.
- [12] Egerton, R. F. *Electron Energy-Loss Spectroscopy in the Electron Microscope*; Plenum: New York, 1996.
- [13] Cueva, P. et al. *Data Processing for Atomic Resolution Electron Energy Loss Spectroscopy*. Microscopy and Microanalysis, 2012. **18**(4): p. 667–675.
- [14] Diaz-Egea, C., et al., *High spatial resolution mapping of surface plasmon resonance modes in single and aggregated gold nanoparticles assembled on DNA strands*. Nanoscale Research Letters, 2013. **8**(1): p. 337.
- [15] Arenal, R., et al., *Local Plasmonic Studies on Individual Core–Shell Gold–Silver and Pure Gold Nano-Bipyramids*. The Journal of Physical Chemistry C, 2014. **118**(44): p. 25643-25650.
- [16] Myroshnychenko, V., et al., *Modelling the optical response of gold nanoparticles*. Chem. Soc. Rev., 2008. **37**: p.1792-1805
- [17] Nelayah, J., et al., *Mapping surface plasmons on a single metallic nanoparticle*. Nature Physics, 2007. **3**(5): p. 348-353.
- [18] Sherry, L.J., et al., *Localized Surface Plasmon Resonance Spectroscopy of Single Silver Triangular Nanoprisms*. Nano Letters, 2006. **6**(9): p. 2060-2065.

- [19] Chan, G.H., et al., *Localized Surface Plasmon Resonance Spectroscopy of Triangular Aluminum Nanoparticles*. The Journal of Physical Chemistry C, 2008. **112**(36): p. 13958-13963.
- [20] Wu, C., X. Zhou, and J. Wei, *Localized Surface Plasmon Resonance of Silver Nanotriangles Synthesized by a Versatile Solution Reaction*. Nanoscale research letters, 2015. **10**(1): p. 1058-1058.

Chapter 6 Thermal stability of gold nanostructures

Gold nanostructures have recently received considerable research interest since they exhibit chemical stability and biocompatibility which make them suitable for use in biological applications and they also present shape-dependent optical properties [1-4]. Gold nanostructure synthesis has been intensively researched allowing easy size control of gold nanoparticles and well-defined shape synthesis. In chapter 4, I have presented a set of facile synthesis methods for obtaining gold nanostructures with well-defined morphologies and different sizes including AuNPs, AuNRs, AuNBPs, and AuNTs. By tailoring the size and refining the morphology of these particles, their SPR absorption peaks can be tuned and shifted into the near infrared (NIR) wavelength region [2, 5] for the purpose of in-vivo biomedical applications such as photothermal therapy [6-9] and ultrasound imaging [8, 9]. This NIR region offers low energy absorption and scattering with low damage to allow high penetration of irradiated light into tissues [10].

Gold nanostructures have been employed in a number of photothermal therapy experiments due to their light-to-heat conversion property [11]. Among these gold nanostructures, AuNRs are receiving much interest in terms of thermal therapy due to the fact that the longitudinal SPR can be easily tuned over the NIR region. As discussed in previous chapters, AuNRs exhibit two SPR absorption peaks: a transverse SPR mode and a longitudinal SPR mode. The longitudinal SPR mode is very sensitive to AR. In AuNRs, there is a decrease in the AR during exposure to ultrafast pulsed laser radiation and thermal heating [12-15]. Similar results have been reported in the literature for the other particle shapes when used in applications involving increases in temperature [16-18]. Furthermore, SPR spectra in all synthesized Au nanostructures are very sensitive to shape and size, thus any slight change in shape of gold nanoparticles is dramatically reflected in their optical properties as presented in chapter 4 and 5. Therefore, the thermal stability of Au nanostructures is of interest both fundamentally and for their use in specific medical applications.

In this chapter we present time-resolved in-situ TEM heating experiments of Au nanostructures including AuNPs, AuNRs, AuNBPs, and AuNTs as well as a comparison of different surface coatings (CTAB, PSS, and silica) in AuNRs. These studies provide direct observation of the structural changes in the gold nanostructures as well as their shape deformation mechanism. The effect of size and geometry of the Au nanostructures on the thermal stability were investigated as well as the effect of surface modification. The results

from these experiments can aid determination of the usable range of Au nanostructures in applications which require no change in optical properties as a result of thermal excitation.

6.1 Experimental procedure

6.1.1 Preparation of gold nanostructures

Gold nanostructures were freshly synthesised via the wet chemical synthesis procedures discussed in chapter 3. Citrate-stabilized AuNPs were synthesized as detailed in chapter 3, section 3.1.1. The modified seed mediated method was used to synthesize AuNRs (chapter 3, section 3.1.2). The as-prepared AuNRs were stabilized and surface modified with CTAB, PSS, and silica coatings (detailed in chapter 3, section 3.1.5). CTAB-coated AuNBPs were fabricated using a two-step seed mediated method described in chapter 3, section 3.1.3. The synthesis of CTAC-stabilized AuNTs was achieved with a one-step synthesis method detailed in chapter 3, section 3.1.4.

6.1.2 Materials Characterization and TEM heating experiments

Before being characterized, all Au nanostructures were centrifuged twice and redispersed with the same amount of Milli-Q water to remove the excess surfactant. They were then characterized by UV-vis spectroscopy, TEM and DLS using the procedures described in chapters 3 and 4.

In-situ TEM heating experiments

The thermal stability of Au nanostructures was studied via in-situ TEM heating experiments. The samples were prepared by dropping 2 μ l of a centrifuged Au suspension onto a Si₃N₄ heating chip (DENS solutions) which was then allowed to dry naturally. The chip was loaded into the in-situ DENS heating holder and inserted into the TEM. The detailed of experimental workflow is presented in figure 6-1. The chip was heated from room temperature up to 1100°C, applying a 50°C increase every 5 minutes (10 °C/min). The morphology of the sample in the centre of the heating chip was monitored (figure 6-2).

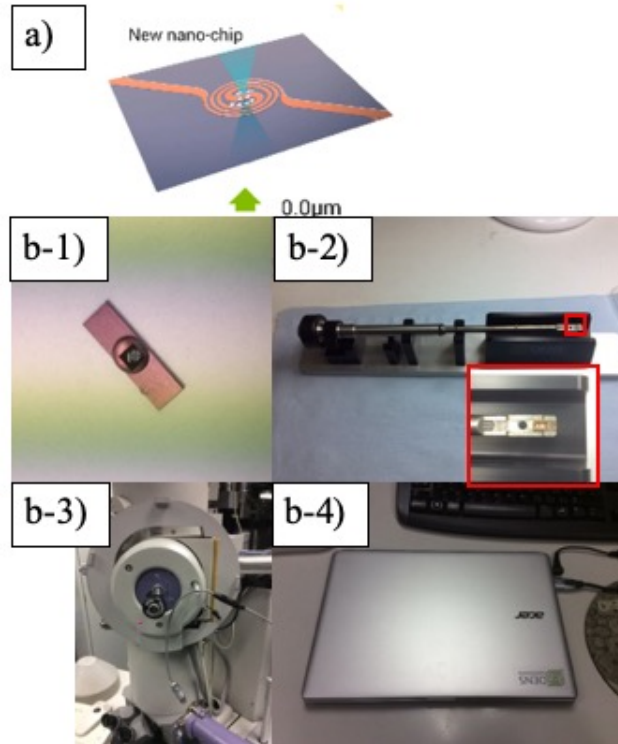


Figure 6–1: In-situ TEM heating experimental set up: a) schematic of Si_3N_4 heating chip; b) The TEM heating set up steps: 1) drop $2 \mu\text{l}$ of Au nanostructures on the back of heating chips; 2) mount TEM heating chip in TEM heating holder; 3) load TEM heating holder into the TEM; and 4) connect all wires with controller unit and set up heating experiment.

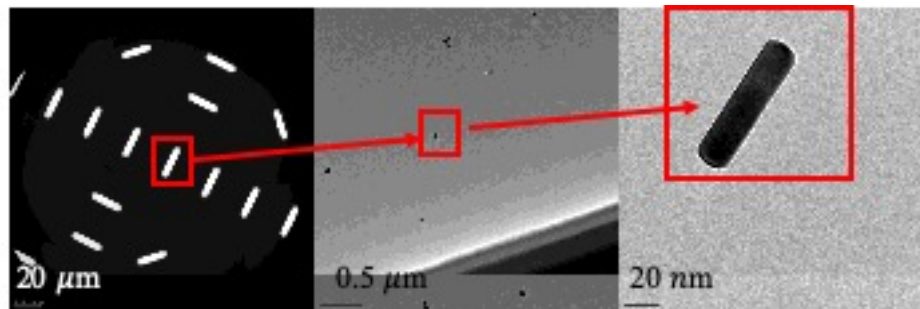


Figure 6–2: TEM micrographs of TEM heating chip with selected AuNRs at the centre.

6.2 Results and discussion

6.2.1 The effect of size and geometry on the thermal stability of Au nanostructures

Citrate-stabilized Au nanoparticles (AuNPs)

Figure 6-3 showed that the diameter of AuNPs did not significantly change during the heating experiment. The TEM images reveal minor structural changes and an increasing spherical morphology as the temperature increased (figure 6-3a). This deformation mechanism arises from the minimization of surface energy to become more thermodynamically stable via a transition from a higher radius of curvature to a lower radius of curvature resulting in the particle becoming more spherical as the temperature increased. The heating profile is plotted in figure 6-3b and suggests that this spherical geometry shows a high thermal stability up to 1000°C.

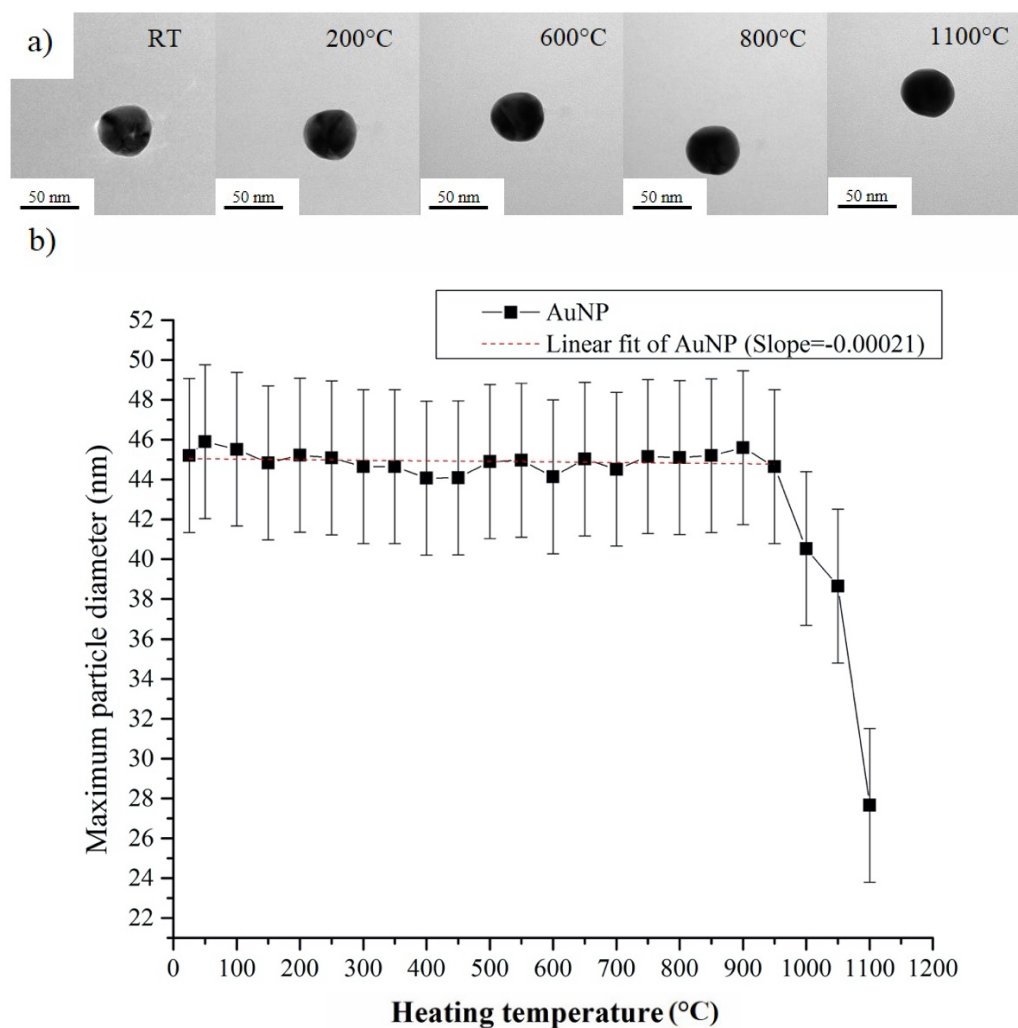


Figure 6-3: a) TEM micrographs of a 45 nm diameter citrate-stabilized AuNP at different temperatures: RT, 200°C, 600°C, 800°C and 1100°C; b) The maximum particle diameter with temperature and the associated linear fit.

CTAB-capped Au nanorods (AuNRs)

The heating results illustrated a structural change of AuNRs with increasing temperature (figure 6-4a), notably a decrease in aspect ratio. The changes in AR for different rods over the heating temperature profile are shown in figure 6-4b. It was found that the aspect ratio of the rods initially began to change at low temperatures ca. 100°C, with a relatively slow rate. More significant changes were then observed at higher temperatures, with the rod length decreasing and the rod width increasing. The slopes of the graphs in figure 6-4b revealed the rate of change of the AR as a function of temperature. At temperatures up to ca. 300°C, the rate was highest and then reduced and became relatively constant at higher temperatures. For temperatures >600°C, particles became increasingly spherical for all rods monitored. There was some variation in results with some rods exhibiting a significant change in AR at high temperatures, e.g. > 700°C for rods 1, 2 and 3.

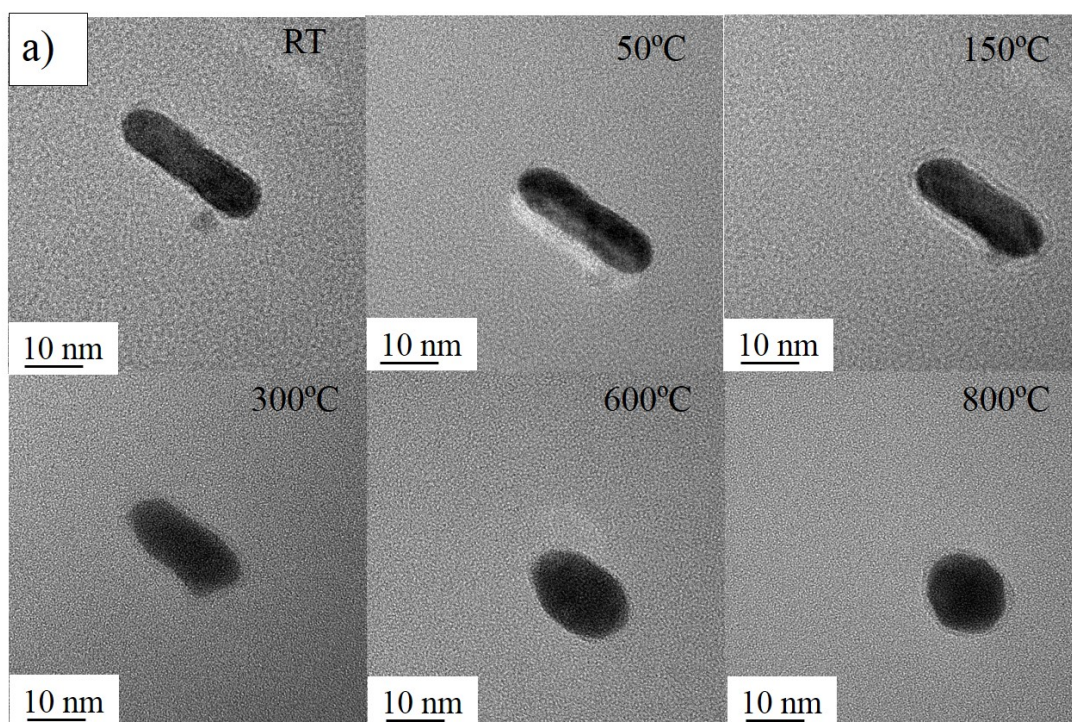


Figure 6-4: a) TEM micrographs of a CTAB-coated AuNR with an AR of 3.82 (rod 4) at different temperatures: RT, 50°C, 150°C, 300°C, 600°C and 800°C.

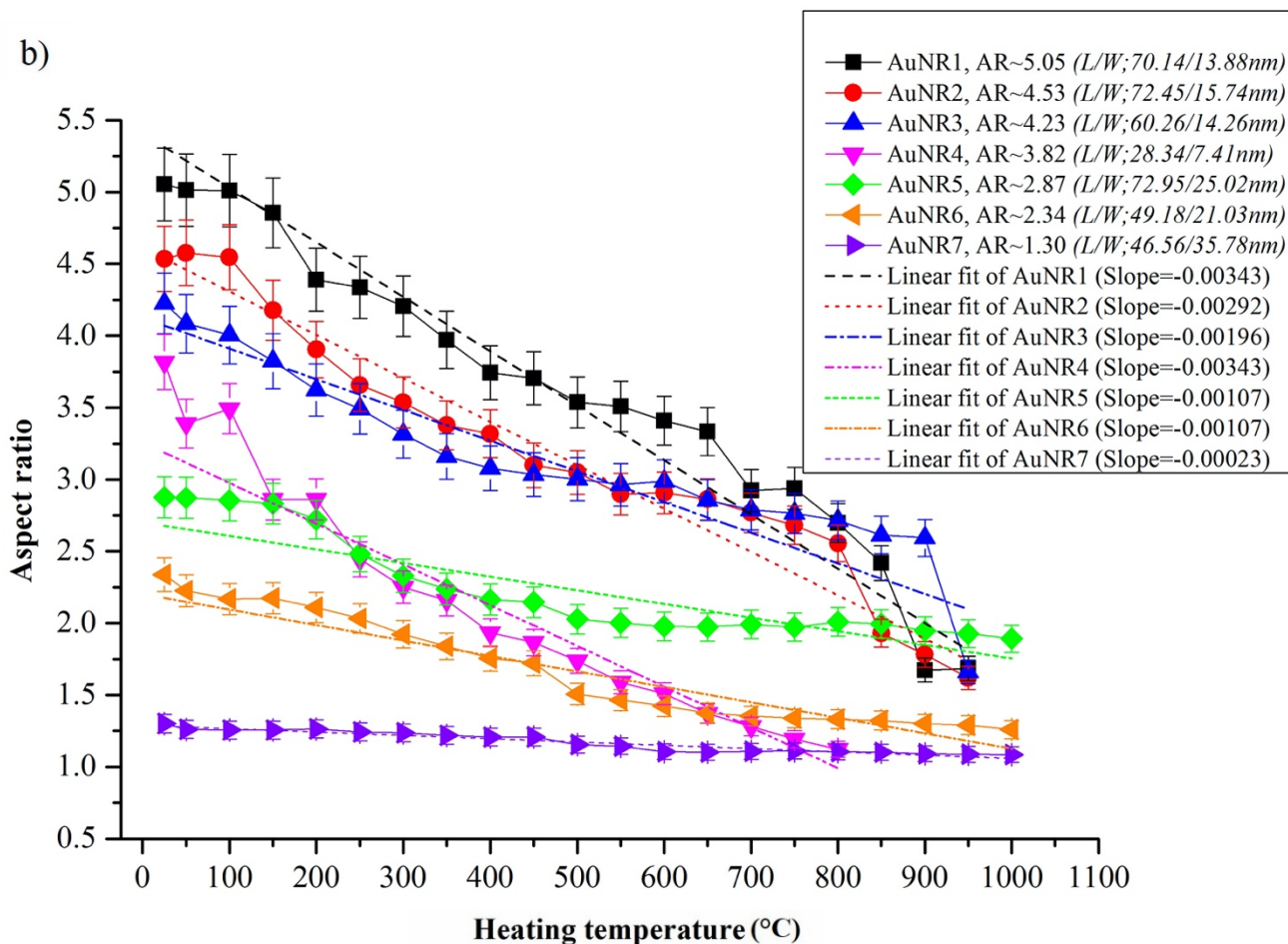


Figure 6-4: b) The change in rod AR with temperature and associated linear fits for different AR rods.

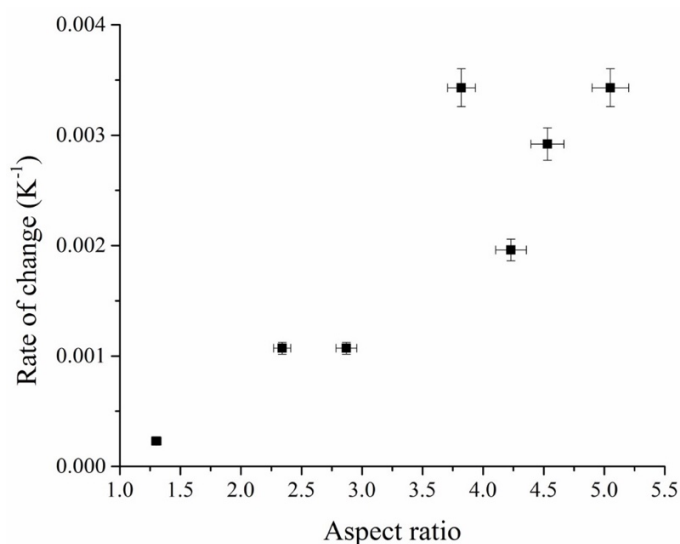


Figure 6-4: c) The rate of change of rod AR with respect to temperature plotted as a function of the original aspect ratio for different CTAB-capped AuNRs.

The observed rate of change of rod aspect ratio with respect to temperature (in units of K^{-1}) is plotted as a function of the original rod aspect ratio in figure 6-4c. The values are also summarized in Table 6-1. It can be seen that longer rods exhibited a higher rate of change than shorter rods with a nearly linear relationship of the slope with original aspect ratio. Hence longer rods were found to be more thermally unstable with respect to their morphology, which is in agreement with previous studies [12, 19, 20]. Such behaviour is in agreement with the modelling studies of Taylor et al. [19] who proposed that the surface diffusion coefficient was a function of the rod aspect ratio; increased tip curvature in longer AR rods resulting in a lower activation energy for surface diffusion.

Table 6-1: Summary of the rate of change of Au nanostructure morphology with respect to particle dimensions.

Sample		Aspect ratio	Rate of change ($\frac{dAR}{dT}$, K^{-1})
Citrate stabilized	AuNP	1.05	-0.00021
CTAB-capped	AuNR 1	5.05	-0.00343
	AuNR 2	4.53	-0.00292
	AuNR 3	4.23	-0.00196
	AuNR 4	3.82*smallest size	-0.00343
	AuNR 5	2.87	-0.00107
	AuNR 6	2.34	-0.00107
	AuNR 7	1.30	-0.00023
CTAB-capped	AuNBP 1	2.58	-0.00149
	AuNBP 2	2.49	-0.00128
CTAC-capped	AuNT 1	Edge ~ 104.6 nm	-0.00349
	AuNT 2	Edge ~ 83.0 nm	-0.00385
	AuNT 3	Edge ~ 69.2 nm	-0.00712
PSS-coated	AuNR 1	4.17	-0.00130
	AuNR 2	3.82	-0.00120
	AuNR 3	3.23	-0.00110
	AuNR 4	2.81	-0.00113
	AuNR 5	2.53	-0.00039
Silica-coated	AuNR 1	3.52	-0.00045
	AuNR 2	3.12	-0.00036
	AuNR 3	2.53	-0.00014
	AuNR 4	2.21	-0.00004

The change in AR also depended on the surface area to volume ratio [21]; thinner rods (rods 1-4) exhibited a more rapid decrease in AR with respect to temperature as compared to thicker rods (rods 5-7). For rods with different lengths but the same width, the longer rods showed more a significant change with temperature than the shorter rods. Interestingly, rod 4, which is thinnest rod (an AR of approximately 3.8 with length 28.3 nm and width 7.4 nm), illustrated that the surface of AuNR started melting and diffused from the tip to the middle of the rod at ca. 150. At 300, a significant decrease in length was observed. At higher temperatures the rate of change increased, and the rod transformed into a sphere at about 800 (figure 6-4a).

In terms of volume change, initial room temperature TEM images (figure 6-3a) were compared with those at the end of heating profile. Assuming a cylindrical rod with two hemispherical endcaps, the estimated initial volume was nm^3 whilst the spherical particle volume after heating was nm^3 . This perhaps indicates a slight change in volume which may occur during to surface melting via evaporation or diffusion onto the support film. It is also noted that CTAB could transform to become an amorphous carbon layer possibly preventing surface diffusion and the deformation of AuNRs [22]. The effect of different types of surface modification is studied in section 6.2.2.

CTAB-capped Au nanobipyramids (AuNBPs)

The influence of shape on thermal stability was studied by heating AuNBPs with an AR of about 2.5 (length 67.5 nm and width 26.6 nm). Figure 6-5 suggests that, in general, the rate of change of AR with respect to temperature of AuNBPs increases with increasing temperature similar to the behaviour of CTAB-capped AuNRs. However, the rate of change of AR at low temperatures ca. < 200 is slightly smaller when compared to AuNRs of similar dimensions (e.g. rod 5 in figure 6-4b). This suggests that bipyramids can retain their shape to slightly higher temperatures relative to AuNRs. The bipyramids reduced AR by shrinking from the tips and depositing in the middle part of the AuNBP between ca. 300 to 600 with a relatively constant decrease in. Above 600, the morphology changes much more rapidly becoming spherical, illustrating the higher rate of change of AR with increasing temperature, as shown in figure 6-5a and b.

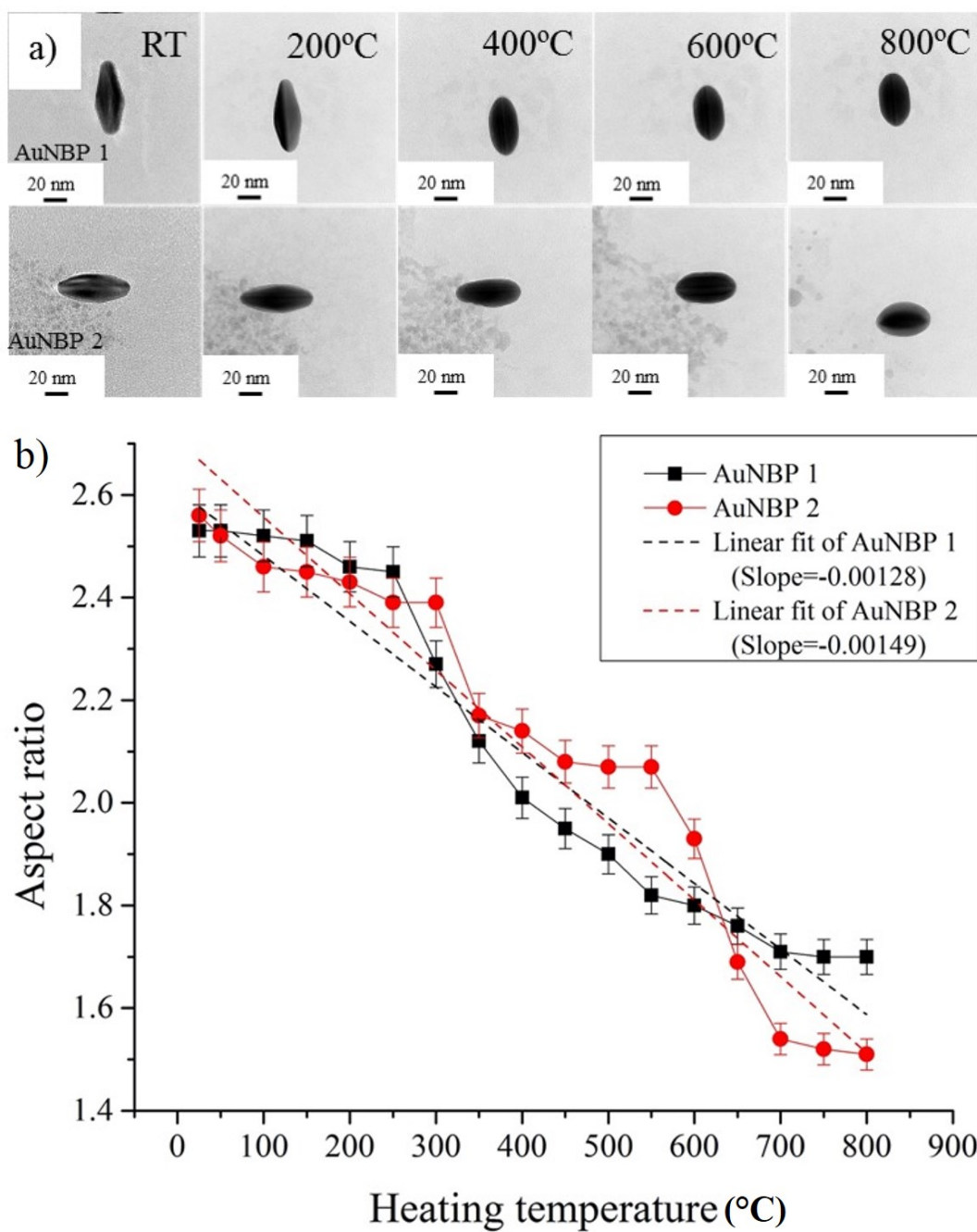


Figure 6-5: a) TEM micrographs of CTAB-capped AuNBPs at different heating temperatures: RT, 200°C, 400°C, 600°C and 800°C; b) The change in AR with heating temperature for two different AuNBPs with an AR of about 2.5 (length 67.5 nm and width 26.6 nm)

CTAC-stabilized Au nanotriangles (AuNTs)

The thermal stability of AuNTs was also explored. TEM images of three AuNTs with different initial edge lengths of 104.6nm, 83 nm and 69.2 nm at different temperatures revealed a structural change from triangular plates to more spherical structures. The rate of change in edge length dimension of the AuNTs with respect to temperature increases with increasing heating temperature, as illustrated in figure 6-6. However, the evolution from a triangle to a sphere is relatively constant up to ca. 800; different sized AuNTs behaved in a similar way. However, at higher temperatures, a significant change was first observed for the smallest triangle (edge length ~ 69.2 nm), similar to the result reported by Kan and co-workers [23]. Reconstruction of the sharp tip to become more rounded occurred first, followed by redeposition in the middle of the edge and finally transformation to a sphere at a temperature above 1000. Larger AuNTs showed a slightly lower rate of change (at lower temperatures) due to the lower surface area to volume ratio. This implies that AuNTs are stable under working temperatures up to ca. < 700-800 , depending on the size of AuNT.

Fast-ramp heating

Fast-ramp thermal heating experiments were performed by increasing the temperature from room temperature to 900 within a time period of 2 seconds. TEM micrographs before and after fast-ramp heating are shown in Figure 6-7 and showed structural changes in AuNRs and AuNPs similar to those observed at lower heating rates. For example, the AuNR in figure 6-7, which has initial AR of about 4.6, decreases to a final AR of about 2 at 900. This result is similar to those obtained when using much slower heating presented in figure 6-4b. AuNPs deformed to become more rounded morphologies while AuNRs decreased in AR and became spherical. This rapid heating experiment was designed to have a heating rate and duration time more similar to that experienced during photothermal irradiation and it confirms that the heating temperature is the dominant influence rather than the ramp rate and the duration of heating time, in agreement with literature [19, 24].

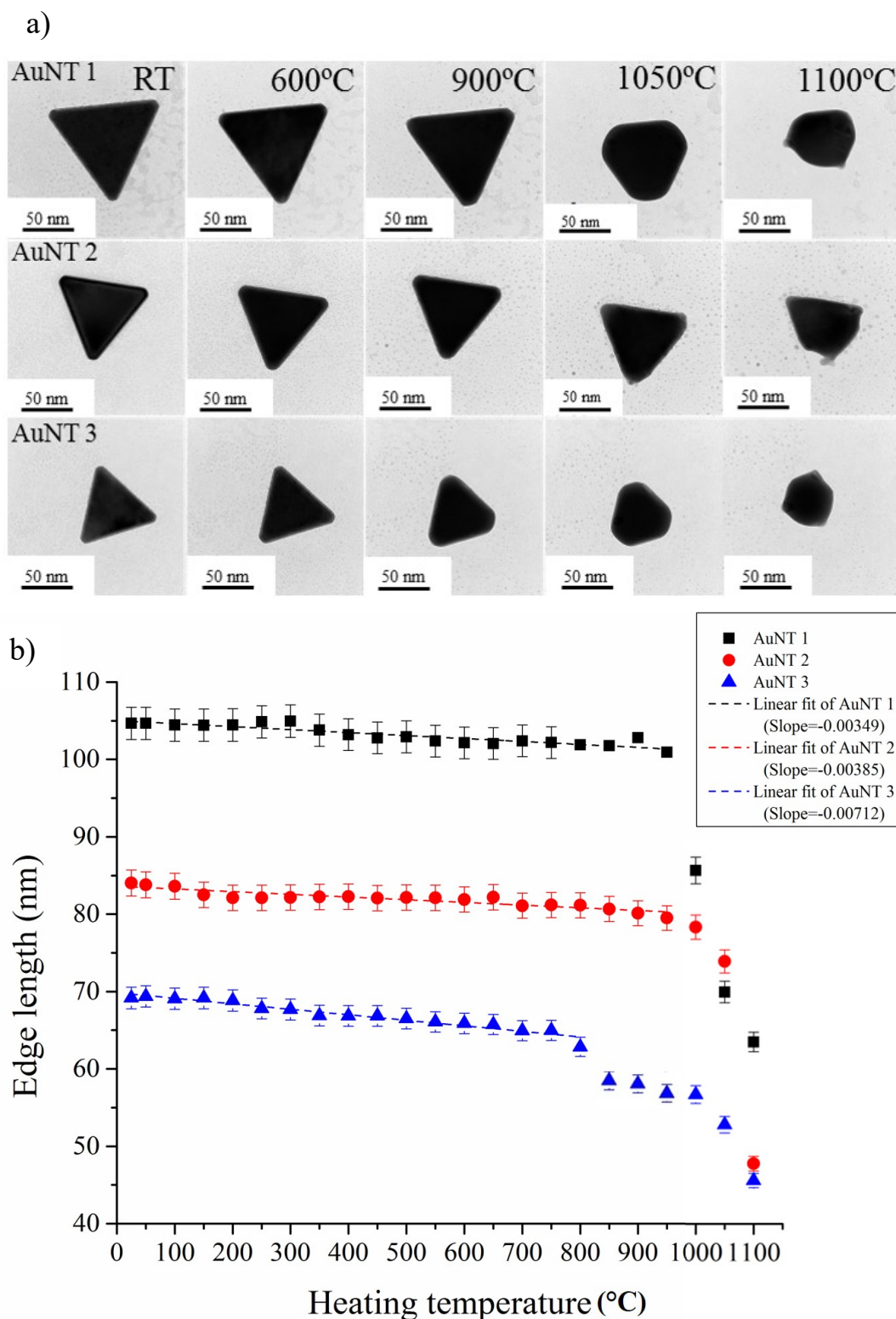


Figure 6-6: a) TEM micrographs of CTAC-stabilized AuNTs at different heating temperatures: RT, 600°C, 900°C, 1050°C and 1100°C; b) The change in edge length with heating temperature for AuNTs with initial edge lengths of 104.6 nm (black), 83.0 nm (red), and 69.2 nm (blue).

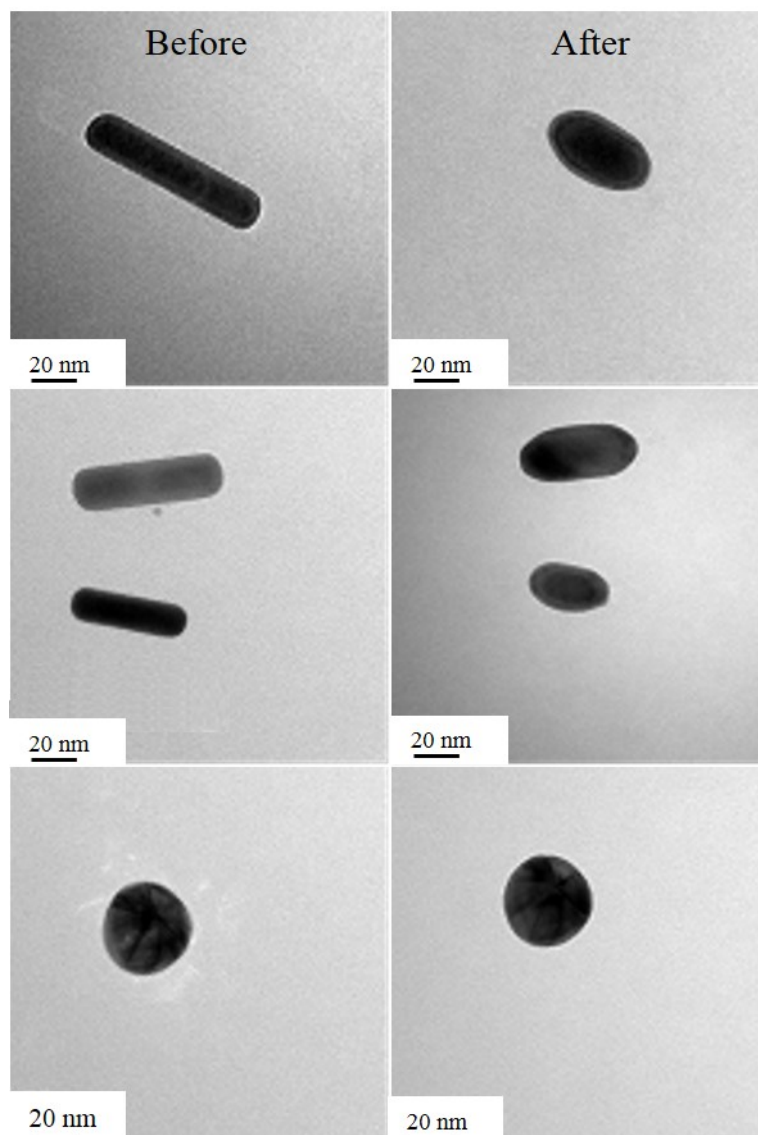


Figure 6–7: Example of TEM images of fast ramp, in-situ TEM heating experiments on AuNRs and AuNPs. The TEM micrograph before heating is shown on the left and after heating is presented on the right hand side.

6.2.2 The effect of surface modification on the thermal stability of Au nanostructures

In the previous section, it was seen that the thermal properties of Au nanostructures clearly depend on temperature in terms of their shape deformation. Different types of surface modification have been employed to provide promising properties for many applications of Au nanostructures. This experiment aims to reveal more understanding of effects of the coating on the thermal stability. The different surface modifications of AuNRs with PSS and silica were used to compare their thermal stability with those of solely CTAB-capped AuNRs. PSS-coated AuNRs with different ARs were examined using the same heat treatment as for CTAB-capped AuNRs. The rate of change of AR is extremely low for temperatures up to ca. 150, shown in figure 6-8. Above this temperature there was a slower deformation than for

CTAB-capped AuNRs, with only a gradual decrease in AR. At ca. 800, with increasing temperature there was a significant change in shape of PSS-capped AuNRs, with them ultimately reaching a final spherical shape. The additional PSS layer may hinder surface diffusion and hence deformation.

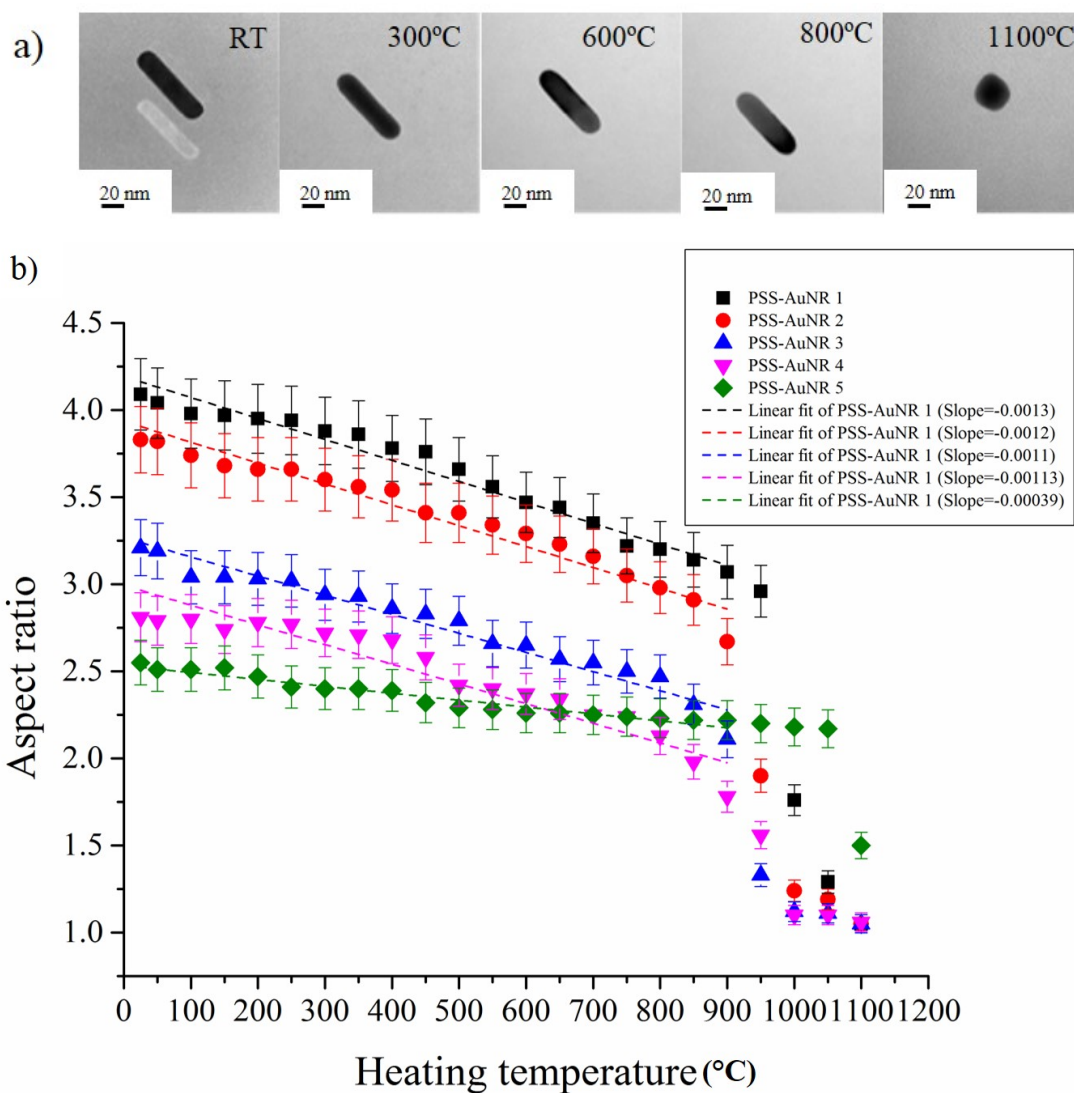


Figure 6–8: a) TEM micrographs of PSS-coated AuNRs with an AR of 3.83 (rod 2) at different temperatures: RT, 300°C, 600°C, 800°C and 1100°C; b) The change in AR with temperature and associated linear fits for different AR rods. Note: The change in dark blue graph is taken from AuNPs heat treatment.

In order to compare the effect of surface modification further, in-situ TEM heating of the silica-coated AuNRs was performed. Figure 6-9a shows that there is relatively constant rate of change of the rod AR with temperature. As expected, the silica-coated surface with a higher melting point (silica melting point is 1710) can retain the rod shape over a larger range of heat treatment. Indeed, silica AuNRs retained their original AR up to ca. 300 before any reshaping was observed. The AR of the silica-coated rods then slightly decreased with increasing temperature up to 800. More significant changes were noticed at a temperature of 1100. For example, the silica-coated AuNR sample with an AR of 3.1 changed to an AR of 2.9 and 2.5 at 800 and 1100, respectively. Even when the temperature was higher than the melting point of bulk gold (1064), the silica-coated AuNRs showed little deformation in AR and retained a rod-shaped morphology. At lower temperatures where the rod-like morphology remains with little or no change in AR, there was a decrease in the thickness of the silica coating from 4.6 nm to 3.6 nm (as measured directly from figure 6-9a). During the heat treatment, a structural rearrangement within the silica coating was observed. The rearrangement of silica could occur at the glass transition temperature (the state between a glass and a supercooled liquid) of amorphous silica [25, 26], resulting in a slight decrease in AR. The heat treatment profiles of silica-coated AuNRs are presented in figure 6-9b. Furthermore, Table 6-1 summarises the rate of change of AR with respect to temperature of all Au nanostructures. It was found that higher rates of change were observed in AuNR with high ARs and the smallest size such as NR diameter (e.g. AuNR 4) and smallest triangles. For a direct comparison, AuNRs with an AR of about 4.2 were selected for CTAB and PSS coating. The results showed that the rate of change of AR with temperature for CTAB-capped AuNRs (slope = 0.00196 K^{-1}) was slightly higher than that for PSS-capped AuNRs (slope = 0.0013 K^{-1}). The rate of change was significantly decreased for silica-coated rods.

Overall these results indicate that the deformation of Au nanostructures is strongly dependent on heating temperature. The rate of change of the morphology is enhanced at higher temperatures, and results in rapid deformation at temperatures >800 . The duration of heating is not that significant for the rate of change, but needs to be considered. However, the surface coating of Au nanostructures also has a dominant influence on surface diffusion depending on the type of coating and its inherent thermal stability.

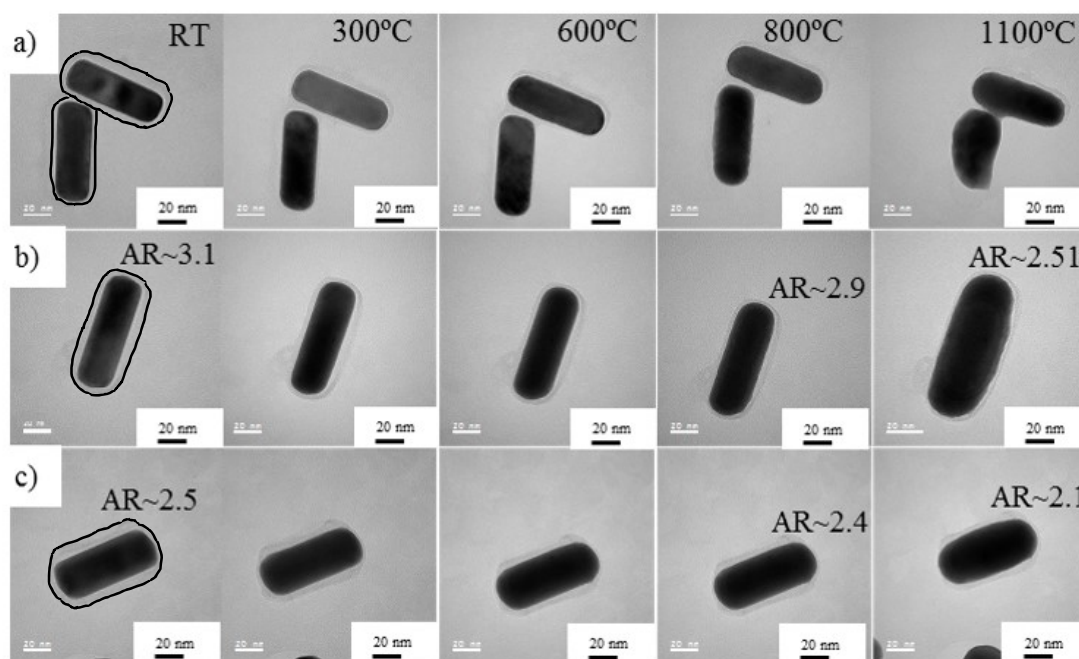


Figure 6-9: a) Examples of TEM micrographs from in-situ TEM heating experiment on silica-coated AuNRs at different temperatures: RT, 300°C, 600°C, 800°C and 1100°C. (Note: The black drawings in the RT images on the LHS were used as the guidelines for silica coating for all heated AuNRs)

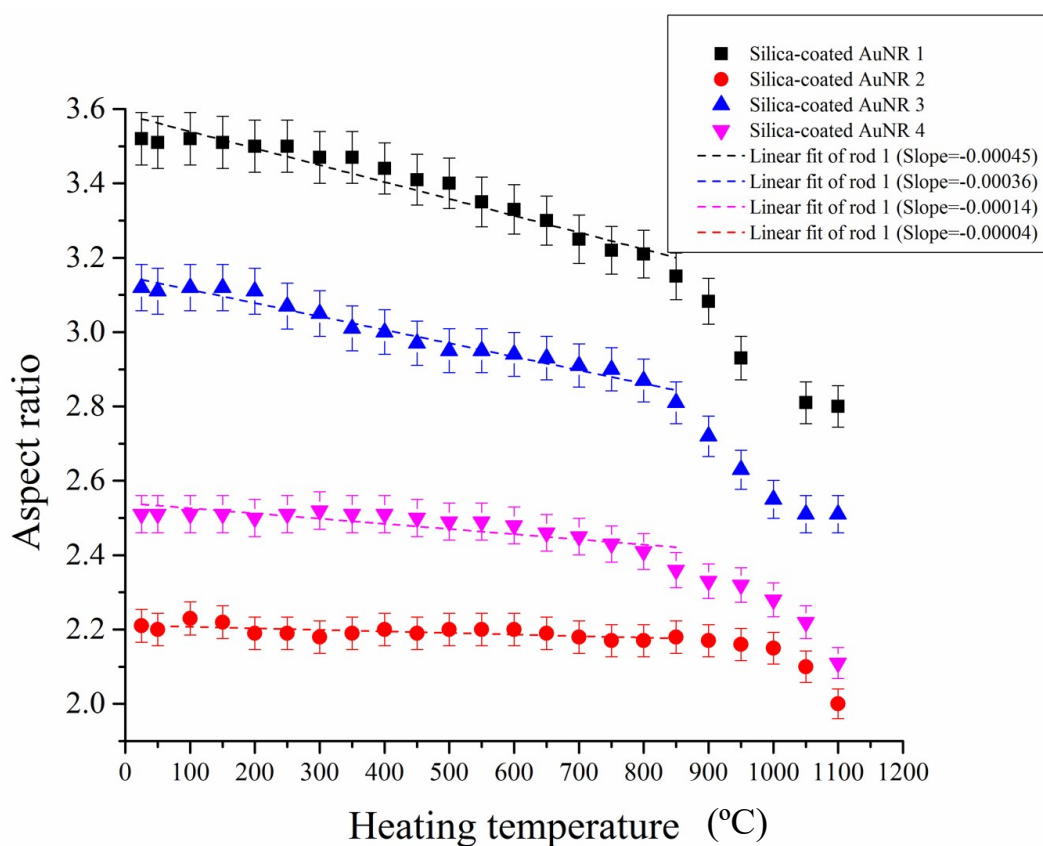


Figure 6-9: b) The change in AR with temperature and associated linear fits for different silica-coated AR rods

6.2.3 Thermal deformation mechanism

Low temperature in-situ TEM heating experiments

The thermal transformation mechanism of rods was revealed by heating at lower temperatures for prolonged time periods. Based on the results in figures 6-4 and 6-5, the heating temperature was chosen to be 100°C and 150°C for AuNRs and 250°C for AuNBPs with a heating time of 15 min in order to investigate the thermal deformation behaviour. The data showed good agreement with the literature [20, 24]. Atoms from the tip rearranged and redeposited towards the middle part of AuNR, which showed a surface roughening in figure 6-10a. As the temperature was increased, the rate of change of AR with respect to temperature increased to form a shorter AR AuNR (figure 6-10b). A similar behaviour was found in heat treatment of AuNBPs, as illustrated in figure 6-10c). Although NBPs appeared more thermally stable compared to the NRs, the data suggest that only surface atoms can move and rearrange by surface diffusion at these temperatures to produce shorter and wider AuNBPs.

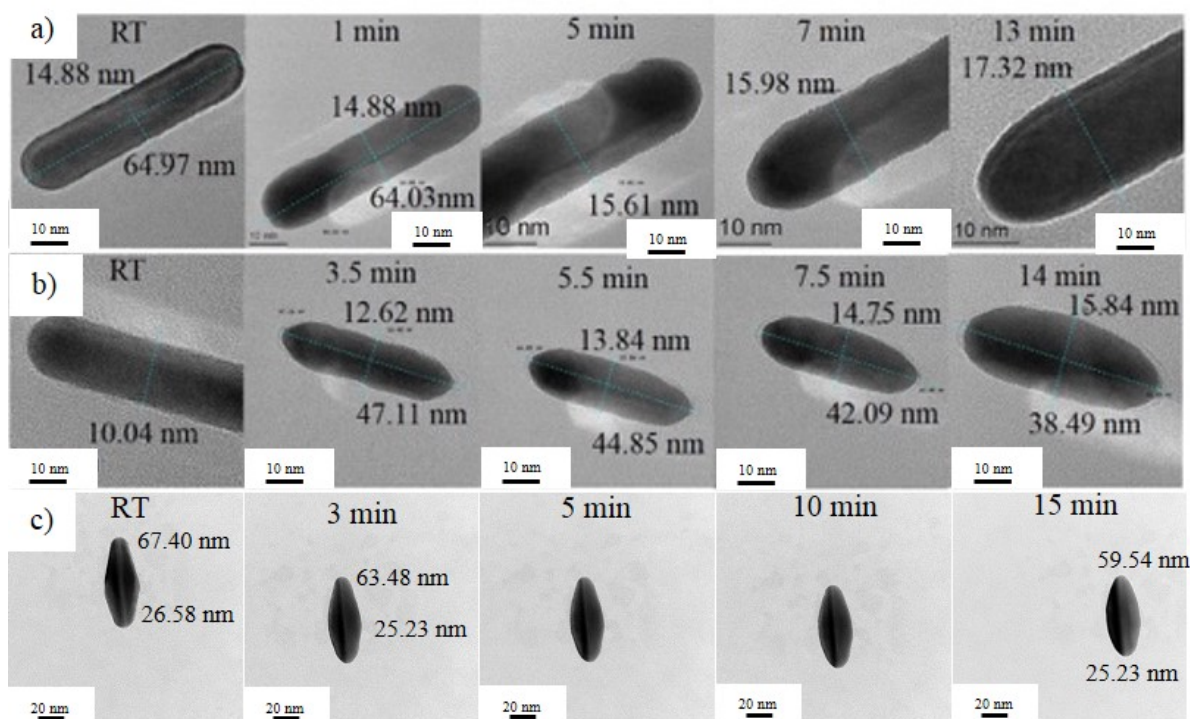


Figure 6–10: TEM images of AuNRs from in-situ TEM heating experiments at low temperature: a) 100 °C and b) 150 °C for 15 mins, illustrating surface melting starting from tip and redeposition in the middle of the rods. (c) TEM micrograph of an AuNBP during heat treatment at 250 °C for 15 mins, showing similar behaviour to the results from the AuNRs.

For the general case of a planar surface, surface diffusion is usually accepted to begin becoming significant at a few hundred degrees below the bulk melting point [27-30] and/or at some fraction of the bulk melting temperature; estimates vary but range between 0.3-0.5 of the bulk melting point [31]. The melting point of bulk gold is 1064°C and according to the seminal work of Buffat et al. [32], depression of the melting point of gold nanoparticles only occurs for particle sizes < 10nm. We can estimate the radius of curvature at the end of the nanorods, from the end diameter giving 14.88 and 10.04 nm in figures 6-10a) and 6-10b) respectively. Hence, we might expect that melting point depression is relatively insignificant and surface diffusion would only become important at temperatures of the order of 300-400 °C. However, for the AuNRs surface diffusion is evident at much lower temperatures and we believe that this is promoted by the curved surface at the tips of the rods [19].

This results reveal evidence for surface melting and more importantly surface diffusion at temperatures much lower than the melting point of bulk gold, arising from the increased surface energy for a curved surface [17, 20, 24]. Surface diffusion of Au atoms is more significant at the tip with a higher radius of curvature, relative to the middle of the rod, where there is a lower curvature of the surface. Taylor et al. [19] have proposed that curvature at the tip of the nanorod is dependent on both rod AR and rod length. The activation energy for surface diffusion is an inverse function of the tip curvature and therefore the surface diffusion coefficient depends strongly on both the rod aspect ratio and rod length. This is therefore curvature driven surface diffusion.

6.3 Conclusions

Structural deformation of Au nanostructures is controlled predominantly by the heating temperature, with the heating duration and heating ramp rate being much less significant. The deformation mechanism during thermal heating results from atom diffusion from sharpest part (tips) towards the middle parts which possess a lower radius of curvature. The higher the radius of curvature, such as in high AR rods and at sharp tips of nanotriangles, the more reactive and easier it is to deform. Thus, the thermal stability of both AuNRs and AuNBPs decrease as their AR increases. The thermal stability of Au nanostructures can be categorized from the most stable to least stable as follows: AuNPs > AuNTs > AuNBPs > AuNRs. However, the thermal stability can also be increased by tailoring the surface modification. In this case the stability is increased from CTAB-capped AuNRs to PSS-capped AuNRs and finally to silica-coated AuNRs. Additionally, the size and thickness of Au nanostructures also affect their deformation; the smaller and thinner particles appear to be more easier to reshape (e.g. CTAB-AuNR4) the morphology at lower temperatures as compared to the larger NPs (e.g. 104.6 nm CTAC-AuNT).

In-situ TEM heating experiments can directly investigate the mechanism of the morphology change during the heating of individual Au particles. These changes will have a significant impact on optical properties. Overall the studies have revealed the useful ranges of temperature, whereby heating does not significantly change optical properties, were up to 100°C, 200°C, 800°C, for CTAB-capped AuNRs, CTAB-capped AuNBP and CTAC-stabilized AuNTs, respectively. Surface modification could significantly enhance these usable ranges of temperature. This work provides guidance to select Au nanostructures with high thermal stabilities and stable optical properties in the NIR region that would be good candidates for nanomedical applications.

6.4 References

- [1] Chen, H., et al., *Gold nanorods and their plasmonic properties*. Chemical Society Reviews, 2013. **42**(7): p. 2679-2724.
- [2] Qin, Z., et al., *Quantitative Comparison of Photothermal Heat Generation between Gold Nanospheres and Nanorods*. Scientific Reports, 2016. **6**: p. 29836.
- [3] Nehl, C.L. and J.H. Hafner, *Shape-dependent plasmon resonances of gold nanoparticles*. Journal of Materials Chemistry, 2008. **18**(21): p. 2415-2419.
- [4] Baumann, V., et al., *Highly stable and biocompatible gold nanorod–DNA conjugates as NIR probes for ultrafast sequence-selective DNA melting*. RSC Advances, 2016. **6**(105): p. 103724-103739.
- [5] Murphy, C.J., et al., *Anisotropic Metal Nanoparticles: Synthesis, Assembly, and Optical Applications*. The Journal of Physical Chemistry B, 2005. **109**(29): p. 13857-13870.
- [6] Huang, X., S. Neretina, and M.A. El-Sayed, *Gold Nanorods: From Synthesis and Properties to Biological and Biomedical Applications*. Advanced Materials, 2009. **21**(48): p. 4880-4910.
- [7] Dickerson, E.B., et al., *Gold nanorod assisted near-infrared plasmonic photothermal therapy (PPTT) of squamous cell carcinoma in mice*. Cancer Letters, 2008. **269**(1): p. 57-66.
- [8] Haine, A.T. and T. Niidome, *Gold Nanorods as Nanodevices for Bioimaging, Photothermal Therapeutics, and Drug Delivery*. Chemical and Pharmaceutical Bulletin, 2017. **65**(7): p. 625-628.

- [9] Jang, B., et al., *Gold Nanorod–Photosensitizer Complex for Near-Infrared Fluorescence Imaging and Photodynamic/Photothermal Therapy In Vivo*. ACS Nano, 2011. **5**(2): p. 1086-1094.
- [10] Hainfeld, J.F., et al., *Infrared-transparent gold nanoparticles converted by tumors to infrared absorbers cure tumors in mice by photothermal therapy*. PloS one, 2014. **9**(2): p. e88414-e88414.
- [11] Jiang, K., D.A. Smith, and A. Pinchuk, *Size-Dependent Photothermal Conversion Efficiencies of Plasmonically Heated Gold Nanoparticles*. The Journal of Physical Chemistry C, 2013. **117**(51): p. 27073-27080.
- [12] Petrova, H., et al., *On the temperature stability of gold nanorods: comparison between thermal and ultrafast laser-induced heating*. Physical Chemistry Chemical Physics, 2006. **8**(7): p. 814-821.
- [13] Link, S., et al., *Laser-Induced Shape Changes of Colloidal Gold Nanorods Using Femtosecond and Nanosecond Laser Pulses*. The Journal of Physical Chemistry B, 2000. **104**(26): p. 6152-6163.
- [14] Harris-Birtill, D., et al., *Gold nanorod reshaping in vitro and in vivo using a continuous wave laser*. PLOS ONE, 2017. **12**(10): p. e0185990.
- [15] Fales, A.M., et al., *Pulsed laser damage of gold nanorods in turbid media and its impact on multi-spectral photoacoustic imaging*. Biomedical optics express, 2019. **10**(4): p. 1919-1934.
- [16] Kalies, S., et al., *Investigation of Biophysical Mechanisms in Gold Nanoparticle Mediated Laser Manipulation of Cells Using a Multimodal Holographic and Fluorescence Imaging Setup*. PLOS ONE, 2015. **10**(4): p. e0124052.
- [17] Inasawa, S., M. Sugiyama, and Y. Yamaguchi, *Laser-Induced Shape Transformation of Gold Nanoparticles below the Melting Point: The Effect of Surface Melting*. The Journal of Physical Chemistry B, 2005. **109**(8): p. 3104-3111.
- [18] Brann, T., et al., *Gold Nanoplates as Cancer-Targeted Photothermal Actuators for Drug Delivery and Triggered Release*. Journal of Nanomaterials, 2016. **2016**: p. 11.
- [19] Taylor, A.B., A.M. Siddiquee, and J.W.M. Chon, *Below Melting Point Photothermal Reshaping of Single Gold Nanorods Driven by Surface Diffusion*. ACS Nano, 2014. **8**(12): p. 12071-12079.

- [20] Zou, R., et al., *Thermal stability of gold nanorods in an aqueous solution*. Colloids and Surfaces A: Physicochemical and Engineering Aspects, 2010. **372**(1): p. 177-181.
- [21] Jana, N.R., et al., *Anisotropic Chemical Reactivity of Gold Spheroids and Nanorods*. Langmuir, 2002. **18**(3): p. 922-927.
- [22] Albrecht, W., et al., *Impact of the electron beam on the thermal stability of gold nanorods studied by environmental transmission electron microscopy*. Ultramicroscopy, 2018. **193**: p. 97-103.
- [23] Kan, C., et al., *Structure and thermal stability of gold nanoplates*. Applied Physics Letters, 2006. **88**(7): p. 071904.
- [24] Vanrompay, H., et al., *3D characterization of heat-induced morphological changes of Au nanostars by fast in situ electron tomography*. Nanoscale, 2018. **10**(48): p. 22792-22801.
- [25] Ebnesajjad, S., *Introduction to Plastics*, in *Chemical Resistance of Commodity Thermoplastics*, E. Baur, K. Ruhrberg, and W. Woishnis, Editors. 2016, William Andrew Publishing. p. xiii-xxv.
- [26] Ojovan, M.I., *Viscosity and Glass Transition in Amorphous Oxides*. Advances in Condensed Matter Physics, 2008. **2008**: p. 23.
- [27] Dash, J. G., *Surface melting*. Contemporary Physics, 1989. 30(2): p. 89-100.
- [28] Heyraud, J.C., J.J. Métois, and J.M. Bermond., *Surface melting and equilibrium shape; the case of Pb on graphite*. Journal of Crystal Growth, 1989. 98(3): p. 355-362.
- [29] Inasawa, S., M. Sugiyama., and Y. Yamaguchi., *Laser-Induced Shape Transformation of Gold Nanoparticles below the Melting Point: The Effect of Surface Melting*. The Journal of Physical Chemistry B, 2005. **109**(8): p. 3104-3111.
- [30] Schlexer, P., et al., *Size-Dependence of the Melting Temperature of Individual Au Nanoparticles*. Part. Part. Syst. Charact, 2019. 36: p. 1800480
- [31] Wang., Z., L., et al., *Shape Transformation and Surface Melting of Cubic and Tetrahedral Platinum Nanocrystals*. The Journal of Physical Chemistry B, 1998. 102(32): p. 6145-6151.
- [32] Buffat, P. and J.P. Borel, *Size effect on the melting temperature of gold particles*. Physical Review A, 1976. 13(6): p. 2287-2298.

Chapter 7 Interaction of gold nanostructures with a model phospholipid monolayer membrane

Engineered gold nanostructures are candidates for use in biological applications such as thermotherapy and imaging, however there remain concerns about their use in relation to their bio-activity and environmental impacts which may result in toxicity [1-3]. Research on nanoparticle-cell membrane interactions have been intensively carried out in order to investigate nanoparticle toxicity. In previous studies, a model membrane system based on dioleoyl-phosphatidylcholine (DOPC) on a mercury (Hg) film electrode has been developed and designed for investigating phospholipid membrane interactions with both molecular species and also nanoparticles [4]. This model system takes advantage of simplicity and a close structural similarity to biological membranes. The smooth surface of the Hg electrode can minimize the effect of phospholipid layer properties compared to other solid electrodes. Also, the monolayer membrane on the Hg surface can initiate interaction at the phospholipid/water interface in a similar fashion to the assembled bilayer in biological membranes. The model system has been shown to provide similar results to peptide-phospholipid [5] and cholesterol-phospholipid interactions [6] using the classical free-standing bilayer and vesicle biomembrane models.

At present, due to the synthesis of Au nanostructures involving surfactants acting as structural guides, for example, the use of CTAB in AuNRs (where free excess CTAB is known to cause membrane disruption and hence toxicity), a study of the interaction of gold nanostructures with phospholipid membranes would help to provide understanding of the use of these particles in biological applications so as to avoid any toxic event. The interaction of gold nanoparticles with the simple DOPC membrane can be investigated using the current response during rapid cyclic voltammetry (RCV) by monitoring both the shift in potential and suppression of the voltammetric peaks associated with phase changes in the phospholipid monolayer. RCV measurements show consecutive capacitance current peaks representing phase transitions of the lipid layer corresponding to a fast negative followed by a fast-positive voltage ramp. The interaction of nanoparticles with the membrane presents as a depression in these capacitance current peaks arising from negative potential-induced phospholipid phase transitions [7, 8]. On the other hand, an increase in the capacitance current base line shows the penetration of nanoparticles into the DOPC layers [7]. In this chapter the interaction of the synthesized Au nanostructures with a model biomembrane is studied using RCV. This

study was intended to investigate the relationship between both the surface coating and the morphology of Au nanostructures on biomembrane activity.

7.1 Experimental procedure

7.1.1 Preparation of gold nanostructures

All gold nanostructures including citrate-stabilized AuNPs, CTAB capped AuNRs, PSS-capped AuNRs and CTAC stabilized AuNTs were freshly synthesised via the wet chemical synthesis protocols described in chapter 3.

7.1.2 Materials characterization

All gold nanostructures were centrifuged and redispersed twice to remove the excess surfactant before further characterization using UV-vis spectroscopy, TEM and DLS (detailed in chapter 3). Before investigating the nanoparticle interaction with the phospholipid membrane, all gold nanoparticles were kept as dispersions and were redispersed using ultrasonication before use. The mass of Au in 1 ml of the dispersion was determined by centrifugation, removal of the supernatant, drying and then weighing the resultant residue (assuming solely gold) to provide an approximate concentration of the original dispersion. The synthesized Au nanostructures are summarized in table 7-1. Citrate stabilized AuNPs with diameters of approximately 20.9, 36.6, and 58.3 nm denoted as samples Citrate-AuNP1, Citrate-AuNP2, and Citrate-AuNP3, respectively were tested. CTAB-capped AuNRs and PSS-capped AuNRs with similar ARs of 1.6, 3.1, and 3.5 were also tested and denoted as CTAB-AuNR1, CTAB-AuNR2, CTAB-AuNR3, PSS-AuNR1, PSS-AuNR2, and PSS-AuNR3, respectively. Finally, CTAC stabilized AuNTs (CTAC-AuNT) with an edge length of about 99.8 nm were tested. 1,2-dioleoyl-sn-glycero-3-phosphocholine (DOPC) with >99% purity was purchased from Avanti polar lipids. Analytical grade KCl, NaOH and KNO₃ were purchased from Sigma-Aldrich to make the electrolyte buffer. Phosphate buffered saline (PBS) consisted of 0.1 mol.dm⁻³ KCl and 0.01 mol.dm⁻³ phosphate in Milli-Q water (ionic strength of 0.125 mol.dm⁻³). All solutions were magnetically stirred and purged with argon before investigating in the flow system.

Table 7-1: Characteristics of the Au nanostructures tested using RCV

Sample	Sample name	Surfactant	DLS size distribution (nm)	Approximate concentration (mmol.dm⁻³)	TEM Size (nm)
AuNP	Citrate-AuNP1	Citrate	15.7	2.5	20.92.7
	Citrate-AuNP2	Citrate	37.8	2.8	36.65.0
	Citrate-AuNP3	Citrate	58.8	3.2	58.36.5
AuNR	CTAB-AuNR1	CTAB	11.7	17.2	AR~1.60.3 Length/width 36.4.2/22.53.3
	CTAB-AuNR2	CTAB	28.2	18.4	AR~3.10.6 52.65.0/17.62.6
	CTAB-AuNR3	CTAB	28.2	10.6	AR~3.50.7 56.27.1/16.22.5
	PSS-AuNR1	PSS	43.8	14.7	AR~1.60.3 36.4.2/22.53.3
	PSS-AuNR2	PSS	78.8	14.2	AR~3.10.6 52.65.0/17.62.6
	PSS-AuNR3	PSS	91.3	15.8	AR~3.50.7 56.27.1/16.22.5
AuNT	CTAC-AuNT	CTAC	78.8	33.5	Edge length ~ 99.824.4

7.1.3 Electrochemical flow system

The electrochemical testing flow system used in this thesis has been previously developed and described in the literature [1, 7, 9], and is shown in figure 7-1. The experiment was conducted in collaboration with Prof. Andrew Nelson's group in the School of Chemistry, University of Leeds. In brief, the RCV testing system consists of: 1) a flow cell containing the Hg electrode; 2) an electrolyte (PBS) buffer; 3) a sample cell for loading 1 mL of gold nanostructure dispersion; 4) a DOPC injection system; and 5) a peristaltic pump and switching valves. All parts were connected by Teflon and silicone rubber tubing. The flow system apparatus has four different settings as follows:

1. Electrolyte buffer is injected from the electrolyte reservoir cell and discharged to waste after passing through the flow cell;
2. Electrolyte buffer is injected from the reservoir and fills the sample cell;
3. Electrolyte buffer is injected from the sample cell and discharged to waste after passing through flow cell;
4. Electrolyte buffer is injected from sample cell to the flow cell and re-enters into the sample cell via a recycling loop after passing through the flow cell.

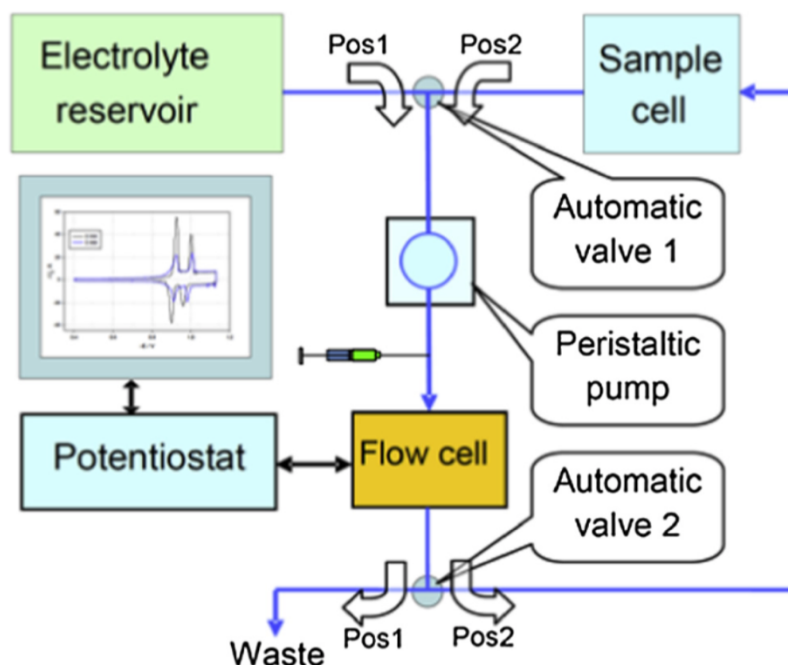


Figure 7-1: Schematic diagram of the electrochemical flow system (figure taken from Ref. [1])

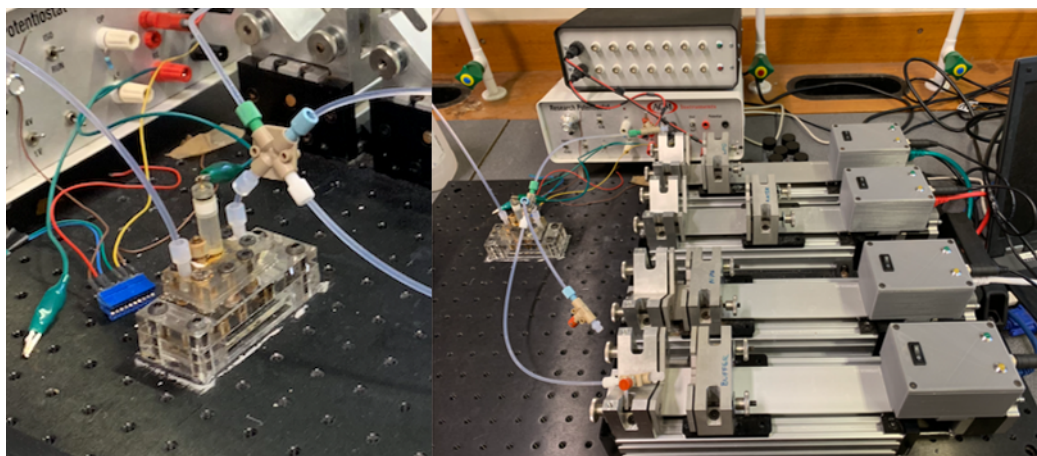


Figure 7–2: Images of the experimental set up: a) flow cell and b) sample and electrolyte loading platform.

The RCV test was started by drawing PBS into the system. Then 300 μL of $0.125 \text{ mol}\cdot\text{dm}^{-3}$ DOPC was injected at a rate of $1.0 \mu\text{L}/\text{min}$ applying RCV from -0.4 to -3.0 V at 80 V/s . After the DOPC membrane formed and the voltammetric peaks appeared, RCV was restarted at an excursion voltage of -0.4 to -1.625 V . Then, the Au nanostructure dispersion (the sample) was released into the system with a flow rate of $1.0 \mu\text{L}/\text{min}$ and the DOPC-coated electrode was exposed to the nanoparticles for approximately 30 sec. To measure the interaction, PBS buffer was then introduced instead of the sample and the electrode was measured by RCV from -0.4 to -1.8 at 40 V/s . Then the RCV was terminated and the flow system was cleaned using the electrolyte. Then RCV was started again from -0.4 to -3.0 V at 80 V/s in order to clean the Hg electrode. At this point all voltammetric peaks disappeared illustrating that the monolayer DOPC was completely removed. The DOPC can then be re-deposited and the whole RCV experiment repeated by following these steps.

7.2 Results and discussion

The DLS size distribution of all samples is summarized in figure 7-3. As discussed in chapter 4, it was found that only the spherical AuNP sample results could be considered reliable due to the fact that it is only in this case that the hydrodynamic radius from DLS measurement directly reflects the particle size distribution. In chapter 4, DLS measurements were presented in figures 4-2 and 4-13 for citrate-stabilized AuNPs and CTAC-stabilized AuNTs, respectively. It was shown that the citrate-AuNP1 and citrate-AuNP3 samples were homogenous with hydrodynamic radius values of 15.7 and 58.8 nm. This is in a good agreement with TEM micrographs presented in chapter 4, section 4.1. The average particle sizes from TEM were ca. 20.9, 36.6, and 58.3 nm for citrate-AuNP1, 2, 3, respectively. While the DLS measurement of CTAC-AuNT was 78.8 nm, TEM imaging showed an average edge length of about 99.8 nm (see section 4.4). Figure 4-13 showed that there was evidence for

AuNT agglomeration. Lastly, the DLS results from the AuNR samples (illustrated in figure 7-3) indicated that they had high uniformity and were relatively monodispersed. However CTAB-AuNRs presented significant differences from the DLS results of similar samples presented in figure 4-8. DLS showed a relative decrease of the hydrodynamic radius, but this could be the effect of both rotational and translational diffusion which means that it is not straightforward to extract the me average hydrodynamic size due to the rod-shaped geometry. However, the results showed a relative increase of the hydrodynamic radius for PSS coated samples relative to CTAB coated AuNRs. This would imply that the layer of PSS deposits on top of the CTAB layer resulting in an increase in the value derived from the DLS measurement. This coating was also confirmed by Zeta potential measurements which showed a change from positively charged to negatively charged particles following PSS coating.

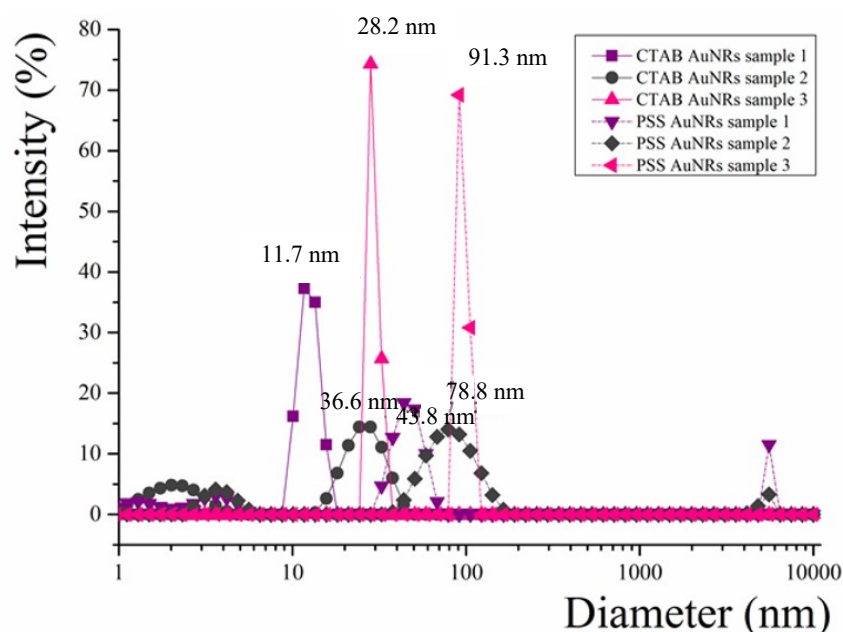


Figure 7-3: DLS particle size distributions of dispersions of CTAB-AuNRs and PSS AuNRs.

Following particle characterization, the electrochemical response induced by the Au nanostructures interacting with the phospholipid membrane were investigated. Figures 7-4 to 7-7 display the effect of the Au nanostructure dispersions on the RCV of the DOPC coated Hg electrode. The interaction of particles, such as particle absorption onto the DOPC surface can cause a depression of the capacitance current peaks. In the absence of nanoparticles, the RCV of the DOPC layer shows well defined voltammetric current peaks including peak 1 and 2, indicated by the blue lines in all the figures. Peak 1 is located at approximately -0.96 V and corresponds to defects in the DOPC monolayer, while growth and bilayer formation, involving structural reorientation of the DOPC monolayer on the Hg surface, is associated with the voltammetric peak at about -1.05 V denoted as peak 2 [7]. All Citrate-AuNP samples

showed a relatively insignificant interaction with the DOPC monolayer. The 2.5 mmol.dm^{-3} citrate-AuNP1 (figure 7-4a) particles with the smallest diameter of 20 nm presented the most interaction in terms of the depression of the capacitance current peak 1 on the RCV plot compared the larger AuNP samples (figure 7-4b and 7-4c). The peak degradation ratio in peak 1 (positive side) of citrate-AuNP1, 2, and 3 samples were 0.82, 0.83 and 0.87, respectively.

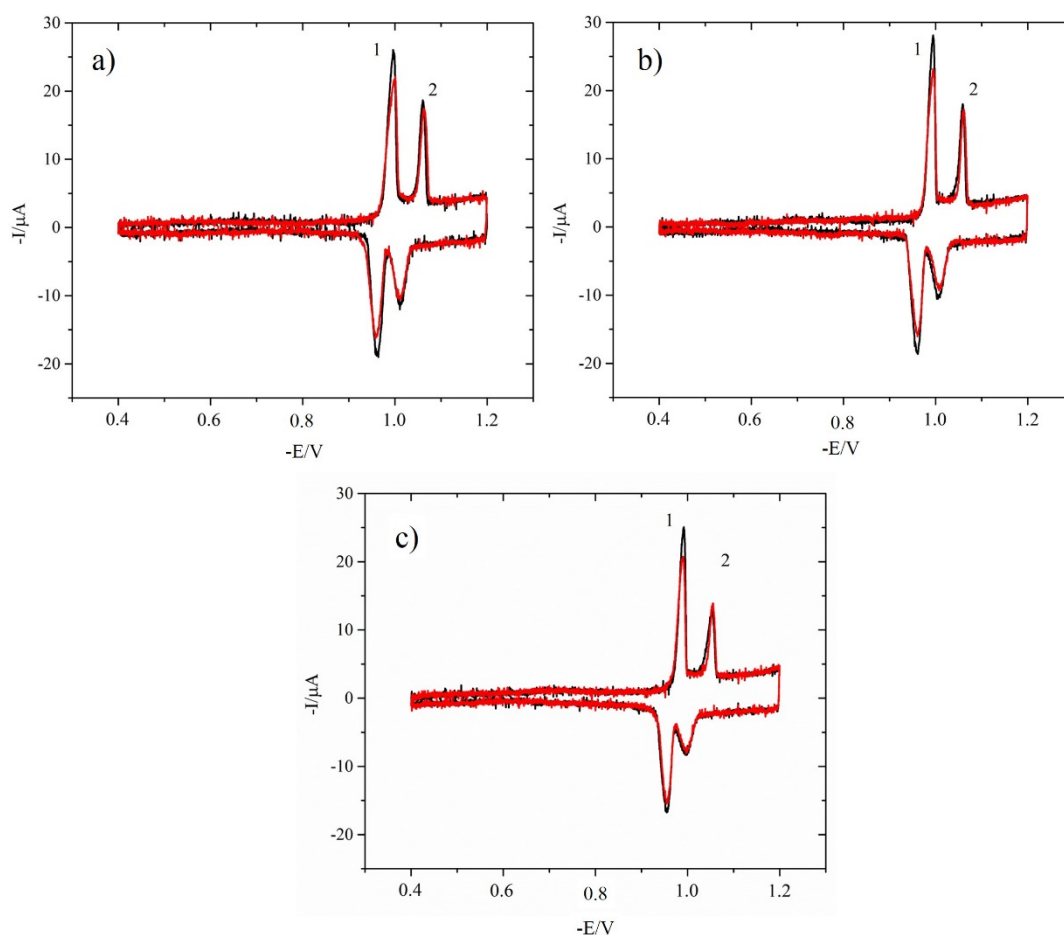


Figure 7-4: RCV of DOPC coated on an Hg electrode in 0.1 mol.dm^{-3} PBS before (black line) and after (red line) exposure to: a) 2.5 mmol.dm^{-3} citrate-AuNP1 with particle size $d \sim 20.9 \text{ nm}$; b) 2.8 mmol.dm^{-3} citrate-AuNP2 with $d \sim 36.6 \text{ nm}$; c) 3.2 mmol.dm^{-3} citrate-AuNP3 with $d \sim 58.3 \text{ nm}$.

Similar results for commercial citrate stabilized AuNPs (albeit at lower concentrations) have been reported in by William et al. [11], presented in figure 7-5. The results in figures 7-5a and 7-5b suggested that $0.03 \text{ mmol.dm}^{-3}$ monodispersed 20 nm and 50 nm citrate-stabilized AuNPs (a commercial AuNP suspension) did not show significant interaction with the model phospholipid. However, for smaller 5 nm NPs, a much stronger interaction effect was apparent. Furthermore, they also reported that NP agglomeration considerably reduced the interaction with the model membrane. The in-house synthesised 50 nm diameter AuNPs ($0.27 \text{ mmol.dm}^{-3}$) showed less interaction compared to the highly monodisperse commercial 50-nm

AuNPs (see 7-5c). This was presumably due to the increased agglomeration in the former sample as measured by DLS. According to the literature [1, 7, 8, 9], only small particles with effective sizes of between 6-25 nm interact strongly with the DOPC coated electrode. These present results are in agreement with this hypothesis and they also illustrate that the citrate coating does not cause any appreciable interaction with the lipid membrane (see figure 7-5d) and so is useful for biological applications.

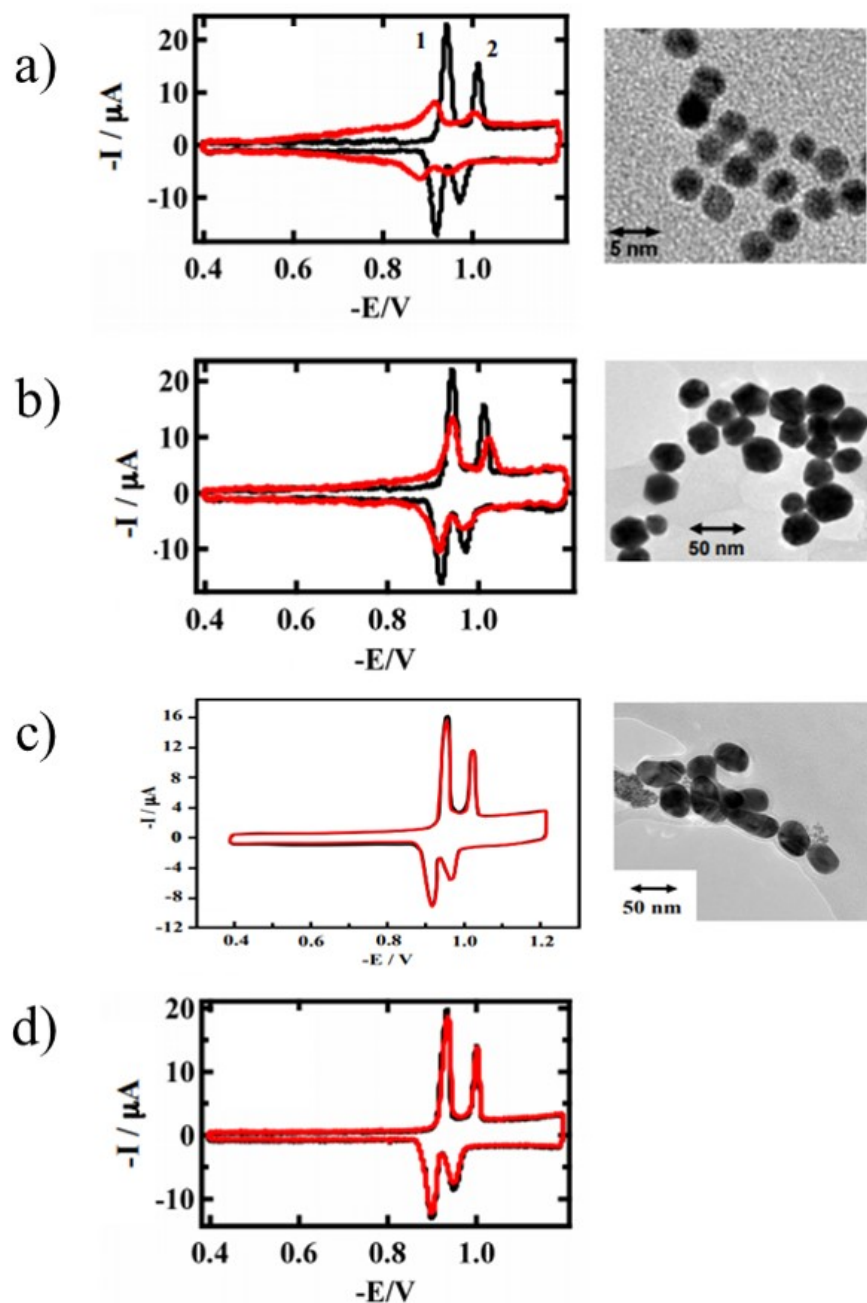


Figure 7-5: RCV of DOPC coated on an Hg electrode in 0.1 mol.dm^{-3} PBS before (black line) and after (red line) exposure to: a) $0.03 \text{ mmol.dm}^{-3}$ 5nm-commercial citrate-AuNP; b) $0.03 \text{ mmol.dm}^{-3}$ 50-nm-commercial-citrate-AuNP; c) $0.27 \text{ mmol.dm}^{-3}$ 50-nm-inhouse-citrate-AuNP; and d) pure citrate. [Figure taken from Ref. [11]]

In figure 7-6a, the influence of pure 0.2M CTAB was tested. This indicated complete interaction with the DOPC layer with the disappearance of all the capacitance current peaks. The increase in the baseline of the RCV plot indicates penetration into the DOPC monolayer and a direct interaction with the electrode [7]. After the centrifugation and redispersion cleaning process to remove free excess CTAB from the synthesized AuNR dispersion, the activity of the CTAB-capped AuNRs was decreased, as shown in figures 7-6b to 7-6d. However, figure 7-6b still indicates a relatively strong interaction of the $17.2 \text{ mmol.dm}^{-3}$ CTAB-capped AuNR1 sample with the DOPC monolayer. There is a suppression of potential peaks with a positive peak shift and the formation of a very wide depressed peak at about -0.96 V . The degradation of voltammetric peak 1 represents the nanoparticles interacting and binding with the DOPC layer. A similar result has been observed in the literature for the case of SiO_2 nanoparticles [7]. There was also a suppression of voltammetric peak 2 which resulted from the rapid absorption of the nanoparticles onto the DOPC head groups. The origin of this interaction is still unclear and whether it is affected by either the absorbed CTAB or the rod morphology and/or particle size. By considering the size of CTAB-AuNR1 ($L/W = 36.1/22.5 \text{ nm}$), it is considered to be in the range of active sizes for nanoparticles. However, the effect of CTAB appears to be the dominant factor when comparing the results with $18.4 \text{ mmol.dm}^{-3}$ CTAB-AuNR2 ($L/W = 52.6/17.6 \text{ nm}$) and $10.6 \text{ mmol.dm}^{-3}$ CTAB-AuNR3 ($L/W = 56.2/16.2 \text{ nm}$), shown in figures 7-6c and 7-6d. Thus, even after removing excess CTAB from the synthesized CTAB-capped AuNR dispersion, the effect of the surface absorbed CTAB remains significant and results in a strong interaction with the DOPC layer.

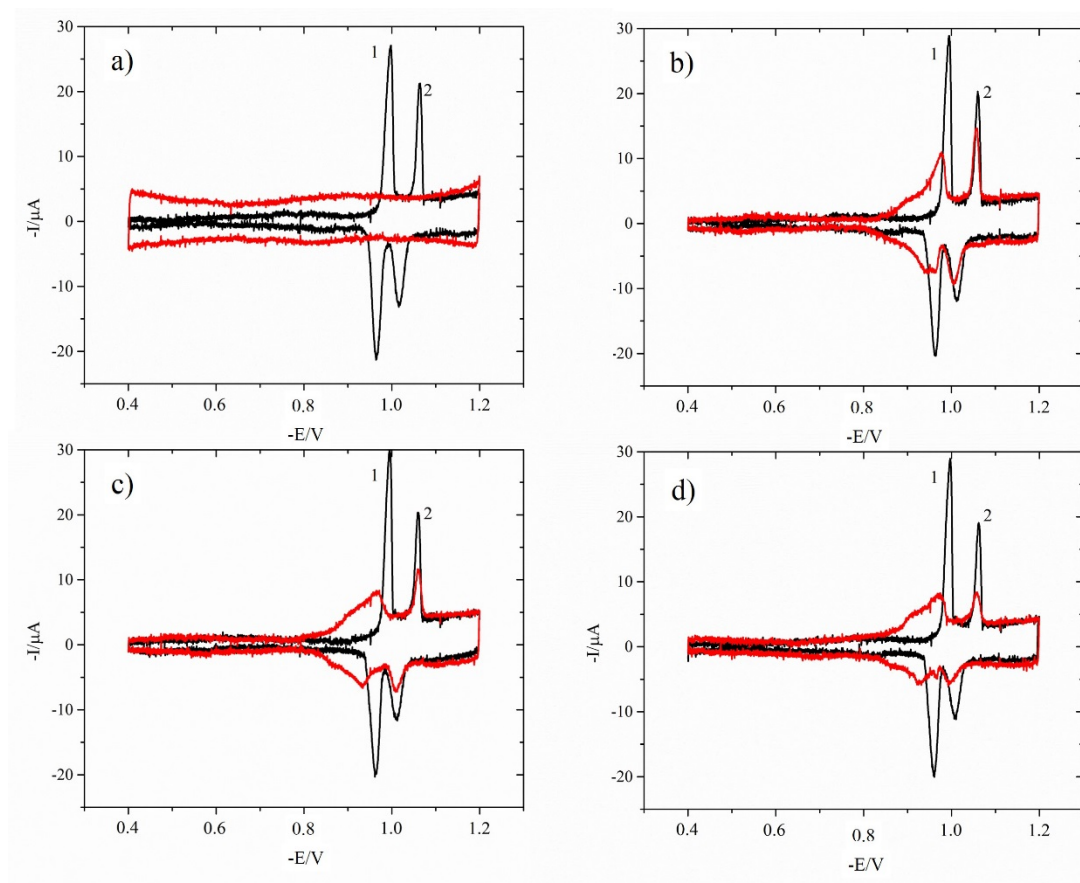


Figure 7-6: RCV of DOPC coated on an Hg electrode in 0.1 mol.dm^{-3} PBS before (black line) and after (red line) exposure to: a) pure 0.2 M CTAB; b) $17.2 \text{ mmol.dm}^{-3}$ CTAB-AuNR1 with an AR of 1.6; c) $18.4 \text{ mmol.dm}^{-3}$ CTAB-AuNR2 with AR of 3.1; and d) $10.6 \text{ mmol.dm}^{-3}$ CTAB-AuNR3 with AR of 3.5.

PSS-coating of CTAB-capped AuNRs was employed in order to address this issue around the toxicity of CTAB, as illustrated in figure 7-7. The purpose of the PSS coating was to encapsulate any surface adsorbed CTAB, so as to prevent exposure and provide non-toxicity for further use in biological applications. Figure 7-7a showed that a pure PSS solution interacts significantly with the DOPC monolayer, however, in relative terms the effect is smaller than that observed with CTAB-capped particles. The results indicated that the voltammetry peaks decreased in height with only one broad negative potential peak, with the other peak disappearing completely. This indicates that PSS was binding with the DOPC monolayer causing the degradation of the voltammetric peaks. The PSS-capped AuNRs showed a smaller interaction with the DOPC layer. The smaller size AuNRs with the concentration of $14.7 \text{ mmol.dm}^{-3}$ showed a broad peak between -0.85 to -0.95 V on the negative current side and also the capacitance current peaks were more degraded relative to the higher AR PSS-capped AuNRs. Overall, the PSS-capped AuNRs show more promise in terms of toxicity as less membrane interactions were detected in the RCV results.

The effect of CTAC-AuNTs ($33.5 \text{ mmol.dm}^{-3}$) was also studied, and is presented in figure 7-8. There was no significant interaction with the membrane arising from the CTAC surfactant and the triangular morphology of the particles. This may be because the triangles have a slightly larger edge length than the normal active size range of the nanoparticle-DOPC interaction.

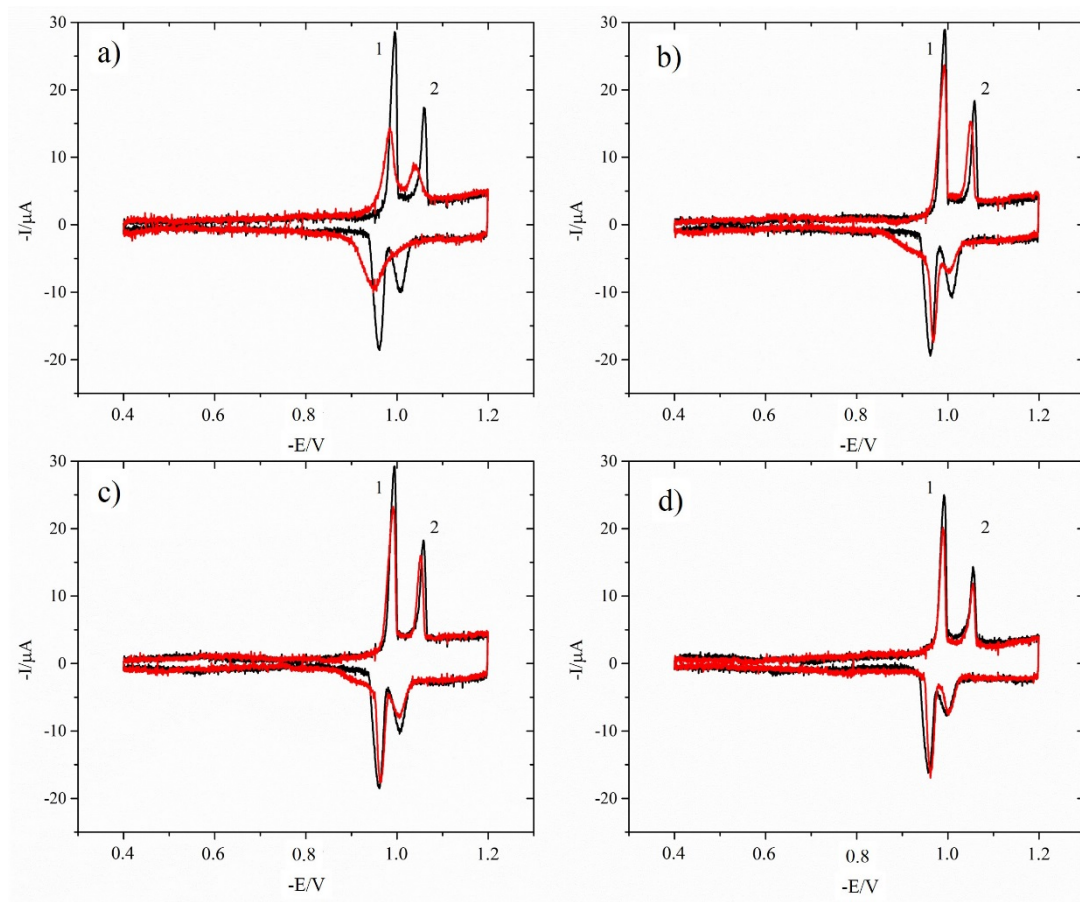


Figure 7-7: RCV of DOPC coated on an Hg electrode in 0.1 mol.dm^{-3} PBS before (black line) and after (red line) exposure to: a) pure $0.2\text{mg}/10\text{mL}$ DI water PSS; b) $14.7 \text{ mmol.dm}^{-3}$ PSS-AuNR1 with an AR of 1.6; c) $14.2 \text{ mmol.dm}^{-3}$ PSS-AuNR2 with AR of 3.1; and d) $15.8 \text{ mmol.dm}^{-3}$ PSS-AuNR3 with AR of 3.5.

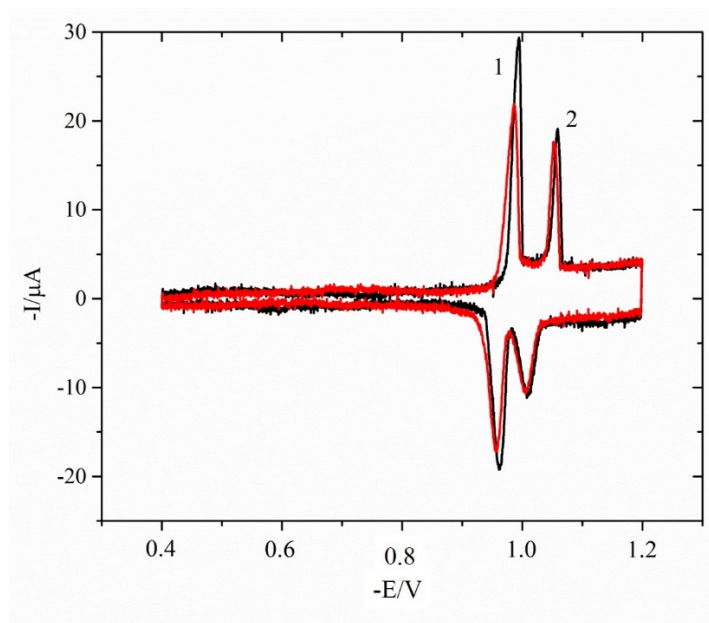


Figure 7-8: RCV of DOPC coated on an Hg electrode in 0.1 mol.dm^{-3} PBS before (black line) and after (red line) exposure to $33.5 \text{ mmol.dm}^{-3}$ CTAC-AuNTs with an edge length of 99.8 nm

For the case of AuNBPs, these were not tested owing to the purification problem, whereby the dispersions consisted of both spherical and bi-pyramidal particles. This complication could affect the evaluation of the results from the model membrane interaction studies.

Ignoring any effect due to the surface coating on the nanoparticle, the proposed model to describe interaction of nanoparticles with the phospholipid domains is based on previous work involving SiO_2 nanoparticles [7]. It considers the surface to volume ratio of the particles relative to an interfacial contact area with the membrane. This interfacial contact area parallel to the monolayer plane is the area of interaction and smaller diameter nanoparticles can adsorb onto the DOPC monolayer with high interfacial contact area compared to larger sized nanoparticles, as shown in figure 7-9. Thus smaller nanoparticles should have a stronger interaction with membrane, freezing the lipid phase transitions, and should result in increased suppression of the voltammetric current peaks in RCV associated with the DOPC monolayer. Also, the binding of these particles to the membrane can be affected by electrostatics, hydration and van der Waals forces. DOPC monolayers exhibit a positive surface potential [7, 12, 13]. In case of AuNRs, CTAB-capped AuNRs are positively charged particles which interact strongly with the DOPC surface, presumably because the electrochemical interactions are dominant, rather than electrostatic forces. This suggests that the CTAB chemical interaction dominates over electrostatic repulsion. In contrast, PSS-coated AuNRs are negatively charged and could bind by electrostatic attraction with the polar phospholipids in the DOPC monolayer, resulting in degradation of the voltammetric current peaks. These findings are in good agreement with previous toxicological studies, in which the effect of

surface charge is a dominant factor on toxicity. Because bilayer cell membranes are negatively charged [14-16], positively charged particles show increased toxicity [17,18] as a result of greater electrostatic interaction.

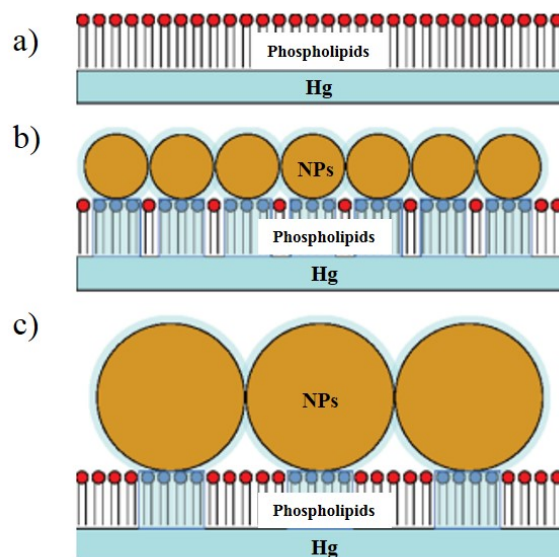


Figure 7–9: Schematic view of NPs interaction with the phospholipid membrane, including a) deposited DOPC monolayer on the Hg surface; b) small NPs adsorbed on the monolayer with large interfacial contact area illustrated in blue area; and c) large NPs adsorbed on the monolayer showing smaller interfacial contact area. (Figure taken from Ref. [7]).

7.3 Conclusion

Even though ultrasmall AuNPs can cause an interaction with the model membrane which may indicate toxicity, gold nanostructures still have a relatively high biocompatibility. It can be concluded that Au nanostructures do not significantly interact with the DOPC monolayer in term of their particle morphologies. Only the smallest size of AuNPs show a significant interaction. The presence of agglomeration in the dispersions is also an effect to take into consideration.

The effect of the surface coating on the Au nanostructure, however, appears to be the dominating factor controlling membrane interaction, depending on the type of surface coating. The relative order of interaction with the DOPC-coated Hg electrode was CTAB > PSS > CTAC > Citrate-coated Au nanostructures after the C/R purification step. Hence, citrate- and PSS-coated gold nanostructures with a dimension larger than 20-25 nm should exhibit little cell membrane interaction and would be suitable candidates in terms of their use in healthcare applications. From these results we can also predict the response of SiO₂-coated AuNRs. With their relatively large size in the longitudinal dimension, only the effect of the

SiO₂ should be observed. The effect of SiO₂ nanoparticles is described in [7] and suggests that SiO₂ structures of this size should present little interaction.

7.4 References

- [1] Vakurov, A., et al., *ZnO nanoparticle interactions with phospholipid monolayers*. Journal of Colloid and Interface Science, 2013. **404**: p. 161-168.
- [2] Hapeman, C.J., et al., *Agrochemical and Nutrient Impacts on Estuaries and other aquatic systems*. Journal of Agricultural and Food Chemistry, 2002. **50**(15): p. 4382-4384.
- [3] Lok, C.-N., et al., *Proteomic Analysis of the Mode of Antibacterial Action of Silver Nanoparticles*. Journal of Proteome Research, 2006. **5**(4): p. 916-924.
- [4] Coldrick, Z., et al., *Phospholipid monolayer coated microfabricated electrodes to model the interaction of molecules with biomembranes*. Electrochimica Acta, 2009. **54**(22): p. 4954-4962.
- [5] Ringstad, L., et al., *An Electrochemical Study into the Interaction between Complement-Derived Peptides and DOPC Mono- and Bilayers*. Langmuir, 2008. **24**(1): p. 208-216.
- [6] Nelson, A. and N. Auffret, *Phospholipid monolayers of di-oleoyl lecithin at the mercury/water interface*. Journal of Electroanalytical Chemistry, 1988. **244**(1-2): p. 99-113.
- [7] Vakurov, A., R. Brydson, and A. Nelson, *Electrochemical Modeling of the Silica Nanoparticle–Biomembrane Interaction*. Langmuir, 2012. **28**(2): p. 1246-1255.
- [8] Ormategui, N., et al., *Interaction of poly(N-isopropylacrylamide) (pNIPAM) based nanoparticles and their linear polymer precursor with phospholipid membrane models*. Bioelectrochemistry, 2012. **87**: p. 211-219.
- [9] Vakurov, A., et al., *Significance of particle size and charge capacity in TiO₂ nanoparticle-lipid interactions*. Journal of Colloid and Interface Science, 2016. **473**: p. 75-83.
- [10] Zhang, S., et al., *Electrochemical modelling of QD-phospholipid interactions*. Journal of colloid and interface science, 2014. **420**: p. 9-14
- [11] Wiliam, N., et al., *The interaction of gold and silver sub-micron particle dispersions with phospholipid layers: effect of particle size, concentration, coating*

- and aggregation state.* in Proceeding paper in submission to Langmuir, 2019. The University of Leeds.
- [12] Peterson, U. et al., *Origin of membrane dipole potential: Contribution of the phospholipid fatty acid chains.* Chemistry and Physics of Lipids, 2002. **117**(1): p. 19-27.
- [13] Brockman, H., *Dipole potentials of lipid membrane.* Chemistry and Physics of Lipids, 1994. **73**(1-2): p. 57-79.
- [12] Schaeublin, N.M., et al., *Surface charge of gold nanoparticles mediates mechanism of toxicity.* Nanoscale, 2011. **3**(2): p. 410-420.
- [13] Carnovale, C., et al., *Identifying Trends in Gold Nanoparticle Toxicity and Uptake: Size, Shape, Capping Ligand, and Biological Corona.* ACS Omega, 2019. **4**(1): p. 242-256.
- [14] Cooper, G.M., *The Cell: A Molecular Approach.* 2nd edition. Sunderland (MA): Sinauer Associates; 2000. Structure of the Plasma Membrane. Available from: <https://www.ncbi.nlm.nih.gov/books/NBK9898/>
- [15] Ma, Y., et al., *Introducing Membrane Charge and Membrane Potential to T Cell Signaling.* Front Immunol, 2017. **8**: p. 1513.
- [16] Chen, B., et al., *Targeting Negative Surface Charges of Cancer Cells by Multifunctional Nanoprobes.* Theranostics, 2016. **6**(11): p. 1887-1898.
- [17] Wang, C., et al., *Gold nanoparticle-based colorimetric sensor for studying the interactions of β -amyloid peptide with metallic ions.* Talanta, 2010. **80**(5): p. 1626-1631
- [18] Yah, C.S., *The toxicity of Gold Nanoparticles in relation to their physiochemical properties.* Biomedical Research, 2013. **24**: p. 400-413.

Chapter 8 Conclusions and future work

This thesis has successfully synthesized well-controlled and reproducible Au nanostructures via a wet-chemical synthesis approach. These consisted of AuNPs, AuNRs, AuNBP, and AuNTs, with absorption spectra that could be tuned over the NIR region. Characterization of the synthesized nanostructures was undertaken using DLS and TEM imaging. Optical and plasmonic properties were investigated using uv-vis spectroscopy. Electron energy loss spectroscopy (EELS) revealed plasmonic properties particularly the electric field distribution and coupling effects in Au nanostructures. Additionally, the thermal stability was investigated through in-situ TEM heating and a thermal deformation mechanism resulting from heat treatment has been proposed. Finally, the electrochemical interaction of the Au nanostructures with a model phospholipid monolayer has been used to investigate their potential toxicity.

Firstly, wet chemical synthesis approaches were studied and employed to develop novel Au nanostructure with NIR absorption spectra. Tunable Au nanostructures with differing optical properties including AuNPs of differing sizes, AuNRs with various aspect ratios, AuNBPs with different ARs, and AuNTs with different edge lengths were achieved. Useful synthesis parameters have been proposed to engineer the SPR of the NPs over the NIR region.

Secondly, plasmonic properties of Au nanostructures have measured using experimental uv-vis spectroscopy and compared with absorption spectra obtained using finite element COMSOL simulations. The electric field enhancement of individual Au nanostructures of different morphologies and the coupling effect between Au nanoparticle clusters were both investigated using EELS.

Thirdly, the effect of heat treatment on the differing Au nanostructures was investigated using in-situ TEM heating experiment. The thermal stabilities have been discussed and a thermally activated deformation mechanism proposed.

Finally, the toxicology of the different Au nanostructures has been investigated using an electrochemical sensor based on a model phospholipid (DOPC) monolayer membrane and the results discussed in terms of the size, shape, and surface coating of the Au nanostructure.

8.1 Research summary

Chapter 4: Citrate-stabilized AuNPs with progressively increasing size were successfully synthesised by a modified seed-step by step growth synthesis method using citrate reduction. This used previously synthesized AuNPs as starting seed particles for further growth. For elongated Au nanostructures, CTAB acts as a structural guiding surfactant to form a rod-like particle shape, and well-controlled and reproducible CTAB-capped AuNRs with various ARs were produced using a kinetically controlled modified seeded mediated method. By increasing the amount of AgNO_3 up to 350 L, the AR of the AuNRs can be tuned up to a value of 4.2 which exhibited a longitudinal SPR in the NIR region. CTAB-capped AuNBPs were fabricated from twinned seeds formed from a citrate seed solution in a seed-mediated synthesis method. The longitudinal SPR of AuNBPs were engineered to lie in the NIR region by varying the seed amount (80 μL) injected into the growth solution. An increase in gold ion concentration resulted in a decrease of rod AR. Lastly, CTAC-stabilized AuNTs were successfully synthesized with an increasing edge length, via pH adjustment, so as to provide an SPR in NIR region. Finally surface modification of CTAB-capped AuNRs with a PSS-coating resulted in a red-shift of the SPR which can provide more suitable optical and toxicological properties for Au nanostructures used in biomedical applications.

Chapter 5: The plasmonic properties of Au nanostructures were investigated using STEM/low-loss EELS analysis. The surface plasmon modes, electric field enhancement, and the coupling effect between nanostructures were spatially characterized. EELS results showed good agreement results with FEM computational simulations and experimental uv-vis spectra. The optical and plasmonic properties of Au nanostructures are unique properties which are size- and shape-dependent. The localized SPR maps exhibited localized field enhancement at the sharp tips of the particles. By increasing the curvature of the particles (i.e. a sharper tip or a higher AR), the SPR mode can be shifted into the NIR region with strong field enhancement. However, coupling effects resulting from clusters of particles, where two distinct hybridized SPR modes co-exist could directly affect the SPR response and its frequency.

Chapter 6: The thermal properties of Au nanostructures were investigated by in-situ TEM heating experiments. By monitoring the morphology of the particles as a function of temperature, the useful range of temperatures for the different nanostructures whereby heating does not significantly affect the optical properties was determined. A thermally driven deformation mechanism was proposed according to curvature driven surface diffusion where atoms diffuse from areas of high radii of curvature towards areas with lower radii of curvature. It was found that the thermal stability of Au nanostructures followed the pattern from most stable to least stable as follows: AuNPs > AuNTs > AuNBPs > AuNRs. The proposed useful

ranges of temperature were up to 100°C, 200°C, 800°C, for CTAB-capped AuNRs, CTAB-capped AuNBPs and CTAC-stabilized AuNTs, respectively. The thermal stability of particles was increased by surface modification of the NPs from a CTAB coating, through PSS and finally to a silica coating.

Chapter 7: The interaction of Au nanostructures, consisting of citrate-stabilized AuNPs, CTAB-capped AuNRs, PSS-capped AuNRs and CTAC-stabilized AuNTs, with a model membrane based on DOPC on an Hg/Pt electrode was measured the RCV. Changes in the capacitance current peaks were monitored after injection of Au nanoparticles. The effects of morphology and surface coating of Au nanostructures on biomembrane activity were investigated. It was found that generally the Au nanostructures exhibited high biocompatibility and did not cause significant interaction with the DOPC monolayer in terms of their morphology. However, the size of the NPs can affect the interaction and cause a degradation of the current peak with smaller AuNPs with diameter of ca. 20 nm showing a significant interaction. Additionally, the surface coating of Au nanorods was found to be a more significant effect on the interaction with the model membrane with the order of interaction ranging from CTAB > PSS > CTAC > Citrate coated Au nanostructures. Hence this suggests that citrate- and PSS-coated gold NPs with dimensions larger than approximately 20-25 nm would be good candidates to avoid a toxicological response.

8.2 Main findings from the research

- This research demonstrates a full characterization of Au nanostructures, including AuNPs, AuNR, AuNBPs, and AuNTs, in terms of their structural properties, optical and plasmonic properties, thermal properties, and their interaction with a model biomembrane. This helps select potential candidate nanostructures for use in photothermal healthcare applications. Based on these findings, the most suitable candidates for potential application are: 1) PSS-coated AuNRs with AR over 4 due to their facile synthesis method; and/or 2) CTAC-capped AuNTs with an edge length over 100 nm because of their excellent SPR and high thermal stability.

- These findings may also be of use for possible gold nanostructures requiring similar criteria for other applications such as plasmonic sensing and catalytic applications.

- This research demonstrates the potential novel synthesis methods for Au nanostructures that allow engineering of their SPR absorption into the NIR region via control of their size and shape.

- This research has clearly demonstrated the spatially resolved plasmonic properties of individual Au nanostructure through STEM/EELS measurements. The maps of localized

SPR field enhancements map including coupling effects between nanostructures can provide better understanding for the design of gold nanostructures with an SPR in the NIR region and to provide hot spot area of high field intensity.

- This research demonstrates the useful range of temperatures over which there is no change in SPR response, which would benefit all applications of gold nanostructures.

- This research demonstrates the key factors which govern the interaction between gold nanostructures and model bio-membranes interaction helping the design of suitable candidate nanostructures for healthcare applications.

8.3 Future work

There are number of research areas that would be benefit from future work. These may be categorized as follows:

Synthesis method development

- The synthesis conditions for Au nanostructures could be changed to provide more homogeneous samples designed for specific SPR absorption. For example, AuNRs could be synthesised with even longer ARs (AR~4-6) by employing bi-surfactants such as CTAB and BDAC. This idea could equally apply in the synthesis of AuNBPs to provide higher ARs.
- Particle separation in a post-synthesis protocol could be further investigated, benefitting samples such as AuNBPs that contain by-products leading to increased homogeneity of the samples.
- Other surface modification procedures, such as different surfactant coatings and ligand exchange could be studied instead of PSS and silica-coated Au nanostructures. Potential surface functionalization candidates include PEG and MUA.

Characterization methods

- The use of in-situ TEM heating can investigate real-time deformation mechanisms. More supporting data on the thermal properties of Au nanostructures would be of interest for morphologies such as cubes, dumbbell-liked NPs, nanostars, and even more complex structures.
- In principle EELS could highlight and expand the knowledge on how Au nanostructures interact and respond in real plasmonic systems.
- To identify more clearly the effect of silica coated AuNRs on bio-model membrane interaction, the synthesised silica coated AuNRs should be investigated using RCV

testing. Moreover, the effect of the concentration of NPs needs to be considered to provide more data in terms of their actual use in biomedical applications.

Applications

- Synthesised particles such as high AR PSS-AuNRs and large edge length AuNTs could be applied in photothermal treatment for cancer therapy. The effect of heat generation should be studied by both modelling and by experiment in living cells. Additionally, different surface functionalization using, for example PEG and MUA could help accelerate their advance in biomedical applications.
- In-vitro cellular uptake studies of the proposed Au nanostructures should be undertaken and provide useful data on their potential application and toxicology.
- The findings of this research could attract interest, not only in healthcare applications, but also in applications involving photocatalysis and plasmonic sensing.